



HAL
open science

Novel ultra-dense thin film and alternative micro-structured scintillators for synchrotron X-ray imaging

Laura Wollesen

► **To cite this version:**

Laura Wollesen. Novel ultra-dense thin film and alternative micro-structured scintillators for synchrotron X-ray imaging. Physics [physics]. Université Claude Bernard - Lyon I, 2023. English. NNT : 2023LYO10077 . tel-04639362

HAL Id: tel-04639362

<https://theses.hal.science/tel-04639362>

Submitted on 9 Jul 2024

HAL is a multi-disciplinary open access archive for the deposit and dissemination of scientific research documents, whether they are published or not. The documents may come from teaching and research institutions in France or abroad, or from public or private research centers.

L'archive ouverte pluridisciplinaire **HAL**, est destinée au dépôt et à la diffusion de documents scientifiques de niveau recherche, publiés ou non, émanant des établissements d'enseignement et de recherche français ou étrangers, des laboratoires publics ou privés.



**THESE de DOCTORAT DE
L'UNIVERSITE CLAUDE BERNARD LYON 1**

**Ecole Doctorale ED52
Physique et Astrophysique (PHAST)**

Discipline : Physique

Soutenue publiquement le 23/05/2023, par :
Laura Wollesen

**Nouveaux films minces scintillants
ultra-denses et solutions alternatives
pixélisées pour l'imagerie synchrotron
par rayon X**

Devant le jury composé de :

Pillonnet, Anne Professeure des Universités, Université Lyon1

Présidente

Camy, Patrice Professeur des Universités, Université De Caen

Rapporteur

Potdevin, Audrey Maître de Conférences, Université Clermont

Rapporteuse

Pena Revellez, Alexandra Chargée de Recherche, Université Grenoble Alpes

Examinatrice

Dujardin, Christophe Professeur des Universités, Université Lyon1

Directeur de thèse

Douissard, Paul-Antoine Ingénieure, ESRF Grenoble

Co-Directeur de thèse

Tran Caliste, Thu Nhi Ingénieure, ESRF Grenoble

Invitée



DOCTORAL THESIS FROM THE UNIVERSITY CLAUDE BERNARD LYON 1

Defense date: 23/05/2023, by:
Laura Wollesen

Novel ultra-dense thin film and alternative micro-structured scintillators for synchrotron X-ray imaging

Members of the jury:

Pillonnet, Anne	University professor, Université Lyon1	President
Camy, Patrice	University professor, Université De Caen	Referee
Potdevin, Audrey	Maître de Conférences, Université Clermont	Referee
Pena Revellez, Alexandra	Chargée de Recherche, Université Grenoble Alpes	Examiner
Dujardin, Christophe	University professor, Université Lyon1	Thesis director
Douissard, Paul-Antoine	Engineer, ESRF Grenoble	Thesis co-director
Tran Caliste, Thu Nhi	Engineer, ESRF Grenoble	Invited

Mor og far, tak for jeres evige støtte.

Acknowledgements

First of all, a big thanks to Patrice Camy and Audrey Potdevin for reading and evaluating my thesis. I hope you enjoyed it.

Many have helped me in various ways during the last three and a half years, and for each and one of them, I am especially grateful for answering my many questions.

My ESRF supervisor, Paul-Antoine Douissard, thank you for being patient and accepting that I am "a bit" stubborn. You have taught me so much and have been a great support. My university supervisor, Christophe Dujardin, thank you for believing in me and letting me know when I do well. This has been very important for me during these years.

I want to thank the detector unit for welcoming me to the ESRF. A few of the members I owe special thanks to. Julien Mathieu, for always taking the time to help when needed and especially for testing and finding the best pain au chocolate in Grenoble. Kristof Pauwels, for always taking the time to discuss the simulation tool and especially for writing working code for me. Simon Benichou, for being the executor of some of my ideas and making them real with 3D printing. Outside the detector unit, many more from the ESRF have supported me. Alexander Rack, thank you for being my mentor and including me on your mailing list, sharing publications on scintillators. Phil Cook, the beamline scientist at BM05, should have a big thanks for the help on the beamline and for always being kind. Thu-Nhi Tran Caliste and Carsten Detlefs for taking me on adventures.

Outside ESRF, more have helped perform various experiments and answered my questions about those experiments and the results. Here among are Irina Sniguirev for performing SEM-EDX on my many samples, Jeremie Margueritat for performing Raman measurements, Brice Gautier for performing PFM, and Ingrid C. Infante for performing XRD. Ingrid and Brice should have a special thanks for introducing me to the ferroelectric community and finding the titanates samples interesting. Pavel Loiko and Gurvan Brasse, besides helping me perform various measurements, I owe you special thanks for welcoming me at CIMAP.

Genevieve, my French teacher for more than two years, you should have a big thanks for your extensive patience with me. You made a lot of effort trying to make me accept French. I am sorry I did not do better.

Covid hit a few months after I arrived in Grenoble. As much as I hated being stuck inside and unable to go to the laboratory and perform experiments, it ensured the manuscript of my first publication. So a tiny thanks to covid for forcing me to sit down and write.

I am so lucky to have ensured myself a Grenoble family. I cannot thank each one personally here because it would end up being many pages long, but I am grateful for each of you and the times we spent together. Grateful for the adventures, the board games, the beers, the dancing, and the support.

This final part is dedicated to my family.

Kære familie. Jeg ved udemærket godt, at I ikke kommer til at læse en eneste side af denne afhandling. Det kan jeg godt forstå, den er skide lang og kedelig. Jeg har dog gemt nogle hyggelige billeder i den, som jeg håber I vil nyde når I lige bladre igennem. Jeg er ikke sikker på I ved det, men uden jeres opbakning ville jeg ikke være hvor jeg er i dag. Jeres støtte og den stolthed jeg kan mærke I har for hvor jeg er og hvad jeg har opnået, giver mig gnisten til at knokle videre. Tak for jer.

Contents

Acknowledgements	vii
List of Abbreviations	xiii
Résumé	xv
Summary	xix
1 Introduction	1
1.1 Synchrotron radiation	1
1.1.1 ESRF-EBS and the DDP	1
1.1.2 X-ray imaging	3
1.1.2.1 Techniques	4
1.1.2.2 Detectors	5
1.1.2.3 Experimental goals	6
1.1.3 Scintillators	8
1.1.3.1 Types	8
1.1.3.2 Physics of scintillation process	9
1.1.3.3 Interaction mechanisms	10
1.1.3.4 Materials and forms	11
1.1.4 Scintillating single crystalline films	13
1.1.5 Detector characteristics	15
1.2 High spatial resolution X-ray imaging detectors	16
1.2.0.1 Spatial resolution limitations	16
1.2.0.2 The high-energy, high-resolution challenge	18
1.2.1 Detector characterization	18
1.2.1.1 Detective quantum efficiency	18
1.2.1.2 Resolution and contrast	19
1.2.1.3 The slanted edge method	21
1.2.2 State-of-the-art scintillators	23
1.3 Liquid Phase Epitaxy	24
1.3.1 The setup	24
1.3.2 The procedure	25
1.3.3 Concept and considerations	26
1.4 This thesis	29

2	Predicting the spatial response of single crystal film scintillators	31
2.1	Introduction	31
2.2	Geant4, Monte Carlo simulation tool	32
2.2.1	Geant4 configuration	33
2.2.2	Blurring by optics	34
2.2.3	Investigated materials	35
2.3	Simulation outputs	36
2.3.1	Energy Deposition	36
2.3.2	Spatial resolution and contrast	37
2.4	Results	38
2.4.1	Influence of X-ray fluorescence	38
2.4.2	Combined influence of SCF and substrate	43
2.4.3	Including optics	44
2.4.4	A Figure of Merit	46
2.5	Experimental validation	48
2.6	Prospective materials	50
2.6.1	Light yield considerations	52
2.7	Conclusions	53
3	Growth of ultra-dense thin films	55
3.1	Introduction	55
3.1.1	Project evolution	56
3.1.2	Simulations	59
3.2	Growth of hafnates	61
3.2.1	LPE conditions	61
3.2.2	Film growth	64
3.2.3	Elemental composition	65
3.2.4	Surface morphology	66
3.3	Structural considerations	73
3.3.1	Fluorite, pyrochlore, and delta structures	73
3.3.2	Raman spectroscopy	76
3.3.3	X-ray diffraction	77
3.4	Scintillating $\text{Lu}_2\text{Hf}_2\text{O}_7:\text{Eu}$	82
3.4.1	Literature	82
3.4.2	Luminescence	83
3.4.2.1	Annealing procedures	83
3.4.2.2	Photoluminescence	83
3.4.2.3	Radioluminescence	85
3.4.3	Light output	87
3.4.4	Decay	88
3.4.5	At the beamlines	89
3.4.5.1	Spatial resolution	89

3.4.5.2	Imaging at beamlines	92
3.5	Possible optimization	96
3.5.1	The substrate	96
3.5.2	The films	97
3.6	Conclusions	98
4	Preparation and growth of micro-structured scintillators	99
4.1	Introduction	99
4.1.1	Micro-structures	99
4.1.1.1	Concept	101
4.1.1.2	Substrates	102
4.2	Laser treatment of substrates	103
4.2.1	Patterning methods	103
4.2.1.1	Sample reference names	104
4.2.2	Structural changes	104
4.2.2.1	Raman mapping	104
4.2.2.2	X-ray diffraction	105
4.3	Liquid phase epitaxy on laser-treated substrates	108
4.3.1	Substrate preparation	108
4.3.2	Growth	110
4.4	Micro-structured LSO:Tb	111
4.4.1	Sample morphology	111
4.4.2	Structural considerations	116
4.4.2.1	X-ray diffraction	116
4.4.2.2	Raman spectroscopy	118
4.4.3	Luminescence	119
4.4.3.1	Photoluminescence	119
4.4.3.2	Radioluminescence	120
4.4.3.3	Comparison	121
4.4.3.4	Color camera	122
4.5	Micro-structured GGG:Eu	123
4.5.1	Sample morphology	123
4.5.1.1	Etching	128
4.5.2	Structural considerations	128
4.5.2.1	X-ray diffraction	128
4.5.2.2	Raman spectroscopy	131
4.5.3	Luminescence	131
4.5.3.1	Photoluminescence	131
4.5.3.2	Radioluminescence	133
4.5.3.3	Comparison	134
4.6	Comparison and optimization	135
4.6.1	Results	135

4.6.1.1	Laser treatment and LPE growth	135
4.6.1.2	Morphology	135
4.6.1.3	Structure	135
4.6.1.4	Luminescence	136
4.6.2	Future perspectives	136
4.7	Conclusions	139
Bibliography		141
A	Published: Scintillating thin film design for ultimate high resolution X-ray imaging, 2022	151
B	Published: Tunable crystalline structure and electrical properties in (Pb,Sr)TiO₃ films grown by Liquid Phase Epitaxy, 2023	161
C	Experimental technical details	175
C.1	Microscopes	175
C.1.1	Optical	175
C.1.2	Confocal	175
C.2	Raman spectroscopy and photoluminescence	175
C.3	Radioluminescence and light output	175
C.4	Diffractionmeter	176

List of Abbreviations

CCD	Charge-Coupled Device
CDIC	Circular Differential Interference Contrast
CT	Computed Tomography
CN	Coordination Number
DoF	Depth of Field
DQE	Detective Quantum Efficiency
DDP	Detector Development Plan
ESF	Edge Spread Function
ESRF	European Synchrotron Radiation Facility
EBS	Extremely Brilliant Source
FFT	Fast Fourier Transform (FFT)
FoV	Field of View
LSF	Line Spread Function
LPE	Liquid Phase Epitaxy
MTF	Modulation Transfer Function
NA	Numerical Aperture
OTF	Optical Transfer Function
PSF	Point Spread Function
QE	Quantum Efficiency
SNR	Signal-to-Noise Ratio
SCF	Single Crystalline Film
sCMOS	scientific Complementary Metal–Oxide–Semiconductor
XRD	X-ray Diffraction
Z	Atomic number
GGG	$\text{Gd}_3\text{Ga}_5\text{O}_{12}$
GdAP	GdAlO_3
LuAG	$\text{Lu}_3\text{Al}_5\text{O}_{12}$
LSO	Lu_2SiO_5
LYSO	$\text{Lu}_{1.8}\text{Y}_{0.2}\text{SiO}_5$
YbSO	Yb_2SiO_3

Résumé

Introduction

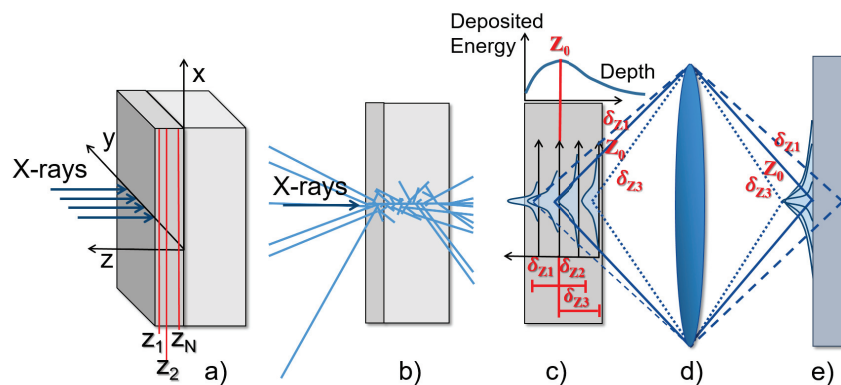
Les scientifiques utilisent le rayonnement synchrotron pour étudier différents types d'échantillons et extraire des informations sur la structure atomique, la micro-structure, la teneur en éléments et bien plus encore. Le rayonnement synchrotron a connu un développement spectaculaire depuis ses débuts et, ces dernières années, de nouvelles sources synchrotron de 4^{ème} génération sont lancées. L'ESRF-EBS est le premier et actuellement le seul synchrotron de 4^{ème} génération à haute énergie au monde. Cette modernisation de l'ESRF a permis d'obtenir une cohérence et une brillance du faisceau de rayons X inégalées, ce qui rend accessible à un plus grand nombre les expériences utilisant rayons X à hautes énergies. Pour tirer véritablement parti de cette nouvelle génération de sources synchrotron, les détecteurs doivent eux aussi être mis à niveau et donc faire l'objet de recherches et de développements.

Pour réaliser une imagerie à l'aide de rayons X avec la plus haute résolution spatiale et un contraste optimum, des films minces scintillants, dont l'épaisseur correspond à la profondeur de champ de l'optique, sont requis. En conséquence de cette faible épaisseur, l'efficacité d'absorption des rayons X est considérablement réduite, mais elle peut être maximisée en utilisant des scintillateurs à très haute densité et un numéro atomique effectif Z élevé. Une autre approche consiste à utiliser des scintillateurs micro-structurés qui peuvent, en principe, restreindre la diffusion latérale de la lumière en la guidant vers le capteur, tout en préservant une résolution spatiale acceptable, combinant ainsi efficacité et résolution.

Ce projet de doctorat vise à développer des scintillateurs nouveaux alternatifs permettant de rivaliser avec les scintillateurs de pointe actuellement utilisés dans les synchrotrons pour les expériences d'imagerie par rayons X à haute résolution. Les deux approches discutées ci-dessus ont été utilisées pour atteindre l'objectif de la thèse. La première consiste à développer par la méthode d'Épitaxie en Phase Liquide (LPE) des films minces scintillants à très haute densité et numéro atomique effectif élevés. Pour ces composés, la Fonction de Transfert de Modulation (MTF), la résolution spatiale, ainsi que le dépôt d'énergie effectif dans les films scintillants, ont été étudiés au préalable à l'aide d'un outil de simulation mis au point au sein du groupe détecteur de l'ESRF. La réponse spatiale potentielle a été étudiée par un outil de simulation et a donc été évaluée au préalable. La seconde approche consiste à faire croître des scintillateurs sous forme de couches minces de manière micro-structurée toujours en utilisant la même technique d'LPE.

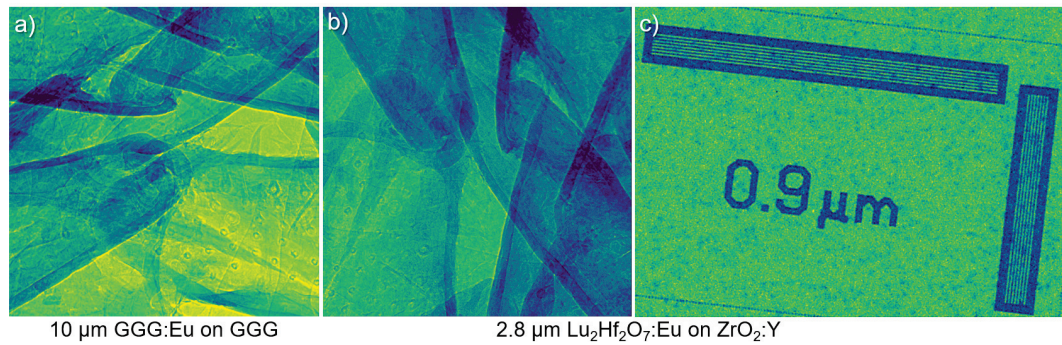
Prédire la Fonction de Transfert de Modulation des films scintillants monocristallins

Un outil de simulation Monte Carlo Geant4 et des calculs analytiques développés ultérieurement ont été utilisés pour prédire la MTF des films scintillants monocristallins. L'outil estime la probabilité qu'une particule se déplaçant dans le matériau interagisse avec un type d'atome spécifique et décrit le dépôt d'énergie. La distribution spatiale de l'énergie déposée dans les films est ensuite extraite et la fonction de dispersion linéaire sur-échantillonnée (LSF) est déduite. À partir de la LSF, la MTF peut être obtenue.



Représentation schématique du concept de l'outil de simulation.

L'influence de la fluorescence X sur la résolution spatiale a été mise en évidence à partir des LSF et MTF simulées pour des énergies des rayons X au voisinage des seuils d'absorption des éléments composants le film mince et leurs substrats. L'utilisation d'énergies supérieures aux énergies des seuils K d'absorption d'éléments à Z élevés dans le substrat entraîne une dégradation significative de la MTF, alors qu'au-dessus d'éléments à Z élevés du film, la MTF est au contraire améliorée. La diminution s'explique par le fait que la fluorescence du substrat atteint le film et dépose de l'énergie loin de l'interaction initiale entre le rayon X primaire et le film. L'augmentation s'explique par le fait que les photoélectrons créés dans le film juste au-dessus de son seuil K, ont par conséquent une longueur d'atténuation courte et déposent donc l'essentiel de l'énergie très près du point d'interaction initial. Une figure de mérite est proposée pour évaluer les performances potentielles des films minces scintillants. Elle comprend la MTF à 500 lp/mm (correspondant à des caractéristiques de l'ordre du micron) et la fraction d'énergie déposée dans le film qui dépend de l'énergie des rayons X entrants. Cela permet d'évaluer la réponse du contraste en fonction de la fréquence spatiale (MTF) et l'efficacité d'absorption du scintillateur, qui sont toutes deux essentielles pour réaliser des expériences d'imagerie par rayons X à haute résolution spatiale dans les synchrotrons. Les simulations ont été validées expérimentalement pour des scintillateurs actuels et confirment ainsi le bon fonctionnement de l'outil.



Radiographies utilisant GGG:Eu et Lu₂Hf₂O₇:Eu15%.

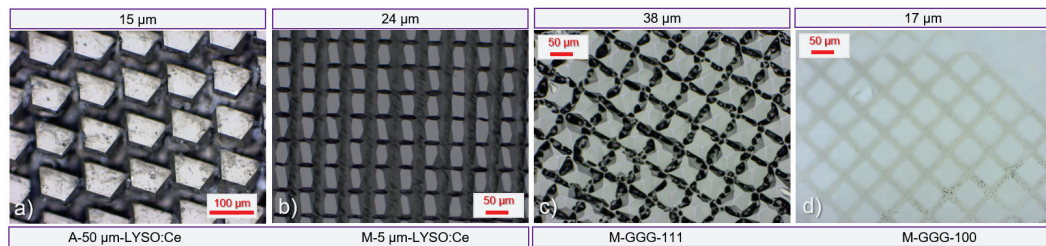
Croissance de couches minces scintillantes ultra-denses

Divers composés de hafnate ont été développés avec succès par EPL sur des substrats de ZrO₂:Y avec les orientations cristallographiques (100) et (111). Parmi ces compositions Lu₂Hf₂O₇ possède une densité et un nombre Z effectif très élevés, ce qui la rend potentiellement idéale pour l'imagerie à haute résolution spatiale pour les sources synchrotron. La structure a été étudiée par diffusion Raman et Diffraction par Rayons X (DRX) et s'est avérée correspondre, pour tous les films, à la structure fluorine désordonnée avec le groupe d'espace *Fm3m*, similaire à celui du substrat. Les différences de paramètres de maille du réseau ont été extraits et étaient tous inférieurs à 1%, ce qui indique une bonne correspondance structurale entre les films et le substrat. Lu₂Hf₂O₇ dopé à l'euporium a présenté des propriétés de scintillation modérée. Les MTF des échantillons Lu₂Hf₂O₇:Eu ont été extraites expérimentalement et une bonne réponse spatiale a été trouvée. Cependant, ces MTF mesurées sont inférieures aux MTF simulées. Ceci est attribué à la scintillation intrinsèque du substrat, même si celle-ci est extrêmement faible en comparaison de celle de la couche. En appliquant un filtre optique passe-bande, qui devrait soustraire partiellement l'émission du substrat, la MTF des échantillons étudiés est améliorée, ce qui signifie qu'un meilleur contraste est obtenu. Le rendement de scintillation augmente avec la teneur nominale en euporium, pour atteindre la valeur de 10 % du standard de référence pour une concentration d'euporium de 45% dans la solution. Lors de l'utilisation des films hafnates pour les radiographies et la tomographie, les faibles fréquences spatiales sont résolues, en particulier lorsque les expériences sont réalisées en dessous du seuil d'absorption K du zirconium.

Préparation et croissance de scintillateurs microstructurés

Des scintillateurs microstructurés GGG:Eu et LSO:Tb ont été développés avec succès par PLE sur des substrats traités par laser picoseconde. Deux types de traitements laser ont été testés, l'ablation et la modification, et avec ceux-ci, le modelage des tranchées a été effectué. Après croissance PLE, la morphologie des piliers obtenus varie en fonction du composé et de l'orientation de la surface du substrat utilisé.

Pour tous les cas étudiés, il y a également une croissance dans les tranchées. Cette croissance est plus importante pour les substrats ayant subi une ablation laser que pour les substrats modifiés. La structure atomique et les propriétés lumineuses des microstructures sont similaires à celles des films non structurés. La lumière issue de la scintillation semble être extraite favorablement des piliers pour les micro-structures obtenues sur les substrats modifiés par laser, alors qu'elle est extraite en grande partie par les tranchées pour les substrats ayant subi une ablation laser. L'hypothèse retenue est la rugosité plus importante et à la croissance relativement importante dans les tranchées résultantes d'une ablation.



Morphologie des piliers pour différents composés et orientations.

Cette étude démontre que les scintillateurs microstructurés peuvent effectivement être obtenus par LPE sur des substrats traités au laser picoseconde.

Summary

Scintillators with high stopping power for high spatial resolution X-ray imaging at synchrotrons have been developed by employing two approaches.

The first approach was to grow thin Single Crystalline Films (SCFs) of high density and high effective atomic number by Liquid Phase Epitaxy (LPE). This aimed to reach a high spatial resolution while maximizing the absorption efficiency of the films. Prior to LPE process development, the compounds were investigated with a Geant4, Monte Carlo simulation tool, combined with subsequent analytical calculations to evaluate their scintillating spatial response and X-ray stopping power. Following this study, ultra-high density compound, $\text{Lu}_2\text{Hf}_2\text{O}_7$, and other hafnates were successfully grown on $\text{ZrO}_2\text{:Y}$ substrates. The atomic structure of the films was confirmed to be iso-structural with the substrate and have a low lattice mismatch. It was observed that various elements could enter the structure, and the flexibility of the hafnate system for LPE growth was thereby realized. The grown films of $\text{Lu}_2\text{Hf}_2\text{O}_7$ doped with europium were detected to scintillate. However, the substrate itself displays low-intensity emission. The films have a low light output compared to state-of-the-art LPE-grown scintillators but deliver a good spatial response, validated by MTFs as well as radiography and tomography experiments.

The second approach was to grow state-of-the-art SCF scintillators in a micro-structured manner by LPE. The aim was to increase the stopping power by having tall pillars containing light while maintaining a good spatial response. LSO:Tb and GGG:Eu , were grown micro-structured onto laser-treated LYSO:Ce and GGG substrates, respectively. The morphology of the pillars varies depending on the compound and the substrate orientation. The atomic structures and luminescent properties are comparable to their normal SCF counterparts. Therefore, a proof of concept has been demonstrated.

Chapter 1

Introduction

1.1 Synchrotron radiation

Since its discovery in 1895 by Wilhelm Conrad Röntgen, X-ray radiation has been used extensively for medical purposes as well as research [1]. The following rapid evolution of X-ray sources confirms the importance of this discovery [2, 3]. Going from using only X-ray tubes to having synchrotron radiation was merely one of the first steps in an incredible evolution, and today the 4th generation synchrotrons are being taken into use, making it possible to conduct experiments scientists have only been dreaming about earlier [4]. Synchrotrons show many benefits compared to X-ray tubes, one being a much higher flux of photons and another the beam coherence. A value describing well the performance of synchrotrons is the brilliance. X-ray tubes typically have brilliance below 10^9 photons/s/mm²/mrad²/0.1%BW, where most modern synchrotrons today reach above 10^{21} photons/s/mm²/mrad²/0.1%BW (see Figure 1.1) making it possible to conduct various experiments such as imaging, scattering, and absorption spectroscopy.

1.1.1 ESRF-EBS and the DDP

The European Synchrotron Radiation Facility (ESRF) has received users since 1992 and has been striving to create the best conditions for scientists to carry out research [6]. It recently upgraded its storage ring to a 4th generation synchrotron source and started welcoming users again in August 2020. The upgrade is named the “Extremely Brilliant Source” (ESRF-EBS), and not without reason. Indeed, the upgrade led to drastic improvements in both coherence and brilliance [7]. Two other 4th generation synchrotrons are currently in operation, namely, MAX IV in Sweden [8], and SIRIUS in Brazil [9]. In addition, more upgrades are planned for current synchrotron sources worldwide, leaving promises for excellent future science [4, 10, 11]. Among these current 4th generation synchrotrons, ESRF-EBS is the only one operating at high X-ray energies and is currently the brightest synchrotron light source in the world [12, 13, 6]. Inevitably, this makes it unique, and its performance paves the way for the ESRF beamlines to perform more experiments, there among imaging, at high X-ray energies (typically above 30 keV) without compromising the X-ray flux. The high flux together with the outstanding coherence of the beam, makes phase contrast imaging

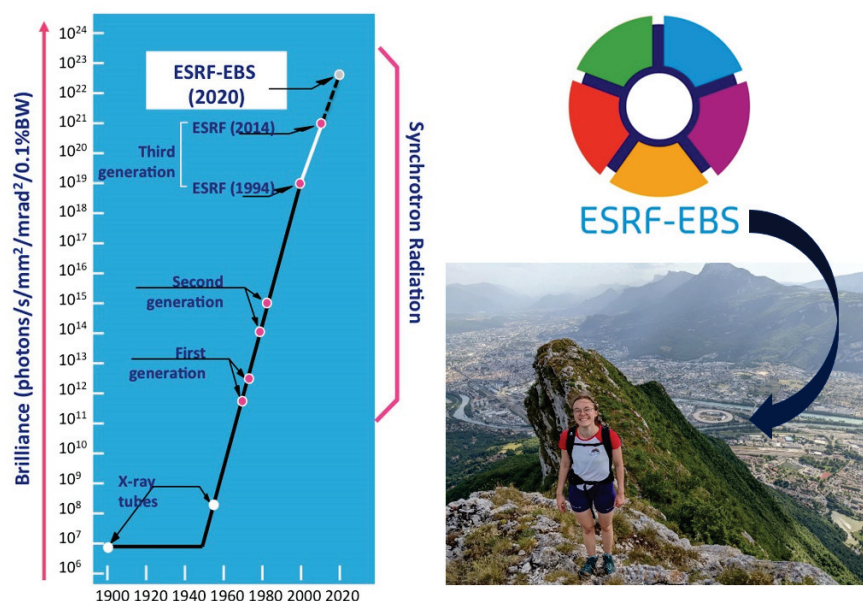


FIGURE 1.1: a) The evolution of synchrotrons in terms of the brilliance of the X-rays produced [5]. b) Photograph from Néron with the view of Grenoble and the ESRF-EBS. Photo credit: Michal Ronovský

experiments possible at larger and denser samples at high energies while obtaining incredible contrast and resolution. For example, the new ESRF BM18 beamline takes advantage of this, where at the moment, the samples are limited to a maximum of 30 kg, and 30 cm [14], which is already impressive. However, when the beamline is fully finished, it will be possible to perform imaging at objects up to 2.5x0.6 meters and 300 kg due to the possibility of using X-ray energies up to 350 keV. This will allow imaging of a full post-mortem human body, with the ability to zoom-in in any location with a spatial resolution down to 0.7 μm [15].

These high fluxes and the possibility of conducting experiments at higher X-ray energies than ever pose significant challenges to the current detectors. It is, therefore, necessary to perform elaborate research and development on the detector aspects to fully benefit from the powerful new generation of synchrotrons.

The ESRF council officially accepted the detector development plan (DDP) proposal in November 2016. This opened the possibility, both in terms of staffing and financially, to explore and develop the detector technologies that can fulfill the needs of the beamlines and the scientists using them [16, 17]. Within the DDP, new detector systems have been investigated, but also the performance of existing systems has been challenged, as well as the read-out schemes. Two great examples of new detector systems developed in the DDP framework are XIDER and SPHIRD. XIDER is a high-dynamic range detector applicable for scattering and diffraction experiments [18, 19]. The sensor is made of high Z-materials, CdTe or CdZnTe, and can efficiently detect high-energy X-rays (30-100 keV). It aims to be operated under high fluxes with high dynamic range (up to 10^{10} photons/s/mm²) and is capable of doing time-resolved

experiments due to its novel read-out scheme based on incremental digital integration [20]. The aim is to distinguish pulses in the 16-bunch filling mode of the synchrotron, reaching a time resolution of 176 ns.

SPHIRD is a direct photon-counting pixel detector being developed for coherent scattering and diffraction. It will be used at energies below 35 keV and aims to be noise-free while coping with the ESRF-EBS beam high fluxes and maintaining a high spatial resolution [21]. In addition to new detector developments, the boundaries by combining state-of-the-art components of detector systems have also been investigated for indirect X-ray detection (involving X-ray to optical photon conversion). Combining a commercial sCMOS camera with fiber-optics plate coupling and a $\text{Gd}_2\text{O}_2\text{S:Tb}$ powder-based scintillator, single-photon sensitivity was obtained [22]. Regarding data acquisition, a novel acquisition system for high-performance applications has also been developed, namely, RASHPA. It takes up the challenge of managing and storing the acquired data efficiently since the experiments performed at the beamlines now can produce data faster and in larger volumes than ever [23, 24]. These are just a few examples of what the DDP is working on and has achieved for future detector systems.

The projects of this thesis have been in the framework of the DDP as well, and the aim is to explore new scintillators for high spatial resolution X-ray imaging, also at high energies combined with high stopping power. Before moving to the details, the concepts required to understand the different projects will be presented, and an overview of the projects that have been ongoing throughout the thesis will be given.

1.1.2 X-ray imaging

Most are familiar with X-ray imaging and encounter it repeatedly throughout their life. If the doctor suspects a bone is broken, this will be investigated by radiography. Before taking an airplane to visit your loved ones at home or going on new adventures, airport security checks the luggage using X-ray imaging, ensuring restricted items will not be brought on the airplane. The technique is powerful for many reasons, one being that it is (most of the time) almost non-destructive to the material being exposed, and another that X-ray imaging makes it possible to see what the eye cannot, meaning the inner structure of a sample. At synchrotron facilities, the material exposed to X-rays is rarely living humans or luggage. Instead, researchers bring various samples to the beamlines to be investigated. The samples could be small, such as microscopic biological crystals, or larger, such as batteries, human organs, or fossils.

An example is the X-ray imaging performed at the ESRF ID19 beamline of fragile, non-hatched, fossilized dinosaur eggs of the South African dinosaur *Massospondylus carinatus* [25]. The studied clutch of fossilized eggs is shown in Figure 1.2a. Each egg was first imaged individually with a voxel (volume pixel) size of $13.11 \mu\text{m}$ with 4998 projections with an exposure time of 0.1 s for each projection. Then the resolution was increased to a voxel size of $2.98 \mu\text{m}$ to investigate the embryonic skulls closer, having 8000 projections with an exposure time of 0.25 s per projection. It was performed

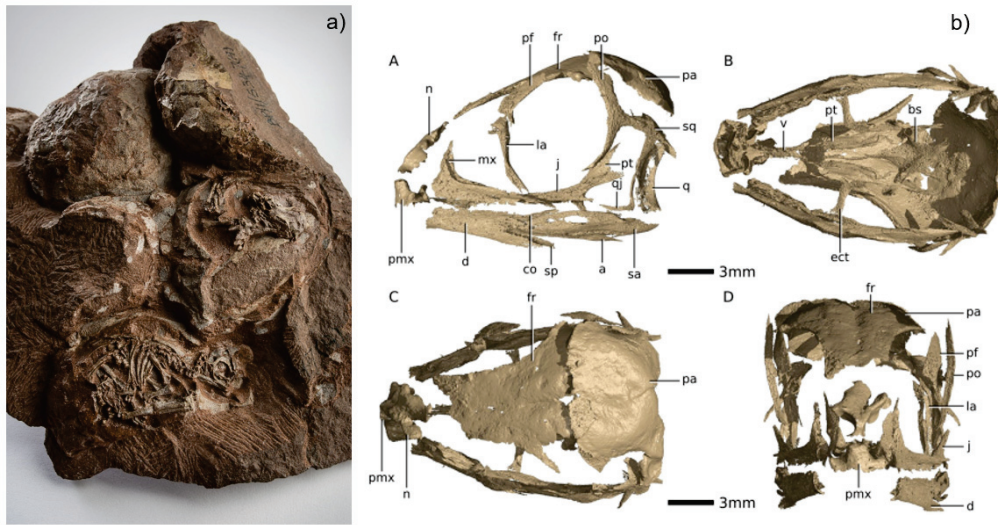


FIGURE 1.2: a) A clutch of fossilized *Massospondylus carinatus* eggs. Credit: Brett Eloff. b) From [25]. Digital reconstructions of *Massospondylus carinatus* embryonic skulls based on μ CT data measured at ID19, ESRF.

using a filtered white beam with detected total integrated energy of 175 keV and 166 keV, respectively. The research team was, from this data, able to reconstruct the skull of the embryos presented in Figure 1.2b, and found that they develop in the same order as those of crocodiles and chickens of today.

1.1.2.1 Techniques

There are various approaches to perform X-ray imaging at the ESRF beamlines. Some examples are phase contrast [26], absorption contrast [27], tomography, diffraction contrast tomography [28], topo-tomography [29], and ghost imaging [30, 31].

Absorption contrast X-ray imaging is used at synchrotron sources but also commonly in hospitals and industry. The contrast in the image depends on differences in the absorption of the incoming X-rays in the imaged sample. This will be affected by differences in density, the thickness of the sample, and the X-ray absorption K-edges of the elements composing the object of interest, where higher-density features and thicker samples absorb more X-rays and vice versa. The technique is often referred to as radiography for 2D imaging. When 3D images are reconstructed from radiographs recorded while rotating the sample, it is referred to as absorption tomography or computed tomography (CT) [32].

Phase contrast X-ray imaging is commonly employed at synchrotrons and can be performed differently. The contrast is driven by the beam coherence and the phase shift induced by it passing through the sample. The phase shift is not measured directly but is observed as variations in the beam intensity. This technique often gives better contrast than absorption contrast for samples with low Z-numbers since subtle variations in density are not detrimental. This is otherwise the case for absorption

contrast. To perform phase contrast imaging, it is crucial to have an increased sample-to-detector distance, as it enhances the contrast and to have a coherent beam. Phase contrast tomography can also be performed by rotating the sample while recording 2D images to be combined into a 3D construction. The enhanced coherence of the ESRF-EBS beam makes it possible to perform phase contrast imaging with better contrast than ever. ESRF beamline BM18 is indeed exploiting the coherence of the beam while having a higher flux at higher energies [16]. It is possible to have the detector up to 38 meters away from the sample [15] taking full advantage of the EBS beam.

1.1.2.2 Detectors

A detector is needed to record the data when performing any experiment. Depending on the experiment type and the scope of the investigation, the detector should be chosen wisely to match those needs. 2D detectors (or area detectors) are typically used to perform X-ray imaging experiments. There are various types of 2D detectors, which can be divided into two categories depending on their detection schemes: direct or indirect. *Direct detectors* have a semiconductor image sensor that converts the X-ray photons directly into an electrical signal. *Indirect detectors* have one more step involved. The X-ray photons are first converted into optical photons before reaching an imaging Charged Coupled Device (CCD) or Complementary Metal–Oxide–Semiconductor (CMOS) camera, where they are converted into an electrical signal. The screen that absorbs the X-rays and converts them into optical photons is called a scintillator. An indirect detection scheme is chosen for most X-ray imaging experiments at synchrotrons. There are several reasons for this, some being it is a much cheaper solution than direct detectors, and they can withstand intense X-ray beams without getting damaged. When working at higher X-ray energies, the electronics behind the sensor of a direct detector can be damaged. The state-of-the-art direct area detectors currently used at synchrotrons are often based on high-Z sensors instead of the otherwise typical silicon sensor. This is to increase the detection efficiency at energies above 15 keV. However, these high-Z sensors suffer from defects, which can impose issues, especially when high X-ray fluxes are used. These defects can vary with time and radiation dose, complicating the implementation of image flat field corrections. When the detector is uniformly illuminated with X-rays (not only a few pixels, as typical for X-ray diffraction experiments), another issue can be the limitation of the global count rate of the detector. Direct detectors typically have a minimum pixel size of 50 μm , which is unsuitable for imaging experiments where micron-to-sub-micron spatial resolution is required unless X-ray lenses are used for magnification. Whereas CCD or sCMOS cameras can have a pixel size down to a few microns, and by combining with optics, the effective pixel size can easily be reduced to sub-micron for indirect detection. The effective pixel size is the size of the pixel after magnification by the optics, $\text{PS}_{eff} = \text{PS}/M$. Some of these advantages and disadvantages of direct and indirect detectors are summarized in Table 1.1.

	Direct	Indirect
Advantages	High dynamic range Noise free No tails in the PSF Very high frame rates	High spatial resolution Robustness in beam Versatility (optics, scintillator) Low cost in general
Disadvantages	Expensive Large pixel size Limited count rate Defects in high-Z sensors	Noise Low abs. efficiency at high energy Tails in the PSF

TABLE 1.1: Overview of some advantages and disadvantages for direct and indirect detector systems.

Detectors can, depending on the architecture of the sensor and read-out electronics, use different operation modes, namely, photon-counting or integrating.

Photon-counting detection is generating a pulse or burst of signal from each X-ray photon impinging on the sensor. The pulses are then counted, and information such as the time of arrival of the single photon and its energy can be extracted. It can be advantageous to use photon-counting mode since a threshold above the noise level can be chosen to reject any noise, where this is not possible for integration mode detectors. Some modern pixel photon counting detectors even have several thresholds, which allow, for example, the elimination of cosmic events or high X-ray energy harmonics, typical when using synchrotron beams. Single photons can only be counted if the flux is not too high. Otherwise, photons will be missed in the count due to pile-up, and the amplitude measurement will be inaccurate or wrong. This is the typical detection mode used in direct detectors.

Integrating detection accumulates the created charge for the chosen exposure time, and the total signal is read at completion. The information is the charge generated by the total amount of photons detected during the exposure time. For X-ray imaging experiments at synchrotrons, the integration operation mode is mostly used for the indirect detectors. However, as mentioned earlier, it is also possible to use single photon counting for indirect detection [22].

1.1.2.3 Experimental goals

It is now concluded that to perform X-ray imaging at synchrotron beamlines, 2D indirect detection systems using integration operation mode are often the optimum choice. However, there are different goals when performing imaging experiments, and compromises depending on these have to be made. This section will give a few examples of the needs and aspects that can be compromised to extract the desired information from imaging experiments with various goals.

Ultrafast imaging: If the goal is to investigate ultrafast mechanisms and the spatial resolution can be compromised, a pink beam (non-monochromatic X-ray beam) can be applied to obtain a higher X-ray flux as opposed to a monochromatic beam [33]. The scintillator thickness can be increased to increase the X-ray absorption and

thereby lower the exposure time per frame, which is essential to record ultrafast events. However, a larger scintillator thickness degrades the spatial resolution of the image, which will be discussed in detail later. This approach was used in a study performing ultrafast X-ray imaging at ID19 during 3D printing that helped reveal the mechanisms of microstructure formation [34]. A pink beam was applied for the experiments, and an X-ray imaging system consisting of a 200 μm thick LuAG:Ce scintillator. A Photron FASTCAM SA-Z 2100 K at 40 kfps was applied to maintain a high time resolution. This combined setup gave a spatial resolution of approximately 4.76 μm per pixel and an exposure time of 12.5 μs .

Biological samples: For imaging of biological samples, it is generally essential to have a low radiation dose in the investigated specimen. Using very high fluxes can create radiation damage to the samples. This can be reduced with proper sample preparation, such as paraffin embedding [33]. However, this is not always possible, for example, when the sample is alive. When imaging small animals, it is also beneficial to have a large field of view. An example is the imaging of anesthetized pigs weighing more than 40 kg, a field of view of 150 mm x 150 mm was utilized [35]. By choosing to use lower magnification optics, the field of view is not reduced, and using a scintillator with a large thickness increases the detection efficiency and thereby reduces the dose. For experiments with a monochromatic X-ray beam at ID17 (ESRF beamline), it is reported that combining a 350 μm thick YAG:Ce scintillator with a CMOS camera and optics giving an effective pixel size of 3.1 μm is a good compromise between spatial resolution and detection efficiency as well as a large field of view (7.04 mm x 5.94 mm) [36].

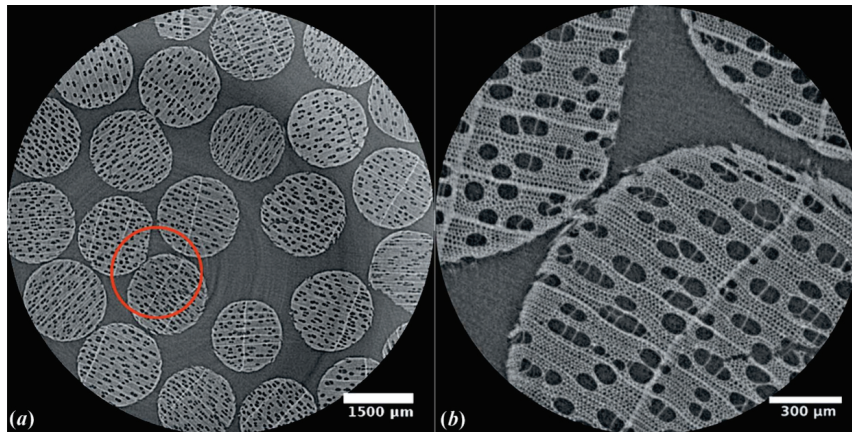


FIGURE 1.3: (a) Wooden tips bundle with a voxel size of 6.5 mm x 6.5 mm x 6.5 mm. (b) Corresponding higher-resolution image with a voxel size of 0.7 mm x 0.7 mm x 0.7 mm adopted from [36].

High spatial resolution imaging: An SCF on a substrate should be chosen if having a high resolution of the images is crucial. The film should be thin, and the optics of relatively high magnification to reach a sub-micron resolution. It can be beneficial for imaging beamlines to operate with multi-resolution systems first to have a large overview of the sample and then to select an area of interest and then perform

high-resolution imaging. The power of operating a multi-resolution system was demonstrated by imaging a bundle of wooden tips. This is presented in Figure 1.3. The low-resolution option of the system consisted of a 500 μm LuAG:Ce scintillator with magnification optics x1, and the high-resolution option using a 19 μm GGG:Eu on GGG scintillator combined with an objective with x10 magnification and 0.28 numerical aperture [36].

1.1.3 Scintillators

There are different types of scintillators, each having advantages and disadvantages. The scintillator type should be chosen depending on the information wanted from the imaging experiment. Unfortunately, compromises have to be made since there is no such thing as a universal scintillator.

1.1.3.1 Types

Scintillators come in many flavors and shapes. They can be organic or inorganic crystals, plastics, liquids, glasses, and even gases [37].

Liquid scintillators are fluorophors (scintillating activators) suspended in a solvent. They cannot be used directly for imaging experiments since they would need to be encapsulated in some way to maintain a spatial response. It has been proposed to contain liquid scintillators in fibers for X-ray imaging purposes [38]. Liquid scintillators are typically used for rapid neutron detection because of their high content of hydrogen.

Plastic scintillators are very simply put fluorophors suspended in a solid plastic matrix. To have good transparency and light output, the polarization conditions have to be controlled [39]. Plastic scintillators are simple to produce, very flexible, easy to shape, and possible to produce in very large sizes. Of all the scintillators, this is the cheapest option. They generally show a fast response (decay time 0.3-280 ns) and a reasonable luminosity (up to 10,000 ph/MeV) but generally suffer from radiation damage and have very low density (1.04-1.56 g/cm³) and effective Z-number (typically around 5.7), which reduces radiation absorption [39]. There are ways to reduce this issue, for example, by introducing organometallics or inorganic high-Z nanoparticles in the plastic [40]. It was found that by combining a scintillating metal-organic framework (with a high atomic number) with a thermally activated delayed fluorescence chromophore in a nanocomposite film, a spatial resolution of 441 μm for X-ray imaging was managed.

Glass scintillators are typically cerium-activated lithium or boron silicates. They are used primarily for neutron detection due to the high thermal neutron cross-sections of lithium and boron. Attempts have been made to make them suitable for X-ray imaging applications. An example of this attempt is by embedding nano-crystals into oxyfluoride glass ceramics [41, 42].

Gaseous scintillators are often noble gases and are generally used in experiments with heavily charged particles or fission fragments. It can only be used as an imaging detector if it is encapsulated in a microstructure, like a capillary plate [43], guided towards the imaging plate.

Organic crystal scintillators are typically aromatic hydrocarbon compounds that contain benzene ring structures interlinked in various ways. It has been a general idea that organic scintillators are not fitting for radiation detection due to their light element composition, which reduces radiation absorption. However, in recent years more are reporting for alternatives, especially since they are cheaper and easier to produce than inorganic crystals. For example, by doing X-ray imaging using a scintillating 9,10-diphenylanthracene it was reported that a spatial resolution of 20 lp/mm was reached (using Au anode X-ray tube and a Nikon D90 digital camera) [44] and organic manganese halides with an estimated resolution of 322 μm (18 keV at a synchrotron source) [45].

Inorganic scintillators are most often crystals grown with various techniques. They can be challenging to synthesize due to their high melting points. However, due to their often high Z-numbers, they absorb more of the incoming radiation in the case of γ or X-rays. This is beneficial for several reasons, such as lower radiation doses in patients for medical imaging.

In this thesis, only inorganic scintillators are considered. These are currently the best option for X-ray imaging at synchrotrons as they are the densest materials, which is crucial to obtain maximal X-ray absorption efficiency.

1.1.3.2 Physics of scintillation process

Scintillation can occur from a material after illumination with any ionizing radiation, and it is widely documented. Here only X-rays below 100 keV will be considered since it is only relevant to the scope of this thesis. Many things affect if a material will be scintillating, but as a first step, it is necessary to have a wide band gap for inorganic crystals. The scintillation process can roughly be described with three stages: Conversion, transport, and luminescence [46]. This concept is used in Figure 1.4 to illustrate these three stages together with the description below.

Conversion: The X-ray photon interacts with the crystal lattice of the scintillator, and its energy is absorbed through the photoelectric effect. This creates a hot electron and a deep hole that will continue to interact in the material and multiply through ionization processes such as electron-electron inelastic scattering and Auger emission. This energy exchange continues until their energy is too low to create further excitations. Thermalization then occurs until the electrons reach the bottom of the conduction band (CB) and the holes at the top of the valence band (VB), meaning they interact with phonons and thereby reduce their energy.

Transport: The thermalized electrons and holes are now transferred toward the luminescent centers. During transport, they migrate through the material, and due to

defects, they may recombine through non-radiative processes and be trapped and de-trapped. This leads to delayed luminescence, generally known as afterglow and bright burn also known as radioluminescence sensitization. Holes and electrons are finally reaching the luminescent centers.

Luminescence: They ideally return to the ground state through a radiative process (luminescence). Alternatively, the emission center can return to the ground state through non-radiative processes.

The scintillation mechanism is different for organic and inorganic scintillators [37] but the organic mechanism is out-of-scope for this thesis.

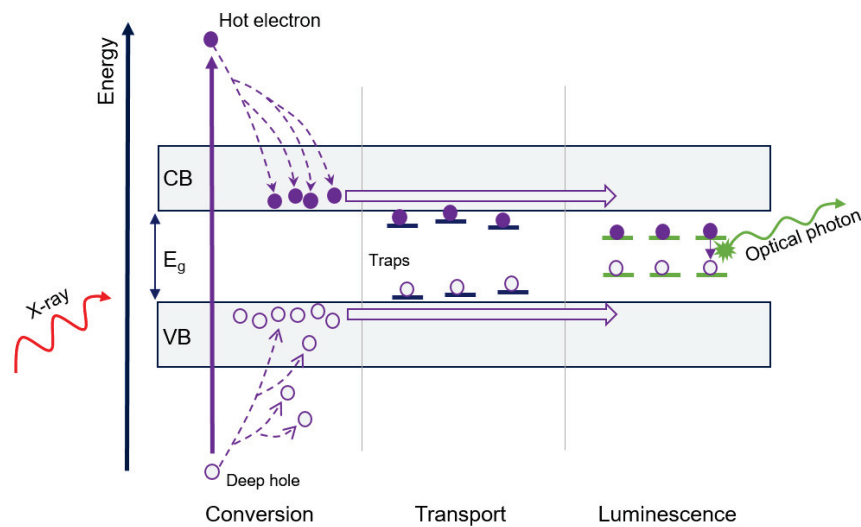


FIGURE 1.4: Schematic of the scintillating process in a wide band-gap inorganic single crystal. The process is described with three stages: Conversion, transport, and luminescence. VB: Valence band, CB: conduction band.

1.1.3.3 Interaction mechanisms

Some relevant interaction mechanisms are displayed as simple schematics in Figure 1.5. Ionizing radiation interacting with matter mainly occurs as photoelectric absorption, Compton scattering, and pair production. For this thesis, X-ray energies below 100 keV are mostly relevant, especially for the results from using the simulation tool discussed in Chapter 2. Below 100 keV pair production is negligible, and the contribution from Compton scattering is small. The photoelectric absorption through the *photoelectric effect* is hence the main interaction for X-ray photons with matter at these energies. The incoming photon is completely absorbed, and the residual energy is transferred to the produced photoelectron. For *Compton scattering*, the incoming X-ray photon is deflected and transfers part of its energy to an electron. The incoming X-ray photon can also interact coherently with an atom. Without transferring any of its energy, it is deflected from its initial path, typically referred to as *Rayleigh scattering* [47].

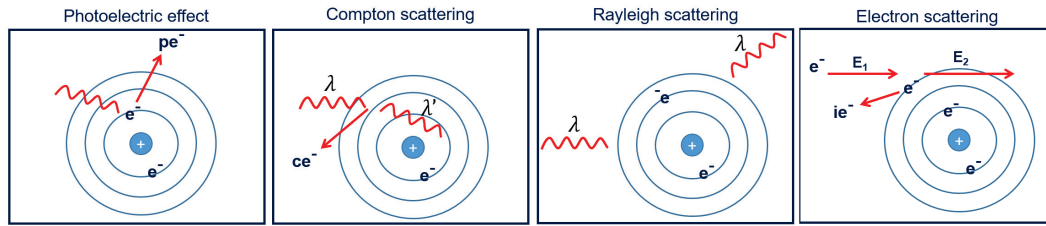


FIGURE 1.5: Schematics of interactions mechanisms. pe: Photoelectron, ce: Compton electron, ie: ionized electron from electron scattering.

1.1.3.4 Materials and forms

Inorganic scintillators can be produced in various materials and forms, which will be presented here. A general overview of the advantages and disadvantages is displayed in Table 1.2. Due to the differences in properties and price, the different forms of scintillators are used for various applications.

	Advantages	Disadvantages
Powders	Easy to prepare Large FoV Relatively rad-hard High efficiency Cheap	Low spatial resolution Low packing density
Ceramics	High packing density High transparency	Afterglow Non-uniformity (grain boundaries)
Micro-structured	Combines resolution+abs. eff.	High afterglow (CsI:Tl) Complicated fabrication Not radiation hard
SCF	High density High optical quality Highest spatial resolution	Difficult to fabricate Expensive Low DQE at high energies (thin)

TABLE 1.2: Overview of advantages and disadvantages for inorganic types of scintillators.

Scintillating powder screens can provide a large field of view and are cheap and easy to manufacture compared to the other scintillator types. The biggest drawback is their limited spatial resolution, which approximately equals the screen thickness, caused by scattering on grain boundaries and pores that then diffuses the light, see, for example, Figure 1.6a. $\text{Gd}_2\text{O}_2\text{S:RE}$, where RE is rare earth elements (often referred to as GOS, Gadox, or P43), is a well-known and highly used scintillating powder [48]. The screen can easily be produced to provide a large field of view and has a high conversion efficiency (55 ph/keV). The spatial resolution is approximately equal to the thickness of the screen [49], and as a consequence, this limits the absorption efficiency. This is especially critical for the performance since the packing density of the powders is around half that of the single crystal. Scintillating powders are the optimum choice when the spatial resolution can be compromised for higher conversion efficiency, and a cheaper solution is more important.

Ceramic scintillators manufacturing has been refined considerably since its beginning. They are typically produced from pressed or cast nanopowders and subsequently sintered. Highly transparent ceramics is thereby obtained with a packing density very close to those of a single crystal. $\text{Gd}_2\text{O}_2\text{S:RE}$ can be synthesized as a ceramic [50] as well as other well-known scintillators. In the grain boundaries, defects are often present that can generate afterglow. This thereby also influences the homogeneity of the scintillator screen, creating artifacts on the extracted image.

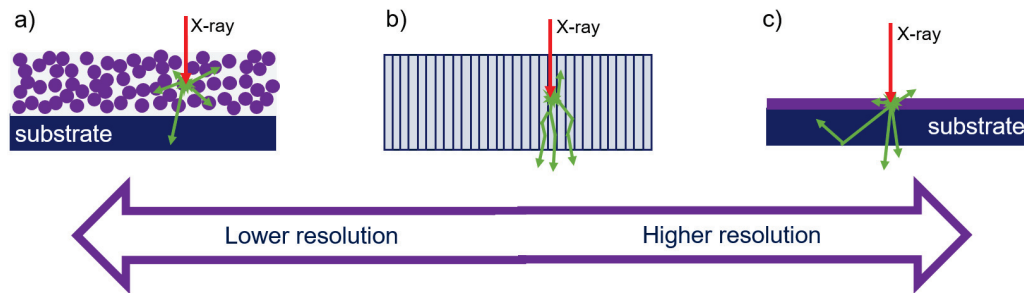


FIGURE 1.6: a) Powder, scattering on grains. b) Structured, restricts light mostly in columns. However, cross-talk occurs. c) Single crystalline film on a substrate, total reflection happens on the backside of the substrate, which enhances the resolution but reduces the extracted light.

Crystalline micro-structured scintillators are of great interest due to the structure serving as a light guide with the walls working as an optical barrier to reduce cross-talk between adjacent columns. The existing technologies are limited to micro-columnar CsI:Tl [51] and micro-structured CsI:Tl screens [52]. They can often be synthesized tall (above $100\ \mu\text{m}$ and up to $600\ \mu\text{m}$), providing a thick scintillator to benefit from a high absorption efficiency while containing and guiding the light in the columns and thereby maintaining the spatial resolution. A fiber optic plate is typically used to couple the micro-structured scintillator to the camera directly. In the case of an effective pixel size of the camera being smaller than the column diameter, the spatial resolution is limited firstly to the column diameter whereas the technology today is limited to a few microns at its best. Secondly, the column length is crucial for the spatial resolution due to cross-talking between columns for increasing thickness [53], see Figure 1.6b. In addition, the column walls must be smooth to avoid scattering on the roughness. If the structure is not deposited on a substrate, the issue of total internal reflection that otherwise reduces the light extraction for thin SCFs grown on substrates is avoided, and the light extraction is increased. The structured scintillators are a good option for applications where a high light efficiency is required, combined with a high stopping power and a high spatial resolution. However, for sub-micron spatial resolution, they are not suitable. Unfortunately, the commercial availabilities of columnar structures are currently limited to compositions such as CsI:Tl, which does not satisfy the current need for synchrotron applications.

Single Crystalline Film (SCF) scintillators often consist of high-density inorganic compounds. Due to their very good optical quality, almost without diffusive centers, there is no scattering on grains, and the packing density is at its maximum. SCFs are always coupled to the camera by lens optics, which introduces a Depth of Field (DoF). The thickness of the film can be selected to be in the range of the DoF and thereby reach a high resolution that is better than what can be reached for powder screens and ceramics of the same thickness. It is therefore required to use SCFs to reach micron to sub-micron spatial resolution in X-ray imaging experiments [54, 55, 56]. However, total internal reflection can occur that reduces the light collection but ensures a higher spatial resolution, see Figure 1.6c. For reaching the highest possible spatial resolution, the SCF thickness must remain in the order of the DoF of the used optics. The image will otherwise be partly out of focus and induce blurring in the final image. However, reducing the SCF thickness decreases the X-ray absorption in the SCF, especially if high-energy X-rays are used for the experiment. The optimum SCF scintillator thickness is, therefore, a balance between the desired SCF X-ray absorption efficiency and spatial resolution, both related to the X-ray beam energy.

1.1.4 Scintillating single crystalline films

Thin film deposition techniques: Many technologies exist that allow the preparation of thin films. Here among sol-gel, Molecular Beam Epitaxy (MBE), Chemical Vapour Deposition (CVD), Liquid Phase Epitaxy (LPE), and thinning of bulk single crystals. Thinning can be done of substrates by polishing [57] but are limited to around 25-50 μm when freestanding. When glued to a substrate, they can be polished to around 5 μm , but the glue usually degrades when exposed to high X-ray fluxes on synchrotron sources and are therefore not a good choice.

Technique	Advantages	Disadvantages
Sol-gel	Less substrate constrained	Low crystallinity
MBE	No flux impurities	High defect density
CVD	No flux impurities	High defect density
LPE	High quality, low defect density	Substrate constrained

TABLE 1.3: Overview of main advantages and disadvantages of thin film techniques in relation to growth for high spatial resolution X-ray imaging.

The main advantages and disadvantages of some thin film growth techniques are presented in Table 1.3 in relation to producing scintillating SCFs for high spatial resolution imaging. Some general disadvantages are the slow growth rate for the sol-gel, MBE, and CVD techniques compared to LPE. The growth rate using LPE is in the range of 0.1-1 $\mu\text{m}/\text{min}$ which is 10 to 100 times faster than molecular beam epitaxy (MBE) or metalorganic vapor-phase epitaxy (MOVPE) [58]. Therefore, for SCFs with thickness in the micrometer range, LPE is superior. For MBE and CVD, the films are deposited at extremely high supersaturation far from thermodynamic equilibrium. The films, therefore, often suffer from a high density of defects, which

can harm the scintillating properties. LPE is a near thermodynamic equilibrium technique, and the growth temperature is considerably lower than for bulk crystal growth resulting in high-quality SCFs with a low defect density [59, 60]. For sol-gel the risk of lower crystallinity and the presence of multiple structural phases is neither desirable for this application. For the targeted thickness and quality desired for the SCFs in the framework of this thesis, LPE is the suitable and typical technique [61, 62, 63, 64, 65]. The LPE technique will be described in depth in Section 1.3.

Important parameters for SCF scintillators: To have a good scintillating SCF, many parameters should be considered. Table 1.4 presents parameters fulfilled for an ideal SCF scintillator.

<i>Film</i>	Comments
Emission wavelength	Should fit QE of camera
High density and Z_{eff}	For high stopping power
No birefringence	Can otherwise degrade image quality
Thickness	Around DoF, for highest spatial resolution
High light yield	Otherwise increases exposure time
Low decay time	Affects speed of the scintillating response
No afterglow	Affects speed of scintillating response
No bright burn	Better stability of quantitative measurements
Good radiation hardness	Increases scintillator lifetime and stability
<i>Substrate</i>	Comments
Transparent	To not reabsorb emission from SCF
Emission-free	Otherwise degrades resolution
High quality	Single crystalline, surface well polished
Structural matching	With the film
Commercial available	For practical reasons
Cheap	For financial reasons
Good radiation hardness	Increases scintillator lifetime and stability

TABLE 1.4: Important SCF and substrate characteristics. QE: Quantum efficiency.

The efficiency of the camera to convert photons into electrons, also known as Quantum Efficiency (QE), depends on the photon wavelength. It is, therefore, optimal to have a scintillator with an emission wavelength matching the sensor QE.

The decay time and afterglow are related to the timing of the scintillating processes. The decay time is related to the speed of the scintillating conversion process and is the short-time component of the scintillator. Scintillators with a low decay time can be used for fast X-ray imaging experiments. The afterglow is related to traps from crystalline defects and is the long-time component (microseconds to days). The afterglow can impose issues if it is longer than the camera dead time, meaning the time when the camera reads out the data between images, then the signal would build up. Having afterglow can therefore create artifacts in the tomography reconstructions.

As is underlined in the table, the substrate also influences the quality and properties. The structural aspects will be discussed in several sections and chapters later in this thesis but are essential to consider when performing LPE. Regarding the optical

parameters, the substrate should be transparent, at least for the SCF emission, to avoid optical re-absorption. Another crucial point is that it should preferably be non-luminescent itself or at least not have overlapping emission lines with the SCF. For non-overlapping emission, the substrate emission can be filtered out using optical filters inserted in the optical path of the detector.

1.1.5 Detector characteristics

When considering a detector system, many parameters must be considered, and often, optimizing one parameter is at the expense of another. This is the case when optimizing a scintillator for high spatial resolution the efficiency is degraded. The characteristics important for an ideal scintillator were already listed. Some important parameters for the detector itself are displayed in Table 1.5, of which some are discussed here.

Characteristics	Related to
Dynamic range	Image quality
Linearity	Stability
Lag	Stability
Frame rate	Readout time
Number of pixels	FoV
Size of pixels	Spatial resolution
MTF	Spatial resolution
DQE	Global efficiency

TABLE 1.5: Relevant detector characteristics.

The Dynamic range is the ratio of the maximum signal (before saturation) to the system noise (for low exposure time, the system noise can be approximated to the readout noise). The maximum signal (in electrons) depends on the full well capacity of the sensor, while the total noise results from the quadratic sum of dark noise and readout noise. For indirect detection, it also depends heavily on the uniformity of the scintillator and its optical quality. For instance, in a region of the scintillator where the light emission is significantly higher compared to the average, for example, on scattering centers such as scratches or crystal inclusions, the exposure time should be reduced to avoid saturation, leading as a consequence to a reduction of the dynamic range. Afterglow from the scintillator can raise the noise level and reduce the dynamic range.

Frame rate is the frequency at which consecutive images are acquired, measured in frame per second (fps). It can also be referred to as frame frequency and expressed in Hertz (Hz). It is the inverse of the time the camera needs to acquire an image and read the data. If the exposure time is 1 s, the camera needs additional time to read the data, making the total time above 1 s often referred to as the dead time. This is especially important when doing time-resolved imaging where the frame rate should be high.

1.2 High spatial resolution X-ray imaging detectors

To reach micron to sub-micron spatial resolution when performing X-ray imaging experiments at synchrotrons, thin SCF scintillators are required. The whole detector system is composed of an SCF scintillator, microscope optics, and a CCD or CMOS camera [54, 56]. See Figure 1.7 for a schematic of an imaging experiment with this setup. The sample is positioned in the X-ray beam. It absorbs and changes the phase of the X-rays. The transmitted X-rays are then partly absorbed by the scintillator, which converts them into optical photons. An optical image is created in the total thickness of the active layer, which is enlarged by the optics and projected through the lenses onto the camera. The camera creates an electrical signal in each pixel from the optical photons, and this is then processed on the computer as a 2D image. Multiple images acquired at different angles lead to so-called tomography where a 3D reconstruction of the collected images can be created.

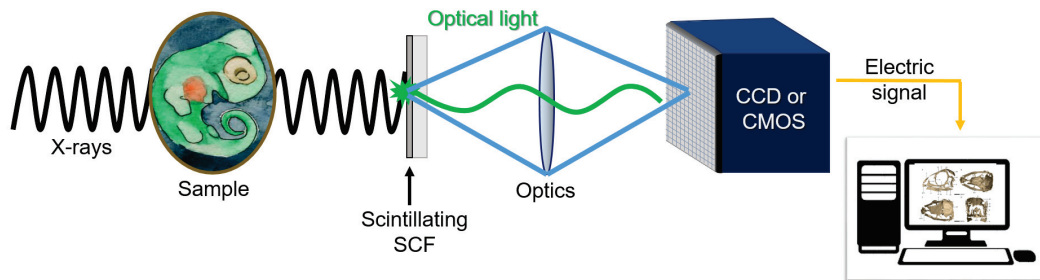


FIGURE 1.7: A schematic of an imaging experiment at a synchrotron beamline using a high-resolution setup. The sample is a watercolor painting of the *Massospondylus carinatus* embryos, image credit: Mélanie Saratori.

1.2.0.1 Spatial resolution limitations

The spatial resolution of the final image depends on all three detector components (scintillator, optics, and camera) that can each influence the resolution and should therefore be considered and optimized.

The Scintillator degrades the spatial resolution along two aspects. First, when the X-ray photons reach the scintillator and deposit energy not only at the initial interaction point but as many interactions subsequently arise, the energy deposition is spread spatially in the scintillating layer. This has a blurring effect on the optical image created from it. The interactions influencing this are discussed in detail in Chapter 2. In addition, to reach an ultimate high spatial resolution, apart from the optical quality of the layer, which may induce diffusive centers, the thickness of the SCF scintillator should match the DoF of the optics used for the experiment. The DoF is defined as follows [66]:

$$DoF = \frac{\lambda_{emis} \cdot n}{NA^2} + \frac{n \cdot PS}{NA \cdot M} \quad (1.1)$$

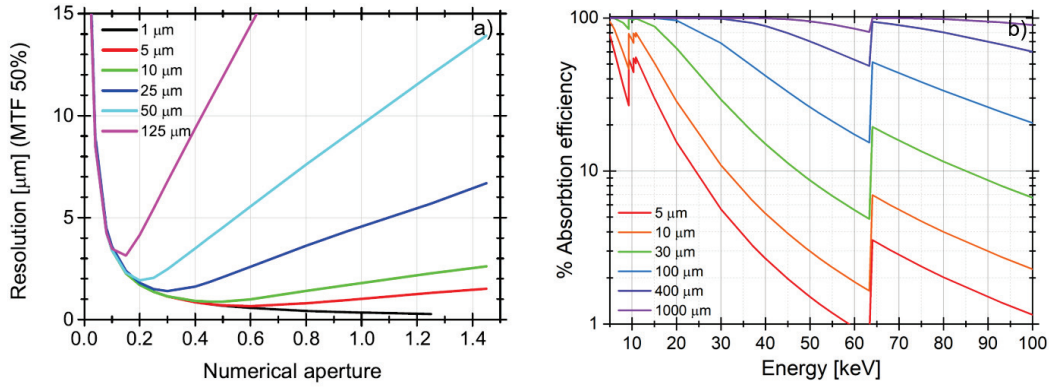


FIGURE 1.8: a) The spatial resolution limit as a function of NA, calculated including light diffraction and defect of focus due to the scintillator thickness, for $\lambda=550$ nm. The figure is from the Ph.D. thesis of Federica Riva [70], and a similar result was already published by Koch et al. in [56]. b) The calculated absorption efficiency of LSO for different thicknesses. Data obtained from the NIST database [71].

Where λ_{emis} is the emission wavelength of the scintillator, PS is the pixel size of the detector, M is the total magnification imposed by the optics (objective and eyepiece), NA is the numerical aperture of the objective, and n is the ambient index of refraction, which is 1 when working with non-liquid optics (otherwise 1.5). The resolution is plotted as a function of the NA for various SCF scintillator thicknesses in Figure 1.8a. It shows the importance of matching the scintillator thickness with an appropriate NA or vice versa to exploit the possible spatial resolution. It is especially important not to choose a higher NA without reducing the scintillator thickness since this can reduce the spatial resolution considerably. It also shows that to reach higher spatial resolutions, a high NA should be chosen combined with thin scintillating SCFs below $10 \mu\text{m}$ thickness. Thus, the system faces a contradictory criteria quality since a smaller thickness decreases the X-ray absorption, as is illustrated in Figure 1.8b.

The optics are limiting the spatial resolution due to the Abbe diffraction limit for a microscope given by [67]:

$$d = \frac{\lambda_{emis}}{2 \cdot n \cdot \sin(\theta)} = \frac{\lambda_{emis}}{2 \cdot NA} \quad (1.2)$$

The optics will therefore have a large impact on the spatial resolution, which will also be shown in detail by simulations in Chapter 2, using simulations at various X-ray energies and NAs.

The detector is limited to a spatial resolution of approximately twice the effective pixel size ($PS_{eff}=PS/M$). This is valid for 2D cameras and is defined according to the Nyquist-Shannon sampling theorem [68, 69]. As long as the effective pixel size of the camera combined with the optics is lower than the diffraction limit of the optics, the camera is not the limiting factor for the resolution. The detector system is then said to be diffraction-limited.

1.2.0.2 The high-energy, high-resolution challenge

Performing X-ray imaging where the detector is coupled to optics makes it possible to resolve micrometer details, even of dense and large specimens such as fossils [72, 73]. A stunning example that exhibits the performance and strength of X-ray imaging techniques, is the imaging of entire human organs, such as a covid infected lung [74]. The X-ray imaging technique used for this is here referred to as hierarchical phase contrast tomography. The whole lung is first imaged with low resolution and subsequently, interesting areas are imaged with a higher resolution. Regional changes in the tissue architecture of the covid infected lung were identified, which is novel information in the study of the effect of covid on the lungs. For this experiment, the smallest voxel size was $2 \mu\text{m}$, sufficient to resolve the desired features using an X-ray energy of 78 keV. This study has also resulted in a highly interesting project named the human organ atlas, where data from the experiments are available, as well as 3D constructions of a covid infected lung and a whole brain [75]. The EBS upgrade has made experiments like this possible, with the increased flux and coherence, especially at high energies.

High X-ray energies are required in such experiments to penetrate large and dense specimens to reduce the sample absorption, otherwise detrimental to the contrast. However, working at high energies with thin SCFs reduces the absorption efficiency of the SCF considerably. Figure 1.8b shows the absorption efficiency for Lu_2SiO_5 (LSO) calculated from data from the NIST database [71] for various thicknesses. The thinner the scintillating SCF, the fewer X-rays it absorbs, ultimately reducing light production. The absorption efficiency (η_{abs}) of scintillators is proportional to the density (ρ) and effective atomic number (Z_{eff}) of the material [56]:

$$\eta_{abs} \propto \rho \cdot Z_{eff}^4 \quad (1.3)$$

And can thereby be maximized by tailoring the SCF to have a high density and Z_{eff} . This is why in high-resolution X-ray imaging communities, there is an ongoing quest for compounds fulfilling these criteria while meeting the many other requirements for scintillators as listed in Table 1.4.

1.2.1 Detector characterization

The performance of the detector system depends on each component as already shortly described above. It is indeed challenging to consider every parameter at the same time. However, there are different methods to evaluate the imaging performance of detector systems. Some of these will be presented in this section.

1.2.1.1 Detective quantum efficiency

The Detective Quantum Efficiency (DQE) is an important value for evaluating detector systems. It combines the effects of the signal (related to image contrast) and noise

performance of an imaging system, generally expressed as a function of spatial frequency. It describes how effectively an X-ray imaging system can produce an image with a high Signal to Noise Ratio (SNR) relative to an ideal detector. The DQE is a value that ranges from 0 to 1, typically presented as a function of spatial frequency. If the detector detects no signal, the DQE will be 0. For an ideal detector, the DQE will then be 1. A perfect detector does not exist since any statistical process, background noise, or loss of events involved in the detection process lowers the DQE. The DQE can be expressed in various ways, where a popular one is the transfer of the square of the signal-to-noise ratio (SNR) at the output relative to the input [76]:

$$DQE = \frac{SNR_{out}^2}{SNR_{in}^2} \quad (1.4)$$

The final output signal is influenced by all the components starting from the input signal going through the scintillator, then the optics, reaching the camera, and being processed.

The DQE can be expressed as a function of spatial frequency as well:

$$DQE(\nu) = \frac{G \cdot S_0 \cdot MTF(\nu)^2}{N \cdot NPS_0(\nu)} \quad (1.5)$$

Where G is the gain, S_0 is the average image signal per pixel, MTF is described further in the next section but is related to the spatial resolution and contrast, NPS_0 is the image noise power spectrum, and N is the number of points in NPS_0 [77]. From this, it is clear that the detector system depends on the noise in the system as well as the image contrast of the system.

According to [56] for sufficiently high conversion and optics collection efficiency of the detector system, the DQE can be approximated to:

$$DQE \approx \eta_{abs} \quad (1.6)$$

Which emphasizes the importance of having scintillators with high absorption efficiency.

1.2.1.2 Resolution and contrast

To validate the spatial response of an indirect detector system, the Modulation Transfer Function (MTF) is very useful. It describes the spatial response of the detector system by combining the concepts of resolution and contrast. The spatial resolution of a system quantifies the smallest features that can be fully resolved. In literature, there is no complete agreement on how to refer to the spatial resolution of a detector system, but it generally corresponds to the spatial frequency for which the MTF value equals $\sim 10\text{--}20\%$. The contrast, or modulation, is defined as [78]:

$$C(\nu) = \frac{I_{max} - I_{min}}{I_{max} + I_{min}} \quad (1.7)$$

for alternate black and white lines at a given frequency (ν). I_{max} and I_{min} are the corresponding maximum and minimum intensities (number of optical photons detected). A contrast of 100% is obtained when the I_{min} is 0. See Figure 1.9 for a visual explanation of this.

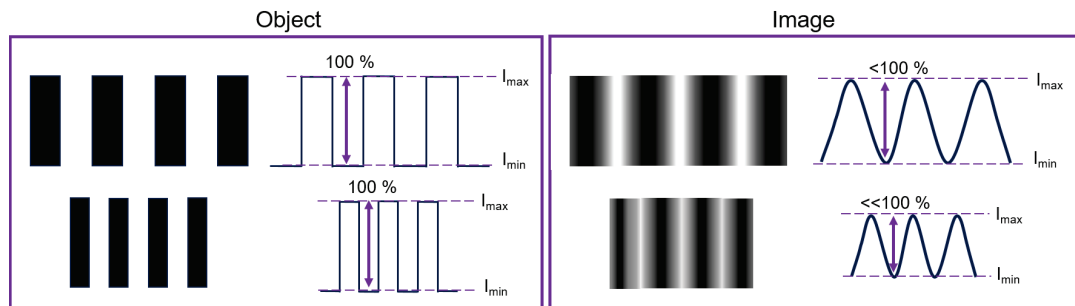


FIGURE 1.9: A schematic of alternate black and white lines and the contrast profile for two different frequencies shown by the actual object (left) and how the image could be (right). For the images, the lines start to overlap when the distance between lines is close to the spatial resolution limit, reducing the contrast.

The MTF basically provides the transmission of contrast through the system at different spatial frequencies, and like the DQE, it ranges from 0 to 1. If there is no contrast at a given spatial frequency, the MTF will be 0, and where there is the perfect contrast, the MTF will be 1. Therefore, the MTF usually ranges from 1 to 0, starting from 0 lp/mm and going towards higher spatial frequencies. See Figure 1.10a for a schematic of an MTF. It differs from the DQE as it only considers resolution and contrast, whereas the DQE takes many other things into account, such as the different sources of noise in the system, as will be seen in the next paragraph on DQE. The counterpart of the MTF, the Line Spread Function (LSF), helps understand specific trends in the MTFs further because it directly shows the spatial distribution of detected optical photons around the position of the primary interaction between the X-ray photon and the SCF (see Figure 1.10b for a schematic of the LSF).

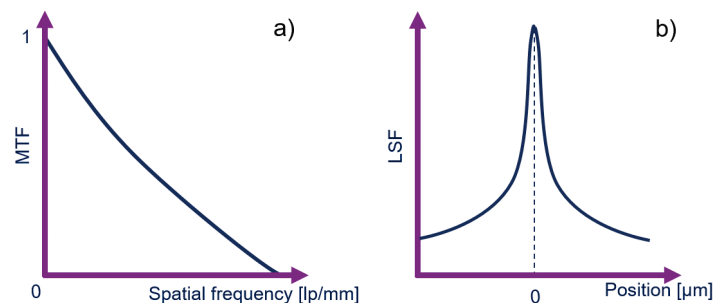


FIGURE 1.10: Schematics of a) MTF, and b) LSF.

The energy of the incoming X-rays has a significant impact on the spatial distribution of deposited energy in the SCF and thereby the obtainable spatial resolution and contrast of the final image. Generally, when increasing the X-ray energy, the generated

secondary particles (X-rays, electrons) deposit energy at an increasing distance from the initial point of interaction, resulting in a decreasing contrast. However, increases and decreases in the spatial resolution arise when applying X-rays of energies around the absorption edges of the elements in both the SCF and substrate. It is thus crucial to consider the major impacts on the contrast occurring around the absorption edges. These are factors that will be discussed in Chapter 2.

1.2.1.3 The slanted edge method

To experimentally extract LSFs and MTFs, the slanted edge method [79, 80] can be used and was also practiced for experimental validation for the samples under study in this thesis. As the name of the method indicates, the measurement involves an edge. The edge is of GaAs and is either cleaved or polished to have an almost atomically flat surface. If the edge is not flat enough, it might give the illusion of the detector system not being able to resolve certain details, which appear in the extracted MTF. The edge should therefore be of better quality than the resolution limit of the detector system. Since we strive to reach a sub-micron spatial resolution, the edge needs to be almost perfectly flat. The edge is positioned 1-3 mm away from the detector system to absorb part of the X-ray beam when an image is acquired with the high-resolution setup. The setup used at ESRF BM05 beamline, including the edge, is shown in Figure 1.11. The setup consists of slits to shape the beam to fit the field of view of the camera, the edge, then the scintillator, followed by a microscope objective, a mirror to direct the optical photons upwards, then an eyepiece, and finally, the camera. A monochromatic X-ray beam is always used for these measurements since we are evaluating scintillators for high spatial resolution X-ray imaging.

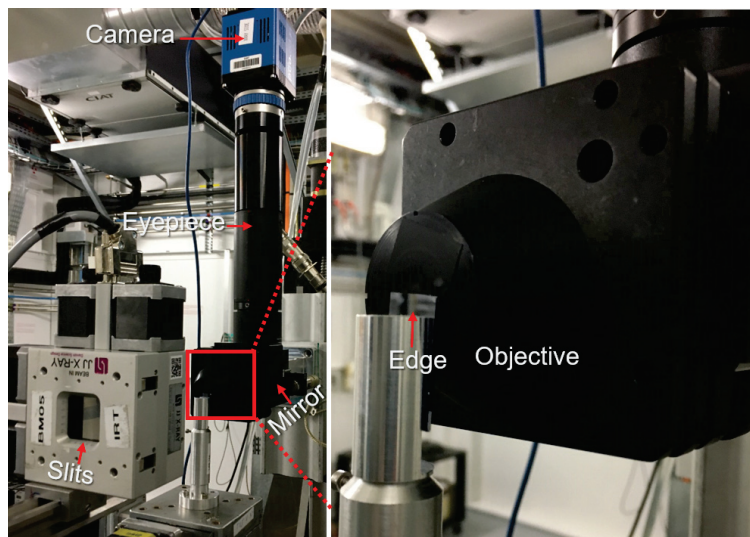


FIGURE 1.11: The high-resolution setup for the slanted edge method at ESRF BM05 beamline. Here equipped with a PCO edge 4.2 camera.

A few alignment procedures have to be performed before acquiring the images used to find the MTF of the detector system in combination with a specific scintillator.

First, the focus should be adjusted when changing the scintillator. Being out of focus will degrade the MTF due to blurriness. Then, it is important the edge is perpendicular to the X-ray beam. A series of images with the edge tilt varied perpendicular to the beam is acquired to find the optimum tilt angle. This is only performed once since it depends on the tilt according to the incoming X-ray beam.

To extract the MTF, the general procedure is as follows. Radiographs are acquired with the edge cutting approximately half the image. It is before further analysis, corrected by flat-field and dark images, meaning no edge image with and without the X-ray beam, respectively. From this, the Edge Spread Function (ESF) is computed, which is merely a curve showing how step-like the edge is imaged with the setup. The LSF can then be calculated by taking the derivative of the ESF. Finally, the MTF can be calculated by doing a Fast Fourier Transform (FFT) of the LSF. This procedure is shown in Figure 1.12.

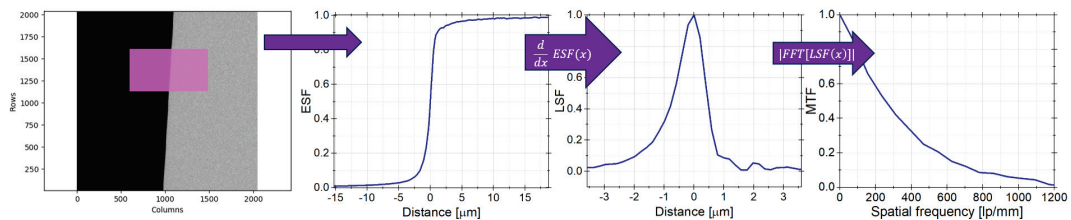


FIGURE 1.12: The procedure to obtain the MTF. From left: An image of the GaAs edge cutting the image in half where a region of interest is chosen to ease the computing time. The ESF is first found from the image, then the derivative gives the LSF, and the FFT finally gives the MTF.

1.2.2 State-of-the-art scintillators

Even though this thesis focuses on spatial resolution combined with a high X-ray stopping power, other important characteristics should be considered. Table 1.6 displays some of these characteristics of the current state-of-the-art scintillators used at synchrotrons for high spatial resolution X-ray imaging experiments. It is important to mention that these values can vary to some extent from sample to sample depending on various small changes in the production procedure.

<i>Film</i>	LSO:Tb	LYSO:Ce	GGG:Eu	LuAG
<i>Substrate</i>	YbSO	YbSO	GGG	Non
Density [g/cm ³]	7.4	7.2	7.1	6.7
Effective Z number	65	65	53	59
Emission wavelength [nm]	550	420	595	550
Decay	1 ms	35 ns	1 ms	70 ns
Afterglow [%]	<0.001	<0.001	<0.001	0.005-0.08
Light output [ph/keV]	30-40	15-20	25-35	25-35
Substrate scintillation	No	No	Slight*	No substrate

TABLE 1.6: Overview of characteristics for state-of-the-art scintillators. Afterglow is at 20 ms after 0.1 s exposure (percent). *scintillation from the substrate can be filtered out.

1.3 Liquid Phase Epitaxy

Many samples for various projects have been produced for this thesis, and the common factor for them is they have been grown by LPE. In this section, this interesting growth technique will be presented, and various considerations in relation to it are explored to give the reader an idea of how much time and effort is put into the use of this technique and the growth of the samples studied in this thesis.

The term epitaxy comes from the Greek *epi*, meaning "above", and *taxis*, meaning "an ordered manner". Epitaxy is a crystal growth type where new crystalline layers are formed with a well-defined orientation with respect to the single crystalline seed layer (for example, a substrate). The grown or deposited SCF is referred to as an epitaxial film or epitaxial layer. Epitaxial crystal growth can be performed from a vapor, liquid, or solid state. In this thesis, only growth from the liquid phase has been used due to its superiority for the growth of scintillating SCFs for high-resolution X-ray imaging.

Epitaxial growth from the liquid phase is referred to as liquid phase epitaxy (LPE). It is a high-temperature solution growth technique used to grow complex oxides supported by single crystalline substrates. Parallels can be drawn from the flux growth method since the growth is initiated from a supersaturated solution comprised of the desired SCF oxide components, referred to as the solute, and an appropriate solvent, typically also oxides. The role of the solvent is, first of all, to lower the growth temperature since the solute oxides often have very high melting temperatures that can be higher than the working temperature for many furnaces (>1800 °C). The lower growth temperatures also ensure a high quality of the SCFs with fewer defects. Using a solvent makes it possible to lower the growth rate giving better control of the SCF thickness and growing on substrates without risking melting them.

In this section, the LPE technique will be presented in more depth. The setup is shown and described in detail, followed by details on the procedures from before assembling the furnace to the growth. Finally, considerations such as the content of the melt, lattice mismatch, and ionic radii of dopants are presented.

1.3.1 The setup

The solution is contained in a platinum crucible positioned in the lower part of a specially designed vertical furnace for LPE. See schematic in Figure 1.13a. The furnace consists of two resistive heating zones to better control the heat gradient, which the sample especially will be affected by when entering and exiting the furnace. Three thermocouples are used to control and monitor the temperatures. One is positioned directly on the crucible, one on the lower part of the tube, and the last at the upper part of the tube. A careful furnace design allows for temperature fluctuations of only 0.1 °C, which is important to control the growth fully.

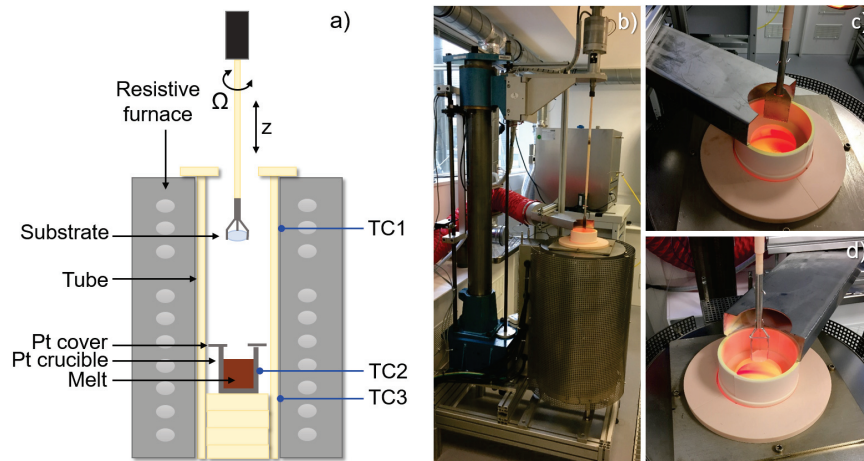


FIGURE 1.13: a) The Schematic depicts a cross-section of the applied vertical dipping method LPE furnace, where the yellow is ceramic parts, and TC is thermocouples. The sample rotation (Ω) and vertical translation (z) can be controlled, as well as the temperature of the two resistive heating zones. b) Photograph of the furnace. c) Photograph of the furnace entrance with the stirrer ready. d) Photograph of the furnace entrance with a sample ready before growth.

1.3.2 The procedure

Solution preparation: It is important to have high-purity powders of the solution components. Otherwise, impurity atoms can be included in the grown SCF, potentially resulting in a larger lattice mismatch or as light quenching centers reducing the scintillation light output. All the oxide powders are mixed thoroughly and pressed into a cylinder to fit in the platinum crucible. The furnace is heated to 1100 °C to melt the powders. Subsequently, the solution is stirred with a customized platinum paddle (see Figure 1.13c) to ensure all the powders are dissolved and the solution is homogeneous. Stirring is repeated before each growth to ensure similar solution homogeneity for each growth. The stirring is performed at elevated temperatures to avoid crystallization on the paddle. After the stirring, the solution is cooled to the growth temperature and ready for the growth procedure.

Growth: The substrate is carefully inserted in a specially customized platinum holder on a rod. The growth is induced by the vertical dipping method [81], in which the substrate is transferred into the solution. See the growth procedure as a schematic in Figure 1.14. There are other procedures to perform LPE, for example, by sliding boat technique [60]. During growth, the sample is rotating, with alternating directions, to ensure the homogeneity of the solution also during growth. The growth time is typically 5-60 minutes depending on the desired SCF thickness (longer growth, thicker SCF). This procedure results in films on both faces of the substrate. After growth, the sample is translated just above the melt, and an ejection procedure is performed to remove as much as possible of the flux still present on the sample surface, which can otherwise lead to uncontrolled growth.

After growth: After the sample is transferred out of the furnace, is it cleaned, and finally, the thickness of the SCFs is estimated from their density and weight gain after growth.

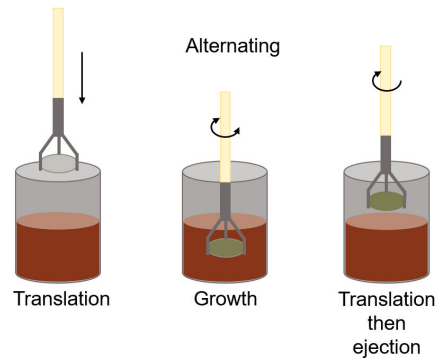


FIGURE 1.14: Schematic showing the LPE growth procedure.

1.3.3 Concept and considerations

Performing and developing the LPE procedure for new materials is a time-consuming and expensive task. There are many things to consider before initiating the preparation for the LPE experiment, especially if there is no literature on previous LPE growth of the compound or similar. Of course, a literature review should be performed on the targeted compound, and information like crystalline structure, melting temperature, potential growth by LPE, and/or other high-temperature solution growth should be studied. If there are any phase diagrams, these should be studied in order to understand if there are any phase transitions that could be affecting the growth in some way.

Crystalline structures: The crystalline structure of the targeted SCF and the substrate is very important to consider and should be known prior to any growth attempts. They should preferably be iso-structural or at least have a high degree of structural matching. Otherwise, growth will not be possible with LPE. The lattice mismatch is a practical way of evaluating how well the crystalline lattice of the SCF and substrate fit each other. It is often defined as:

$$\Delta a = \frac{a_{film} - a_{substrate}}{a_{substrate}} \cdot 100\% \quad (1.8)$$

Where a is the unit cell length. The lattice mismatch is preferred to be as low as possible, with a rule of thumb is having it below 1%. However, even when doing homoepitaxy (SCF host structure being the same as substrate structure), introducing a dopant (luminescent activator) can increase the lattice mismatch too much depending on the used concentration and the ionic radii. The consequence of this varies depending on the SCF being grown but could be lowering the growth rate until there is no growth at all or introducing increased strain in the SCF that could negatively influence the scintillating properties and the optical quality of the film. The lattice mismatch

can be predicted from the reported unit cell lengths of the targeted compound and substrate found in databases. The estimated lattice mismatch can hint if the SCF and substrate are too different and allows for considering substitutions or similar to alter the structure of the SCF to fit the substrate better or even change the substrate or the substrate composition if possible. The effect on the lattice mismatch by introducing dopants depends on the type of dopant and what element it is substituting in the structure. This can be predicted by considering the ionic radii of the two. An example using LSO:Tb (Lu₂SiO₅ doped with Tb³⁺), terbium occupies the lutetium site in the structure. The ionic radii of Lu³⁺ with coordination number (CN) 6 is 0.861 Å and for Tb³⁺ with CN=6 it is 0.923 Å [82]. The lattice normally expands when a bigger ion is introduced into the lattice. However, other factors can also affect the expansion or contraction of the lattice, for example, doping that induces oxygen vacancies.

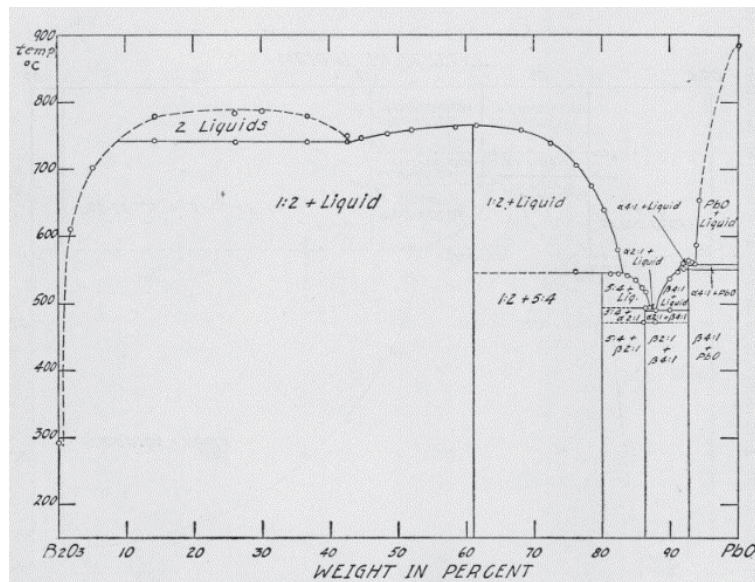


FIGURE 1.15: PbO-B₂O₃ phase diagram from [83].

Solution content: The SCF components (solute) are dissolved in a flux (solvent). The solvent should be chosen wisely. For the production runs of state-of-the-art scintillators grown by LPE at the ESRF, PbO-B₂O₃ is typically used as the solvent. This is usually a very good solvent due to its high solubility of solute material and low solution viscosity for high PbO content. B₂O₃ itself has a very high viscosity, and therefore increasing the B₂O₃ content in the solvent increases the viscosity. The advantage of including B₂O₃ is due to the eutectic system it forms with PbO. One can see their phase diagram in Figure 1.15. Therefore, a way to decrease the growth temperature is to increase the B₂O₃ content with the sacrifice of increasing the viscosity. Having a higher viscosity can make it harder or even impossible to remove the residual flux on the sample surface after growth, which can lead to uncontrolled growth on the SCF surface. A downside of the PbO-B₂O₃ solvent is its high toxicity. Therefore, it is worth considering if other solvents can be applied in certain cases. Also, for certain films, Pb can potentially act as an unwanted impurity, which may

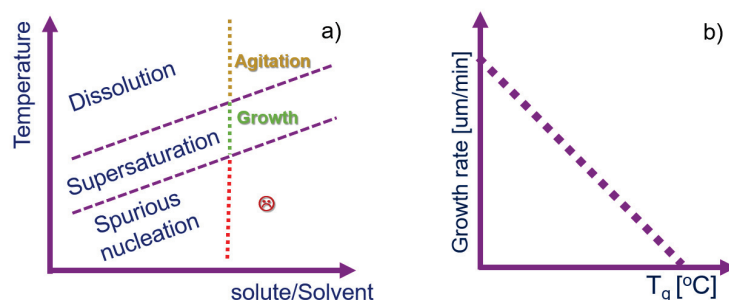


FIGURE 1.16: a) A schematic describing the principles of the LPE growth having the temperature as a function of the solute over solvent ratio. b) A schematic of the growth rate as a function of the growth temperature (T_g).

act as a luminescence quencher.

Many factors influence the growth temperature. Other than the solvent composition, another factor is the solute-solvent ratio (solute/solvent) which normally increases the growth temperature with increasing solute/solvent. This is because the solute components have considerably higher melting point temperatures than the solvent. A big advantage of the LPE technique is its ability to grow high melting point compounds at reduced temperatures compared to bulk growth. This is indeed due to the dissolution of SCF components in the solvent. The composition of the solution influences the growth rate, the SCF quality, the dopant incorporation, and much more. It should therefore be carefully optimized on all parameters to obtain the best possible SCF quality and scintillation properties.

Consider Figure 1.16a, showing the temperature as a function of the solute/solvent. As already discussed, the agitation is performed at elevated temperatures. It is essential to exceed the supersaturation temperature to avoid crystallization on the paddle and crystals forming at the solution surface. After, the temperature is lowered to have a supersaturated melt. This is important to obtain high-quality epitaxially grown SCFs. The temperature range where the solution is supersaturated varies depending on the solution composition. The growth rate in the supersaturated temperature range normally varies according to Figure 1.16b. Decreasing growth temperature gives increasing growth rates. Increasing the solute/solvent results in this preferred growth range being shifted to higher temperatures and vice versa. If the growth temperature is lowered too much, spurious nucleation occurs, and crystals will typically form at the solution surface and/or deposit on the SCF. This is not desirable since it can reduce the quality of the SCF.

Despite its complexity, LPE is ideal for growing scintillating high-quality SCFs on substrates. To exploit the technique fully, it is important to understand the growth, especially regarding the substrate and film structure, including the dopant incorporation.

1.4 This thesis

The goal of this thesis has been to develop new scintillating screens combining high spatial resolution X-ray imaging at synchrotrons with high stopping power, especially for high X-ray energies. Two approaches to fulfill this have been used. The first was to grow high density and high effective atomic number (Z_{eff}) thin SCFs with LPE for reaching an ultimate high spatial resolution. The second was to grow state-of-the-art SCF scintillators but with a microstructure, with the scope of compromising the resolution for an effectively higher stopping power. In this framework, several projects have been explored over the last three years and have opened new pathways for further developments to reach a functional material. The projects have been ongoing in parallel, and as a result, some are more advanced than others. This last section will conclude the introduction chapter by presenting these various projects while giving the thesis structure.

A simulation tool: To predict the spatial response and determine the critical mechanisms degrading it for potential scintillating SCFs combined with substrates and compare them with state-of-the-art scintillators, a simulation tool was developed. It is based on Geant4, Monte Carlo simulations, and the code was developed by former Ph.D. student Federica Riva and is described in detail in her thesis [70]. During this thesis, it has been used to understand the effects arising from using optics, different SCF thicknesses, and especially when using varying X-ray energies, and the consequences it has on spatial resolution. A manuscript was published in the Royal Society of Chemistry, Journal of Materials Chemistry C in May 2022, concerning the tool, including careful descriptions of the studies regarding X-ray energies and absorption edges in the SCF and substrate [84]. More importantly, the simulation tool has been used to pre-select the potential SCFs combined with substrates. These investigations resulted in the initiation of LPE growth of hafnates and titanates. The publication is displayed in Appendix A, whereas Chapter 2 presents the simulation tool and the results of the investigations using it in more detail.

The hafnates: Various hafnate compounds were grown by LPE on $ZrO_2:Y$ substrates and characterized. Especially $Lu_2Hf_2O_7$ is very relevant for this thesis since it has a very high density and Z_{eff} . An extensive understanding of the hafnate system has been achieved through comprehensive characterization and varying conditions for the LPE growth. The hafnate system is highly flexible for LPE growth on the $ZrO_2:Y$ substrates. $PbO-B_2O_3$ is typically used as a solvent for LPE growth of state-of-the-art SCF scintillators but was found to impose challenges and restrictions to the LPE growth of the hafnates. A new solvent, $Bi_2O_3-B_2O_3$, was successfully used and has opened up for further developments of this system. An overview of the various types of hafnate samples grown by LPE and the characterization of these is presented in Chapter 3.

The titanates: This project concern the growth and subsequent characterization of $PbTiO_3$ films on $SrTiO_3$ substrates. Since $PbTiO_3$ has a rather high density of

7.95 g/cm³ it was an obvious candidate. Unfortunately, the titanate samples did not show any promising scintillation properties. The project details will, therefore, not be dedicated to a chapter but only be summarized here.

We managed to grow PbTiO₃ films on SrTiO₃ substrates, but the films are highly strained and have a very rich domain structure. At room temperature, PbTiO₃ has a tetragonal structure, and above around 490 °C [85], it becomes paraelectric with the cubic structure, which is the same structure as the substrate, SrTiO₃, at room temperature. The film, therefore, grows cubic, but when cooled, it undergoes a phase transition, and domain formation is initiated that creates strain. To reduce this, strontium was substituted onto the Pb-site, (Pb,Sr)TiO₃. It is reported for Pb_{1-x}Sr_xTiO₃ that the tetragonality of the structure is reduced and the cubic structure is reached at room temperature for x=0.5 [86, 87, 88]. Films of Pb_{1-x}Sr_xTiO₃ with nominally x=0.33, 0.39, and 0.43 were successfully grown with LPE. Several dopants were tested for both the PbTiO₃ and (Pb,Sr)TiO₃, but unfortunately, without obtaining more than indications of scintillation. Also, the strontium substitution significantly reduces the density of the film, resulting in much less promising prospects for the scintillation properties in the framework of this thesis. Simulations were conducted using the simulation tool described in Chapter 2. On this background, the project was terminated since it was simply out of scope, even though there were ideas on how to improve sample quality. Nevertheless, the growth and structure are of interest to the ferroelectric community. PbTiO₃ is a promising and well-studied multiferroic material and is extensively studied with various substitutions to obtain different polar phases and tunable piezoelectric and ferroelectric properties [89, 90, 91]. The project resulted in a publication named: "Tunable crystalline structure and electrical properties in (Pb,Sr)TiO₃ films grown by Liquid Phase Epitaxy", in the Royal Society of Chemistry, CrystEngComm in February 2023 [92]. The publication is presented in Appendix B, and the interested reader is encouraged to study the main findings on the titanate project there.

Micro-structured scintillators: Finally, we also investigated an alternative solution based on waveguided scintillators allowing to enlarge the scintillator thickness without significantly degrading the spatial resolution. Substrates were laser-treated with grids leaving pixels, and the goal is to grow pillars in these pixels by LPE, resulting in micro-structured growth. In this framework, typical state-of-the-art scintillators, LSO:Tb and GGG:Eu, were grown in a micro-structured manner on the laser-treated substrates, LYSO:Ce and GGG. This is the seed for a hopefully much longer project, but the findings and understanding of the growth and the characterization of samples provide a first proof of concept. Descriptions from the laser treatment to the growth and characterization of the properties are presented in Chapter 4.

Details concerning technical aspects of the instruments used for measurements performed during this thesis are presented merely in Appendix C not to overwhelm the reader with too many details.

Chapter 2

Predicting the spatial response of single crystal film scintillators

2.1 Introduction

Developing new scintillators can be a time-consuming and expensive process, especially when targeting scintillators for high-resolution X-ray imaging, where very high-quality thin SCFs (Single Crystalline Films) are required [54, 55, 56]. We have developed an important tool to avoid blindly trying to grow different films with the time-consuming LPE technique. It predicts the potential scintillating performance of thin SCFs, thereby letting us investigate if the targeted materials can possibly compete with or preferably outperform the state-of-the-art scintillators utilized at the synchrotron beamlines for high-resolution X-ray imaging. The simulations allow us to consider more materials and limit the development and optimization of the LPE growth to the more promising candidates. It saves time and money and provides a more profound understanding of the performance of scintillators at various X-ray energies.

Many additional factors than the potential scintillating performance have to be accounted for before initiating the LPE growth procedure. Some examples are the crystal structure of the SCF with respect to the substrate, which has to be iso-structural or at the least have close structural matching. If phase diagrams are available, these should be investigated carefully, especially because phase transitions and competing phases can limit the growth and quality of SCFs. For a presentation of a more in-depth evaluation of the LPE technique and the challenges encountered when working with it, see the LPE section in Chapter 1.

The simulation tool, which was developed in the frame of Federica Riva's thesis [70], and large parts of the work presented in this chapter were published in May 2022 in the Journal of Materials Chemistry C, Royal Society of Chemistry [84].

2.2 Geant4, Monte Carlo simulation tool

The proposed simulation tool evaluates the X-ray imaging performances of the SCFs focusing on their spatial resolution limitations and X-ray stopping power. The former depends on the absorption processes in the screen, for example, the SCF and substrate, combined with the light collection through the optics. The latter depends on the energy deposition driven by the composition and the screen geometry. The light yield, as well as the matching of emission wavelength with the spectral sensitivity of the camera, do not impact the spatial resolution, only the statistics, which can be compensated by increasing the exposure time. In addition, the light yield of scintillators often highly depends on the synthesis method, potentially leading to various defects and impurities. For state-of-the-art SCF scintillators, it can vary from sample to sample and cannot be predicted. Because we are focusing on the impact of the energy deposition on the spatial resolution, we have considered the same proportionality factor between the deposited energy and the number of emitted optical photons. In other words, the light yield is not considered at this stage.

The tool is based on Geant4, a well-established Monte Carlo simulation package [93] and subsequent analytical calculations. Geant4 predicts the spatial distribution of deposited energy in the SCF, resulting from the material interacting with incoming X-rays, and gives a spatial mapping of the deposited energy. We assume here that the deposited energy provides the scintillator response. Since the target and focus here is high-resolution X-ray imaging and this type of experiment is performed with monochromatic X-rays at synchrotrons, the simulations are also performed using monochromatic X-rays. In this thesis, simulations and corresponding results are performed at a broad range of energies (5-100 keV) because the applied X-ray energy at the beamlines depends on parameters such as the thickness and density of the sample as well as the beamline energy range(s). In the case of fast or ultrafast imaging, where the resolution can be compromised, a pink beam (non-monochromatic X-ray beam) can provide a considerably higher X-ray flux [33]. However, this is out of scope for this thesis but could easily be implemented in the tool. Analytical calculations then compute the blurring by optical transport of the resulting image, including diffraction of light and out-of-focus contributions. The resulting LSF and MTF can then be extracted. We assume to be in a configuration where the camera does not influence the spatial resolution, which is the case when the effective pixel size and pitch are significantly smaller than the resolution limit. For a typical setup used in this thesis, an effective pixel size of $0.2 \mu\text{m}$ is reached, and the resolution limit according to the Rayleigh criterion is around $0.9 \mu\text{m}$. An overall scheme representing the applied principles is presented in Figure 2.1, and each step will be presented in detail and evaluated in the following sections.

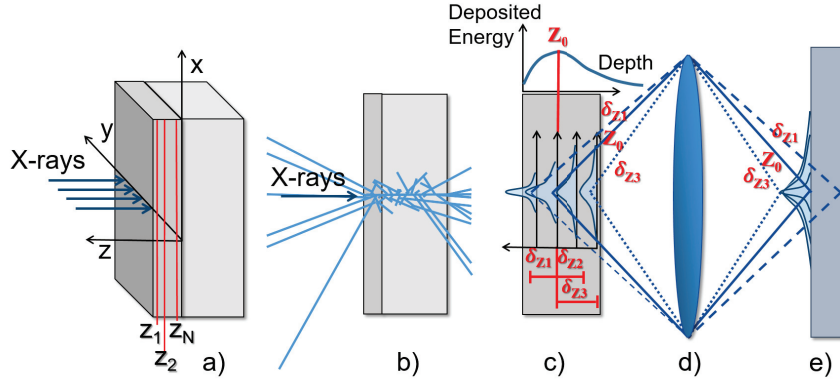


FIGURE 2.1: Schematic presentations of: a) Geometry and axis conversion applied in the simulation tool. b) Geant 4, Monte Carlo simulations tracking the incident X-rays and the resulting secondary particles. This reveals the spatial distribution of the deposited energy in the SCF, which (we assume) correspond to the scintillator response. c) A matrix describing the energy distribution for the depth of the scintillator. d) Optics blurring is estimated by taking the simulation's output and using it as input for the analytical calculations. e) Final response on the sensor, which is assumed as the sum of the response to every plane in the SCF.

2.2.1 Geant4 configuration

The SCF geometry is defined as a slab with thickness t_S and a lateral length of 1.4 cm. For consistency, all simulations presented in this study were performed with $t_S=5 \mu\text{m}$ except for those in the experimental validation section. The SCF is supported by a second $150 \mu\text{m}$ thick slab representing the substrate corresponding to the currently applied substrates in high-resolution X-ray imaging for the state-of-the-art scintillators. The SCF has a surface normal to the incoming X-ray beam along the z-axis. When running the simulation, a monochromatic one-dimensional X-ray pencil beam distributed along the y-direction hits the SCF perpendicularly to its surface (see Figure 2.1a).

The following three classes are mandatory to construct the simulation code with Geant4: `G4VUserDetectorConstruction` to describe the sample geometry and material, `G4VPhysicsList` defines the physical model, and `G4VPrimaryGenerator` is the primary particle generator hence the incoming X-ray beam. Integrated quantities must be calculated while the simulation runs to get useful output. In our tool, the class `G4VSensitiveDetector` is applied for this purpose by increasing the activated counters in the bin associated with the position of the interaction. Different counters can be defined, also simultaneously. The counter for energy deposited registers the energy distribution in the SCF. Other counters can track, for example, the energy deposited by a specific particle type (for example, only electrons), by a specific phenomenon (for example, only Compton scattering), or count the number of interactions, the number of secondary particles. The low-energy Livermore model [94, 95] is selected as the physical model. It has been validated for electrons and X-rays, or gamma

photons in the energy range from 250 eV to 1 GeV [94]. Every primary X-ray and generated secondary cascading particle are tracked individually (see Figure 2.1b) with a production threshold for secondary particles set at 250 eV. Consequently, a particle is not generated if it would have an energy lower than 250 eV. Instead, it is accounted for as if it deposited its energy in this bin. Low energy phenomena in solid-state physics are therefore not taken into account. This threshold is not critical for our model since we are studying diffraction-limited resolution, which is larger than the attenuation length of electrons at 250 eV. The diffraction limit for the setup used for this thesis is typically around $0.75 \mu\text{m}$, and the attenuation length for an electron with an energy of 10 keV is around $0.5 \mu\text{m}$ [96].

The modeling approach used for this tool does not consider solid-state physics entities such as electronic bands, phonons, and excitons. The compounds investigated as SCFs and substrates are merely defined by density and elemental stoichiometry. In the simulations, they are random distributions of atoms respecting the defined stoichiometry without considering their crystallinity. The program estimates the probability for a particle traveling in the material to interact with a specific type of atom and potentially deposit energy.

The energy deposition map provided by Geant4 is a two-dimensional matrix containing the spatial distribution of the energy deposited in the SCF. The substrate is not considered to scintillate and is therefore not accounted for in the energy deposition map, but this could be implemented. Every line corresponds to the LSF obtained at a different depth (z_i) in the SCF (Figure 2.1c). The LSF and MTF as a function of the z-coordinate, the total LSF and MTF (without any consideration of the optical effects) can be deduced, as well as the energy deposited in the SCF as a function of depth ($E_{dep}(z_i)$).

2.2.2 Blurring by optics

The modeling of the optical transport to the camera is based on the analytical model described by Hopkins [97], which calculates the response of an aberration-free optical system. Considering the diffraction of light and the defect of focus (δz), the optical transfer function (OTF) of a defocused optical system is calculated as a convergent series of Bessel functions. The optics blur the image from each plane as a function of the position of the plane along the thickness of the SCF (Figure 2.1d). Assuming the system is focused at a specific position, z_0 (the focal plane), the planes within a thickness dz equal to the depth of field (DoF) around z_0 are projected as a focused image and thus only blurred by the diffraction of light. The planes outside dz are additionally blurred as a function of the distance from z_0 (denoted δz). The total MTF is then calculated as the average of every plane in the SCF, weighted by the deposited energy in the i^{th} slice (E_i^{dep}) while assuming the system is focused on the j^{th} bin in z:

$$MTF_{z_0=j}^{tot}(f) = \frac{\sum_{i=1}^N MTF_i^{scint}(f) \cdot MTF_i^{opt}(\delta z, f) \cdot E_i^{dep}}{\sum_{i=1}^N E_i^{dep}} \quad (2.1)$$

Where N is the total number of bins along z , $MTF_i^{scint}(f)$ is here the MTF calculated from the energy deposited in the i^{th} slice obtained from the Geant4 simulations, $MTF_i^{opt}(f)$ is the modulus of the OTF and f is the spatial frequency in the object plane. The position of z_0 was selected by calculating the maximum total MTF as a function of the focus position along z . This then provides the final estimate of the actual response, as seen by the imaging camera (Figure 2.1e).

2.2.3 Investigated materials

To validate the simulation tool, state-of-the-art SCF scintillators have been used and compared to prospective scintillators, notably LSO:Tb on YbSO, GGG:Eu on GGG, and freestanding LuAG:Ce, all applied on X-ray imaging beamlines today [98]. LuAG:Ce can also be grown by LPE on YAG substrates [64], and for the sake of comparing the different SCFs, the simulations include a YAG substrate. Furthermore, the two more recently explored high-density SCFs: Lu₂O₃:Eu on Lu₂O₃[99] and GAP:Eu on YAP [100] are included for comparison as well as the prospective scintillating SCFs investigated in this thesis namely.

A list of all the materials and the parameters used for the simulations and optics calculations (stoichiometry, density, λ_{emis} , refractive index) are summarized in Table 2.1. The applied emission wavelength (λ_{emis}) of the SCFs is consistent with the usual dopants for the state-of-the-art SCF scintillators. For the prospective scintillating SCFs, it was chosen to be 615 nm. The emission from different dopants is rarely just one wavelength. However, for the sake of simplicity of the optics calculations, the commonly most intense or relevant emission wavelength for the specific dopant has been used. In the case of europium, the two main peaks are 595 and 710 nm, but a wavelength of 615 nm was applied as a compromise.

Short name	Chemical formula	Dopant	λ_{emis} [nm]	Density [g/cm ³]	n	Substrate
GAP	GdAlO ₃	Eu	615	7.50	1.97	YAP
	Lu ₂ O ₃	Eu	615	9.50	1.935	Lu ₂ O ₃
LSO	Lu ₂ SiO ₅	Tb	550	7.40	1.82	YbSO
LuAG	Lu ₃ Al ₅ O ₁₂	Ce	540*	6.73	1.84	YAG
GGG	Gd ₃ Ga ₅ O ₁₂	Eu	615	7.10	1.97	GGG
GdLuAP	Gd _{0.5} Lu _{0.5} AlO ₃	Eu	615	8.00	1.935	YAP
PTO	PbTiO ₃	Eu	615	7.95	2.70	SrTiO ₃
PST	Pb _{0.5} Sr _{0.5} TiO ₃	Eu	615	6.70	2.70	SrTiO ₃
LHO	Lu ₂ Hf ₂ O ₇	Eu	615	10.00	2.00	ZrO ₂ :Y
	Tm ₂ Hf ₂ O ₇	Eu	615	9.71	2.00	ZrO ₂ :Y
	HfO ₂	Eu	615	10.00	2.1114	ZrO ₂ :Y

TABLE 2.1: Commonly used short names if any, chemical formula, dopant, and corresponding typical value for emission wavelengths, (λ_{emis}) where * indicates emission is normally a broadband, density, refractive index (n), and substrate of the various materials investigated with the simulation tool. P=Perovskite, G=Garnet.

2.3 Simulation outputs

2.3.1 Energy Deposition

As already discussed, having the scintillating SCF thicker than the DoF will induce blurring of the final image. To achieve the highest spatial resolution ($\sim 1 \mu\text{m}$ or better), it is a requirement that the SCF is very thin. Let us consider, for example, a GGG:Eu SCF combined in an imaging system with $\text{NA}=0.4$, total magnification of $\times 33$, and a camera pixel size of $7.4 \mu\text{m}$. For such a system, the DoF is around $4.4 \mu\text{m}$ (Equation 1.1). This indeed renders the X-ray absorption critical, especially when detecting high-energy X-rays. The X-ray absorption efficiency affects the Detective Quantum Efficiency (DQE) of the system and should therefore be considered when examining the overall performance of potential SCF scintillators.

In low-dimensional systems, the effective energy deposition differs from the attenuated energy due to the escape of fluorescent X-rays. For this reason, the effective energy deposited in some SCFs has been extracted from our simulations at X-ray energies from 15 to 100 keV (Figure 2.2b). Comparing it to the attenuated energy in the freestanding SCFs using the photon cross-section database from NIST [71] (Figure 2.2a), notable differences at high energy are apparent. This is mainly visible at energies higher than the X-ray absorption K-edge of the high Z element, where the escape of secondary X-rays increases for both the SCF and the substrate.

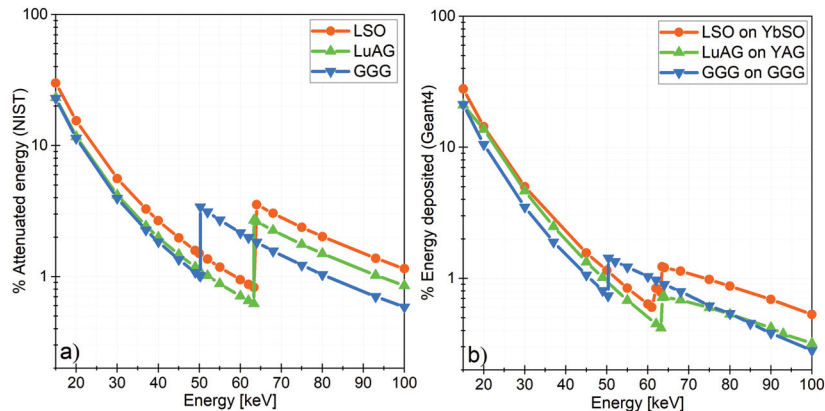


FIGURE 2.2: a) Percentage of incident beam energy attenuated by $5 \mu\text{m}$ thick SCFs of various materials, calculated using data from the NIST database [71]. b) Percentage of incident beam energy deposited in various $5 \mu\text{m}$ SCFs supported by $150 \mu\text{m}$ substrates, estimated by tracking all the (secondary) X-rays and electrons using our application based on the Monte Carlo Geant4 toolkit.

As computed from the photon cross-section, the attenuation provides a fair approximation of the effective deposited energy at X-ray energies below the K-edge energies of the high Z elements in the SCF. When the X-ray energy exceeds these K-edge energies from the SCF, the modeling of X-ray fluorescence is thus needed to obtain an accurate estimate of the energy deposit. Secondary X-rays with these energies can easily escape the thin SCF and do not deposit their energy within the SCF.

Opposite, when the primary X-ray photons interact in the substrate, the secondary particles generated there can reach the SCF and deposit energy, potentially far from the primary interaction.

The contributions from the different particles were isolated to investigate further the effects of exceeding absorption edge energies of elements in the SCF and the substrate. With the simulation tool, we have isolated the deposited energy distribution of the following particle types: primary X-rays, secondary X-rays, photoelectrons created from interactions with either primary or secondary X-rays, and resulting electrons from electron-electron scattering. The interaction mechanisms were briefly discussed in Section 1.1.3.3. We do not consider Compton electrons since the working energies are lower than 100 keV, making their contribution insignificant. It is important to note that in reality, the X-rays do not deposit their energy directly; instead, they generate secondary electrons that eventually deposit energy. As mentioned, in the Monte Carlo model, an energy threshold is set at 250 eV for the production of the secondary particles. This results in secondary particles with an energy lower than the threshold are not generated and, therefore, not considered. The remaining energy is hence counted as deposited by the X-rays in the position of the interaction. It is essential to keep in mind that the energy seemingly deposited by X-rays, therefore, depends on this production threshold. In our case, it corresponds to the amount of energy electrons deposit with a diffusion length shorter than the size of the voxel defined in the simulation.

2.3.2 Spatial resolution and contrast

The energy of the incoming X-rays significantly impacts the spatial distribution of deposited energy in the SCF and, thereby, the obtainable spatial resolution and contrast of the final image. Generally, when increasing the X-ray energy, the generated photoelectrons deposit energy at an increasing distance from the first point of interaction (between the primary X-ray beam and the SCF) due to their increasing kinetic energy:

$$E_{kin} = E_{Xray} - E_{binding} \quad (2.2)$$

where E_{Xray} is the energy of the incoming X-ray and $E_{binding}$ the binding energy of the electron. This effect will induce blurring of the image resulting in a decreasing contrast. It is thus crucial to consider the major impacts on the contrast occurring when applying X-rays of energies close to the X-ray absorption edges of the elements in the SCF and substrate.

In the following sections, quantitative improvement and degradation of the contrast when varying the X-ray energy will be presented and discussed for a selected set of relevant materials, restricting the description to the energy deposition effect.

2.4 Results

The energy of the secondary particles determines their attenuation length and plays, therefore, a major role in the spread of the deposited energy, as already discussed. The estimated attenuation length for electrons and photons in LuAG is displayed in Figure 2.3a and b and can act as guidelines to understand the features in the energy spread, which will be discussed in this chapter.

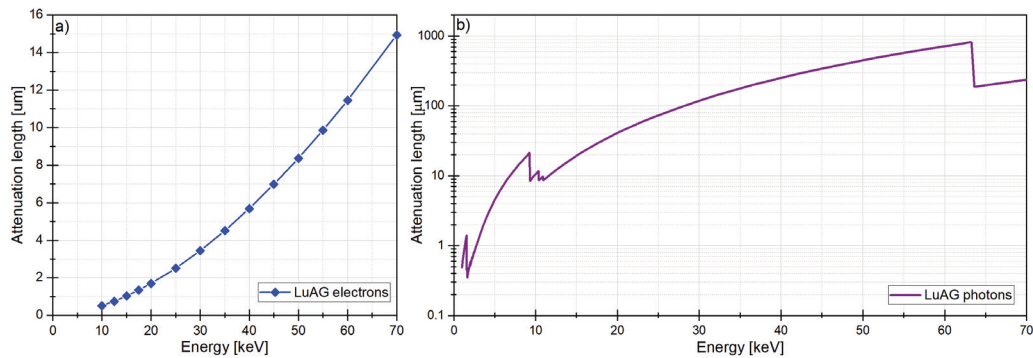


FIGURE 2.3: a) The attenuation length of electrons in LuAG, calculated from data from the NIST database [96]. b) Attenuation length of photons in LuAG calculated from data from the NIST database [101].

2.4.1 Influence of X-ray fluorescence

It is known that X-ray fluorescence in scintillating materials degrades the spatial resolution because they can deposit their energy far from the initial interaction point. This section details this effect, and the role of the absorption edges of high Z elements of the substrate and film is demonstrated. For this part, simulations were performed on a typical SCF, namely LuAG:Ce supported by YAG substrate. The purpose is to highlight the effects on the LSF and MTF when imaging is performed with X-ray energies below and above the L- and K-edge of the heaviest element of the SCF and the K-edge of the heaviest element of the substrate. Relevant high Z element edges for LuAG on YAG are listed in Table 2.2.

Element	Edge	Energy [keV]
Lu	K	63.31
	L3-1	9.24-10.87
	M5-1	1.59-2.49
Y	K	17.04
	L3-1	2.08-2.37

TABLE 2.2: Relevant absorption edges [102] for high Z elements for LuAG on YAG.

L-edges: As shown in Figure 2.4a, increasing the X-ray energy above the SCF L3-edge initiates an increase of both the tails and broadness of the LSF. The increase in

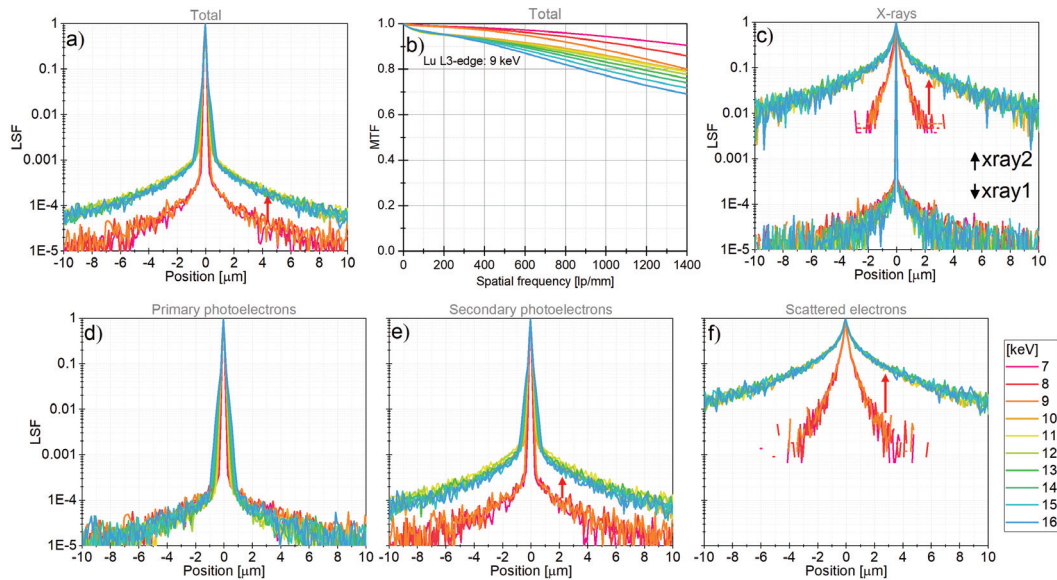


FIGURE 2.4: LSFs and MTFs simulated using X-ray energies close to the L-edges of the SCF high-Z element. Red arrows indicate significant changes in the direction of increasing X-ray energies. a) LSFs and b) MTFs. LSFs from energy depositions of specific particles: c) Primary X-rays (xray1) and secondary X-rays (xray2), d) photoelectrons created from primary X-rays, e) photoelectrons created from secondary X-rays, and f) resulting electrons from electron-electron scattering. Simulations are performed on $5\ \mu\text{m}$ LuAG:Ce on $150\ \mu\text{m}$ YAG.

tails is a result of more energy being deposited 1 to $10\ \mu\text{m}$ away from the initial interaction point. The increase in broadness is then a result of the very localized particles depositing energy slightly further into the SCF. Note the y-axis is a logarithmic scale, so the increase in the tails is relatively small. Secondary particles (secondary X-rays, secondary photoelectrons, and electrons from electron-electron scattering) cause this spread in energy deposition (see Figure 2.4c,e,f). Note also that the scattered electrons and fluorescent X-rays below the L3-edge only deposits energy a few microns away, whereas above, it is more than $10\ \mu\text{m}$. This is a consequence of these being the first energies where the fluorescent X-rays have enough energy to reach further away from the initial interaction point before depositing energy. The probability then increases to create secondary photoelectrons with a resulting higher energy already created further away from the first interaction point. The tails in the LSF of the primary photoelectrons are the same above and below the L3-edge, but the broadness of the peak is larger when above the L-edge. This is due to their increasing resulting energy. Considering the MTF in Figure 2.4b, the contrast is at maximum reduced 3-4%.

Lu also has M-edges between 1.6 and 2.5 keV (See Table 2.2). However, there are no significant effects on the energy spread in the SCF because the energy of the resulting fluorescent X-rays is also very small, and therefore the attenuation length. The energy is deposited very close to the first interaction point and does not cause any degradation of the LSF and MTF.

K-edge of the substrate: As shown in Figure 2.5b, increasing the X-ray energy above

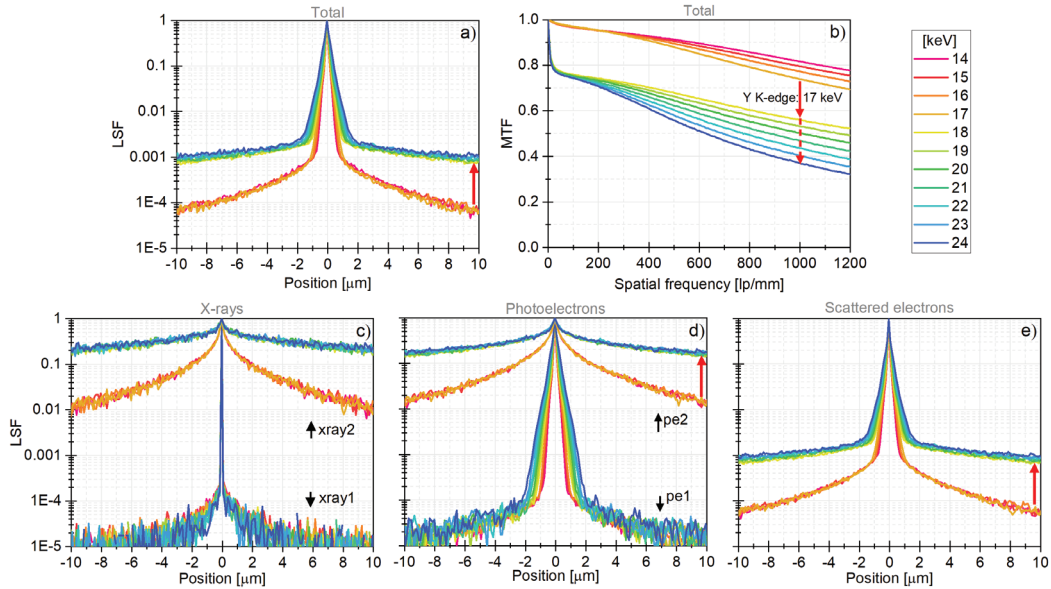


FIGURE 2.5: LSFs and MTFs simulated using X-ray energies close to the K-edge of the substrate high-Z element. Red arrows indicate significant changes in the direction of increasing X-ray energies. a) LSFs and b) MTFs. LSFs from energy depositions of specific particles: c) Primary X-rays (xray1) and secondary X-rays (xray2), d) photoelectrons created from primary X-rays (pe1) and secondary X-rays (pe2), and e) resulting electrons from electron-electron scattering. Simulations are performed on $5 \mu\text{m}$ LuAG:Ce on $150 \mu\text{m}$ YAG.

the substrate K-edge initiates a sharp decrease of $\sim 20\%$ in contrast of the MTF. This drop close to 0 lp/mm corresponds to the increase of the tails in the LSF in Figure 2.5a. The isolated LSF contributions from the relevant particle types are presented in Figure 2.5c-e. All secondary particles deposit significantly more energy far from the first interaction point when the incoming X-ray energies exceed the substrate K-edge. This agrees with fluorescent X-rays generated in the substrate that then interact and deposit energy in the SCF. The primary photoelectrons only deposit energy continuously further away, corresponding to their increasing energy after the photoelectric interaction.

K-edge of the film: As shown in Figure 2.6b, when exceeding the K-edge energy of the SCF, here of Lu, there is a sudden increase in contrast of $\sim 25\%$ of the MTF. Further increase of the X-ray energy induces a continuous increase in contrast until it stabilizes around 70 keV with an additional gain of $\sim 10\%$. In the corresponding LSF (Figure 2.6a), the effect is observed as a sudden decrease of the tails, followed by a continuous reduction between 0.3 and $4 \mu\text{m}$ with increasing X-ray energy. In Figure 2.6c-e are the isolated LSFs for the different particle contributions at these energies presented. When exceeding the SCF K-edge, all types of generated electrons deposit more of their energy very close or directly at the initial interaction point, giving rise to the sudden decrease in the LSF. This results from the increased probability of the photoelectric effect when the incoming X-ray beam has energy above the SCF K-edge. The fluorescent X-rays (secondary X-rays) also slightly increase the tails of

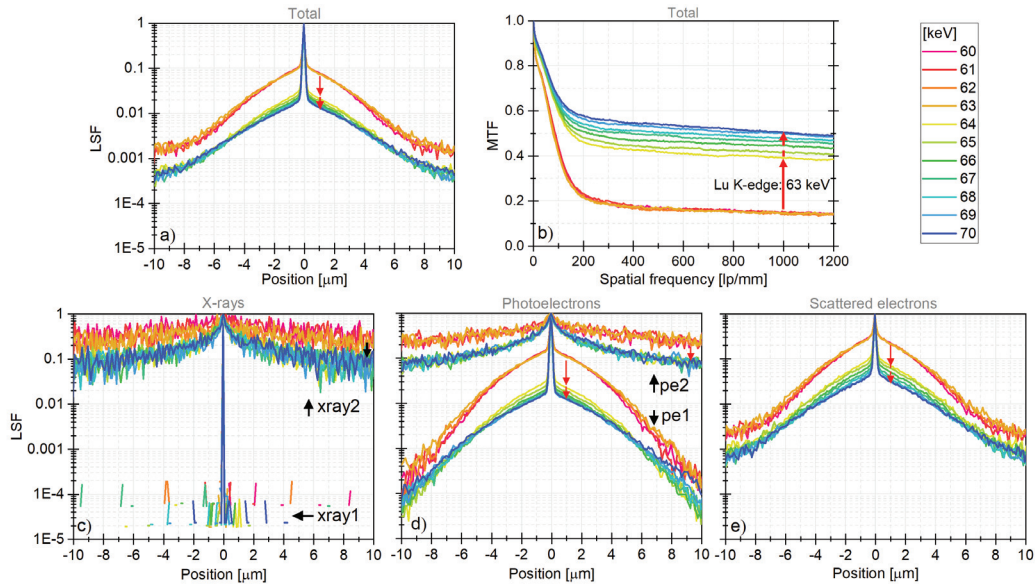


FIGURE 2.6: LSFs and MTFs simulated using X-ray energies close to the K-edge of the SCF high-Z element. Red arrows indicate significant changes in the direction of increasing X-ray energies. a) LSFs and b) MTFs. LSFs from energy depositions of specific particles: c) Primary X-rays (xray1) and secondary X-rays (xray2), d) photoelectrons created from primary X-rays (pe1) and secondary X-rays (pe2), and e) resulting electrons from electron-electron scattering. Simulations are performed on $5 \mu\text{m}$ LuAG:Ce on $150 \mu\text{m}$ YAG.

the LSF but due to their large energy and, therefore, large attenuation length (see Figure 2.3b), most will escape from the SCF and those that do not contribute to the image. However, the photoelectrons have sufficiently low energy resulting in short attenuation length (see Figure 2.3a), leading them to deposit energy very close to the initial point of interaction. The continuous improvement is ascribed to increased local energy deposition due to the increased X-ray beam energy. Indeed, the energy of the primary electrons will be $\sim 0.7\text{-}6.7$ keV (assuming they are created from primary X-ray photons with energy $64\text{-}70$ keV and the K-shell of Lu) the attenuation length will typically be shorter than $0.5 \mu\text{m}$ (CSDA, NIST [96], see also Figure 2.3), thereby containing the resulting energy deposit very close to the initial point of interaction.

Comparing edges: Figure 2.7 provides an overview of the MTFs for the same $5 \mu\text{m}$ LuAG:Ce on YAG, simulated with incoming X-rays with energies from 5 to 100 keV. In the figure, the type of element, respective type of absorption edge, and corresponding energy are indicated to highlight what was already discussed earlier in this section. The simulations show that the lowest MTF is obtained at around 62 keV for the studied energy range.

In Figure 2.8, the MTFs simulated just above and below the relevant edges are extracted for better visualization. The difference above and below the Lu L3-edge is small (maximum 3-4 %) compared to the Lu K-edge (initial ~ 25 % then additional ~ 10 %) and the Y K-edge (~ 20 %).

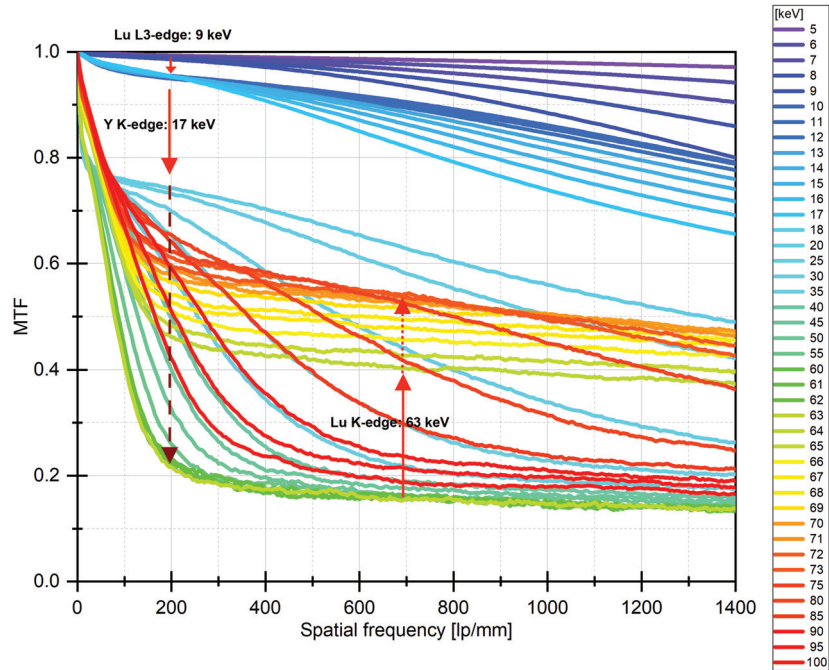


FIGURE 2.7: Overview of MTFs simulated at X-ray energies from 5-100 keV. The X-ray absorption edges causing the main features are indicated in the figure, with the red arrows indicating the direction of increasing X-ray energies. Simulations are performed on $5 \mu\text{m}$ LuAG:Ce on $150 \mu\text{m}$ YAG.

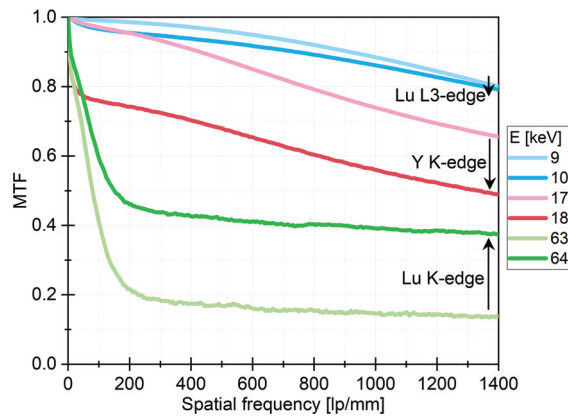


FIGURE 2.8: MTFs simulated at X-ray energies just above and below the X-ray absorption edges causing the main features. Going above the K-edge of the high Z-element of the SCF improves the MTF, whereas the edges in the substrates decrease it. Simulations are performed on $5 \mu\text{m}$ LuAG:Ce on $150 \mu\text{m}$ YAG.

It is tempting to conclude at this point that the X-ray energy of the imaging experiment should be either below or above the high-Z element K-edge of the substrate or films, respectively, to gain spatial resolution. However, the energy at the beamlines is, in reality, chosen according to the sample absorption, so the density, size, and what is feasible at the specific beamline. Indeed, it would benefit the scientists at the beamlines to consider these effects when choosing the energy.

2.4.2 Combined influence of SCF and substrate

We demonstrated above the opposite contribution of the SCF and the substrate on the MTF when the X-ray energy exceeds the absorption edges of their heaviest element. For some scintillators, the substrate and the host structure of the SCF can be of the same type, such as GGG:Eu supported by undoped GGG substrates. We have simulated the LSFs and MTFs at X-ray energies from 48 to 58 keV (Gd K-edge at 50.24 keV) for this particular scintillating SCF.

Figure 2.9 shows that when exceeding the Gd K-edge both effects are visible but at different spatial frequencies. There is a sharp decrease of the MTF at frequencies below 150 lp/mm caused by fluorescent X-rays from the substrate. While at higher frequencies, the contrast is significantly increased owing to the low attenuation length photoelectrons created in the SCF. When further increasing the X-ray energy, the contrast above ~ 200 lp/mm is slowly increased due to the increased energy deposition close to the first point of interaction until it stabilizes and starts to decrease again for higher energies here being with an onset of 58 keV at 1200 lp/mm.

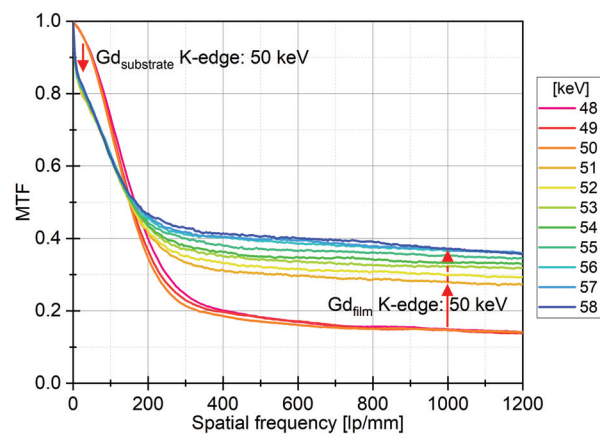


FIGURE 2.9: MTFs simulated around the X-ray absorption K-edge of the high Z-element that is both incorporated in the SCF and the substrate. Red arrows indicate significant changes in the direction of increasing X-ray energies. Simulations are performed at $5 \mu\text{m}$ GGG:Eu on $150 \mu\text{m}$ GGG.

When the X-ray energy exceeds the Gd K-edge energy, two effects occur. First, the X-ray absorption cross-section increases by about one order of magnitude. Secondly, the probability of X-ray fluorescence also drastically increases. If absorption occurs in the substrate, part of the resulting fluorescent X-rays may be reabsorbed far from the first interaction in the SCF, resulting in degradation of the low-frequency contrast. When the interaction occurs in the SCF, the generated photoelectrons have a small mean free path, and the energy deposited is very localized. The situation is degraded when X-ray fluorescence occurs, for instance, when exceeding the L-edges, but its re-absorption will mostly occur out of the SCF when working at higher energies. Exceeding high energy absorption edges improves contrast at high frequencies, and

the optics dominate the image degradation. Further, the continuous improvement when the X-ray energy increases above the K-edge is caused by the increase of the local energy deposition.

2.4.3 Including optics

The deposited energy is converted into optical photons in the SCF through scintillation. Since the energy is deposited along the thickness of the SCF, the scintillation "image" is blurred while projected onto the camera by the microscope optics. Figure 2.10 demonstrates the significant contribution of this blurring. At low X-ray energies especially, the optical blurring strongly degrades the otherwise exceptional spatial resolution expected by only considering the energy deposit contribution. At high energies, however, most of the MTF degradation is caused by the energy spatial distribution in the SCF. Notice at 60 keV, the MTF is better for GGG than LSO, especially without blurring, since we are above the Gd K-edge but still below the Lu K-edge.

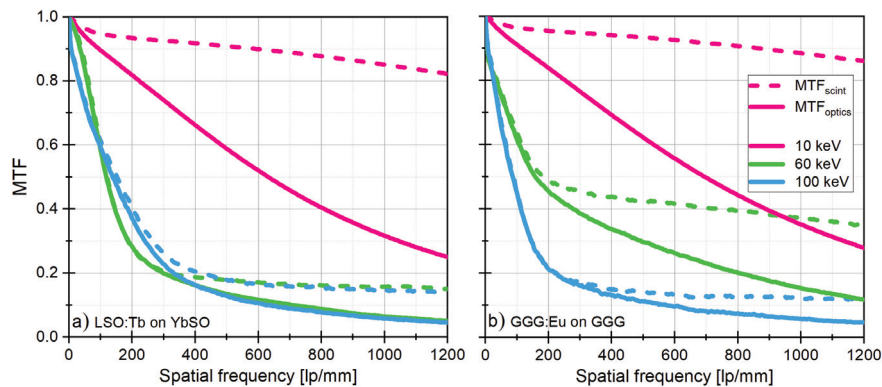


FIGURE 2.10: Comparing simulated MTFs with optics (MTF_{optics}) and without (MTF_{scint}). The optics included here is $NA=0.80$. SCF, substrate, and X-ray energies are indicated in the figures. The simulations are performed for $5 \mu\text{m}$ SCF on $150 \mu\text{m}$ substrate.

In the figure, a Numerical Aperture (NA) of 0.80 is chosen. For the sake of completeness, the influence of the NA at various X-ray energies is presented in Figure 2.11. Here it is seen that at low energy (10 keV), the optics limit the spatial resolution due to light diffraction. However, if the experiment does not require a spatial resolution better than $2.5 \mu\text{m}$ (corresponding to 200 lp/mm), a NA of 0.15 is sufficient (also given by the resolution limit given by Rayleigh criterion). In this case, a thicker SCF scintillator can be selected as long as it is not exceeding the depth of field. If we included SCFs thicker than the depth of field, we would have observed the degradation caused by defocus. The role of the specific material becomes crucial when using energies above the K-edge of high-Z elements of the substrate, which is why the materials perform similarly at 10 keV.

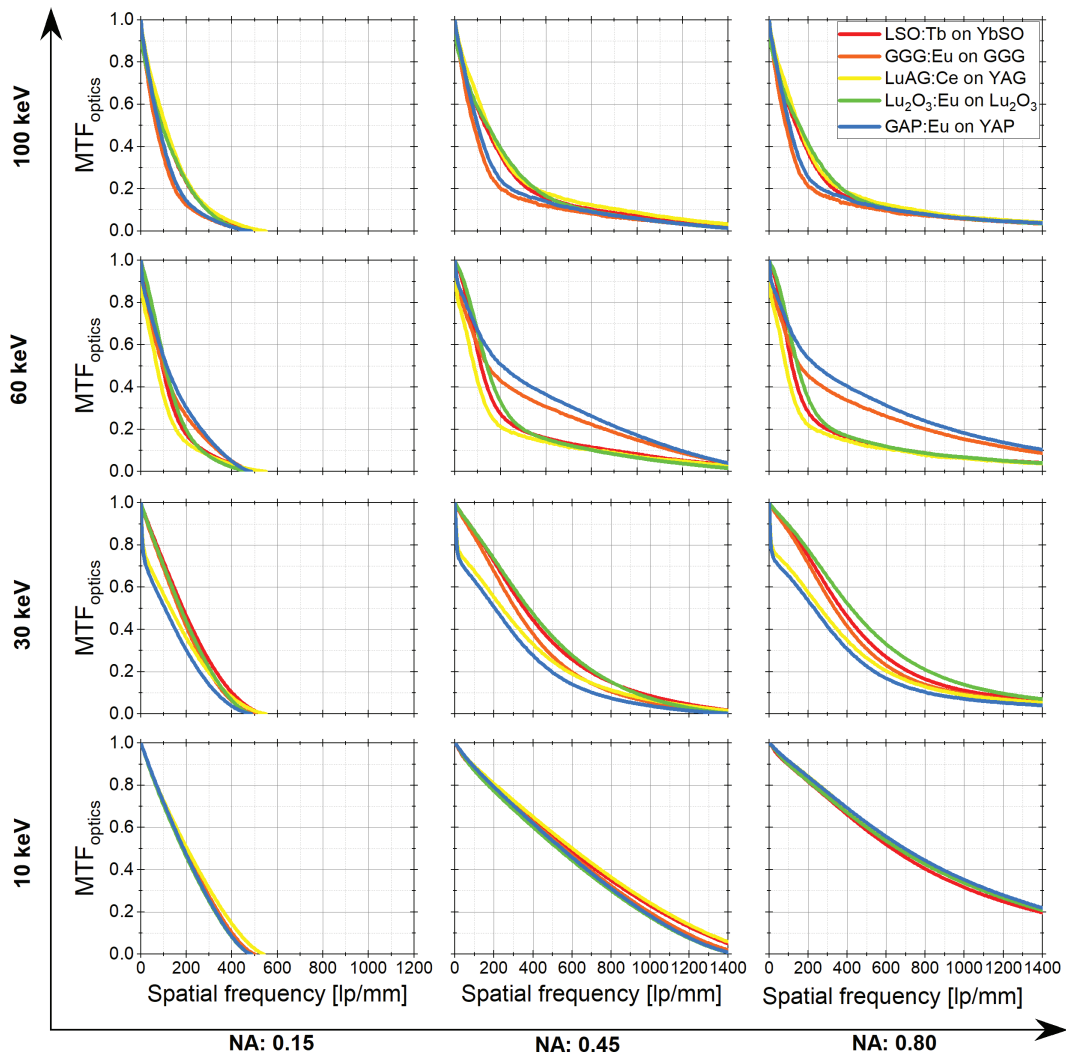


FIGURE 2.11: Evaluation of the effects of using various NA at four X-ray energies on simulated MTFs. SCF and substrate are listed in the legend, NA and X-ray energy is indicated on the two axes. Simulations performed at $5 \mu\text{m}$ SCFs on $150 \mu\text{m}$ substrates.

An evaluation of the scintillators (film+substrate) will not be suggested here, but instead in relation to the figure of merit that is displayed in the next section since it considers more energies as well as other aspects than just the spatial resolution.

2.4.4 A Figure of Merit

Evaluating the achievable performance of scintillating SCFs is not straightforward due to the overwhelming combination of factors that influence them. We thus propose a Figure of Merit (FoM) to estimate the best compromise between a sharp image and an efficient detector:

$$\text{FoM}(E) = \text{MTF}_{500 \text{ lp/mm}}^{NA=0.40}(E) * E_{dep}(E) \quad (2.3)$$

The value of the MTF at 500 lp/mm is applied because it describes how well 1 μm sized features are resolved, thereby fitting the scope of this thesis. $E_{dep}(E)$ is the amount of energy deposited in the SCF extracted using the simulation tool as a function of X-ray energy. This figure of merit allows us to evaluate the materials as a function of X-ray energy while simultaneously considering the spatial resolution, contrast (including blurring by optics), and absorption efficiency.

The performance of the complete detector system will be better described by the Detective Quantum Efficiency (DQE). This figure of merit proposed is merely a simple approach to evaluate and compare SCFs for high-resolution X-ray imaging at synchrotrons. The figure of merit for some state-of-the-art and more recently investigated SCFs is presented at energies from 5 to 100 keV in Figure 2.12b. Below 50 keV and from 64 to 100 keV, Lu_2O_3 is the material that, on these terms, performs the best according to the simulations, while between 50 keV and 64 keV GAP is superior.

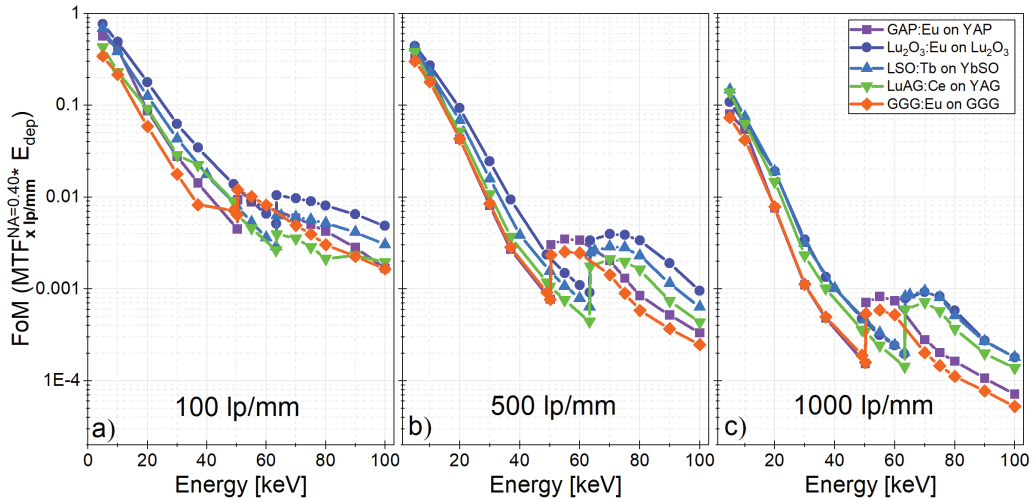


FIGURE 2.12: The proposed Figure of Merit (FoM) calculated from the energy deposited in the SCF and the contrast in the MTF blurred by optics ($NA=0.40$) at a) 100 lp/mm, b) 500 lp/mm and c) 1000 lp/mm. Values are extracted from simulations at X-ray energies 5-100 keV for 5 μm SCFs on 150 μm substrates.

The proposed figure of merit is an appropriate tool for investigating unexplored materials and finding better alternatives to state-of-the-art scintillators. It allows one to perform a thorough screening of materials before attempting to produce them

but is not able to predict if a material will be scintillating in practice. The figure of merit can easily be adjusted to evaluate a different spatial resolution by changing the applied MTF value. This concept is presented in Figure 2.12a and c, where the MTF at 100 and 1000 lp/mm are used for the calculation, respectively. This corresponds to the ability of the system to resolve 5 μm and 0.5 μm details, respectively. However, this figure of merit gives a limited vision of the potential scintillator performance, especially because it only considers the MTF for a single spatial frequency. A more fulfilling figure of merit could be created by integrating the MTF over a range of selected spatial frequencies adjusted to the spatial resolution investigated instead. Additionally, to truly examine and compare already existing scintillators one should consider other parameters like the light yield and adequate matching of the emission spectrum with the spectral sensitivity of the applied detector. The spectral sensitivity depends on the specific sensor applied for the experiment and could be included. However, the light yield is challenging to predict and varies with the growth method.

2.5 Experimental validation

In order to validate the proposed simulation method, MTFs of several scintillating SCFs were evaluated experimentally with the slanted edge method [79, 80]. The concept of this method is described in Section 1.2.1.3. For these specific measurements, a 525 μm thick GaAs edge carefully cleaved and positioned 1-3 mm away from the scintillator was used to absorb part of the X-ray beam. Acquired edge images were corrected by flat-field and dark images. The complete detector system comprises the scintillator under investigation combined with microscope optics (NA of 0.4 and 10x magnification) followed by a 3.3x eyepiece magnification and either a PCO2000 camera (Figure 2.13a-b) or PCO edge 4.2 (Figure 2.13d) having a pixel size of 7.4 μm and 6.5 μm , respectively. The measurements were performed using monochromatic synchrotron radiation at ESRF beamline BM05 using a Si(111) crystal with an energy resolution of $\Delta E/E \approx 10^{-4}$ [103].

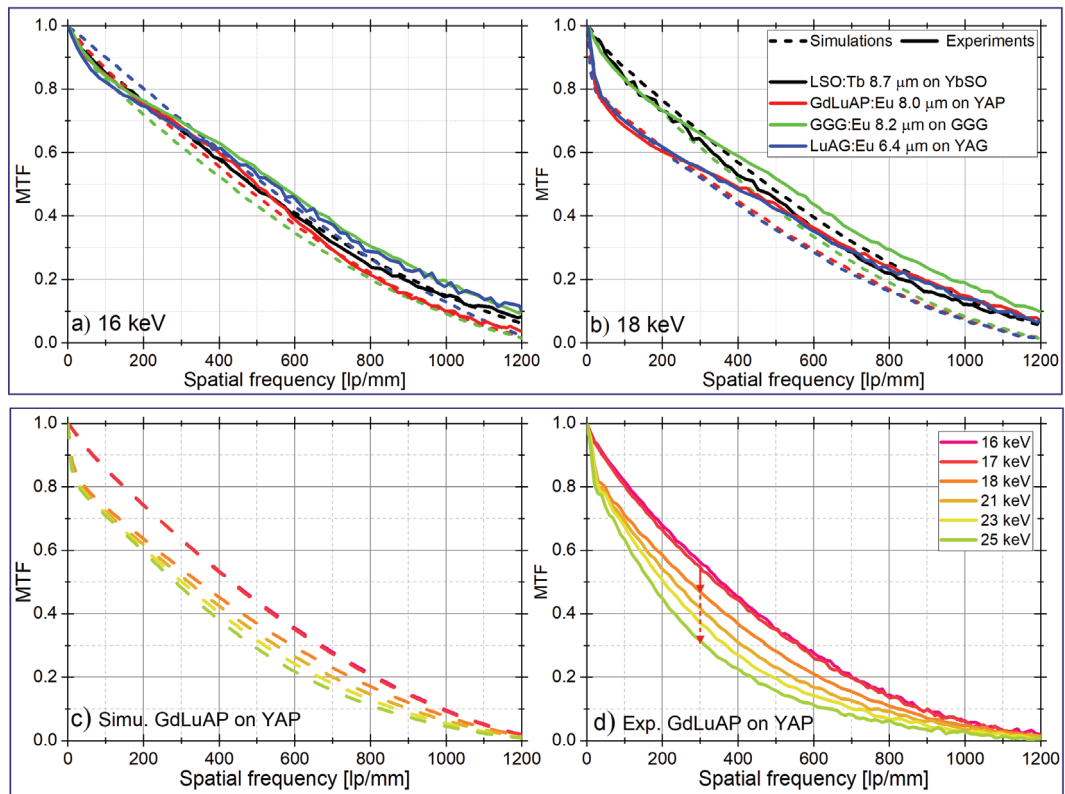


FIGURE 2.13: Experimentally measured (continuous lines) and simulated (dashed lines) MTFs for various scintillating SCFs supported by substrates at a) 16 keV and b) 18 keV. MTFs obtained from simulations c) and experiments d) for an $\sim 11.5 \mu\text{m}$ GdLuAP:Eu scintillating SCF supported by 150 μm YAP, at X-ray energies from 16 to 25 keV. All experiments were performed with a monochromatic X-ray beam at BM05, ESRF.

Figure 2.13a-b shows good agreement between simulations and experimental data. It should here be mentioned that many factors affect the experimental MTF, such as the alignment of the beam and slits, as well as the quality and tilt of the

edge. A small deviation from the simulated curve is difficult to avoid. Also, some of the experimentally obtained MTFs in Figure 2.13 are actually out-competing the simulations. This can be attributed to the effect of phase contrast which enhances the contrast and thereby the MTF. As predicted by the simulations, the MTFs of all the considered scintillators are similar at 16 keV (Figure 2.13a) while at 18 keV (Figure 2.13b) a sudden reduction of the contrast close to 0 lp/mm is observed for scintillators with Y-based substrates (K-edge of Y is 17.04 keV).

To further validate the predicted behavior of the MTFs at energies around the substrate K-edge we have applied the slanted edge method on a $\sim 11.5 \mu\text{m}$ GdLuAP:Eu SCF supported by 150 μm YAP substrate [100]. The experimental MTFs in Figure 2.13d found for X-ray energies from 16-25 keV are again in good agreement with the simulations. The MTF undergoes a sharp decrease close to 0 lp/mm when exceeding the substrate K-edge energy. When further increasing the X-ray energy, the contrast decreases also as expected. However, when carefully comparing the MTFs from simulations (Figure 2.13c) with the experiments (Figure 2.13d) a difference in the contrast up to 15% is observed. There can be several explanations for this. GdLuAP SCFs are found to undergo birefringence, which degrades the MTF. By rotating the SCF perpendicular to the X-ray beam, the degree of birefringence varies and the optimum MTF affected the least by birefringence can thereby be found [100]. The MTFs in Figure 2.13d are recorded at what was found to be the optimum rotation angle at the specific beamtime. Since the rotation is manually adjusted, the angle was maybe not truly optimized. A not-perfect adjustment of the rotation angle results in further degradation of the MTF. Furthermore, the YAP substrate scintillates slightly and to filter out this emission, a bandwidth filter (634 nm, FWHM: 70 nm) was inserted in the optical path. If part of this emission was not fully filtered out it could have partly degraded the MTF. Also, the observed deviation between simulations and experiments can simply be caused by a slight defect of focus in the optics. The experiment nevertheless confirms to a large extent the observed trends in the simulations.

2.6 Prospective materials

This simulation tool has been very helpful in better understanding the consequences of performing imaging experiments above or below the absorption edge energies of the scintillator and substrate. It also supported the pre-selection of materials before performing the growth by LPE since this process is very costly and time-consuming, as already described in Chapter 1. Families of compounds were identified, here among the titanates and hafnates, and investigated using the simulation tool. To evaluate if the LPE procedure should be performed, the simulations of the materials were compared to those of state-of-the-art SCF scintillators. The simulation tool cannot predict other important parameters such as the light yield, afterglow, and bright burn. This section will present and evaluate the results from some of the many simulations performed on prospective materials. The materials will be evaluated with the help of the earlier defined figure of merit and compared to state-of-the-art LSO:Tb on YbSO and GGG:Eu on GGG.

The Titanates: In Chapter 1, the project concerning the growth of titanates was introduced and shortly described. Simulations were performed on these materials to evaluate better the potential of such films. In Figure 2.14a, the figure of merit of PbTiO_3 is compared to the state-of-the-art scintillators. Below 50 keV it is similar to Lu_2O_3 but above it underperforms until reaching 90 keV and higher. However, above 100 keV it is of all the investigated SCFs the best choice. Since the K-edge of Pb is at 88 keV, the figure of merit decreases a lot before having the sudden increase caused by exceeding the high-Z element K-edge and achieving low attenuation length photoelectrons depositing energy close to the first interaction point in the SCF. In Figure 2.14b, the figure of merit for the pristine PbTiO_3 and $\text{Pb}_{0.5}\text{Sr}_{0.5}\text{TiO}_3$ both doped with europium on SrTiO_3 substrates are presented. Since the density for PbTiO_3 is 7.95 g/cm^3 and after the strontium substitution $\text{Pb}_{0.5}\text{Sr}_{0.5}\text{TiO}_3$, 6.7 g/cm^3 , a general decrease in the figure of merit is expected. Initial growth experiments showed that substitution with strontium in the structure is needed (described in Chapter 1), which would then decrease the overall performance of the scintillating SCF. Additionally, initial results did not show significant scintillation after doping with different rare earth elements: chromium, samarium, erbium, and europium. This made us terminate further test growth and development of this material for scintillation purposes.

The Hafnates: In Chapter 3, the growth of various types of hafnates is presented. Some simulations performed in relation to this project are presented in Figure 2.14c. One of the compounds was grown successfully onto $\text{ZrO}_2\text{:Y}$ substrates and displayed a scintillating response: $\text{Lu}_2\text{Hf}_2\text{O}_7\text{:Eu}$. This compound has a density close to 10 g/cm^3 , which is higher than most other SCFs we investigated. Its calculated figure of merit from simulations compared to the other materials is presented in Figure 2.14a, and it shows that it could indeed compete with and outperform the state-of-the-art scintillators used in this field. It is rather comparable to $\text{Lu}_2\text{O}_3\text{:Eu}$, which received

a lot of interest recently in the field due to its promising scintillation properties and high density. $\text{Lu}_2\text{O}_3:\text{Eu}$ have been grown successfully by LPE on Lu_2O_3 substrates earlier [104]. However, Lu_2O_3 substrates are not sold commercially since it is highly challenging to grow bulk due to its high melting point of 2490 °C. $\text{ZrO}_2:\text{Y}$ is, on the other hand, a commercially available substrate. All this makes it motivating to investigate and better understand the growth and properties of high-density $\text{Lu}_2\text{Hf}_2\text{O}_7:\text{Eu}$ on $\text{ZrO}_2:\text{Y}$.

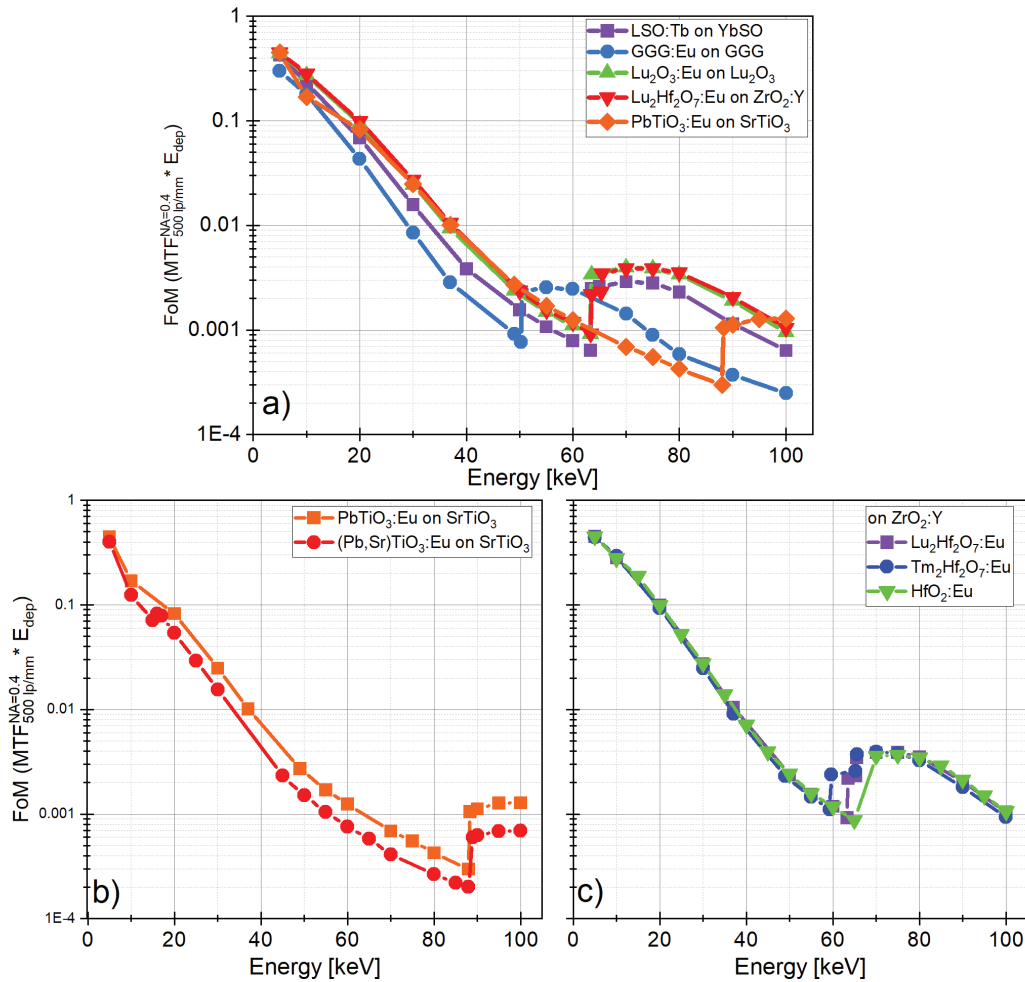


FIGURE 2.14: The calculated Figure of Merit (FoM) from the simulations, for prospective materials and some state-of-the-art scintillators. a) Some main prospective materials compared to some state-of-the-art scintillators. b) Comparing PbTiO_3 and $(\text{Pb,Sr})\text{TiO}_3$. c) Comparing some Hafnates.

2.6.1 Light yield considerations

The light yield of a scintillator is very difficult to predict and can vary depending on the concentration of dopant in the film. Also, the growth technique can introduce variations such as different types of defects and impurities, and the concentration of these affects the light yield as well. A lower light yield can often simply be compensated by increasing the data collection time. However, this is not always the best option for a specific experiment or if there are time constraints. Figure 2.15 presents a simple evaluation of how much influence the light yield has on the performance of SCFs. Here the formula introduced for the figure of merit has been modified by adding an extra parameter, namely the artificial LY:

$$\text{FoM}(E) = \text{MTF}_{500 \text{ lp/mm}}^{NA=0.40}(E) * E_{\text{dep}}(E) * \text{LY} \quad (2.4)$$

The LY is used to adjust the performance of the $\text{Lu}_2\text{Hf}_2\text{O}_7:\text{Eu}$ compared to $\text{LSO}:\text{Tb}$. When assuming the two SCFs have the same light yield (considered as 100%), $\text{Lu}_2\text{Hf}_2\text{O}_7$ outperforms $\text{LSO}:\text{Tb}$ as already discussed earlier. Similar performance to $\text{LSO}:\text{Tb}$ can be obtained with a light yield at 60% with respect to $\text{LSO}:\text{Tb}$. When lowering the light yield to 10% the performance is predicted to be considerably lower than that of $\text{LSO}:\text{Tb}$. This, therefore, predicts that if the light yield of $\text{Lu}_2\text{Hf}_2\text{O}_7$ is lower compared to $\text{LSO}:\text{Tb}$, down to 60%, it can still compete with it regarding spatial resolution and efficiency. However, with a light yield lower than 60%, it becomes less relevant for this project.

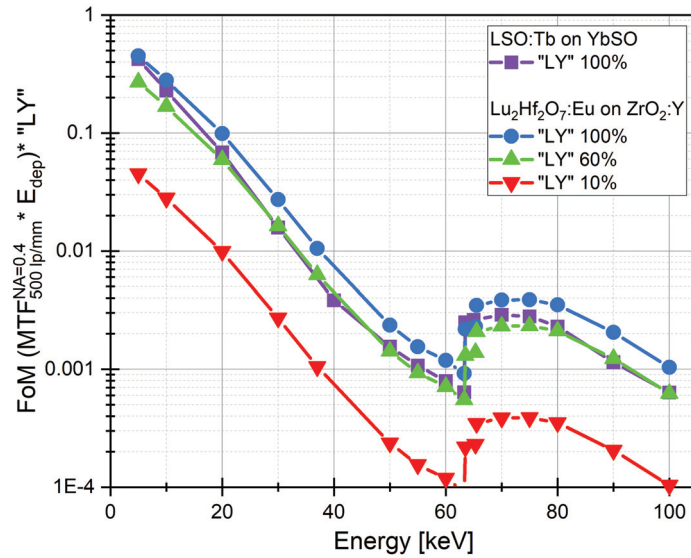


FIGURE 2.15: Comparing an updated figure of merit including light yield considerations, calculated from simulations of $5 \mu\text{m}$ $\text{Lu}_2\text{Hf}_2\text{O}_7:\text{Eu}$ on $150 \mu\text{m}$ $\text{ZrO}_2:\text{Y}$ and $5 \mu\text{m}$ $\text{LSO}:\text{Tb}$ on $150 \mu\text{m}$ YbSO .

2.7 Conclusions

The principles of our Geant4-based simulation tool and subsequent analytical calculations were presented and applied. We investigated how the LSFs and MTFs behave at different X-ray energies for different materials, including potential and state-of-the-art scintillators. The dependence on the X-ray energy was highlighted, as the image quality is affected when using X-ray energies above or below the absorption edges of elements in the SCF and substrate. This proves that both the SCF and the substrate should be chosen wisely, as well as the X-ray energy, to obtain the highest spatial resolution possible. Simulations, including the blurring introduced by microscope optics, were discussed. At low energy, the optics strongly reduce the MTF, whereas, at higher energies, most of the degradation is caused by the spatial energy distribution in the SCF. A figure of merit was proposed to evaluate potential scintillators regarding spatial resolution, contrast, and absorption efficiency. Lu_2O_3 , $\text{Lu}_2\text{Hf}_2\text{O}_7$, and PbTiO_3 have a predicted potential to outperform the other investigated SCFs below 50 keV and above 64 keV. At 90 keV and above, PbTiO_3 is the best choice from this evaluation. The potential performance of materials grown in the framework of this thesis, referred to as "titanates" and "hafnates", was evaluated both through the simulations and some aspects of the growth and their properties.

More generally, this approach is indeed a promising tool for scintillating screen development aiming to reach ultimate performances. The tool can, in addition, easily be adapted to investigate other materials and geometries, as well as to include polychromatic X-rays.

Chapter 3

Growth of ultra-dense thin films

3.1 Introduction

To reach the ultimate high spatial resolution for X-ray imaging at synchrotrons, SCF scintillators with a thickness corresponding to the depth of field of the optics are essential. Consequently, small thicknesses in the range of a few micrometers are required, and the absorption efficiency of the scintillator is reduced considerably, which affects the light output of the scintillator. The absorption efficiency can be increased by selecting materials with high densities and effective atomic numbers (Z). In addition, working at X-ray energies just above the absorption edge energy of the high Z elements in the SCF scintillator improves the absorption and the spatial resolution. For these reasons, the quest for ultra-dense materials that can be grown by LPE as SCFs has been in focus during this thesis. This was discussed in detail in Chapter 1.

Compound	Density [g/cm ³]	Z_{eff}
HfO ₂ [105]	10.1	-
Lu ₂ O ₃ [106]	9.4	69
Lu ₂ Hf ₂ O ₇ [107]	10	69
GGG [62]	7.1	53
LSO [108]	7.4	65

TABLE 3.1: Overview of relevant compounds displaying their estimated densities and effective atomic numbers.

Various hafnate compounds have been studied and attempted to be grown by LPE on ZrO₂:Y substrates with crystallographic orientations (100) and (111). This substrate was chosen due to it being commercially available and reasonably cheap. In Table 3.1, some of the compounds we have attempted to grow are listed with their density and effective atomic number (Z_{eff}) and are compared to GGG and LSO to emphasize their potential. Hafnates generally have a high density and Z_{eff} , making them relevant for this project. The LPE growth of hafnate compounds on zirconia substrates should be possible since HfO₂ and ZrO₂ are iso-structural and behave similarly upon substitutions. At room temperature, they crystallize in a monoclinic structure, and by substituting sufficiently with yttrium, a cubic structure

is stabilized [109]. The substrate utilized for growing the hafnates films is yttria-stabilized ZrO_2 with 19at% yttrium, in this thesis mainly referred to as $\text{ZrO}_2\text{:Y}$. The relationship between the yttria content in ZrO_2 and the structure is discussed further in Section 3.5.1.

3.1.1 Project evolution

Our approach and understanding of the hafnate system evolved immensely as the experiments progressed and the samples were characterized. Six LPE experiments were performed, where the solution compositions were modified and optimized during each experiment. This was to enable the growth of the various hafnate compounds and attempt to obtain scintillation from the films. This evolution will be described below and is summarized in Table 3.2. The references utilized for the samples are already employed in the table. In general, only the solution number (chronological order) and the solvent are used when referring to a specific solution, for example, M1-Pb or M6-Bi. If referring to samples grown from a specific solution composition, the expected composition of the film is also referred to, for example, M3-Pb- $\text{Lu}_2\text{Hf}_2\text{O}_7$. If the crystallographic orientation of the sample is of relevance, this will be added as a suffix. It is important to note that when the dopant is indicated, this is the nominal content of the dopant in the solution and not the expected or deduced content in the grown sample. Therefore, M3-Pb- $\text{Lu}_2\text{Hf}_2\text{O}_7\text{:Eu45\%}$, is not expected to have 45% europium in the structure. Typically when performing LPE, the segregation coefficient for dopants is lower than 1 for incorporation from the solution into the films. Some samples have been annealed. This will be indicated as yet another suffix if relevant to the specific context. For example: M1-Pb-(Sc,Y) $_2\text{Hf}_2\text{O}_7\text{:Tb1\%-100-A}$.

Attempts to predict if compounds could be grown on the substrate were made by considering the potential lattice mismatch displayed in Table 3.3. The ionic radii of elements were also considered to predict which elements would fit into the atomic structures. The ionic radii for relevant are thus displayed in Table 3.4.

M1-Pb: The initial vision was to grow yttria stabilized HfO_2 , with 17 at% yttrium that is reported to be the sufficient concentration for stabilizing the cubic phase [110]. However, no growth was reached with this solution composition. At that time, we suspected the ionic radii of yttrium were too large to fit into the HfO_2 lattice when performing LPE since the difference in ionic radii of Hf and Y in the structure is 0.189 Å. Because scandium and hafnium in the structure have comparable ionic radii with a difference of only 0.04 Å, Sc_2O_3 was added to the solution. Films grew with this solution composition, but only very thin ($<1.1 \mu\text{m}$). Tb_4O_7 was then added to the solution in the effort of activating scintillation. The films were not scintillating as-grown, but indications of scintillation were found after an annealing procedure, which will be described in Section 3.4.2.1.

M2-Pb: For this LPE experiment, the initial vision was to test if HfO_2 without any dopant could be grown on the substrate. Usually, the films are grown by LPE only on

Solution references	Growth?	Scintillation?	Test objective
M1-Pb-HfO ₂ :Y17%	-	-	Similar as substrate
M1-Pb-(Y,Sc) ₂ Hf ₂ O ₇	+	-	Sc ionic radii fit structure
M1-Pb-(Y,Sc) ₂ Hf ₂ O ₇ :Tb1%	+	(+)	Activate by Tb
M2-Pb-HfO ₂	-	-	Monoclinic HfO ₂
M2-Pb-(Hf,Sc) ₂ O ₇	-	-	Sc worked in M1-Pb
M2-Pb-(Sc,Tm) ₂ Hf ₂ O ₇	(+)	-	
M2-Pb-(Sc,Tm) ₂ Hf ₂ O ₇ :Ce3%	+	-	Activate by Ce
M3-Pb-Lu ₂ Hf ₂ O ₇	(+)	-	Lu ₂ Hf ₂ O ₇ , but in what structure?
M3-Pb-(Lu,Tm) ₂ Hf ₂ O ₇	+	-	Increase thickness
M3-Pb-(Lu,Tm) ₂ Hf ₂ O ₇ :Eu10%	+	-	Activate by Eu
M4-Pb-Lu ₂ O ₃	-	-	Lu ₂ O ₃
M4-Pb-Lu ₂ Hf ₂ O ₃	+	-	Lu ₂ Hf ₂ O ₇ was growing in M3-Pb
M4-Pb-Lu ₂ Hf ₂ O ₃ :Eu15%	+	+	Activate by Eu
M5-Pb-Lu ₂ Hf ₂ O ₇ :Tb10%	+	-	Activate by Tb
M5-Pb-Lu ₂ Hf ₂ O ₇ :Tb10%:Ce3%	+	-	Activate by Ce
M6-Bi-Lu ₂ Hf ₂ O ₇	+	-	New solvent
M6-Bi-Lu ₂ Hf ₂ O ₇ :Eu45%	+	+	Activate by Eu

TABLE 3.2: Overview of the six LPE experiments stating if films were grown and if scintillation was obtained. The initial test objective of that specific solution composition is also briefly stated.

iso-structural substrates to reach the appropriate structural matching. Nevertheless, since HfO₂ has a density above 10 g/cm³ it is highly attractive for this project and worth attempting to grow. Assuming the growth will occur with the a and b unit cell parameters in-plane and the c axis out-of-plane of the substrate, the predicted lattice mismatch is between -0.61% and 0.49%, which could be acceptable (see Table 3.3). However, no growth was managed. Since adding Sc₂O₃ triggered the growth for the first solution (M1-Pb), it was added again, but still, no growth occurred. Next, Tm₂O₃ was added, and even though the estimated thickness was minimal (only up to 0.1 μm) there were finally indications of growth, as was seen by investigating the surface with the optical microscope. More Tm₂O₃ was added as well as CeO₂ in the effort to activate scintillation. Thicker films were obtained (up to 4.5 μm) but without any scintillation. Initially, thulium and scandium were expected to enter the structure only as dopants of a few atomic percent. However, elemental analysis (SEM-EDX) revealed that they incorporate significantly more. The results of this are presented and discussed in Section 3.2.3.

These first results initialized further literature studies, which resulted in uncovering Lu₂Hf₂O₇. The atomic structure of this and similar compounds will be discussed in detail in Section 3.3. Lu₂Hf₂O₇ has a high density, around 10 g/cm³, and a high Z_{eff} of 69 (Table 3.1), making it very suitable for the project. Combined with its very low predicted lattice mismatch of 0.02% (Table 3.3), it was ideal.

M3-Pb: The initial composition of this solution targeting Lu₂Hf₂O₇ did not result in any film growth. The amount of solvent was therefore increased in the solution (solute/solvent decreased) to lower the melting point and hopefully the growth region as well (concept detailed in Section 1.3). A film was then later discovered by studying the sample with XRD. Upon performing a 2θ - Ω scan, two peaks were

revealed, one from the substrate and an additional from a film. The film was so thin that it could not be concluded from the usual sample weighing method. However, before this thin film was confirmed, Tm_2O_3 was added to the solution, and films were obtained but still very thin ($<0.6 \mu\text{m}$). Eu_2O_3 was then added to the solution to activate the scintillation, but no scintillation was realized in the samples grown from this solution.

M4-Pb: For this solution, the initial composition aimed for growing Lu_2O_3 . Lu_2O_3 also has a very high density of around 10 g/cm^3 and a Z_{eff} of 69 and is therefore also very suitable for the project. The estimated lattice mismatch is less encouraging than the other compounds, but its structure is cubic, with a unit cell length of approximately twice that of the substrate. Therefore, to match the substrate, the comparison was on half its unit cell of Lu_2O_3 , giving an estimated lattice mismatch of 0.93%. However, we did not manage to grow any Lu_2O_3 films. HfO_2 and additional solvent were added to the solution, and films were then obtained. Adding additional solvent was necessary to keep the melting point in the temperature range of the furnace. Eu_2O_3 was added, and scintillation was finally obtained. The nominal europium content in the solution was then gradually increased to investigate the scintillating properties.

Compound	Space group	a	b	c	Relevant angles
$\text{ZrO}_2\text{:Y}$ [111]	$Fm\bar{3}m$	5.1470 Å	-	-	-
HfO_2 [109]	$P2_1/c$	5.1156 Å	5.1722 Å	5.2948 Å	$\beta=99.11^\circ$
LM	-	-0.61%	0.49%	2.87%	-
$\text{Lu}_2\text{Hf}_2\text{O}_7$ [112]	$Fm\bar{3}m$	5.148 Å	-	-	-
LM	-	0.02%	-	-	-
Lu_2O_3 [113]	$Ia\bar{3}$	10.39 Å	-	-	-
LM	-	* 0.93%	-	-	-

TABLE 3.3: Structure of relevant compounds and the estimated lattice mismatch (LM) with the substrate $\text{ZrO}_2\text{:9.5 mol\% Y}_2\text{O}_3$. * indicates the lattice mismatch is calculated for half its unit cell.

At this point, we managed to grow hafnate films of various nominal compositions, but very thin (maximum a few microns), and it was found that $\text{Lu}_2\text{Hf}_2\text{O}_7$ doped with europium scintillates.

M5-Pb: This solution initially targeted $\text{Lu}_2\text{Hf}_2\text{O}_7\text{:Tb}$ to find if scintillation can be obtained when the host structure, $\text{Lu}_2\text{Hf}_2\text{O}_7$, is doped with another rare earth element than europium. Very thin ($<0.1 \mu\text{m}$) films were obtained but were non-scintillating. More solvent and CeO_2 were added to the solution, and now thicker films were obtained but still non-scintillating.

All the previous LPE experiments persistently had crystals on the solution surface and material deposited on the paddle during the agitation. See the images and discussions on this in the next section. An attempt to avoid this issue was to change the solvent of the solution.

	Element	CN	Ionic radii [Å]
<i>Substrate or film</i>	Zr ⁴⁺	8	0.84
	Hf ⁴⁺	6	0.71
	Hf ⁴⁺	8	0.83
	Lu ³⁺	8	0.977
	Y ³⁺	8	1.019
	Sc ³⁺	8	0.87
	Tm ³⁺	8	0.994
<i>Dopants</i>	Tb ³⁺	8	1.04
	Tb ⁴⁺	8	0.88
	Ce ³⁺	8	0.97
	Ce ⁴⁺	8	0.94
	Eu ³⁺	8	1.066
<i>Solvent</i>	Pb ⁴⁺	8	0.94
	Bi ³⁺	8	1.17

TABLE 3.4: Relevant elements and their ionic radii for relevant oxidation states and coordination numbers (CN) [82].

M6-Bi: Since scintillation was achieved with Lu₂Hf₂O₇:Eu this was the initial composition while using Bi₂O₃-B₂O₃ as a solvent. Growth, as well as scintillation, was successfully achieved with this composition and solvent. The europium content in the solution was again gradually increased to investigate the scintillating properties.

This screening of various hafnates demonstrates that some of the SCFs do not scintillate. A literature review of scintillating hafnates will be presented in section 3.4. The scintillating samples of this project and especially their properties will be prioritized since this is the scope of the thesis. LPE solution aspects, structural considerations, and other conclusions will be drawn from the other films.

3.1.2 Simulations

A useful simulation tool was presented in Chapter 2, and some prospective SCFs were evaluated in the framework of the figure of merit defined in Section 2.6, here among some hafnates. These simulations predicted that these could compete with the state-of-the-art SCF scintillators for high spatial resolution X-ray imaging at synchrotron sources. To underline this, the figure of merit of relevant compounds from this chapter is presented in Figure 3.1 and is compared to GGG:Eu and LSO:Tb. The spatial resolution capabilities and X-ray absorption efficiency are prerequisites for launching the LPE experiments. Investigating the growth and studying their actual properties is the next important step to explore if they can live up to the proposed properties. It should be noted that investigating other compositions can also lead to other potential improvements, such as decay time, radiation hardness, and bright burn.

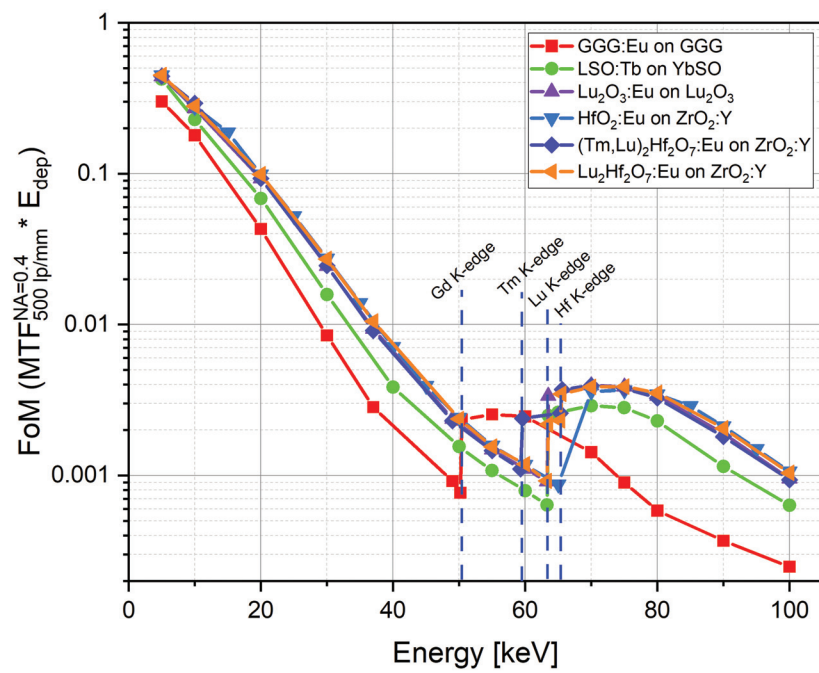


FIGURE 3.1: Figure of Merit (FoM) proposed for evaluating thin SCF scintillators for relevant compounds extracted from simulations performed with the Geant4 tool presented in Chapter 2. All simulations are performed for $5 \mu\text{m}$ thick films on $150 \mu\text{m}$ thick substrates.

3.2 Growth of hafnates

During this project, it has been found that it is possible to grow various combinations of hafnate compounds on the same type of substrate, $\text{ZrO}_2\text{:Y}$. The hafnate system is thereby not as rigid regarding LPE growth as other compounds. There is a certain flexibility to accommodate various hafnate compositions on the same type of substrate. Throughout this section, the procedures and the issues regarding the LPE growth that was encountered and, in some cases, improved will be presented, as well as the investigations on the elemental compositions and surface morphology. A brief overview of some of the parameters important for the solutions is presented in Table 3.6 and compared to the typical values for LSO and GGG LPE solutions.

3.2.1 LPE conditions

The compositions which were attempted and, in some cases, led to the successful growth by LPE on $\text{ZrO}_2\text{:Y19at\%}$ substrates with the crystallographic orientations of (100) and (111) were already presented in Table 3.2.

	Compound	Melting point [°C]
<i>Hafnates</i>	HfO_2	2760
	Lu_2O_3	2490
	Tm_2O_3	2341
	Sc_2O_3	2485
	Y_2O_3	2425
<i>GGG</i>	Gd_2O_3	2420
	Ga_2O_3	1900
<i>LSO</i>	SiO_2	1710
	Lu_2O_3	2490
<i>Solvents</i>	PbO	888
	B_2O_3	450
	Bi_2O_3	817
<i>Substrate</i>	$\text{ZrO}_2\text{:Y}$	2780

TABLE 3.5: Relevant compounds of solute components and their melting points compared to those of GGG, LSO, and the solvent components.

The melting points of the solute components affect the LPE growth temperature, as already discussed in Section 1.3. The melting points of the precursors used for the hafnates, GGG, and LSO solutions, and the solvent components are listed in Table 3.5. HfO_2 has the highest melting point, and the precursors that were used for the growth of the hafnates are generally high, with them all being above 2300 °C. The hafnates are, as a consequence, difficult to dissolve in solvents compared to those of LSO and GGG. Therefore, either the growth temperature will be very high, maybe even above the working temperature of the furnace, or only very little of the solute components should be added to the solution (reducing the $s/(s+S)$ ratio), making it possible to dissolve and still have a not-too-high growth temperature. Therefore, the amount of solute in the hafnate solutions is low compared to the growth of other types of SCFs

by LPE, such as LSO and GGG (see Table 3.6). The composition of the solvent can also be adjusted to reduce the growth temperature. Since the ratio between the two components (Pb/B or Bi/B) affects the growth temperature revealed by their phase diagrams, this can considerably affect the melting temperature and dissolution of the solute in the solvent. This has been explored with some of the LPE experiments within this project. However, a higher boron concentration results in a more viscous solution. This can impose some constraints since it is more difficult to remove the excess solution on the sample after the growth procedure. The A^{3+}/Hf^{4+} ratio can also affect growth. However, no direct correlation was found from these studies to this value affecting the growth.

Solution reference	G	scint	A^{3+}/Hf^{4+}	$s/(s+S)$	Pb/B or Bi/B
M1-Pb-HfO ₂ :Y	-	-	0.20	2.59	5.3
M1-Pb-(Y,Sc) ₂ Hf ₂ O ₇	+	-	0.45	3.10	5.3
M1-Pb-(Y,Sc) ₂ Hf ₂ O ₇ :Tb	+	(+)	0.45	3.12	5.3
M2-Pb-HfO ₂	-	-	0	3.84-4.02	1.99-2.53
M2-Pb-(Hf,Sc)O ₂	-	-	0.02-0.24	4.10-5.54	2.53
M2-Pb-(Sc,Tm) ₂ Hf ₂ O ₇	(+)	-	0.35-0.54	6.0-6.80	2.53
M2-Pb-(Sc,Tm) ₂ Hf ₂ O ₇ :Ce	+	-	0.63	7.36	2.53
M3-Pb-Lu ₂ Hf ₂ O ₇	(+)	-	1	4.2-2.6	5.1
M3-Pb-(Lu,Tm) ₂ Hf ₂ O ₇	+	-	1.5-1	3.3-3.8	5.1
M3-Pb-(Lu,Tm) ₂ Hf ₂ O ₇ :Eu	+	-	1	3.3-3.4	5.1
M4-Pb-Lu ₂ O ₃	-	-	0	2.5	5.3
M4-Pb-Lu ₂ Hf ₂ O ₃	+	-	4	3.0-2.4	5.0-3.1
M4-Pb-Lu ₂ Hf ₂ O ₃ :Eu	+	+	4	2.5-2.7	3.1
M5-Pb-Lu ₂ Hf ₂ O ₇ :Tb	+	-	2.3	2.1	5.3
M5-Pb-Lu ₂ Hf ₂ O ₇ :Tb:Ce	+	-	2.3-1.7	2.0-3.8	5.3
M6-Bi-Lu ₂ Hf ₂ O ₇	+	-	1	2.5-2	0-7.3
M6-Bi-Lu ₂ Hf ₂ O ₇ :Eu	+	+	1.0 (1.0-1.8)	2.0-2.9	7.3
LSO				~ 9	~ 9
GGG				~ 5-10	~ 6

TABLE 3.6: Overview of some parameters of the LPE solution compositions of this project compared to typical parameters growing LSO and GGG. G: Growth, scint: Scintillation, s: Solute, S: Solvent. The atomic contents are presented as the ratio between A^{3+} and B^{4+} elements.

Two different solvents were used. Namely, PbO-B₂O₃ and Bi₂O₃-B₂O₃, and the purpose and details are discussed here.

PbO-B₂O₃: This is a typical solvent used for the growth of, for example, LSO:Tb [62], and GGG:Eu [114] SCFs by LPE. Unfortunately, issues arose employing this solvent for the growth of hafnates. During the agitation procedure, material was deposited on the paddle as displayed in Figure 3.3b. Before growth, the surface of the solution was partly covered by crystals that nucleated during the agitation and while cooling to the growth temperature. An image of the solution surface is displayed in Figure 3.3a. These are both undesirable for the LPE growth since material is extracted from the solution and this alters the solution composition, making controlling the growth more challenging. The deposited material from the paddle was retrieved and ground into powders. To extract information on the

crystalline phases of this material, it was studied with PXRD. It was, in general, found that these powders contain crystalline platinum (space group: $Fm\bar{3}m$) and $PbHfO_3$ (space group: $Pbam$) or $Lu_2Hf_2O_7$ (space group: $Fm\bar{3}m$). Two examples of diffractograms obtained at powders extracted from M1-Pb and M5-Pb are presented in Figure 3.2a and b, respectively. The relevant calculated references are displayed, and a zoom above each diffractogram for better comparison. From this, it is seen that platinum is the dominating crystalline phase in both powders since it accounts for most of the intensity. Extracting platinum from the paddle after using it repeatedly is normal. For M1-Pb, most of the remaining diffraction peaks can be assigned to $PbHfO_3$. Whereas for M5-Pb, $Lu_2Hf_2O_7$ can be assigned. $PbHfO_3$ is a competing phase that must be created by combining the solvent and solute components: PbO and HfO_2 , respectively. $Lu_2Hf_2O_7$ is most likely deposited on the paddle after agitating at too-low temperatures. During the LPE experiments, it was experienced that less material was deposited on the paddle when reducing the agitation temperature, which is why it was reduced during M5-Pb compared to M1-Pb.

These results suggest that by agitating at higher temperatures, $PbHfO_3$ form, whereas at lower temperatures, crystallization of $PbHfO_3$ is avoided, but instead, the crystallization of $Lu_2Hf_2O_7$ is favored. The crystals nucleating on the solution surface, as shown in Figure 3.3a, are likely $PbHfO_3$ or $Lu_2Hf_2O_7$, depending on the agitation temperature. These findings demonstrate that the hafnium concentration dissolved in the solution decreases from the initial concentration, which could explain the low growth rates associated with Pb-based solutions.

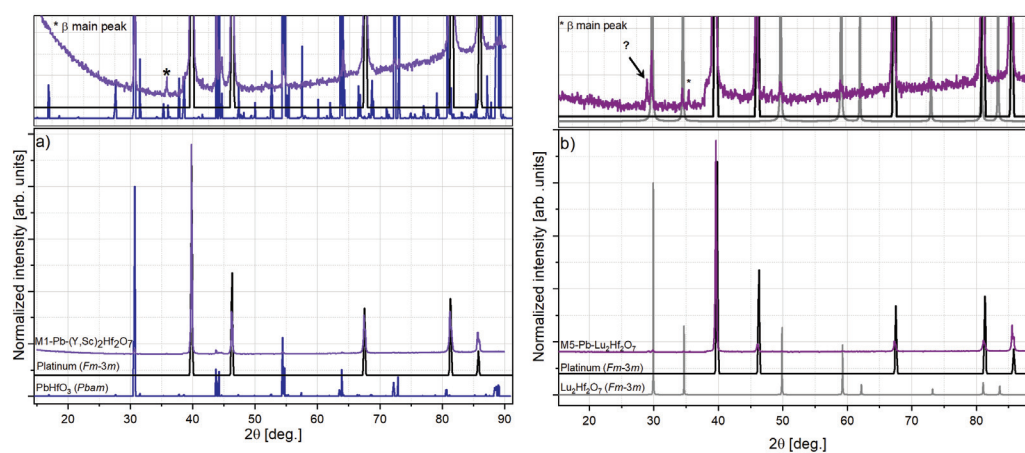


FIGURE 3.2: Diffractograms of powders recovered from the paddle during two LPE experiments. a) M1-Pb-(Y,Sc)₂Hf₂O₇ and b) M5-Pb-Lu₂Hf₂O₇. Calculated references are included for the relevant crystalline phases, and a zoom-in is presented at the top of each figure.

Bi_2O_3 - B_2O_3 : Typically only PbO - B_2O_3 is used as the solvent in the LPE lab at the ESRF. However, changing to Bi_2O_3 - B_2O_3 , ensured $PbHfO_3$ could not crystallize and thereby lower the hafnium concentration in the solution. Using this solvent went successfully, and LPE growth of the hafnates could be performed from the solution after minor composition adjustments. Bi_2O_3 is significantly more corrosive

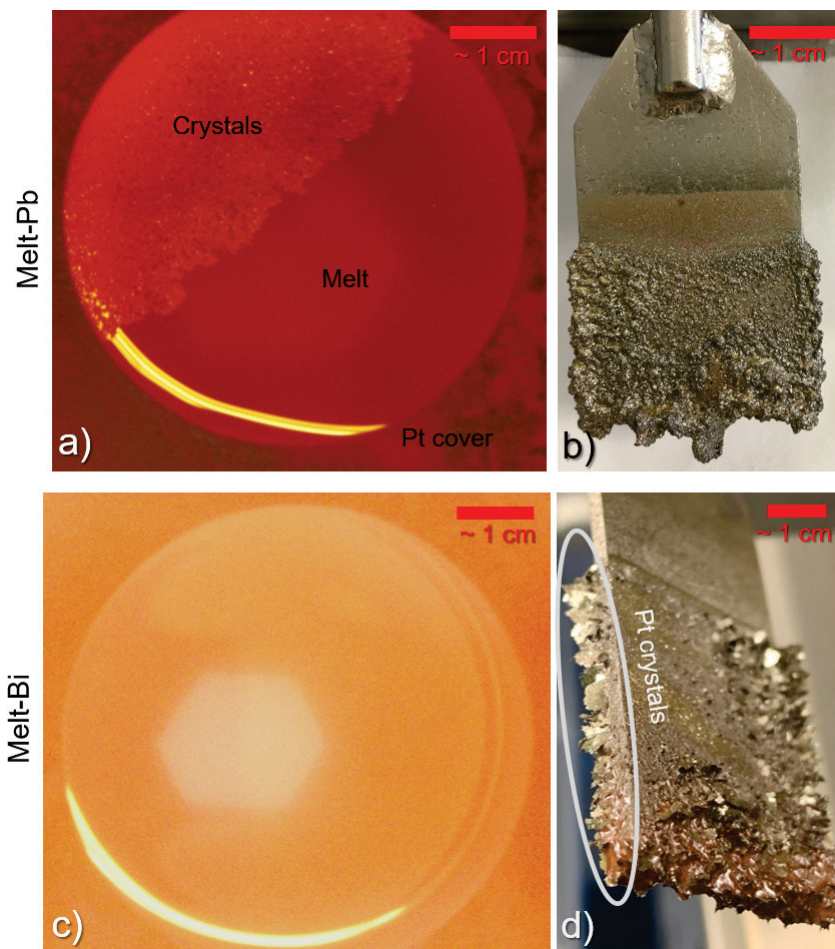


FIGURE 3.3: a) M-Pb: The surface of a solution with many crystals present. b) M-Pb: Paddle with material heavily deposited after several agitations. c) M-Bi: solution surface with no visible crystals. d) M-Bi: Paddle with platinum crystals extracted after several agitations.

to platinum than a PbO-based solvent. This is seen by the heavy extraction of platinum crystals at the paddle after several agitation procedures, as displayed in Figure 3.3d. PXRD confirmed that these crystals are indeed platinum (space group $Fm\bar{3}m$). No crystals visibly nucleated at the solution surface before growth unless the agitation temperature was set too low. The solution generally looked very liquid, as seen in Figure 3.3c. Often crystals nucleated during the growth, indicating the growth temperature was too low and favoring spurious crystallization. Consequently, there are crystal inclusions at the surface of these samples.

3.2.2 Film growth

Depending on the solution composition, the growth temperatures were between 890 and 970 °C, which is considerably lower than the melting temperatures of the solute components (see Table 3.5). The growth rates were consistently low. The typical targeted growth rate for state-of-the-art SCFs by LPE is around 1 $\mu\text{m}/\text{mn}$, but for this project, it was generally between 0 and 0.27 $\mu\text{m}/\text{mn}$, resulting in films

with thicknesses between 0 and 5 μm . Generally, the films grown on substrates with orientation (100) for all solutions grew faster and thicker than those on (111). It is not uncommon having various growth rates when growing on substrates with dissimilar orientations. There can be numerous reasons for this, such as varying quality of the substrates or preferred growth orientations for crystal systems.

The low growth rates are suspected to result from the low concentration of solute components in the solution. As already discussed, the initial solute concentration is lowered compared to the typical due to their high melting points. For the PbO-based solutions, the competing phase PbHfO_3 depositing on the paddle also extracted hafnium, further lowering the concentration. This must ultimately result in lower growth rates since the growth solution has less solute material. This is confirmed by the growth rate generally increased when solute components were added to the solution.

Solution	Max. growth rate
M4-Pb	0.01 $\mu\text{m}/\text{mn}$
M6-Bi	0.27 $\mu\text{m}/\text{mn}$

TABLE 3.7: Comparing the highest obtained growth rate for M4-Pb and M6-Bi.

Changing the solvent for the LPE growth from $\text{PbO-B}_2\text{O}_3$ to $\text{Bi}_2\text{O}_3\text{-B}_2\text{O}_3$ was successful even though it enhanced additional platinum extraction. Indeed the growth rate increased significantly when growing from the Bi-based solution compared to the Pb-based solutions, as displayed in Table 3.7 emphasizing this solvent is a better option for the hafnate growth in general.

3.2.3 Elemental composition

The elemental compositions of selected samples were estimated using SEM-EDX, and some results are presented in Table 3.8. The atomic contents are presented as the ratio between A^{3+} elements and Hf^{4+} . These results suggest that the stoichiometry of samples is close to $\text{A}_2^{3+}\text{Hf}_2^{4+}\text{O}_7$. Samples from M1-Pb have a higher A^{3+} content. In the table, the results extracted from the same sample but at different positions are grouped in columns. From this, the composition seems to vary within the same sample.

The dopants are generally detected in the samples. This confirms the dopants are entering the structure when added to the solution. For samples of $\text{M4-Pb-Lu}_2\text{Hf}_2\text{O}_7\text{:Eu}$ with increasing nominal europium content, the elemental content has also been estimated. From this, there is an increase in europium content in the samples with increasing nominal europium content in the solution. This result is shown in Table 3.9. Here it is also apparent that the europium content estimated in the samples is lower than the nominal content in the solution. Commonly, the segregation coefficient for dopants added to LPE solutions entering the grown films is lower than 1. However, since SEM-EDX is only a semi-quantitative method, the

atomic percentage of the europium content in the samples should not be considered as precise.

Reference	A^{3+}/Hf^{4+}		
$A_2^{3+}Hf_2^{4+}O_7$	1		
M1-Pb-(Y,Sc) ₂ Hf ₂ O ₇	1.27, 1.33	1.70, 1.51	
M2-Pb-(Sc,Tm) ₂ Hf ₂ O ₇ :Ce5%	0.90, 0.84	0.89, 1.06	0.86, 0.89, 0.78
M3-Pb-(Lu,Tm) ₂ Hf ₂ O ₇ :Eu10%		1.06, 0.96, 0.94	
M4-Pb-Lu ₂ Hf ₂ O ₇ :Eu10%		1.05, 1.03, 0.86, 0.99	

TABLE 3.8: Results from SEM-EDX evaluating the ratio between the A^{3+} and Hf^{4+} elements, with the results grouped in the same column for measurements at the same sample.

Nominal Eu-content	Eu-content	A^{3+}/Hf^{4+}
Eu0%	0	0.98
Eu5%	2.9%	0.99
Eu10%	4.8%	0.98
Eu15%	8.2%	0.93

TABLE 3.9: SEM-EDX estimated europium content and elemental ratio for M4-Pb-Lu₂Hf₂O₇-100 samples. Here A: Lu and Eu.

3.2.4 Surface morphology

The aim is to grow SCFs with mirror-like surfaces without crystal inclusions and lines that can otherwise act as diffusive centers when performing X-ray imaging with them. The inspection of the surface morphology is, therefore, essential.

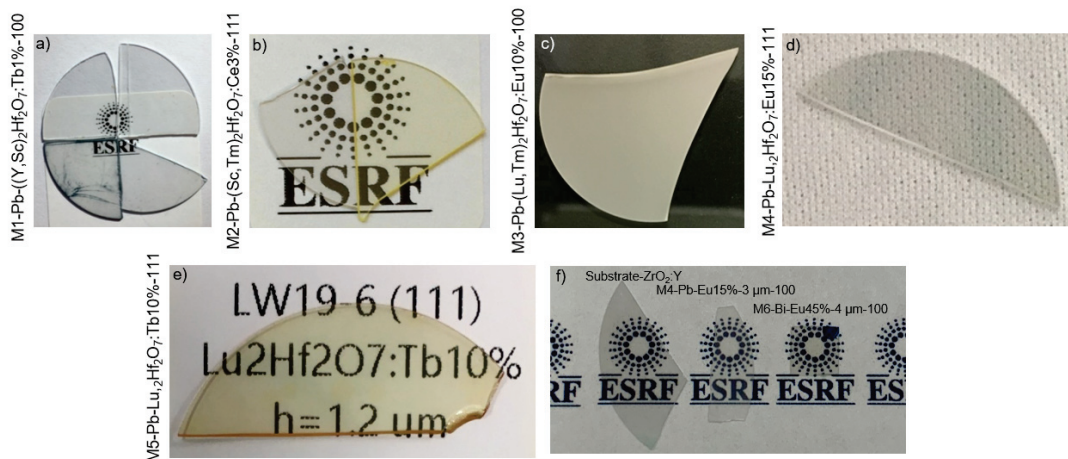


FIGURE 3.4: Overview of some hafnate samples grown from the various LPE solutions with varying content. Notice the difference in color as well as transparency.

Visual inspection: Starting from a visual inspection in Figure 3.4, the substrate is transparent, and most of the films are as well. However, samples grown on (100)

oriented substrates typically have a cloudy appearance making them less transparent. This is especially visible in Figure 3.4c. Terbium and cerium doping seem to give the films a yellow/brown color (Figure 3.4b and e), confirming that the dopants enter the SCFs when added to the solutions.

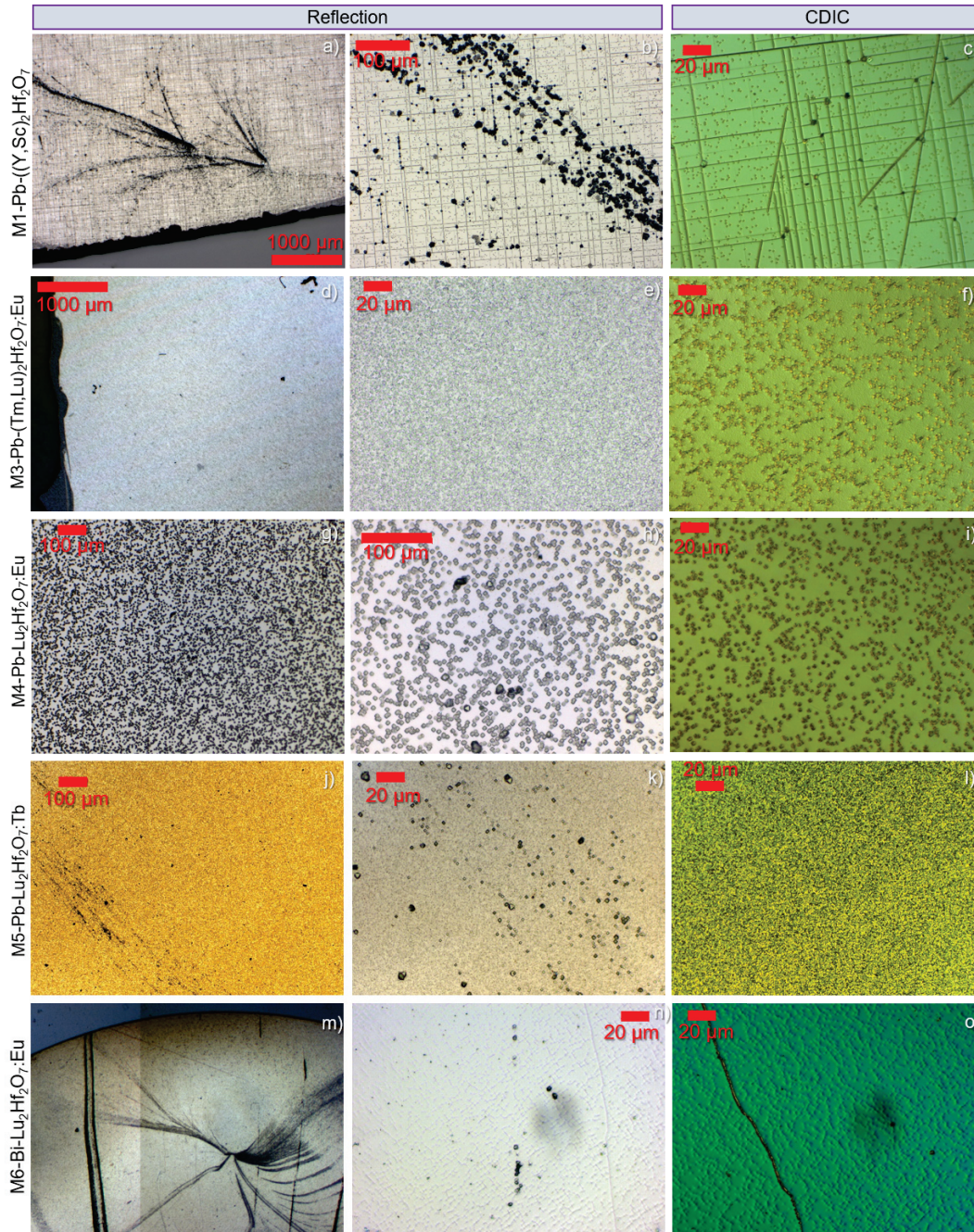


FIGURE 3.5: Micrographs of samples grown on ZrO₂:Y-100, using an optical microscope operated in reflection or circular polarized light–differential interference contrast (CDIC) configuration (stated above each column). The sample reference is stated for each row.

Optical microscope: Studying the samples with an optical microscope, non-perfect surfaces are revealed for the (100) orientation as exemplified in Figure 3.5. Most samples have some crystal inclusions on the surface that result from not optimized

growth conditions. It is seen that what appears visually as cloudy surfaces are caused by various surface irregularities. These surface irregularities are dissimilar when comparing samples from different solutions. Where most of the samples have distinct surface irregularities, the samples from M6-Bi have what seems like a rough surface instead. M1-Pb samples have lines, and this is displayed as well in Figure 3.8a-c. It is typically understood that lines like these are present in films due to a high lattice mismatch or indifferences in thermal expansion coefficients. The lattice mismatch between the substrate and film could be too large, but this will be disconfirmed and discussed in Section 3.3 for these samples. The thermal expansion could be too different between the SCF and substrate, which could at the growth result in a larger lattice mismatch at the growth temperature. However, this is not believed to be the issue for these samples but cannot be omitted. The reason for these lines is unclear but could be caused by local variations in the elemental composition as was presented in Section 3.2.3.

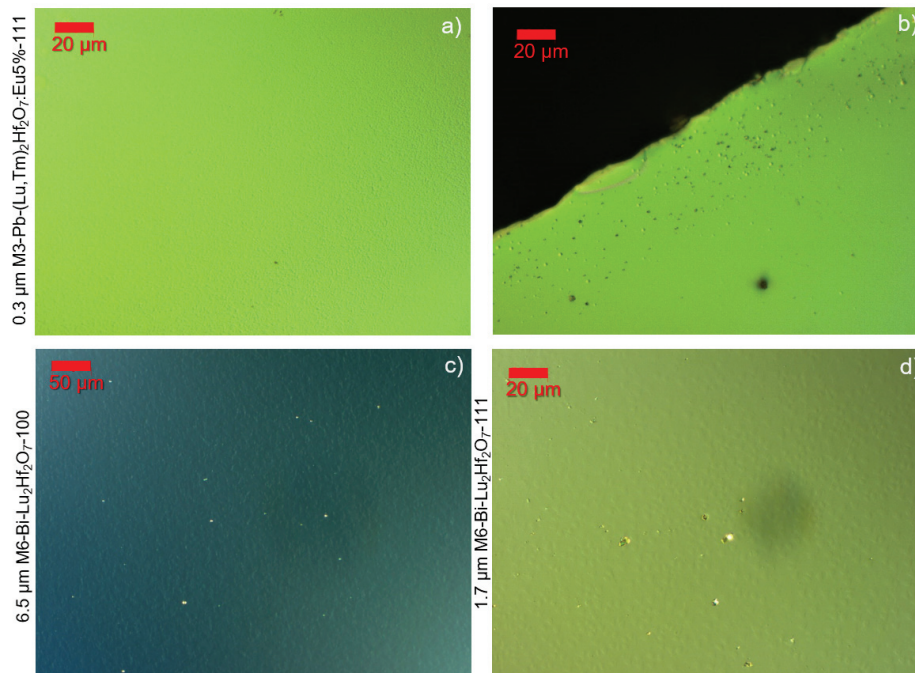


FIGURE 3.6: Micrographs of samples grown on $\text{ZrO}_2\text{:Y}$, using an optical microscope operated in CDIC configuration. The sample reference is stated for each row. The features on the samples are not prominent and can be difficult to identify on a printed version.

The surfaces of samples grown on (111) oriented substrates typically have a more mirror-like appearance, as seen in Figure 3.4b, d, and e. Micrographs showing the surface of a sample grown on (111) substrates are displayed in Figure 3.6a-b. The optical microscope is for these micrographs operated in CDIC configuration to reveal the surface morphologies better. The surfaces have a roughness but not the same surface irregularities as (100) samples from Pb-based solutions, as seen in Figure 3.5. However, as discussed further below, surface irregularities are suspected not to be

present on these samples since they are typically thinner than $1\ \mu\text{m}$ when grown from Pb-based solutions. In Figure 3.6b-c is the surface of M6-Bi-Lu₂Hf₂O₇ samples with (100) and (111) orientation compared. This (111) sample is almost $2\ \mu\text{m}$ thick and has similar surface roughness as the (100) sample from the same Bi-solution. This can be caused by the M6-Bi samples, in general, showing a better surface quality.

SEM and 3D reconstructions: Figure 3.7 displays SEM images of the following samples: M3-Pb-(Tm,Sc)₂Hf₂O₇:Eu and M4-Pb-Lu₂Hf₂O₇:Eu. The appearance of the surface irregularities is more visible here and can be suspected to be either pits or bumps. It is also clear again that they are not identical for the two compositions compared here. In Figure 3.8d-e are 3D reconstructions from confocal microscopy of two (100) samples presented. From this, it is confirmed these surface irregularities are indeed pits and not bumps. The SEM images of a $0.5\ \mu\text{m}$ M4-Pb-Lu₂Hf₂O₇:Eu15%-111 sample in Figure 3.7h-j show its surface do not have these pits. However, this could be caused by these samples are rarely as thick as the (100) samples. The cross-section of a $4.6\ \mu\text{m}$ (100) sample is presented in Figure 3.7a, and it seems the morphology evolves with its thickness (growth direction with the arrow). The first micrometer looks less affected than the last part, and since the films grown on (111) substrates rarely grow thicker than $1\ \mu\text{m}$ this enforces the suggestion of the pits and roughness evolving and increasing with film thickness. However, it cannot be excluded that the substrate could initiate a difference in the growth of the films depending on its orientation. The surface irregularities could arise from defects that evolve as the films grow thicker. This could be defects already present in the substrate or crystal inclusions during growth that evolves as the film grows. Another reason could be that the growth temperatures are too low, giving excessive supersaturation. The films are then, for the specific solution composition, growing very rapidly, and the mirror-like surfaces cannot be reached. Since spurious nucleation occurs on the solution surface, indicating the working temperatures have been too low, this seems like a valid explanation for the surface irregularities.

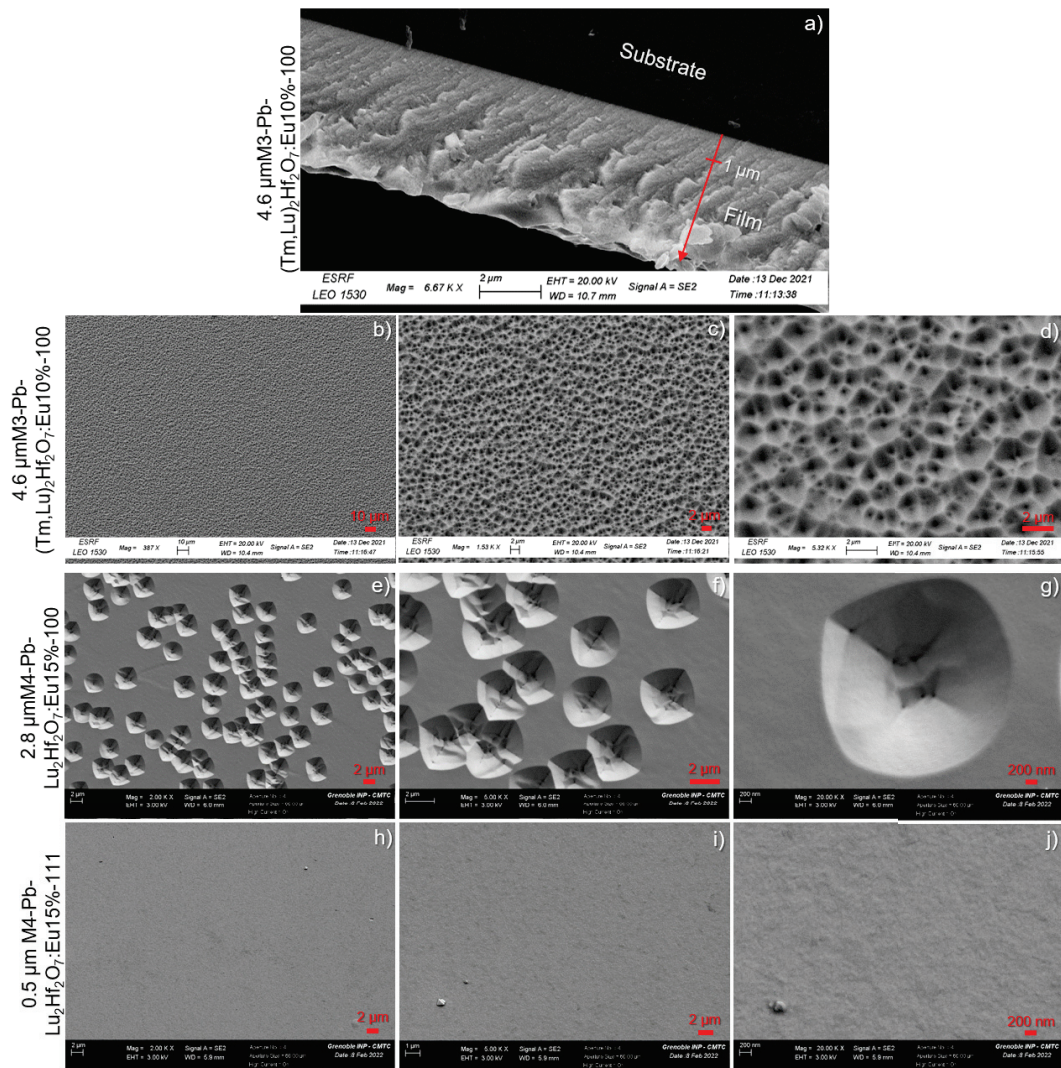


FIGURE 3.7: SEM images of selected samples. a) Cross section. b-j) From above. The sample references are indicated on the left of each row.

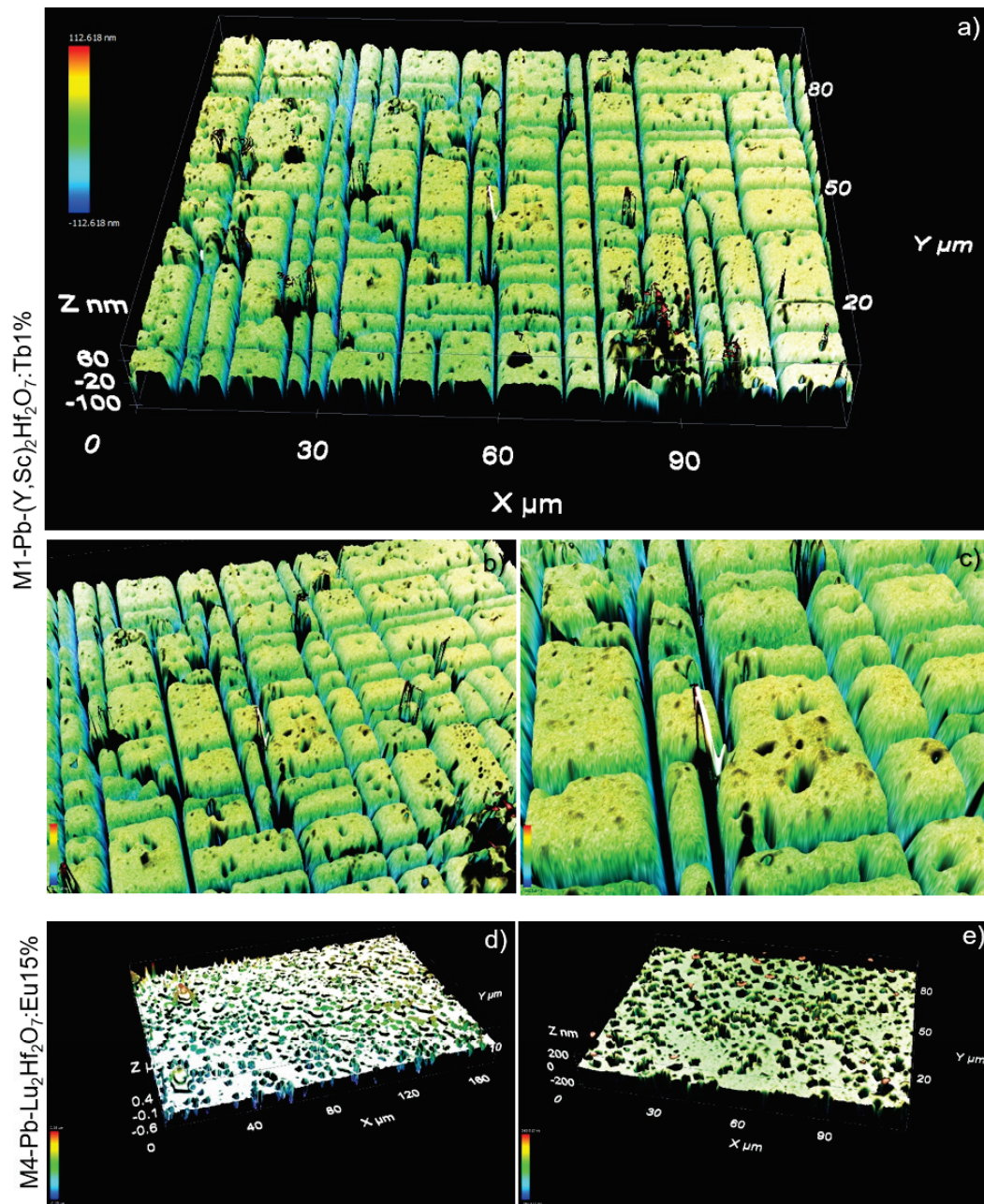


FIGURE 3.8: 3D reconstructed images using a confocal microscope. Sample references are on the left of the figure, both grown on (100) oriented substrates.

Comparing M4-Pb and M6-Bi: It was already concluded the growth rate was increased when using the Bi-based solvent compared to the Pb-based solvent. The film quality was also enhanced because the M4-Pb samples have these distinct surface irregularities that are not present for M6-Bi samples. An overview of the two samples used for testing at the beamlines is presented in Figure 3.9. The results when using them for imaging experiments are presented in Section 3.4.



FIGURE 3.9: Micrographs of M4-Pb-Lu₂Hf₂O₇:Eu15%-100 and M6-Bi-Lu₂Hf₂O₇:Eu45%-100. Both have been lapped and polished on one side as preparation for usage at the beamlines for imaging experiments.

3.3 Structural considerations

When performing epitaxial growth, it is essential to consider the atomic structures before attempting to perform growth. Then, when having successfully grown samples, the structure should also be understood and investigated to optimize the growth. In this section, structural considerations are evaluated in terms of predicting and extracting information on the structures of the grown samples.

3.3.1 Fluorite, pyrochlore, and delta structures

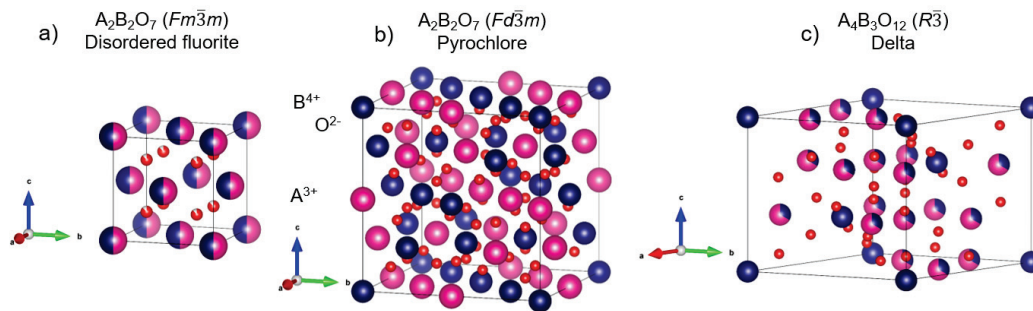


FIGURE 3.10: Relevant structures generated in Vesta from Crystallographic Information Files (CIFs). a) Disordered fluorite displayed with stoichiometry $A_2B_2O_7$, CN(A)=8, CN(B)=8 b) Pyrochlore, CN(A)=8, CN(B)=6. c) Delta, CN(A)=6, CN(B)=6. The space group for each structure is indicated in brackets in the figure. CN: Coordination number. Pink: A^{3+} , Dark blue: B^{4+} and red: O^{2-} .

The substrate used for the LPE growth of the hafnates is $ZrO_2:Y19at\%$. Pristine ZrO_2 is monoclinic at room temperature with the $P2_1/c$ space group. By substituting zirconium with more than approximately 12 at% yttrium, the long-range order of the structure will be stabilized as cubic (space group $Fm\bar{3}m$) and is often referred to as yttria-stabilized ZrO_2 (YSZ) [111]. The *ideal cubic fluorite structure*, BX_2 , with the same space group, can be described by cations (B^{4+}) occupying the regular sites of a face-centered cubic (FCC) structure and anions (X) on the eight tetrahedral interstitial sites [115]. For $ZrO_2:Y$ the description is the same but with yttrium randomly occupying the zirconium site. Introducing the Y^{3+} on Zr^{4+} sites induces oxygen vacancies in the structure that are also not ordered. The structure is therefore often referred to as the *disordered or defective fluorite structure*. This structure is presented in Figure 3.10a with $A_2B_2O_7$ stoichiometry. This structure, as explained, has disordering on both the anion and cation sites, but for some elemental compositions, there can be an ordering on these sites. This is referred to as the *pyrochlore structure* and is a super-structure derivative of the ideal fluorite structure where the A and B cations are ordered along the $\langle 110 \rangle$ direction. The additional anion vacancies reside in the tetrahedral interstice between adjacent B-site cations [116]. This structure is presented in Figure 3.10b. In the figure, one more structure is presented, typically referred to as the *delta-phase* (Figure 3.10c). This structure is not cubic like the others but rhombohedral with space

group $R\bar{3}$. The delta-phase structure is understood as a disordered fluorite structure with oxygen vacancies ordered along $\langle 111 \rangle$. There are two cation sites, and for A^{3+} and B^{4+} cations with dissimilar ionic radii. For example, Lu^{3+} and Hf^{4+} , the B cations are said to exclusively occupy one of these sites, which accounts for 1/7 of all cation sites. It has been proposed intuitively that compounds with similar ionic radii will have less cation ordering than those of dissimilar radii within the delta structure [117, 118].

Whether a compound crystallizes in the disordered fluorite, pyrochlore, or delta structure is reported to depend on the ionic radii ratio: rA^{3+}/rB^{4+} . The stability regions for the three structures described above are reported as: Disordered fluorite $< 1.21 < \text{delta-phase} < 1.42\text{--}1.44 < \text{pyrochlore} < 1.78\text{--}1.83$ and is visually presented in Figure 3.11 [117]. Even though the elements in the different structures have different coordination numbers, they are, for the sake of comparison, assumed for A^{3+} being 8-fold and B^{4+} being 6-fold coordinated, which is only valid for the pyrochlore structure. For lutetium and hafnium, this will result in a $rA^{3+}/rB^{4+}=1.37$, which suggests its stable structure should be the delta-phase.

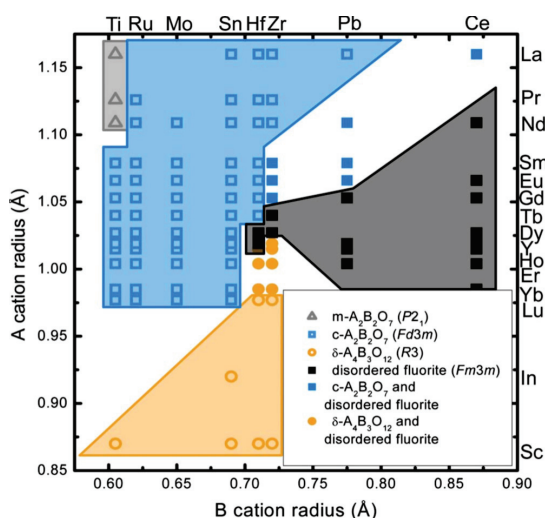


FIGURE 3.11: Structure map from [117].

The available information on lutetium hafnate compounds is not overwhelming. Searching in the Inorganic Crystal Structure Database (ICSD), only one entry is found. This is a report on $\text{Lu}_4\text{Hf}_3\text{O}_{12}$ with space group $R\bar{3}$, the delta structure [119]. There are especially not many reports on single crystals due to the difficulties of growth imposed by the high melting points of HfO_2 and Lu_2O_3 (Table 3.5). However, recently single crystals of $\text{Lu}_x\text{Hf}_{4-x}\text{O}_{8-y}$ were synthesized by arc plasma, and the structure of the produced crystals was concluded to be fluorite (space group $Fm\bar{3}m$) [120]. They also present a phase diagram at high temperatures showing $\text{Lu}_2\text{Hf}_2\text{O}_7$ should crystallize in the fluorite structure. This agrees with another article stating that $\text{Lu}_2\text{Hf}_2\text{O}_7$ at elevated temperatures occupy the fluorite structure, and upon slow cooling, an order-disorder transition to the delta phase occurs [121]. They also found that when cooling faster, for their study being $130\text{ }^\circ\text{C/h}$, maintains the fluorite

structure at room temperature. This suggests that the films grow in the fluorite structure at elevated temperatures and should potentially transition to the delta phase when cooled to room temperature. However, since the cooling rate after LPE growth is considerably faster than 130 °C/h the fluorite structure should, according to this, be stabilized for our samples similar to the single crystals produced by arc plasma [120]. However, due to the lack of literature on the structure and especially because these structures have not before been reported grown by LPE, the samples should be investigated with an open mind.

The atomic structures appear very different when comparing the delta phase and disordered fluorite structure in Figure 3.10. Also, when considering the predicted lattice mismatch, see Table 3.10, the delta structure ($\text{Lu}_4\text{Hf}_3\text{O}_{12}$) has a huge mismatch. It, therefore, seems highly unlikely that the film would grow in the delta phase on substrates with the disordered fluorite structure. The delta phase will, therefore, not be considered further in this study.

Compound	Space group	a	b	c	Relevant angles
$\text{ZrO}_2\text{:Y}$ [111]	$Fm\bar{3}m$	5.1470 Å	-	-	-
$\text{Lu}_2\text{Hf}_2\text{O}_7$ [112]	$Fm\bar{3}m$	5.148 Å	-	-	-
LM	-	0.02%	-	-	-
$\text{Lu}_4\text{Hf}_3\text{O}_{12}$ [119]	$R\bar{3}$	9.6085	9.6085	8.981	$\gamma=120^\circ$
LM	-	*-6.66%	*-6.66%	-	-

TABLE 3.10: Structure of relevant compounds and the estimated lattice mismatch (LM) with the substrate $\text{ZrO}_2\text{:9.5 mol\% Y}_2\text{O}_3$. * indicates the lattice mismatch is calculated for half its unit cell.

It was discussed in Section 3.2 for M1-Pb and M2-Pb that growth was only initiated after increasing the A_2O_3 content in the solution. This is most likely a result of the initial solution composition not containing enough A_2O_3 to stabilize the structure. Meaning if A^{3+} (or B^{4+}) is underrepresented in the solution, growth cannot be initiated. The compounds have mainly been discussed and displayed as $\text{A}_2\text{B}_2\text{O}_7$. Nevertheless, they can deviate from this stoichiometry. This is true for the substrate that is commonly referred to as $\text{ZrO}_2\text{:Y 19at\%}$ but could be expressed as $\text{Y}_{0.76}\text{Zr}_{3.24}\text{O}_{7.62}$. Most of the samples studied by SEM-EDX in this project have been demonstrated to have an elemental composition close to $\text{A}_2\text{Hf}_2\text{O}_7$ except for the M1-Pb samples (Section 3.2.3). In this chapter, all the samples will be referred to as $\text{A}_2\text{Hf}_2\text{O}_7$ for simplicity and as a reference to the structure.

Various techniques can be used to investigate the atomic structure of the grown films. This study has applied Raman spectroscopy and XRD for this purpose. A crucial difference is that Raman probes the local structure, whereas XRD probes the long-range order.

3.3.2 Raman spectroscopy

The $Fm\bar{3}m$ space group has only one active Raman mode, which involves oxygen ion vibration in a tetrahedral environment formed by four cations. Six active Raman modes exist for the $Fd\bar{3}m$ space group. Five involve cation-anion vibration, and the highest wavenumber mode is related only to the oxygen sub-lattice [122]. Each active Raman mode is associated with a peak in the Raman spectra. Since Raman is probing the local structure, disorder in the structure will be revealed in the spectra. Therefore, the spectrum of a sample with the disordered fluorite structure (space group $Fm\bar{3}m$) will not show one well-defined peak as is otherwise expected for its space group. The disorder will cause disturbances in the vibrations and therefore provoke at least a broadness of this peak. Whereas if the films are growing in the pyrochlore structure (space group $Fd\bar{3}m$), well-defined Raman peaks should be seen since the structure has complete ordering. Examples from literature are presented in Figure 3.12a and b, for $\text{La}_2\text{Hf}_2\text{O}_7$ in the pyrochlore structure and $\text{ZrO}_2\text{:Y}$ in the disordered fluorite structure respectively.

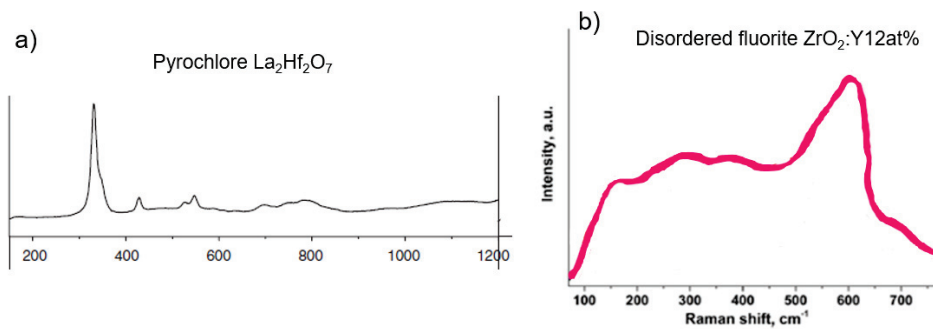


FIGURE 3.12: Raman spectra from literature. a) $\text{La}_2\text{Hf}_2\text{O}_7$ concluded to crystallize in the pyrochlore structure (space group $Fd\bar{3}m$) [112] b) $\text{ZrO}_2\text{:Y}$ 12at% concluded to crystallize in the disordered fluorite structure (space group $Fm\bar{3}m$)[123].

The recorded Raman spectra for selected samples are displayed in Figure 3.13. The samples were excited from the top in Figure 3.13a-c meaning each spectrum is a mixed contribution from the film and the substrate, and the film contribution varies depending on the film thickness. The spectra of the substrates were collected without any films. The sample was excited from the side in Figure 3.13d. Since a micro-source with a focal point of approximately $2\ \mu\text{m}$ was used for the excitations, it was possible to excite the film more individually. The substrate has therefore influenced the collected spectrum of the film much less, if any, compared to those excited from the top. It could have been beneficial to collect the spectra for all samples like this, but since the films are thin, it is more challenging to do so.

The substrate spectra are consistent with the expected broadness arising from the disorder in the structure discussed above and with previously reported spectra on

this structure [123] with a redrawing of this also presented in Figure 3.12b for better comparison.

Considering the spectrum in Figure 3.13d of M4-Pb-Lu₂Hf₂O₇:Eu15% excited from the side, the film has similar features as the substrate but with some variations in the intensities. However, since Raman is probing the local structure, the composition and site occupancy variation can introduce differences like this. This, therefore, strongly suggest that the film is crystallizing in the same structure as the substrate, namely, the disordered fluorite structure.

Considering the spectra collected by excitation from the top of the samples M1-Pb-(Y,Sc)₂Hf₂O₇-100, M2-Pb-(Tm,Sc)₂Hf₂O₇-111 and M4-Pb-Lu₂Hf₂O₇-100 in Figure 3.13a, b and c, respectively. The features of the investigated samples are all similar to those of the substrates. Indeed, these spectra are dominated by the substrate spectra, but if the film has the pyrochlore structure, distinct peaks would have revealed this due to the high degree of ordering in this structure.

It can be reasoned from these investigations that the films crystallize in the same structure as the ZrO₂:Y substrates, namely, the disordered fluorite structure (space group $Fm\bar{3}m$).

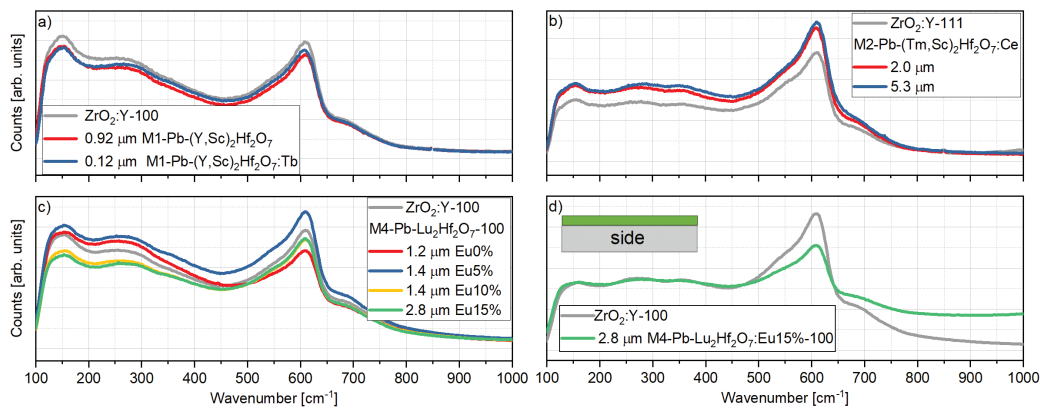


FIGURE 3.13: Raman spectra of selected samples (see sample references in the legends) compared to substrates with appropriate orientations. a-c) The samples are excited from the top. d) The samples are excited from the side, thereby isolating the contributions from the film and substrate. The excitation wavelength for spectra in a) and c) 457 nm and b) and d) 488 nm.

3.3.3 X-ray diffraction

Studying the structure of these samples with XRD can give somewhat restricted information since the films are growing epitaxially on the substrates meaning they should have a high degree of preferred orientation. When performing symmetric 2θ - ω scans on the samples, diffraction will only occur on the planes parallel to the sample surface, making it impossible to evaluate the structure entirely. Calculated diffractograms of Lu₂Hf₂O₇ with the defect fluorite and pyrochlore structure are

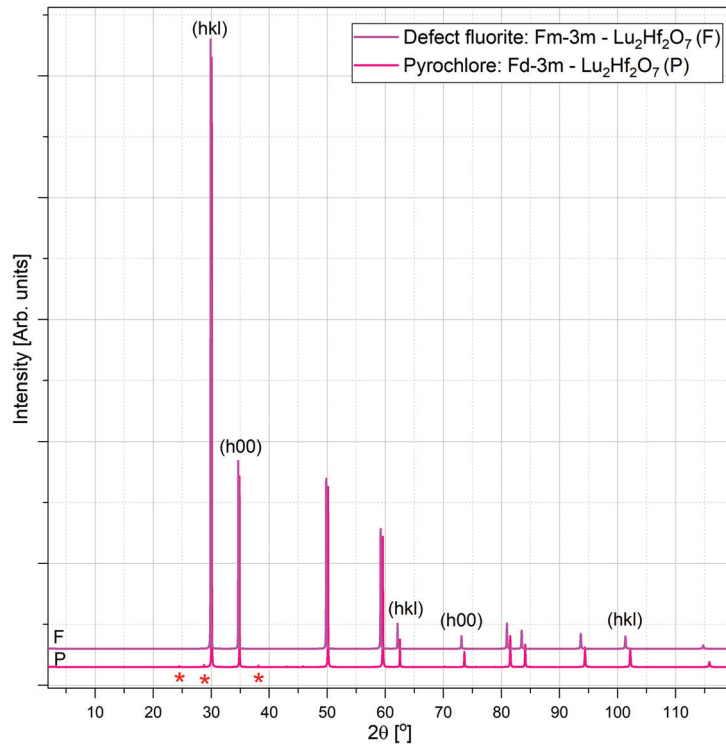


FIGURE 3.14: Diffractograms calculated for two relevant references. Some peaks are referred to as the fluorite (F) and pyrochlore (P) structures corresponding to (hkl) for the (111) oriented samples and (h00) for (100) oriented samples. * indicates the low-intensity peaks unique to the pyrochlore structure.

displayed as references in Figure 3.14. These diffractograms are presented as if they were from powders with no preferential orientation of the planes. Both structures have, at first glance, similar diffractograms. Looking closely, the pyrochlore structure gives rise to a few additional low-intensity peaks. The hafnate samples' single crystalline nature results in a completely preferred orientation. The relevant peaks associated with the two orientations of the substrate are marked in the figure as (h00) and (hkl). These are at similar 2θ values for the pyrochlore and fluorite. This indeed challenges the structure determinations of the films with XRD. The additional peaks from the pyrochlore structure can be revealed by performing asymmetric scans, but this search can be tedious and is not further evaluated here.

With Raman, the difference between the disordered fluorite and ordered pyrochlore is pronounced, as discussed in the section above. However, even though the structure cannot be determined from XRD, other valuable and interesting information can be extracted.

Some of these results extracted from performing XRD are presented in Figure 3.15 for samples M4-Pb-Lu₂Hf₂O₇:Eu15% with orientation (111) and (100). The peaks observable with symmetric 2θ - ω scans and ω scans are displayed, comparing the substrate and film contribution for each sample. The diffraction peaks from the films are generally broader than from the substrates. This is especially evident when

considering the ω scans. This indicates there is a broader range of unit cell lengths, which can be caused by strain in the film lattice or variations in composition as well as slight variations in the parallelity between film and substrate. There are ripples around the film peaks for M4-Pb-Lu₂Hf₂₇:Eu15%-111 in Figure 3.15a. This results from the film being only around 0.5 μm thick and is similar to features that arise when performing X-ray reflectometry on thin film samples.

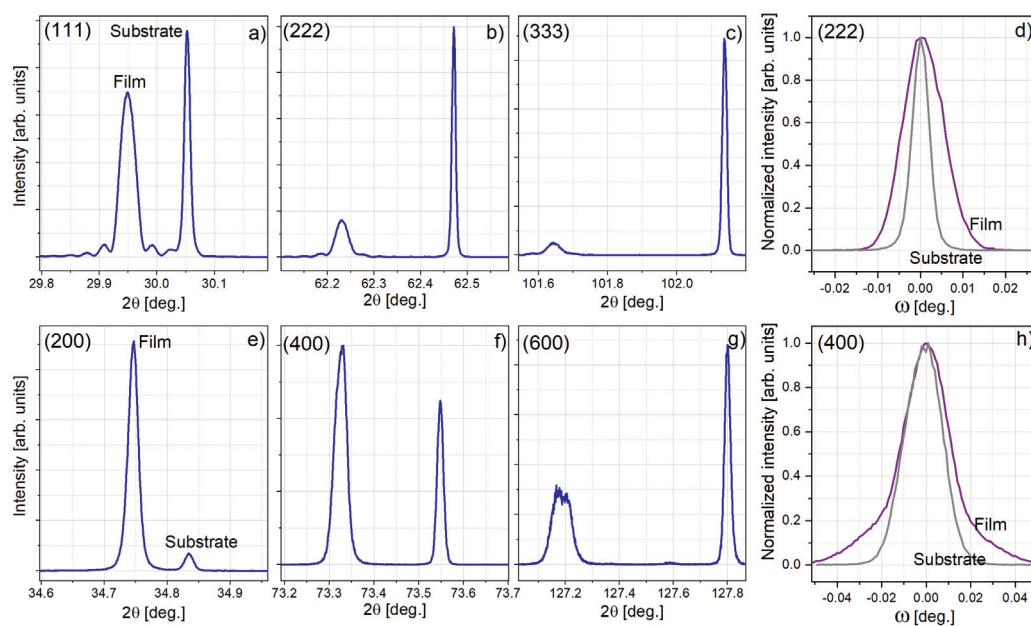


FIGURE 3.15: a-d) 2θ - ω and ω scans for relevant peaks of 0.5 μm M4-Pb-Lu₂Hf₂₇:Eu15%-111. e-h) 2θ - ω and ω scans for relevant peaks of 2.8 μm M4-Pb-Lu₂Hf₂₇:Eu15%-100. $\lambda = 1.5406 \text{ \AA}$ (Copper K $_{\alpha 1}$)

For most of the samples, the XRD results look similar to those presented for the M4-Pb-Lu₂Hf₂₇:Eu15% samples. However, for M1-Pb-(Y,Sc)₂Hf₂O₇, several often partly overlapping peaks would be present for the films, similar to those in Figure 3.16c and d, marked as 1 and 2. The extracted lattice mismatch for this sample is -0.33% calculated for film peak marked 2, which is the furthest away from the substrate, meaning the largest mismatch. Typically, having a lattice mismatch below 1% is not causing significant issues for the film quality, so indeed -0.33% is not an unreasonable lattice mismatch. From SEM-EDX, it was found that films from this solution have variations in the elemental composition. This can result in variations in the unit cell length of the film and thereby give rise to several diffraction peaks. It is noteworthy that the position of the film peak in relation to the substrate peak is reversed compared to the M4-Pb samples, establishing this M1-Pb film has a unit cell length shorter than the substrates, whereas, for the M4-Pb samples, it is larger. This results in a tension of the lattice of M1-Pb samples, which is typically more devastating for the film quality than compression. Combined with the varying elemental composition, this could provoke these films to have lines. The surface of an M1-Pb sample was shown, for example, in Figure 3.8. The extended 2θ - ω scans, like the one displayed for

M1-Pb-(Y,Sc)₂Hf₂O₇ in Figure 3.16a, typically only display peaks arising from the expected (hkl) planes, indicating only a single crystalline phase is present. However, for this sample, additional low-intensity peaks are found (one indicated with a star). These peaks are suspected to arise due to PbHfO₃, but it is challenging to conclude because only a few low-intensity peaks are present. However, this suspicion is supported by the findings presented in Section 3.2 that PXRD identified the material depositing on the paddle during agitation as PbHfO₃. This secondary phase found in the diffractogram of the M1-Pb-(Y,Sc)₂Hf₂O₇ sample most likely originates from the crystals deposited on its surface (see Figure 3.5a-c) and not the film itself. Especially since it can be concluded the additional peaks are not arising from the pyrochlore or the delta phase.

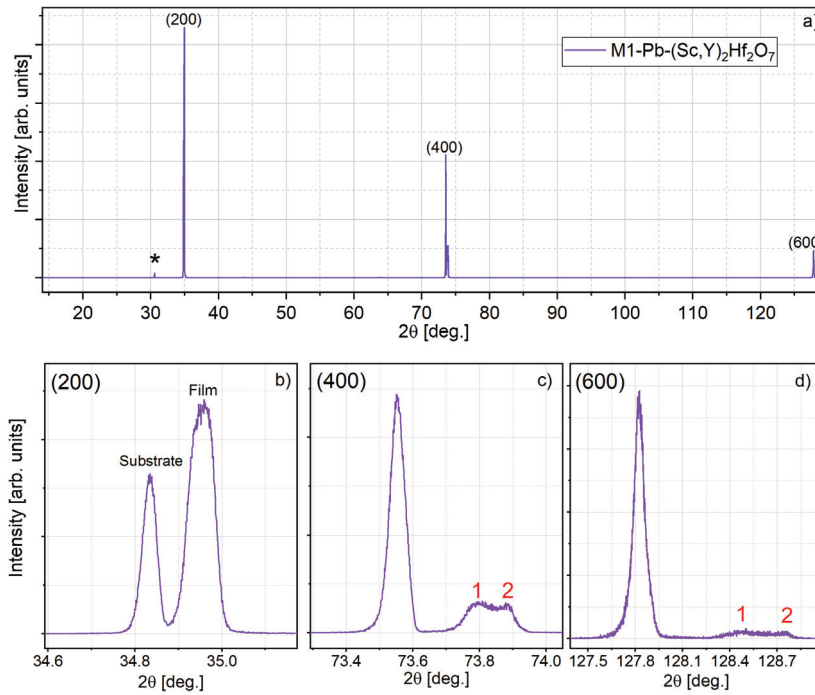


FIGURE 3.16: 2θ - ω scans for a M1-Pb-(Sc,Y)₂Hf₂O₇ sample. $\lambda = 1.5406 \text{ \AA}$ (copper $K_{\alpha 1}$)

An overview of extracted lattice mismatches from samples grown from the different solutions presented in relation to their nominal elemental content is displayed in Figure 3.17. The unit cell parameter, a , is calculated by combining the d-spacing with Bragg's law. For a cubic system, the following is valid:

$$\frac{1}{d_{hkl}^2} = \frac{h^2 + k^2 + l^2}{a^2} \quad (3.1)$$

And combined with Bragg's law, the a -parameter is:

$$a = \left((h^2 + k^2 + l^2) \cdot \left(\frac{\lambda}{2 \cdot \sin\theta} \right)^2 \right)^{1/2} \quad (3.2)$$

The lattice mismatch is then calculated according to equation 4.1. An increase in lattice mismatch with increasing nominal dopant content is generally observed. This indicates the dopants enter the films increasingly with the nominal increase in the solution. This again confirms the great flexibility of this structure. Considering the ionic radii of the rare earth elements in the structure presented earlier in Table 3.4, all dopants are larger than Hf^{4+} , and all except Ce^{4+} are larger than Lu^{3+} . Substituting with these elements will naturally lead to an expansion of the lattice. It is also observed that samples grown on (111) substrates generally have a larger lattice mismatch than for (100). This can explain the slower growth rate of these samples. The lattice mismatch is positive for all compositions except those including scandium (M1-Pb and M2-Pb). The lattice parameters of the films are, therefore, larger than that of the substrate, demonstrating that the films are in compression.

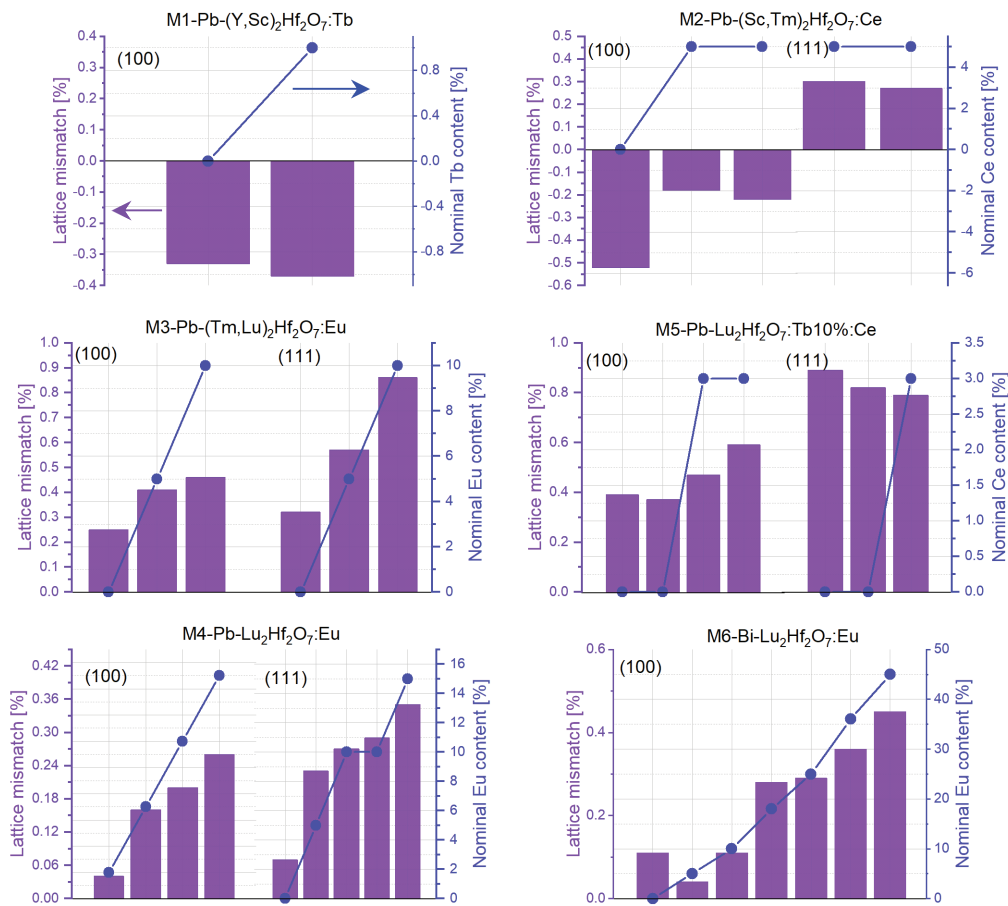


FIGURE 3.17: Overview of the lattice mismatch compared to nominal content of rare earth dopant elements for hafnate samples.

3.4 Scintillating $\text{Lu}_2\text{Hf}_2\text{O}_7\text{:Eu}$

The ultimate goal is to have high-density scintillating screens able to perform high-resolution imaging that can outcompete the current state-of-the-art SCF scintillators. From the simulations, the hafnates are promising candidates. However, as has already been showed, unfortunately, not all grown hafnate compositions demonstrated scintillation. Slight scintillation was found for M1-(Sc,Y) $_2\text{Hf}_2\text{O}_7\text{:Tb}$ after performing an annealing procedure, and reasonable scintillation was obtained instantly for M4-Pb- $\text{Lu}_2\text{Hf}_2\text{O}_7\text{:Eu}$ and M6-Bi- $\text{Lu}_2\text{Hf}_2\text{O}_7\text{:Eu}$ samples. These are, therefore, in focus for this section. First, a literature review will be presented on the scintillation in lutetium hafnates. Then the photoluminescence results of various samples will be presented, and these abilities will be discussed. The remaining part of the chapter is restricted to the scintillating samples, where results on radioluminescence, light output, decay, and imaging abilities at beamlines are presented to thoroughly evaluate their abilities as scintillators.

3.4.1 Literature

Since the general literature on lutetium hafnates is limited, the same is valid for its scintillating properties. A recently published review concerning scintillation in hafnium-based oxide materials also underlines this [124] since only a few compounds are described here. Table 3.11 displays the main results from the literature on scintillation in these compounds.

Compound	Dopant	Growth method	Scintillation	Decay
HfO_2 [125]	Eu:Y	Sol-gel (P)	31000 ph/MeV	9.5 μs
Lu_2O_3 [104]	Eu	LPE (SC)	5-20%**	-
$\text{Lu}_2\text{Hf}_2\text{O}_7$ [126]	Ce	Combustion + sintering (C)	1000 ph/MeV	20 ns
$\text{Lu}_4\text{Hf}_3\text{O}_{12}$ [127]	Eu, Tb, Ce, Pr, Bi	Solid state sintering (C)	Eu: 137%*, Tb: 56%*	-
$\text{Lu}_2\text{Hf}_2\text{O}_7$ [128]	Un-doped	Floating zone (SC)	Low yield	81 ns and 641 ns
$\text{Lu}_2\text{Hf}_2\text{O}_7$ [107]	Ce, Pr, Tb	Floating zone (SC)	Low yield	Pr: 27.2 μs , Tb: 161 μs

TABLE 3.11: Overview of literature on scintillating lutetium hafnates.
P: Powder, C: Ceramics, SC: Single Crystals. *of BGO and **of YAG:Ce.

The report on single crystalline $\text{Lu}_2\text{Hf}_2\text{O}_7$ doped with either cerium, praseodymium, or terbium, states the scintillation from these samples is inefficient. They find that after annealing of $\text{Lu}_2\text{Hf}_2\text{O}_7\text{:Ce}$ at reductive conditions, the emission spectrum change shape, and they suggest the valence state of cerium therefore transforms. They suggest that praseodymium and terbium probably partly remain as tetravalent ions, which may degrade their luminescent properties. It is suggested from these results the Hf^{4+} site is interfering with the preferential substitution of ions and leading to inefficient luminescence properties [107]. However, no direct proof of this claim has been displayed.

Substrate: It has previously been reported that yttria stabilized ZrO_2 exhibit emission [129, 130]. It was suggested that the broad scintillation band arises due to a defect structure with all nearest neighbors of Zr^{4+} being oxygen vacancies. In

addition, they also observed a low-intensity peak around 610 nm, which they suspect is caused by rare earth impurities in the structure [129].

3.4.2 Luminescence

3.4.2.1 Annealing procedures

We briefly investigated the influence of thermal annealing on the luminescent properties. For that purpose, samples of $\text{M1-Pb-(Y,Sc)}_2\text{Hf}_2\text{O}_7:\text{Tb}1\%$, $\text{M3-Pb-Lu}_2\text{Hf}_2\text{O}_7:\text{Eu}$ and $\text{M4-Pb-Lu}_2\text{Hf}_2\text{O}_7:\text{Eu}$ were selected, and the emission spectra under X-ray excitation before and after annealing were investigated. The general annealing procedure was in a muffle furnace in air. The cooling and heating rate was $100\text{ }^\circ\text{C/h}$, and the annealing temperature was $1100\text{ }^\circ\text{C}$ for 12 h.

For $\text{M1-Pb-(Y,Sc)}_2\text{Hf}_2\text{O}_7:\text{Tb}1\%$ samples, indications of Tb^{3+} emission lines were found in the radioluminescence spectra only after the annealing procedure. However, a thermal annealing procedure in air normally transforms Tb^{3+} into Tb^{4+} . The annealing could have reduced a defect concentration in the film that otherwise initially quenched the scintillation. Alternatively, the X-ray flux used for the second measurement was slightly higher, making it possible to detect the low-intensity scintillation. Nominally in the growth solution, there was only 1% terbium, but it has been confirmed by photoluminescence and the change in film color that terbium enters the structure, which will be presented in the next section. The scintillation yield could potentially have been increased by increasing the terbium content. However, this was not pursued. Since scandium and yttrium occupy the structure heavily, as concluded by elemental analysis in Section 3.2.3, the density of these samples is reduced below 6 g/cm^3 making it less relevant in the scope of this thesis.

For $\text{M3-Pb-Lu}_2\text{Hf}_2\text{O}_7:\text{Eu}$ and $\text{M4-Pb-Lu}_2\text{Hf}_2\text{O}_7:\text{Eu}$ annealing in air at $1100\text{ }^\circ\text{C}$ did neither enhance nor reduce its radioluminescence.

3.4.2.2 Photoluminescence

Photoluminescence has been used to extract further information on the dopant incorporation in the lattice and to identify the emission lines better since the radioluminescence is of lower resolution making it harder to identify them.

M1-Pb-(Y,Sc)₂Hf₂O₇:Tb1%-A-100: Figure 3.18a displays the photoluminescence spectra of a $\text{M1-Pb-(Y,Sc)}_2\text{Hf}_2\text{O}_7:\text{Tb}1\%$ -A-100 film and the substrate. The photoluminescence spectra were recorded by exciting from the side of the sample. Since the excitation source has a focal point of approximately $2\text{ }\mu\text{m}$, it was possible to excite the film more individually by exciting mainly the film, thereby reducing the substrate signal and maximizing the film signal. This is meaningful since the emission from M1-Pb films is low intensity, and the film is only $0.12\text{ }\mu\text{m}$ thick. The emission lines characteristic for Tb^{3+} are identified as indicated in the figure, being $^5\text{D}_4$ to $^7\text{F}_j$ ($j=5,4,3$) transitions. Here it is also important to notice that the substrate itself exhibits photoluminescence. The origin of this was discussed above, and for these specific

lines, rare earth impurities must be present in the substrate. It is not unusual having rare earth element impurities in single crystals. To avoid it, the precursors should be very pure, which is very expensive.

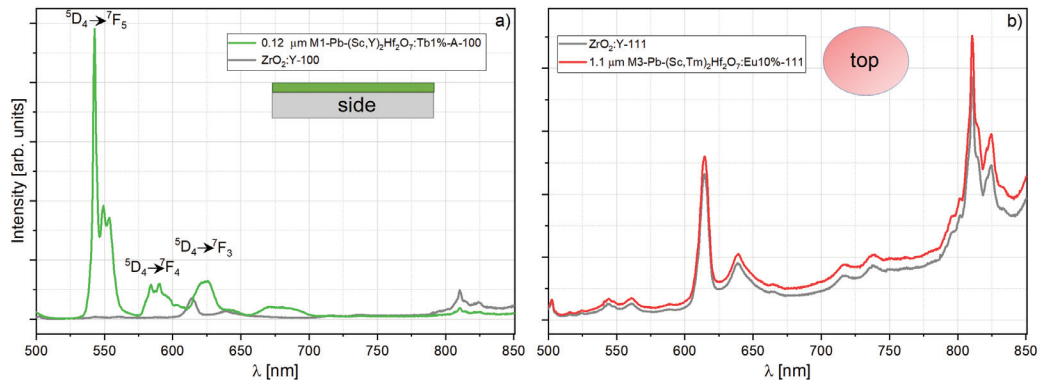


FIGURE 3.18: Photoluminescence spectra a) M1-Pb-100 sample, excitation from the side to excite the film more individually. b) M3-Pb-111 sample, excitation from the top with the laser power for the sample being 5% and for the substrate 1%. The excitation wavelength for all spectra is 488 nm.

M3-Pb-(Sc,Tm)₂Hf₂O₇:Eu10%-111: The spectra of M3-Pb-(Sc,Tm)₂Hf₂O₇:Eu10%-111 is presented and compared to a substrate without film in Figure 3.18b. This sample was excited from the top, meaning the spectrum is a combination of the film and the underlying substrate. For these specific measurements, the power of the laser was 1% for the substrate and 5% for the sample. The sample and substrate spectra are very similar, and the typical emission lines corresponding to europium transitions are absent. This agrees with the absence of scintillation from these samples. However, it was already confirmed europium is incorporated in the structure from the increase in lattice mismatch in section 3.3. Tm³⁺ is typically found to be luminescent itself, but there are reports on concentration quench as well as the initial increase of Eu³⁺ luminescence followed by a concentration quench when co-doped with Tm³⁺ reducing the emission [131]. It is therefore suspected the large concentration of thulium in the structure quenches the Eu³⁺ emission.

M3-Pb-Lu₂Hf₂O₇: The photoluminescence spectra of M3-Pb-Lu₂Hf₂O₇ samples with increasing europium content and a substrate are compared in Figure 3.19a. These spectra are not corrected for the film thicknesses. The typical Eu³⁺ lines characteristic for the ⁵D₀ to ⁷F_{*i*} (*i*=1,2,3,4) transitions are identified for the europium doped samples. The same lines can be identified for radioluminescence (see Figure 3.20). The substrate emission without any films seems very large compared to the films here, but it should be noted that the substrate is 500 μm thick where the films are only a few microns (see figure legend). However, it is also apparent that the substrate emission is dimmed for the samples with the film. The relevant emission lines for scintillation purposes when combined with a CCD or sCMOS camera are studied closer in Figure 3.19b. Here the spectra are corrected for their thicknesses to evaluate their relative intensities. With

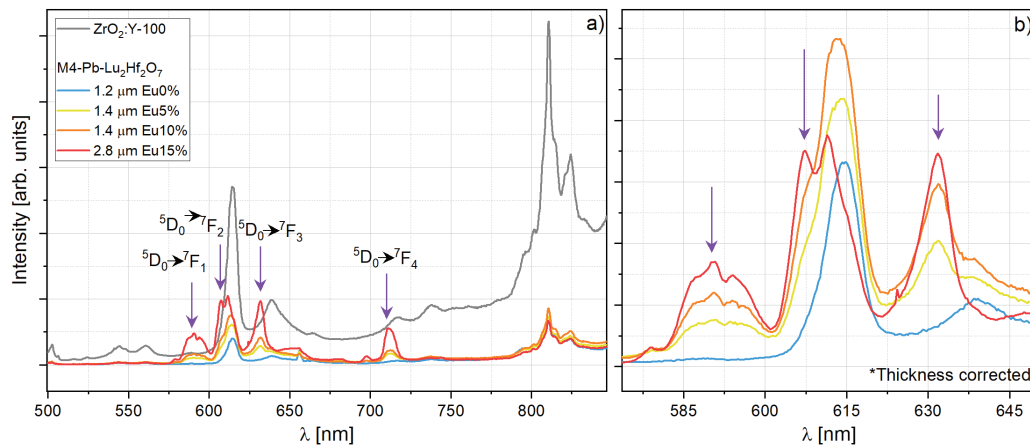


FIGURE 3.19: Photoluminescence spectra M4-Pb-100 samples with varying nominal europium content a) Not thickness corrected. b) Thickness-corrected spectra focusing on the typical europium lines relevant for scintillation purposes. The excitation wavelength for all spectra is 488 nm

increasing nominal europium content, the europium peaks increase in intensity. This is indicated with arrows in the figure. There is also some overlap of lines from the substrate and the film.

3.4.2.3 Radioluminescence

The radioluminescence is, of course, the most relevant since the project aims for scintillation. Comparing the photoluminescence and radioluminescence spectra of $\text{ZrO}_2:\text{Y}-100$ substrate and $\text{M4-Pb-Lu}_2\text{Hf}_2\text{O}_7:\text{Eu}15\%$ in Figure 3.20 overall agreement is found. However, the substrate has a broad emission band in radioluminescence that is absent in photoluminescence. This indicates it requires higher energies to be excited than europium since the europium lines are present both for photoluminescence and radioluminescence. The scintillation from the substrate is a broad band from around 350 nm to 575 nm and a few low-intensity peaks above 600 nm. It has previously been reported that yttria stabilized ZrO_2 exhibit emission [129, 130], and the origin of this was discussed earlier.

The radioluminescence spectra recorded for $\text{M6-Bi-Lu}_2\text{Hf}_2\text{O}_7:\text{Eu}$ samples with increasing nominal europium content is presented in Figure 3.21. The europium-doped samples show an increasing intensity of the emission lines with the nominal europium content. From this, it is also seen the lines are similar regardless of the substrate orientation.

Bandpass filters: Scintillation from the substrate can be detrimental to the final imaging applications at beamlines since this will mimic a much thicker scintillator and generate an image out of the focal plane deteriorating the spatial resolution. Therefore, Two bandpass filters were tested to exclude the emission from the substrate itself while retaining the emission from the films. The characteristics of the two filters are

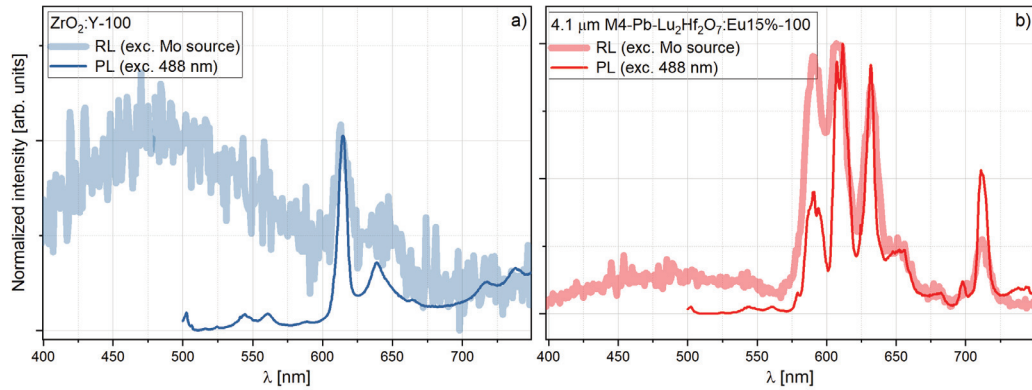


FIGURE 3.20: Comparison of normalized spectra of radioluminescence and photoluminescence for a) $\text{ZrO}_2\text{:Y-100}$ substrate and b) $\text{M4-Pb-Lu}_2\text{Hf}_2\text{O}_7\text{:Eu15\%-100}$.

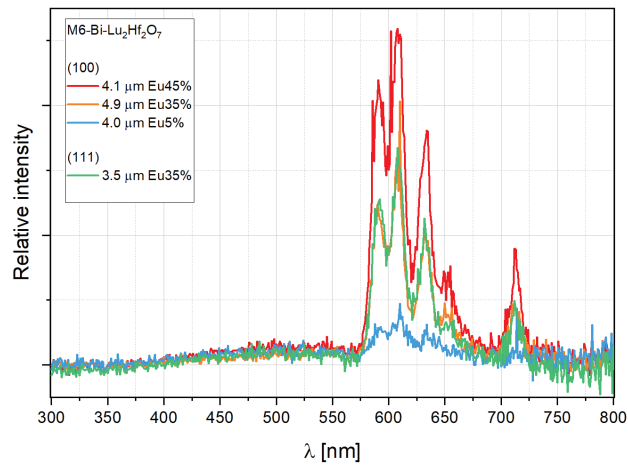


FIGURE 3.21: Radioluminescence spectra of $\text{M6-Bi-Lu}_2\text{Hf}_2\text{O}_7$ samples with increasing europium content. The spectra are corrected for the film thickness. The two samples with Eu35% overlap. Excitation was performed with a molybdenum source.

presented in Table 3.12. The emission spectra collected using the filters are displayed in Figure 3.22a and b for filter1 and filter2, respectively. The substrate emission overlaps with some of the europium lines of the films. Therefore using bandpass filter1, only some substrate emission can be omitted as seen in Figure 3.22a blue curves. When using bandpass filter2, one europium line at 590 nm from the film is transmitted, and the substrate emission seems completely omitted. However, both filters also reduce the film emission, which reduces the overall efficiency of the scintillator. Despite this, the problem of substrate scintillation can be resolved by using bandpass filters like these in the detector setup.

	Central wavelength	FWHM
Filter1	634 nm	70 nm
Filter2	590 nm	10 nm

TABLE 3.12: Overview of the two bandpass filters used for omitting the substrate emission.

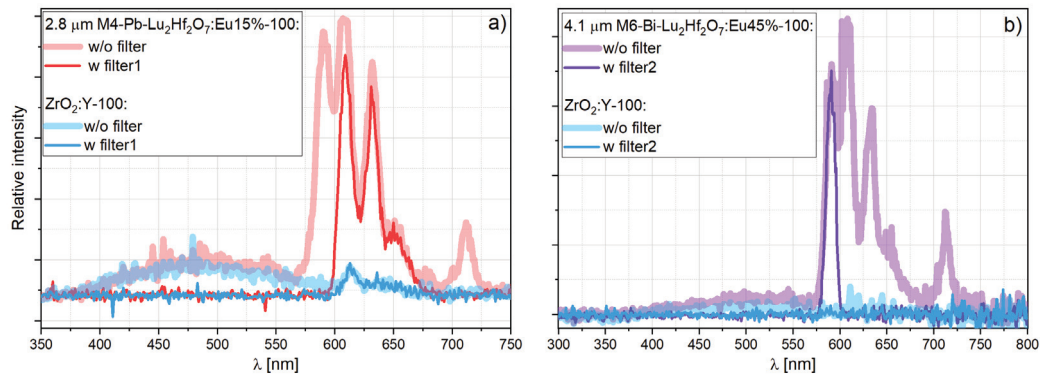


FIGURE 3.22: Radioluminescence spectra a) $\text{M4-Pb-Lu}_2\text{Hf}_2\text{O}_7:\text{Eu}15\%-100$ with and without filter1. b) $\text{M6-Bi-Lu}_2\text{Hf}_2\text{O}_7:\text{Eu}45\%-100$ with and without filter2. See the description of filters in Table 3.12. Excitation was performed with a molybdenum source.

3.4.3 Light output

The light output is difficult to predict since it depends on many factors. Of course, it depends on the band structure itself, but the growth method often influences which and how many defects and impurities are present. However, it is an important parameter for scintillating samples and should be evaluated.

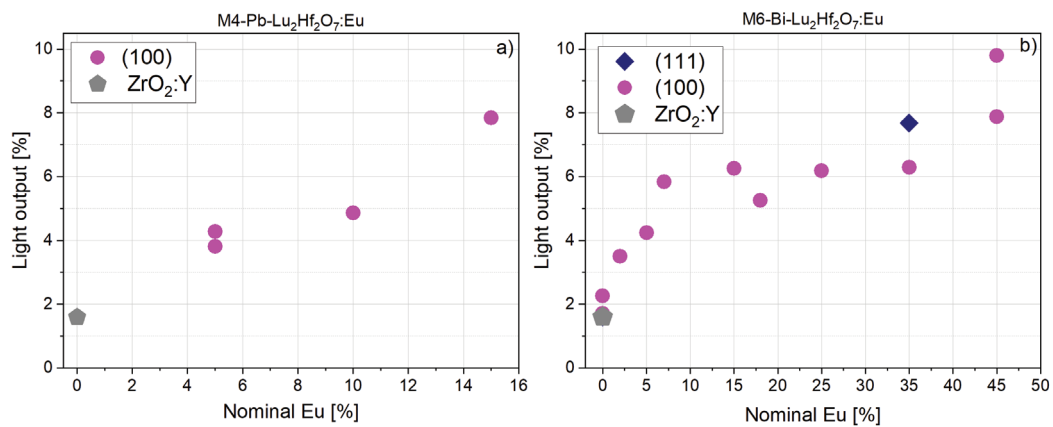


FIGURE 3.23: Light output for increasing europium content in samples: a) $\text{M4-Pb-Lu}_2\text{Hf}_2\text{O}_7:\text{Eu}$. b) $\text{M6-Bi-Lu}_2\text{Hf}_2\text{O}_7:\text{Eu}$. Excitation was performed with a molybdenum source. The light output is calculated relative to a $\text{YAG}:\text{Ce}$ bulk single crystal and is corrected according to the thickness. No bandpass filter has been used for these measurements.

The light output was measured for the scintillating samples relative to the light output of a $\text{YAG}:\text{Ce}$ bulk single crystal and corrected according to the X-ray absorption and, thus, the thickness. The light output is summarized in Figure 3.23 and is presented as a function of the nominal europium content of the samples. It is worth mentioning here again that the nominal and actual europium content is not the same. See more in Section 3.2.3. For both $\text{M6-Bi-Lu}_2\text{Hf}_2\text{O}_7:\text{Eu}$ and $\text{M4-Pb-Lu}_2\text{Hf}_2\text{O}_7:\text{Eu}$, there is an increasing light output dependence with increasing nominal europium content. This is caused by the increased probability of recombining radiative as the

europium content increases, leading to increased light output. Saturation of the light output is not yet reached for these samples as is otherwise typical when increasing the dopant content in scintillating samples. The light output is below 10%, which is considerably less than what was hoped for. The solvent elements (here Pb and Bi) may be incorporated into the films and introduce killing luminescence centers, which reduce or eliminate the light output. As the structure is very flexible for LPE growth, some solvent ions are likely incorporated into the grown films, affecting the light output.

The light output of the substrates is also indicated in the figure and is below 2%. Since the substrate thickness is large in comparison to the thickness of the film and the light output here is corrected for the thickness, even a very low luminescence contribution cannot be ignored since it is enough to spoil the contrast when performing X-ray imaging.

3.4.4 Decay

Decay measurements of M6-Bi-Lu₂Hf₂O₇:Eu samples with increasing nominal europium content are presented in Figure 3.24. The excitation wavelength was 465 nm and the emission wavelength 590 nm to isolate the contribution from the film. Increasing nominal europium content results in a lower decay time. This is a typical phenomenon seen when the dopant level increases since the mean distance an excited electron has to travel before recombining non-radiative decreases. It is important to note that these decay measurements are performed with optical light excitation, not X-rays. The light output measurements are performed using X-ray excitation, and an increase in light output is observed with increasing nominal europium content. For X-ray excitation, electron-hole transfer has to be considered.

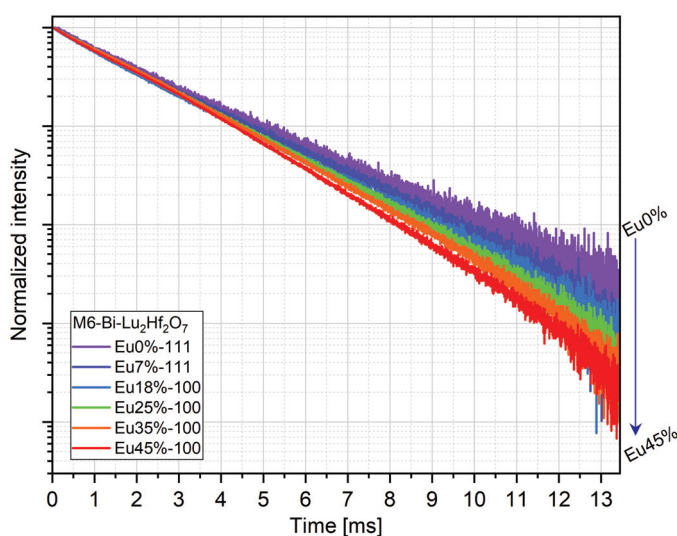


FIGURE 3.24: Decay curves for M6-Bi-Lu₂Hf₂O₇:Eu samples. The excitation wavelength was 465 nm, and the emission wavelength was 590 nm.

The decay time constants have been extracted from the decay curves. For the non-doped sample, M6-Bi- $\text{Lu}_2\text{Hf}_2\text{O}_7$, the curve was described well using two decay constants, being 1.1 μs and 2.3 μs , which must originate from the substrate emission. The sample with nominal Eu5%, $\text{Lu}_2\text{Hf}_2\text{O}_7:\text{Eu}5\%$, three decay constants described the curve well, being 0.58 μs , 2.0 μs , and 3.9 μs . Comparing with the values for decay times listed from literature in Table 3.11 for doped $\text{Lu}_2\text{Hf}_2\text{O}_7$, these decay constants are considerably lower. However, the values are not directly comparable since the decay measurements were not performed with X-ray excitation.

3.4.5 At the beamlines

Before performing any tests of the newly developed hafnate scintillators at the beamlines, the samples had to be prepared. There are films on both sides of the 500 μm thick substrate after LPE. To remove the film and reduce the substrate thickness to around 150 μm the samples were lapped and polished on one side. Micrographs of the two samples prepared for use at the beamlines were presented in Section 3.2, Figure 3.9. Since the M4-Pb- $\text{Lu}_2\text{Hf}_2\text{O}_7:\text{Eu}$ sample was grown some months before the M6-Bi- $\text{Lu}_2\text{Hf}_2\text{O}_7:\text{Eu}$ sample, this was used for the first radiographs at BM05. Due to the better surface quality, M6-Bi- $\text{Lu}_2\text{Hf}_2\text{O}_7:\text{Eu}$ was mainly used for the later experiments performing tomography.

3.4.5.1 Spatial resolution

To experimentally verify the ability of the films to produce high-resolution images, MTFs were extracted from radiographs of a GaAs edge. The method to obtain the MTFs was described in detail in Section 1.2.1.3. These experiments were performed at the ESRF BM05 beamline with monochromatic radiation using a Si(111) crystal monochromator with an energy resolution of $\Delta E/E \approx 10^{-4}$ [103]. The high-resolution X-ray detector system comprised a 10x magnification (NA=0.4) microscope objective and a 3.3x eyepiece. The scintillator was coupled to a Zyla 4.2 sCMOS camera through these magnifying optics. The system allows for the insertion of an optical filter in the infinity-corrected part of the optical path.

To optimize the focus, radiographs of foam were recorded while changing the focus. Uncorrected radiographs of foam and the edge is presented in Figure 3.25, obtained using a M4-Pb- $\text{Lu}_2\text{Hf}_2\text{O}_7:\text{Eu}15\%-100$ sample and M6-Bi- $\text{Lu}_2\text{Hf}_2\text{O}_7:\text{Eu}45\%-100$ sample. The M4-Pb-100 samples have the before-mentioned pits on the surface (see Figure 3.7e-g), and as a consequence, when recording radiographs, the scintillating light is enhanced in these. However, after correcting with a flat field image, these pits do not affect the image quality considerably for the radiographs but could introduce severe issues when performing tomography. The foam and edge radiographs obtained using M6-Bi- $\text{Lu}_2\text{Hf}_2\text{O}_7:\text{Eu}45\%-100$ have a few bright spots. These are due to crystal inclusions on the film surface, enhancing light extraction in those spots acting as diffusive centers.

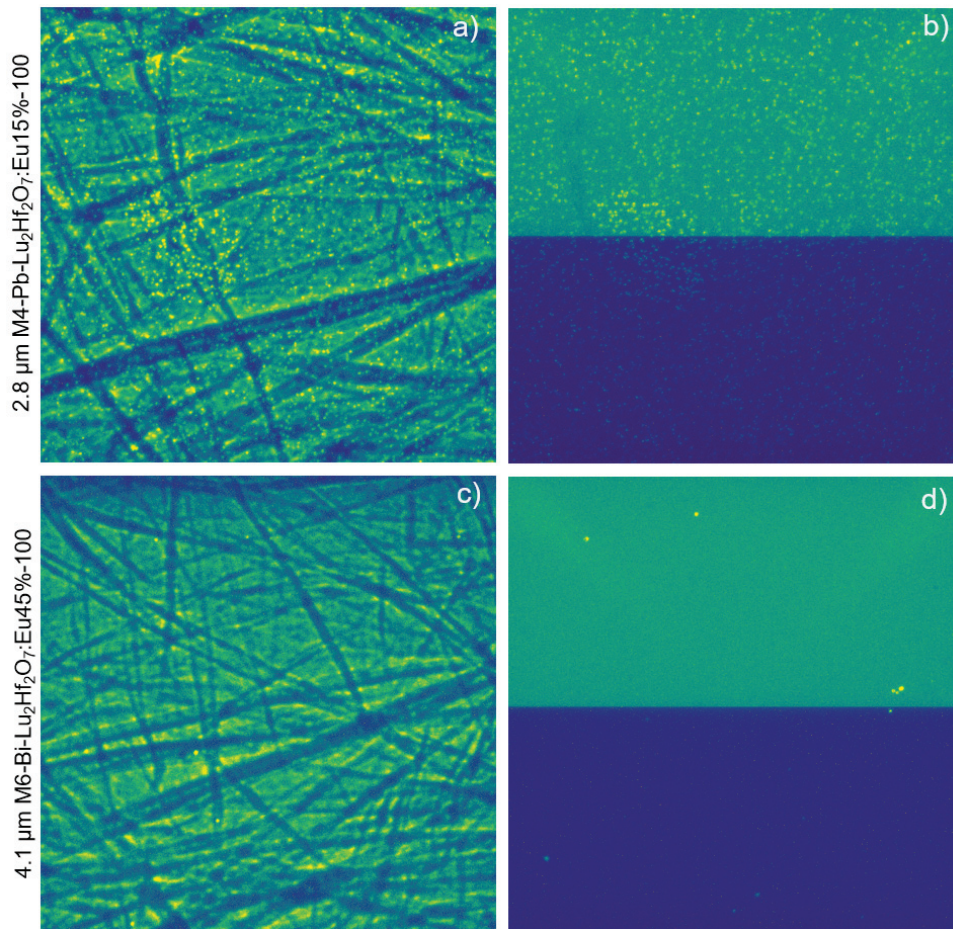


FIGURE 3.25: a) and c) radiographs of foam. b) and c) radiographs of GaAs edge. The scintillator applied is stated on each row, and the images are not dark or flat field corrected. All radiographs are taken using 17 keV monochromatic X-ray energy.

The MTFs extracted at 17 keV using M4-Pb-Lu₂Hf₂O₇:Eu15%-100 and M6-Bi-Lu₂Hf₂O₇:Eu45%-100 are shown in Figure 3.26a and b, respectively including simulated MTFs at 17 keV and 19 keV. Each sample was used with and without filter1 (Table 3.12) to validate that reducing the substrate emission improves the MTFs. The curves have been smoothed using a smoothing average for better comparison. The experimental MTFs for both samples are lower than the simulated MTF at 17 keV. When using filter1, the MTFs are enhanced, indicating filter1 removes sufficiently the emission from the ZrO₂:Y substrate to enhance the MTFs. However, the experimentally obtained MTFs are still not fitting the simulated MTF at 17 keV. It is instead comparable with the simulated MTF at 19 keV, especially below 600 lp/mm. It was discussed in detail in Chapter 2 that using X-ray energies above the absorption K-edge of high-Z elements in the substrates results in a degradation of the MTF, especially at low lp/mm. This effect is seen for the simulated MTFs in Figure 3.26 where energies below and above the zirconium absorption K-edge were used. However, the yttrium absorption K-edge energy is 17.04 keV, meaning just above the energy used for the experiments in Figure 3.26. The absorption edge energies arising from the substrate

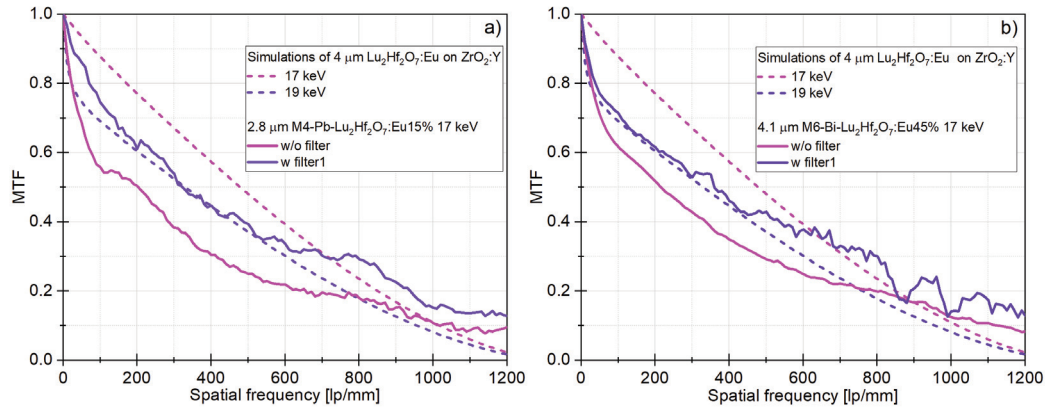


FIGURE 3.26: Experimentally obtained (solid lines) and simulated (dashed lines) MTFs. a) M4-Pb- $\text{Lu}_2\text{Hf}_2\text{O}_7:\text{Eu}15\%$ b) M6-Bi- $\text{Lu}_2\text{Hf}_2\text{O}_7:\text{Eu}45\%$. All radiographs are obtained using 17 keV monochromatic X-ray energy.

are reported in Table 3.13. The monochromatic energy chosen at the beamline should, in principle, be very precise. Nevertheless, these results indicate that the X-ray energy was at least partly above the yttrium absorption K-edge. Comparing the experimental MTFs using M4-Pb- $\text{Lu}_2\text{Hf}_2\text{O}_7:\text{Eu}15\%$ -100 and M6-Bi- $\text{Lu}_2\text{Hf}_2\text{O}_7:\text{Eu}45\%$ -100 in Figure 3.26a and b, it can be concluded they are comparable. The pits present in the M4-Pb- $\text{Lu}_2\text{Hf}_2\text{O}_7:\text{Eu}15\%$ -100 sample are, as already discussed, not decreasing the spatial resolution when used for radiography. Filter2 (Table 3.12) was also tested at the beamline, but the signal was reduced too close to the noise level of the sensor, and the extracted MTFs were highly noisy and will therefore not be presented here.

Element	Edge	Energy [keV]
Zr	K	18.00
Y	K	17.04

TABLE 3.13: Relevant absorption edges [102] for the substrate, $\text{ZrO}_2:\text{Y}$.

Figure 3.27 shows the experimentally extracted MTFs at X-ray energies 17 keV and 19 keV, below and above the zirconium K-edge (Table 3.13), using the M6-Bi- $\text{Lu}_2\text{Hf}_2\text{O}_7:\text{Eu}45\%$ sample compared to the corresponding simulated MTFs. For these measurements, the filter was not applied since using it reduces the scintillating light. The experimental MTF obtained at 17 keV is slightly higher than that at 19 keV, but they are comparable. The typical decrease of the MTF when using energies above the absorption K-edge energy of an element in the substrate is only slightly observed. This supports the suggestion that the 17 keV at the beamline was not the actual energy. It seems it has been higher than the yttrium absorption K-edge energy leading to MTF degradation by substrate fluorescence.

The MTF curves experimentally extracted using the hafnate scintillators generally show good spatial response. They are lower than the simulated MTFs at the initially expected X-ray energy, but this can most likely be ascribed to the substrate scintillation and fluorescence induced by the yttrium. Unfortunately, this last point was not

considered when performing the experiments at the beamline. It would be beneficial to perform the experiments at lower energies to confirm or disconfirm this suspicion. However, it was unfortunately not possible to perform additional measurements before the end of this thesis.

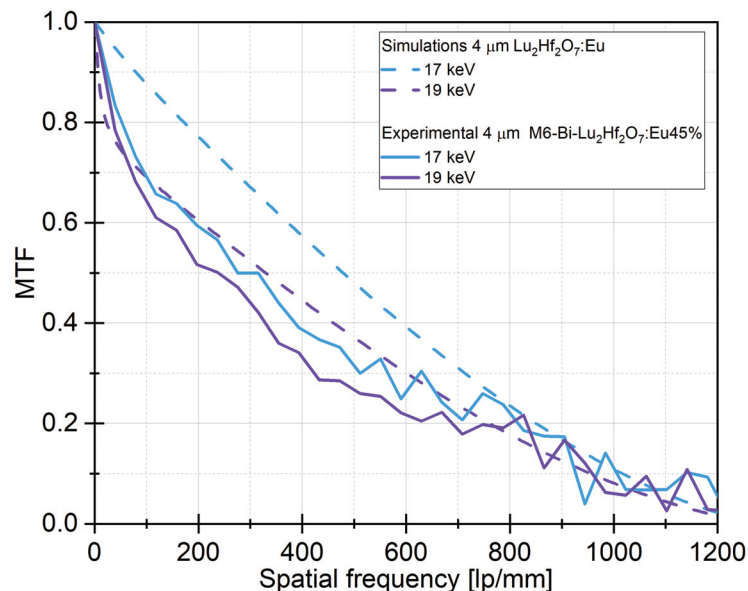


FIGURE 3.27: Experimentally obtained (solid lines) and simulated (dashed lines) MTFs using monochromatic X-rays with energies: 17 keV and 19 keV, which are below and above the zirconium absorption K-edge, respectively. No filter was applied.

3.4.5.2 Imaging at beamlines

Radiographs at BM05

To further explore the abilities of the hafnate scintillators, radiographs were taken of a dead woodlouse (an insect) with the same setup described above for obtaining the MTFs. The woodlouse in front of the setup is displayed in Figure 3.28a. The experiments were performed using 17 keV monochromatic X-rays. This beamtime was performed before growing the samples with the Bi-based flux, and therefore here, the M4-Pb-Lu₂Hf₂O₇:Eu15% sample was compared to a GGG:Eu SCF scintillator. Due to the difference in light output of these two scintillators, the exposure times were not the same. For the 10 μm thick GGG:Eu, an exposure time of 10 s was sufficient to be well above the noise level of the camera. However, for the hafnate scintillator, an effective exposure time of 150 s was necessary.

Radiographs are presented in Figure 3.28c-d, and Figure 3.28b, obtained with M4-Pb-Lu₂Hf₂O₇:Eu15% and GGG:Eu, respectively. These radiographs demonstrate that many small features can be resolved with the hafnate scintillator, witnessing the good contrast and resolution already shown through the MTFs. The pits of the hafnate samples, which act as diffusive light centers as seen in uncorrected images, are not influencing the radiographs when corrected from the dark and flat images. They

do, therefore, not seem to be an issue for the final image quality when performing radiography, as was also concluded from the MTFs.

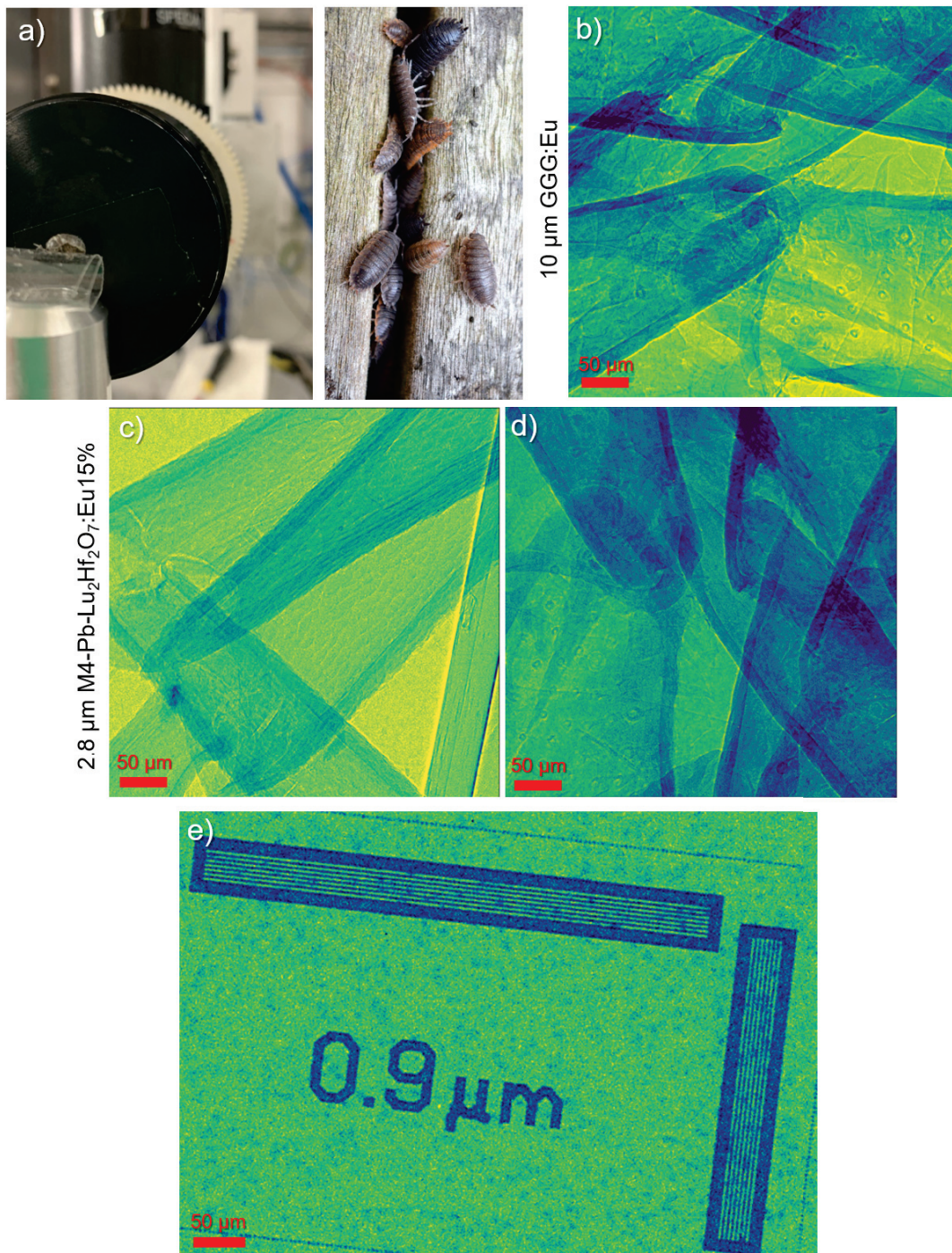


FIGURE 3.28: a) Photograph of the insect used for the radiographs in front of the setup. b) Radiograph using $10\ \mu\text{m}$ GGG:Eu of woodlouse (insect). c-e) Radiographs using $2.8\ \mu\text{m}$ M4-Pb-Lu₂Hf₂O₇:Eu15% of woodlouse (insect) and a resolution target. All radiographs are taken at BM05 using monochromatic X-rays with energy 17 keV and is dark and flat field corrected.

Tomography at ID19

To explore a hafnate scintillator in real beamline conditions, tomography was performed at ID19 (ESRF beamline) on a micro-structured aluminum-silicon alloy. The high-resolution X-ray detector system comprised a 10x magnification (NA=0.3) microscope objective and a 2x eyepiece. The scintillator was coupled to a PCO edge 5.5 camera through these magnifying optics. The system allows for the insertion of an optical filter in the infinity-corrected part of the optical path. The X-ray energy used for the imaging is around 19 keV. Image slices from the tomography experiments are presented in Figure 3.30 comparing M6-Bi-Lu₂Hf₂O₇:Eu45% with and without filter2 and an LSO:Tb with comparable thickness. To better compare the hafnate sample and the LSO:Tb, the acquisition time for the LSO:Tb was reduced to have similar intensity in a radiograph as the hafnate without using a filter.

There are rings present in the image slices using the hafnate. This is normally a result of dust on the scintillator surface or a too-low signal-to-noise ratio. For this specific hafnate sample, it can also be due to crystal inclusions at the surface, which is more likely. The pits on the surface of the samples grown from the Pb-based solution could impose a larger issue when performing tomography than radiography. Comparing the zoom on the heart-shaped feature for each scintillator, LSO:Tb is resolving some features not visible with the hafnate scintillator. From these tomography slices, the filter does not visibly enhance the resolution. However, since the energy applied is around 19 keV it is above the absorption K-edge of zirconium, and therefore the contrast should be better for the LSO:Tb thin SCF scintillator. Some simulations showing this are presented in Figure 3.29.

Nevertheless, it has been successfully demonstrated that Lu₂Hf₂O₇:Eu grown by LPE in a Bi-based solvent can be applied to perform high-resolution imaging at synchrotron beamlines.

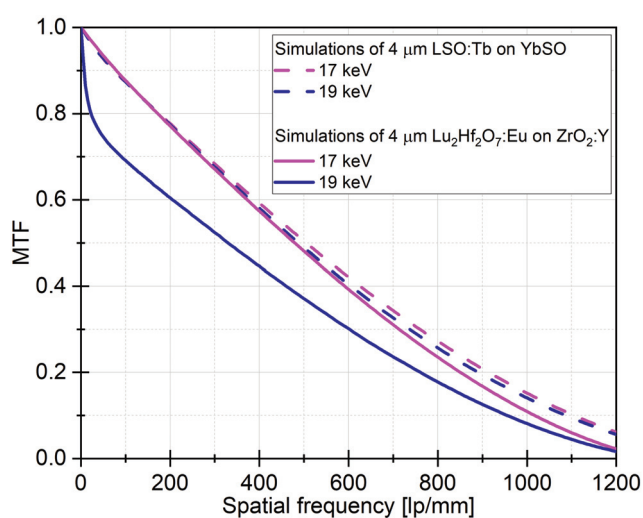


FIGURE 3.29: Simulated MTFs of LSO:Tb (dashed lines) and Lu₂Hf₂O₇:Eu (solid lines) using monochromatic X-rays with energies: 17 keV and 19 keV, which are below and above the zirconium absorption K-edge, respectively.

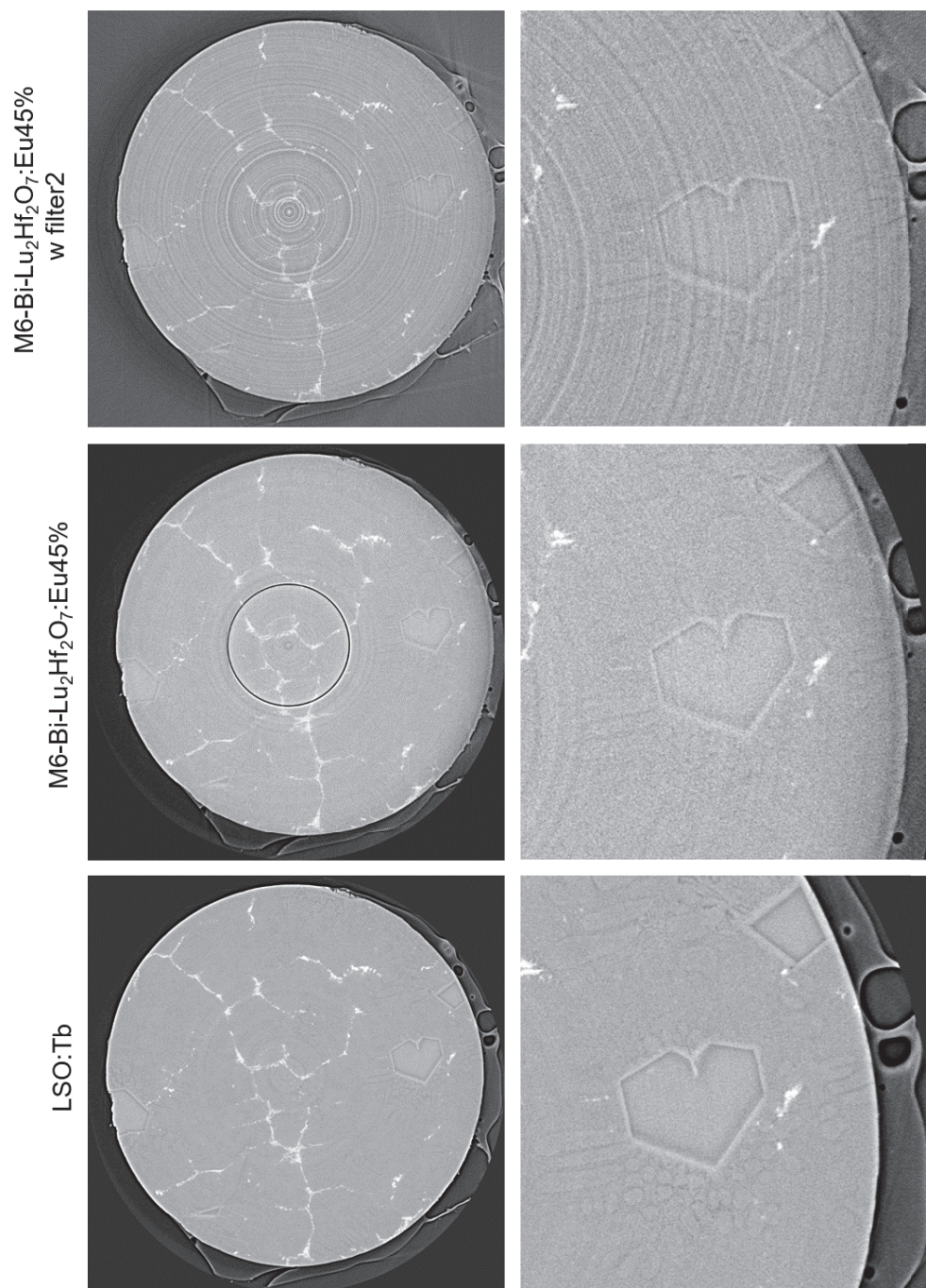


FIGURE 3.30: Tomography slices performed on a micro-structured aluminum-silicon alloy at ID19 (ESRF beamline) using scintillators: a) $4.1 \mu\text{m}$ M6-Bi-Lu₂Hf₂O₇:Eu45% with filter2, b) $4.1 \mu\text{m}$ M6-Bi-Lu₂Hf₂O₇:Eu45%, and c) $4.8 \mu\text{m}$ LSO:Tb on YbSO.

3.5 Possible optimization

As this chapter has hopefully highlighted, extensive research has already been performed on these hafnate compounds. We understand much more than we did at the beginning of the project and the opportunities following it. With the experience from the LPE process and characterization of the grown samples, we understand better how the growth takes place, which crystal structure can be expected, and the possibilities for new compositions. We experienced how detrimental competing phases can be for LPE growth and that it is possible to use Bi_2O_3 as a solvent for the growth of the hafnates. Finally, the most important experience is perhaps the apparent flexibility of this system for LPE growth, allowing a wide range of compositions to be grown on a single type of substrate. This section will present some possibilities for optimizing the samples.

3.5.1 The substrate

This section will briefly discuss some substrate aspects which could be optimized for potential later studies. It should be noted that optimization of the substrate is not in the scope of this thesis.

Substrate structure: The substrates applied for the LPE growth of the hafnates are $\text{ZrO}_2\text{:Y}$ (9.5 mol% Y_2O_3) grown by the skull melting technique [132]. The relation between the amount of yttrium substituted into the structure and the unit cell length is reported to be as follows:

$$a = 5.11742 + 0.00159 \cdot x \quad (3.3)$$

where x is the yttria content in mol% $\text{YO}_{1.5}$ [111]. For our commercial substrates, it is reported $x = 19$ mol% $\text{YO}_{1.5}$, which according to the above formula, results in $a = 5.14704$ Å. From XRD measurements performed on substrates and samples (film on substrates), we generally find that $a = 5.146$ Å for the substrate, fitting quite well with the equation. Since we did not investigate the elemental composition of the substrate, the Y_2O_3 content could vary slightly from the reported content and thereby inducing this difference. Since the yttrium content in the structure determines the unit cell length, the substrate could be modified and optimized to reduce the lattice mismatch. This also allows testing other film compositions, which might be out of reach with the current substrate a -parameter.

Substrate scintillation: As discussed in Section 3.4.3, the scintillation from the substrate cannot be ignored even though it does not seem significant. As seen in Section 3.4.2 the scintillating emission from the substrate is a rather broad band and a low-intensity peak around 610 nm. Even a low impurity level in samples can result in emission, especially for rare earth element inclusions. The peak around 610 nm is suspected to arise due to this. To reduce or avoid substrate emission, the crystal growth procedure should be purified to avoid any rare earth impurities responsible

for the emission. However, some defects are intrinsic to the crystal growth method, for example, oxygen vacancies and anti-site defects. The broad emission band we have observed from the substrate most likely arises due to oxygen vacancies, as discussed earlier, and can, therefore, not be avoided by purifying the substrate crystal growth. However, as already demonstrated this seems to be easily omitted by applying optical filters.

3.5.2 The films

Low light output: Using a scintillator with this low light conversion (<10% of YAG:Ce) efficiency is an issue for practical purposes. It would require to use much longer acquisition times for the imaging experiments and it can therefore not compete with current state-of-the-art LuAG:Ce, LSO:Tb, and GGG:Eu SCFs. Indeed it would be beneficial to perform quantitative elemental analysis to detect precisely the impurity atoms present in the different samples and the dopant levels. This could reveal whether the low light output is caused by low dopant incorporation or too-large impurity levels of elements such as Pt and Pb in the films.

It is worth remarking that the Bi-based LPE solutions for the growth of hafnate compounds have not been fully explored yet. The nominal europium content was increased successfully up to 45%, which resulted in increasing light output. Therefore a study to explore even larger europium content would be valuable. The limit could be the lattice mismatch of the films with respect to the current substrate, but by modifying the composition of the substrate, it could be possible to grow $\text{Eu}_2\text{Hf}_2\text{O}_7$. Other dopants and possibly co-doping could also be investigated to enhance the light output and further annealing studies. Furthermore, due to the apparent large flexibility of the lattice and the possibility to adapt the substrate structure, it opens the opportunity to grow $\text{A}_2\text{B}_2\text{O}_7$ structures with other A and B ions. This requires an extensive bibliographic study beforehand.

3.6 Conclusions

A broad range of hafnate compositions have been explored for LPE growth on $\text{ZrO}_2\text{:Y}$ substrates with crystallographic orientations (100) and (111).

It was found that the hafnate system offers a broad range of compositional options to grow on a single substrate type. Thin films of $(\text{Y,Sc,Hf})_4\text{O}_{8-x}$, $(\text{Sc,Tm})_2\text{Hf}_2\text{O}_7$, $(\text{Lu,Tm})_2\text{Hf}_2\text{O}_7$ and $\text{Lu}_2\text{Hf}_2\text{O}_7$ was successfully grown, proving these hafnates to be a more flexible system for LPE than what is typically observed. Two different solvents, $\text{PbO-B}_2\text{O}_3$ and $\text{Bi}_2\text{O}_3\text{-B}_2\text{O}_3$, were used for these LPE solutions. Changing the solvent from Pb-based to Bi-based was successful, and thicker films of higher quality were obtained. The elemental content estimated from SEM-EDX revealed that most samples have a stoichiometry close to $\text{A}_2\text{B}_2\text{O}_7$. Raman spectroscopy suggests that the films have the disordered fluorite structure, similar to the structure of the substrate. The lattice mismatch extracted from XRD performed on the samples varies from -0.3% to 0.85%, depending on the nominal solution content. From this, it was concluded that they increasingly entered the films by nominally increasing the dopant concentration in the solution. From photoluminescence measurements, the emission lines of terbium were identified for $(\text{Y,Sc,Hf})_4\text{O}_{8-x}\text{:Tb}$ and europium for $\text{Lu}_2\text{Hf}_2\text{O}_7\text{:Eu}$. Significant scintillation was only reached for $\text{Lu}_2\text{Hf}_2\text{O}_7\text{:Eu}$. The light output increased with increasing europium content but was estimated to be lower than 10% of YAG:Ce . The substrate, $\text{ZrO}_2\text{:Y}$, also scintillates. This can be diminished and perhaps eliminated by using optical bandwidth filters that are mainly transparent for film emission. The MTFs were experimentally measured, showing that $\text{Lu}_2\text{Hf}_2\text{O}_7\text{:Eu}$ has a good spatial response. Compared to the simulated MTFs, the experimental MTFs were lower, indicating that something was decreasing the contrast. This is attributed to the substrate emission, and it is postulated that the X-ray energy used for the experiments was slightly higher than expected. This would cause a reduction of the MTF because the K-edge absorption energy of the substrate would then be exceeded, and fluorescence would thereby degrade the spatial resolution. From radiography and tomography experiments, the ability of $\text{Lu}_2\text{Hf}_2\text{O}_7\text{:Eu}$ to perform high-resolution X-ray imaging was explored and validated.

These initial results demonstrate that high density, high effective atomic number, $\text{Lu}_2\text{Hf}_2\text{O}_7\text{:Eu}$ can be successfully grown by LPE, and the samples possess promising scintillating properties. Indeed, these studies have also opened the opportunity to grow a broad range of compounds by LPE on $\text{ZrO}_2\text{:Y}$ substrates, which could lead to exciting materials studies in the future.

Chapter 4

Preparation and growth of micro-structured scintillators

4.1 Introduction

4.1.1 Micro-structures

The microstructure of surfaces is, in numerous cases, of great importance. It is seen in nature for some animals, insects, and plants, where a well-studied example is lotus leaves. Due to their surface structures, they repel water allowing raindrops to roll freely [133, 134]. While rolling, they collect dirt resulting in a self-cleaning effect, sometimes called the lotus effect [135]. Physically creating micro-structuration of material surfaces can enhance specific properties or even provide the material with new properties, such as friction. An example is solar cells. It has been found that structuring the surface with a femtosecond laser increases the photocurrent by about 30% [136], and by controlling the grain growth of nano-beads as a surface micro-structuration, there is a significantly higher conversion efficiency compared to assemblies with just nanoparticles [137].

As discussed in Chapter 1, developing microstructured scintillators has the advantage of having more efficient detection while maintaining a spatial resolution of a few microns at the best case [53]. A very studied structured scintillator, and so far the only commercialized, is the columnar CsI:Tl. The columns are grown on a substrate using vapor deposition, and by varying the deposition parameters, the structure can be controlled and adjusted [51]. However, even though longer columns have a better conversion efficiency, they also have a lower spatial resolution than scintillating SCFs. This is caused by optical photons crossing between the columns or needles, often referred to as the cross-talk problem [53]. Even though sub-micron resolution cannot be obtained with these, the spatial resolution is still high, and combined with the high absorption efficiency, these are ideal for many medical purposes, having a low dose in the patient. An example is displayed in Figure 4.1, a radiograph of a hand obtained with a 500 μm thick CsI:Tl columnar screen. The limitations for usage at synchrotron sources are their poor radiation hardness [138] and high afterglow [51]. The damages created, especially by the high flux and high energy synchrotron beams, result in light output losses and inhomogeneous responses.



FIGURE 4.1: Radiograph of a hand, acquired with a 500 μm columnar CsI:Tl screen, adopted from [51].

Other attempts to create self-growth array-derived structured scintillators are of Lu_2O_3 and ZnO . However, these are less-developed options. The transparent $\text{Lu}_2\text{O}_3:\text{Eu}$ coatings of 6 to 10 μm have been deposited on sapphire substrates by Electron-Beam Physical Vapor Deposition (EBPVD). From SEM images, a columnar appearance of the deposited Lu_2O_3 is observed [139]. By performing radioluminescence microscopy, a cell-based imaging experiment, they compared the $\text{Lu}_2\text{O}_3:\text{Eu}$ sample with a CdWO_4 scintillating screen. They concluded that using the structured $\text{Lu}_2\text{O}_3:\text{Eu}$ could provide a better-resolved cell image than initially used CdWO_4 scintillators. ZnO nanorod arrays have been deposited via magnetron sputtering and treated subsequently with a hydrothermal reaction method [140]. They were fabricated on quartz substrates with an average diameter of 500 nm and a thickness of 18 μm . From imaging an imaging target at a beamline using 20 keV low flux X-rays, they conclude to have obtained a spatial resolution of 513 lp/mm ($\sim 1 \mu\text{m}$) at an MTF of 10% using their sample.

The concept and idea behind structured scintillators are very good and seem promising, especially at high X-ray energies, to maintain spatial resolution. However, the execution of the concept should still be explored and optimized. Especially for use on beamlines, the currently available options are not optimal.

In this chapter, the complete procedure of obtaining the first promising results of LPE grown micro-structured samples will be presented. This includes details about the laser treatment performed at Fraunhofer Institute for Laser Technology (Fraunhofer ILT) on the substrates and the subsequent treatment and preparation before the growth. The LPE growth itself will be described in detail as well as the issues encountered. Finally, the thorough sample characterization that has helped to understand better the sample growth and behavior of them will be presented and discussed. This chapter merely describes the first steps in exploring LPE growth as a valid synthesis route for growing micro-structured samples. Hopefully, many more tests and investigations will be performed in the future.

4.1.1.1 Concept

Before going into details about the different procedures to obtain a structured sample, the concepts, and ideas will shortly be described here. This should provide an overview and understanding of the pathway as well as an overview of the nomenclature used in this chapter for the samples.

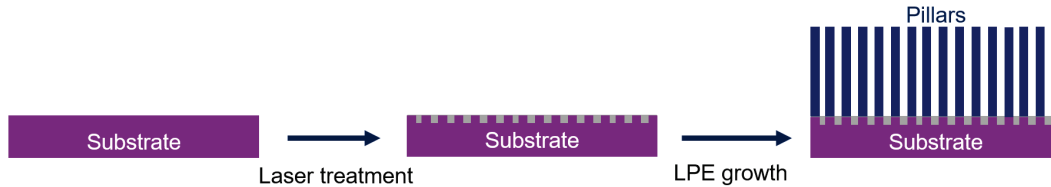


FIGURE 4.2: A schematic showing the simplified idea and concept used in this project to obtain micro-structured samples. In reality, there will be growth of a typical film on the opposite side of the pillars.

The pathway utilized in this project is demonstrated simplified in Figure 4.2, and a schematic of the laser-treated substrates is presented in Figure 4.3. The substrates being objectives for the laser treatments are of the same quality as for conventional LPE growth of single crystalline thin films. These substrates are first treated with a laser that creates trenches vertical and horizontal, leaving squares of $50\ \mu\text{m} \times 50\ \mu\text{m}$ in between them. After growth, these squares will be referred to as pillars. The combination of the horizontal and vertical trenches is referred to as a grid. The laser-treated substrates with several grids are then the subjects for LPE growth. The growth is performed conventionally, but instead of the layer growing homogeneously flat on the substrate, it grows ideally only at the squares and has no or at least very limited growth on the laser-treated trenches. Each of the steps will be described in detail in the following sections.

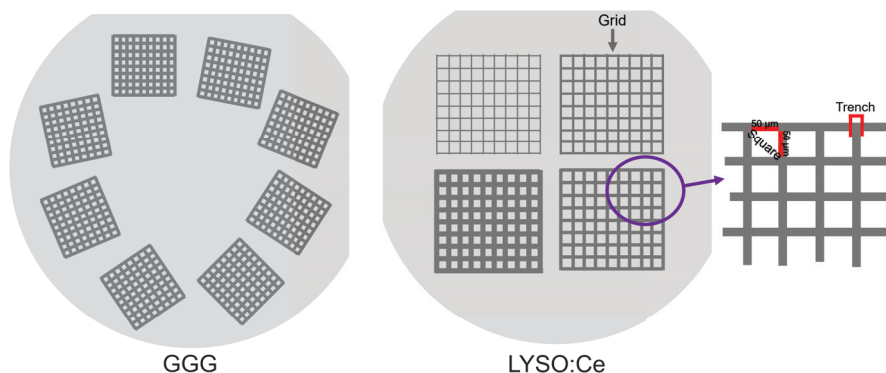


FIGURE 4.3: A schematic of a GGG and LYSO:Ce substrate after laser treatment. For GGG the grids are rotated at eight different orientations, and for LYSO:Ce, the trench size is varied. The schematic also shows what is referred to as a grid, square, and trench.

4.1.1.2 Substrates

Two types of single crystalline substrates were used for the laser micro-patterning and subsequent LPE growth. One is *Cerium doped Lutetium Yttrium Orthosilicate* (LYSO:Ce, $Lu_{1.8}Y_{0.2}SiO_5$):Ce grown by the Czochralski method. Two crystallographic orientations have been used. One is (010), and the other is an unknown orientation. Several attempts have been made to determine the orientation of this substrate by Laue diffraction, but due to its low symmetry (monoclinic), it is challenging to determine. This, unfortunately, also makes it difficult to correlate the growth behavior of the two different orientations. All LYSO:Ce substrates are disks with 1 inch diameter and 0.5 mm thickness. It crystallizes in a monoclinic lattice (space group: $C2/c$) with cell parameters $a = 14.245 \text{ \AA}$, $b = 6.635 \text{ \AA}$, $c = 10.242 \text{ \AA}$, $\beta = 122.188^\circ$. The other type of substrate is undoped *Gadolinium Gallium Garnet* (GGG, $Gd_3Ga_5O_{12}$) also grown by the Czochralski method. Two crystallographic orientations have been used: (100) and (111). The (100) substrates are $10 \text{ mm} \times 10 \text{ mm} \times 0.5 \text{ mm}$, and (111) are disks of 1 inch in diameter and 0.5 mm thickness. GGG crystallizes in a cubic lattice (space group: $Ia\bar{3}d$) with $a = 12.383 \text{ \AA}$.

The laser treatments on the substrates will be summarized in the next section. The section after will encompass the preparation performed of the micro-patterned substrates before the LPE growth as well as some growth parameters. The results and discussion on LSO:Tb and GGG:Eu will be separated into two sections to make a comprehensible overview of these. Finally, a comparison and discussions on the future of the project as well as the possible approaches to optimize the micro-structured samples, is discussed in the last section of this Chapter.

4.2 Laser treatment of substrates

A very important step in growing micro-structured scintillators is the laser treatment performed on the substrates. This treatment was performed at Fraunhofer ILT in close dialog with the person responsible for the project. Before the complete treatment of the grid on the substrates, initial testing was performed to have optimized the lasing parameters for the best outcome. Some parameters tested were: pulse duration, repetition rate, scan speed, pulse energy, line spacing, and the number of repeats. The numerous parameters were studied to avoid the formation of cracks and obtain the most uniform laser treatment. Many more parameters could have been varied and tested, but this was a compromise between the quality of laser treatment, time, and price.

4.2.1 Patterning methods

All the laser patternings were performed with a laser working at the wavelength 1030 nm with the beam focused through an objective giving an approximately $2 \mu\text{m}$ focal spot. Different laser treatments were tested to find which is better to grow structured scintillators by LPE. Here, a brief summary of the initial tests conducted on LYSO:Ce substrates will be provided.

Modification: This laser treatment results in the material are not removed but only modified. What the modification results in from a structural point of view have been investigated further by Raman and XRD and will be described in the following section. Back-side modification was initially tested and as the names suggest, the focus of the laser would be from the back side of the substrate, modifying volume under the substrate surface.

Ablation: This type of laser treatment results in the removal of material. This creates a difference in height from the bottom of the trench to the squares already before LPE growth. Ablation was tested as both front and back-side. With the back-side ablation cracks and some in-homogeneity in the ablation profile was found. Since the back-side ablation is also more complex, front-side ablation was preferred.

Trench width [μm]	Initial trench depth [μm]
5	2-3
10	7-12
25	20-23
50	22-32

TABLE 4.1: Estimated depth range for A-LYSO samples from measurements of the profiles.

LYSO:Ce was initially tested with three methods, and the most promising methods were the back-side modification and front-side ablation. These were then used for the final treatment of the LYSO:Ce substrates. Different trench widths (5, 10, 25, 50 μm) were made to study this effect on the micro-structured growth when performing the

LPE. For the ablated substrates, the depth of the trenches has been estimated from their profile, and the estimated depth range is displayed in Table 4.1.

For the GGG substrates, only front-side modification was tested and optimized. For the final laser treatments, the trench width was constantly $15\ \mu\text{m}$, but different grid orientations were made as depicted in Figure 4.3. This is to investigate if the grid orientation in relation to the orientation of the atomic structures impacts the growth and especially the morphology of the micro-structure.

Patterning type	Trench width [μm]	Substrate type	Substrate orientation	Number of grid orientations
A	5, 10, 25, 50	LYSO:Ce	???	1
M	5, 10, 25, 50	LYSO:Ce	010	1
M	15	GGG	111	8
M	15	GGG	100	8

TABLE 4.2: Overview of laser-treated substrates. A: ablated, M: modified. All square sizes are $50\ \mu\text{m} \times 50\ \mu\text{m}$.

4.2.1.1 Sample reference names

The following reference names are applied in this chapter to deviate between the samples in this study easily. An A (ablation) or M (modification) will be used as a prefix to the substrate type to indicate when a substrate has been laser-patterned. The orientation of the substrate is added as a suffix if it is relevant to the discussion, for example, M-LYSO:Ce-010. Referring to a sample after growth could be as follows: $10\ \mu\text{m}$ LSO:Tb/M- $10\ \mu\text{m}$ -LYSO:Ce. First, stating the estimated thickness and the film type, "/" is used as "on", then the type of laser treatment, followed by the trench width and the substrate type. A normal film is referred to as $10\ \mu\text{m}$ LSO:Tb/LYSO:Ce-010. The same reference system is used for GGG:Eu on GGG. An overview of the final treatments of the different substrates is summarized in Table 4.2.

4.2.2 Structural changes

The ablation results in material removal, whereas modification changes the atomic structure of the material locally. The atomic structure was therefore studied to better understand the material before initiating the LPE growth.

4.2.2.1 Raman mapping

Raman mapping was performed on a M-LYSO:Ce-010 substrate. Spectra were collected spatially by exciting point by point on a defined substrate area. Information from each Raman spectrum has been extracted. This allowed for the study of variations between the modified and non-modified parts. The most intense Raman peak of LYSO:Ce, at $914\ \text{cm}^{-1}$, has been used to extract information. In Figure 4.4 is the mappings showing first a micrograph of the investigated area, then the information extracted from the investigated Raman peak: the intensity, the FWHM, and the peak

position. The intensity of the modified trenches has been reduced, indicating a certain loss of crystallinity caused by the laser modification. The FWHM has been broadened, indicating more defects or a disordered structure. The peak position reveals a slight blue shift of the Raman peak, indicating material modification.

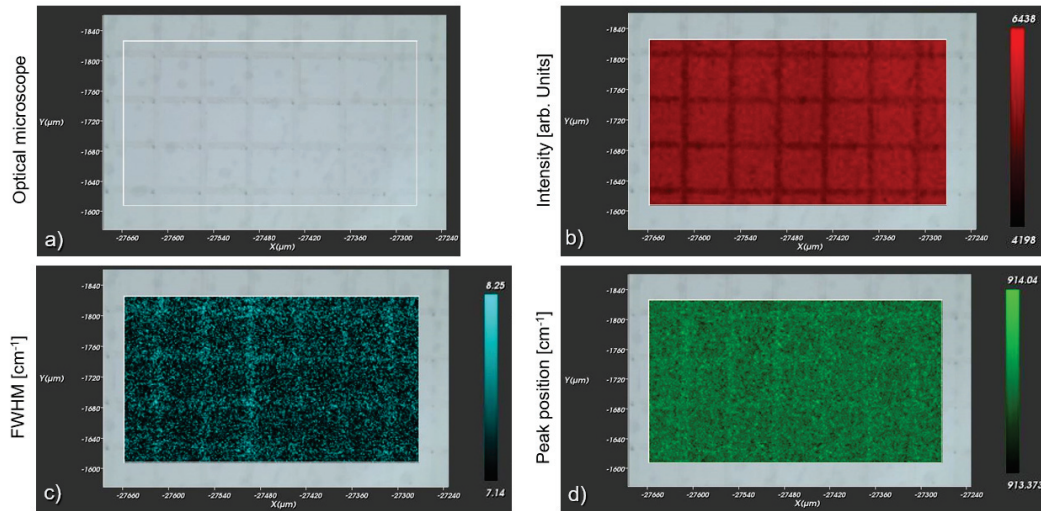


FIGURE 4.4: For a M-LYSO:Ce substrate: a) Optical micrograph. Raman mapping with the most intense Raman peak at 914 cm^{-1} monitored for mapping its b) intensity, c) FWHM, and d) peak position. Objective: 20x. Excitation wavelength: 514 nm.

Indeed, it can be concluded that the laser modification has altered the local atomic structure. It seems especially to have degraded the crystallinity. This is an encouraging result since a reduced crystallinity of the structure in the trenches could diminish the epitaxial growth by LPE here and facilitate the growth of pillars.

4.2.2.2 X-ray diffraction

XRD was performed on the modified substrates to gather more information on the atomic structure, here the long-range order. It is not possible to probe just the trench or a single square with the diffractometer used for these measurements since the beam size cannot be reduced sufficiently. It can be reduced to a grid size (a few millimeters), thereby maximizing the modified contribution to the outcome. Nevertheless, the diffractograms will inevitably be mixed contributions from modified and non-modified materials. It was discussed in Section 3.3.3 that when performing symmetrical 2θ - ω scans on epitaxially grown samples, only information from the planes parallel to the surface is collected. This is also valid for these samples.

There will not be presented results from XRD on M-LYSO:Ce-??? since its unknown orientation does not give rise to any diffraction peaks when performing symmetric 2θ - ω scans. This suggests that the substrate was cut randomly, and the surface does not correspond to a specific crystalline plane or at least a plane that does not give rise to any diffraction peaks.

M-LYSO:Ce-010: Figure 4.5a-c compares the (060) diffraction peak from non-modified and modified substrate areas. The intensity is reduced considerably for the modified area, and the peak has gained additional broadness. This agrees well with the results from Raman scattering, concluding the modification of the substrate leads to reduced crystallinity and induced strain due to the laser treatment. When performing the laser treatment, a heat load will naturally be imposed on the substrate, which can result in strain formation and local structural changes.

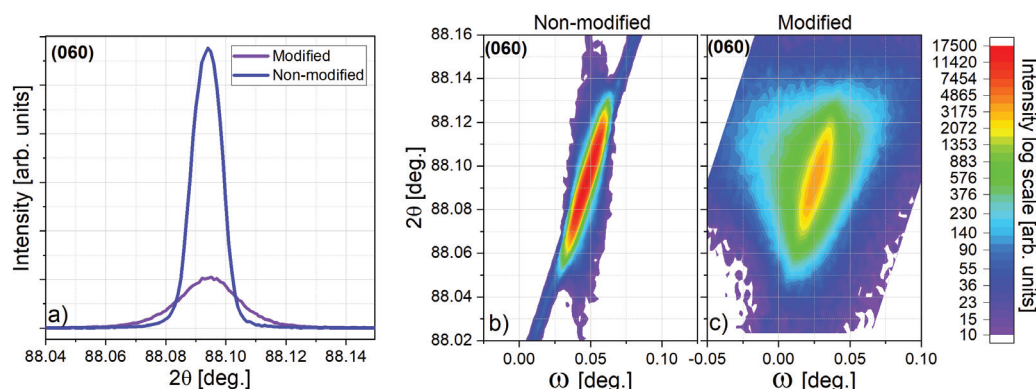


FIGURE 4.5: XRD investigations of (060) peak for M-LYSO:Ce substrate comparing modified and non-modified areas. a) 2θ - ω scans. b-c) Reciprocal space mapping. The elongated shape of the peak originates from the shape of the X-ray beam. $\lambda = 1.5406 \text{ \AA}$ (Copper $K_{\alpha 1}$).

M-GGG: The XRD investigations on these modified samples show a different feature than for M-LYSO:Ce. Indeed there is a broadening of the diffraction peaks after modification, but it seems the laser modification provokes a second peak at slightly lower angles (larger lattice parameter). This is seen for both M-GGG-100 (Figure 4.6b) and M-GGG-111 (Figure 4.7). For the measurement of M-GGG-111, the size of the beam was carefully limited to the area of modification and centered on this to make sure to have as much modified area and as little non-modified area probed by X-rays as possible. Here, the "modified peak" has a maximum intensity as high as the normal (888) peak. It can therefore be concluded, as for the M-LYSO:Ce, that the modification reduces the crystallinity of the GGG substrates.

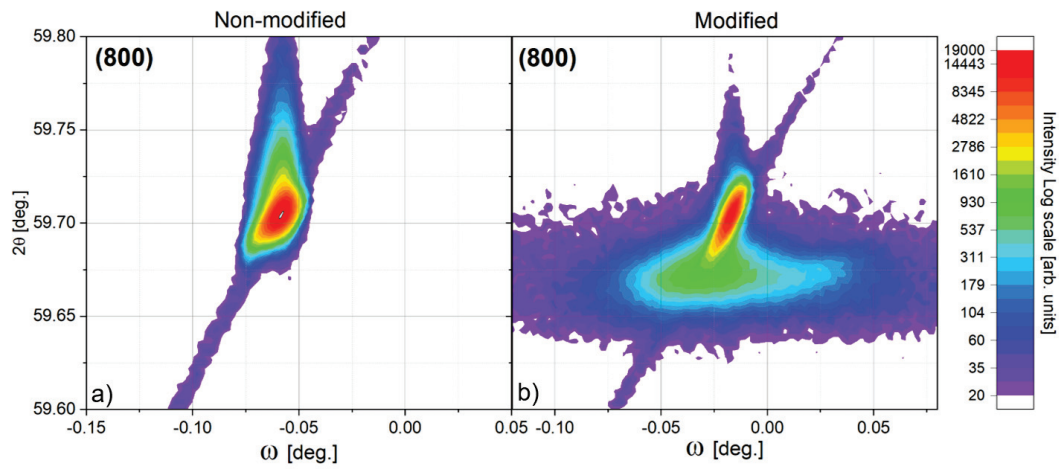


FIGURE 4.6: Reciprocal space mapping of (800) peak of M-GGG-100 substrate. a) Non-modified area. b) Modified area. $\lambda = 1.5406 \text{ \AA}$ (Copper $K_{\alpha 1}$).

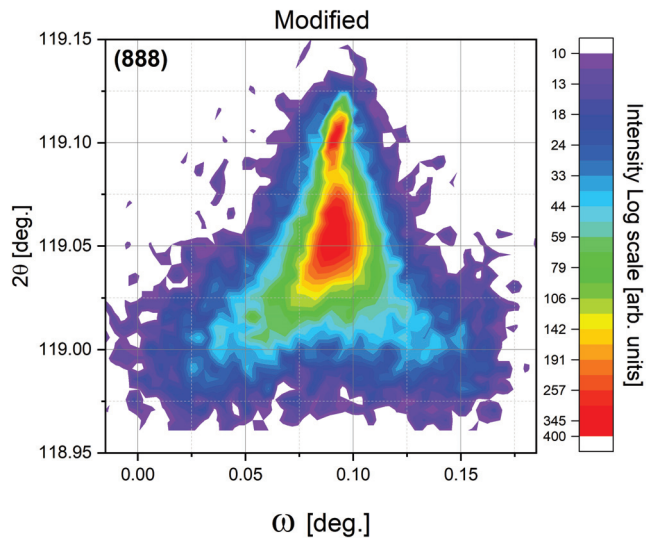


FIGURE 4.7: Reciprocal space mapping of (888) peak of M-GGG-111 substrate limiting the beam size to only the modified area. $\lambda = 1.5406 \text{ \AA}$ (Copper $K_{\alpha 1}$).

4.3 Liquid phase epitaxy on laser-treated substrates

4.3.1 Substrate preparation

Before performing LPE growth, the substrates are prepared differently depending on the laser treatment. This section will briefly present these procedures before describing the LPE growth.

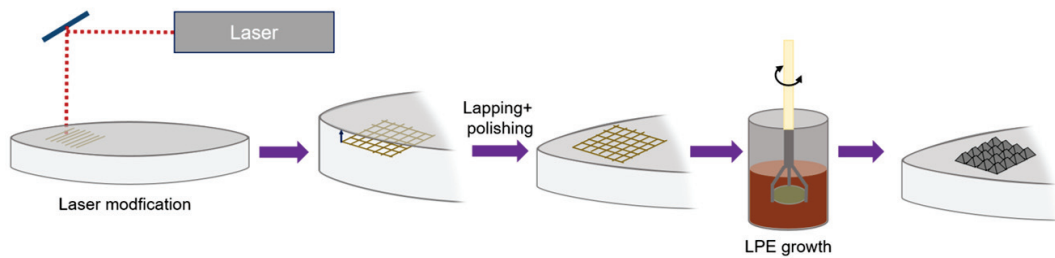


FIGURE 4.8: Concept of the whole process from the laser treatment to the growth on modified samples. The lapping and polishing step is unnecessary for the ablated substrates since the ablation is already at the surface.

Lapping and polishing: The modified material resulting from the laser modification process was located 15-25 μm below the substrate surface. The modified substrates were therefore mecano-chemically lapped and then polished to have the modified patterning at the surface. This procedure is illustrated in Figure 4.8. Since the depth of the modified material is only a few microns, it was necessary to proceed carefully while polishing not to remove the modified volume. Unfortunately, it was impossible for most samples to reveal all of the modifications simultaneously at the surface. In areas of $500\ \mu\text{m} \times 500\ \mu\text{m}$, part of the modification was removed before the rest was fully revealed, as displayed in Figure 4.9a. This was provoked by a slight tilt between the two coordinate systems of the sample translation and laser movement. The laser-treated an area of $500\ \mu\text{m} \times 500\ \mu\text{m}$ at a time, and then the sample was translated for the next area. This is also seen as slight overlaps in the modification, displayed in Figure 4.9b. The ablated substrates were not lapped and polished since the ablation was at the surface.

Annealing: During the first attempted growth, the substrate (A-LYSO:Ce) broke into two pieces while being transferred into the furnace. This is most likely due to when the sample is heated by being transferred into the furnace, cracks appeared caused by the strain formed in the substrate during the laser treatment. In the worst case the cracks make the substrate break. More minor cracks were observed before growth on some of the laser-treated samples, see for example, Figure 4.9c, and for some laser-treated substrates, the cracks were observed to evolve considerably after annealing procedures (see Figure 4.10). To avoid more substrates breaking and releasing any strain caused by the laser treatment, annealing was performed on the remaining samples. They were annealed 8 hours at $1100\ ^\circ\text{C}$ in an air muffle furnace with very slow heating and cooling rates. Some samples would be annealed several

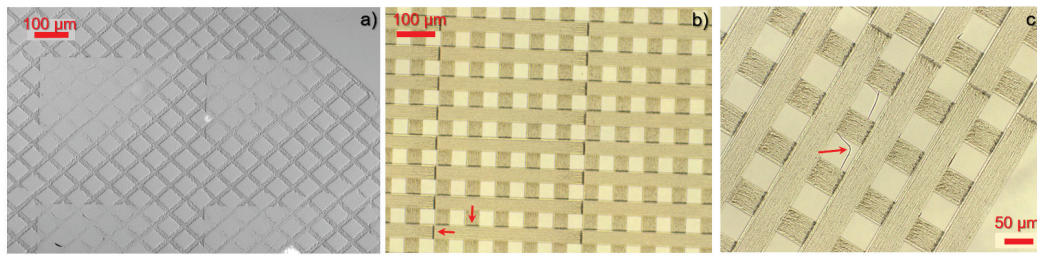


FIGURE 4.9: a) Tilt of $500 \times 500 \mu\text{m}$ during laser treatment is visible. Image using the optical microscope in CDIC configuration for an M-GGG-100 substrate with $15 \mu\text{m}$ trench width. b) M- $50 \mu\text{m}$ -LYSO:Ce. Arrows indicate positions of modification overlap. c) M- $50 \mu\text{m}$ -LYSO:Ce. Arrow indicates a crack. M-LYSO:Ce after lapping/polishing to reach modified volume. Micrographs were obtained with an optical microscope transmission configuration for b and c).

times to release any strain in between other actions, like polishing, to ensure the samples would be ready for the LPE growth.

Cleaning: The A-LYSO:Ce substrates were, after annealing, cleaned thoroughly in an ultrasonic bath since some residuals from the laser patterning could remain in the trenches. The samples were placed in a holder inside an isopropanol bath and dipped in an ultrasonic cleaner until the trenches appeared empty when inspected with an optical microscope. This approach was also used in between growths for samples where the trenches could have residues of flux captured in them.

Before the LPE growth, all the substrates were thoroughly cleaned with alternate baths of isopropanol and de-ionized water in an ultrasonic bath to ensure a clean surface. Since a dirty surface can result in spurious growth during the LPE growth procedure this step is essential.

For the M-GGG, there were severe crack formations in the modified areas already after the laser treatment. It seemed to depend partially on the grid orientation since some orientations had a higher crack density than others. These cracks would extend further and evolve as the substrates were cleaned and annealed. However, they are mostly at the surface since, after lapping and polishing, most of the cracks were removed. See micrographs of a single grid after each step of cleaning or annealing in Figure 4.10.

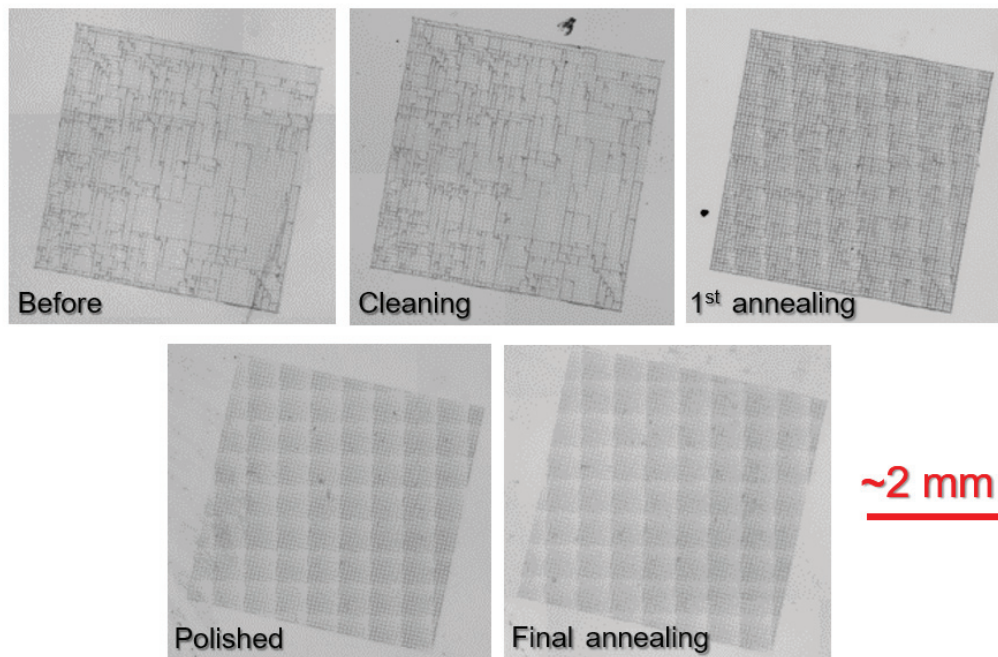


FIGURE 4.10: Micrographs of a M-GGG-111 substrate before and after cleaning, annealing, and polishing treatments to follow the crack formations. The optical microscope is operated in reflection configuration, and the micrographs were stitched together to include the whole grid.

4.3.2 Growth

The LPE solution was prepared as described in Chapter 1, and the standard $\text{PbO-B}_2\text{O}_3$ solvent was used since this is the one typically used for the growth of LSO:Tb on YbSO [62] and GGG:Eu on GGG [114]. The nominal doping level in these melts was 5% europium for GGG:Eu and 15% terbium for LSO:Tb . Note that the doping level here is indicated as the nominal content in the solution and not the actual doping level in the grown samples.

The LSO:Tb micro-structures were grown in the temperature range 1015-1045 °C with growth rates 0.17-2.16 $\mu\text{m}/\text{mn}$ leading to estimated thicknesses in the range 10-25 μm . The GGG:Eu micro-structures were grown in the temperature range 1024-1028 °C with growth rates in the range of 0.9-2 $\mu\text{m}/\text{mn}$ leading to layer thicknesses in the range 8-75 μm . However, the thicknesses are most likely underestimated since less material grew in the trenches, and the calculations assume a SCF. In general, the thicknesses indicated for the samples will be the estimated weight and not the actual one unless otherwise stated.

It is worth mentioning here that a substrate is typically only dipped in the solution once. However, for studying the growth as a function of sample thickness, the substrates for this project were dipped several times and investigated in between to extract as much information as possible.

4.4 Micro-structured LSO:Tb

This section aims to present and discuss the results found on the LSO:Tb micro-structured samples. The morphology of these samples is a crucial topic of investigation and will be presented first. The investigation performed to understand the structure and structural differences will then be presented and discussed. Finally, the luminescent properties, especially the scintillation, will be evaluated.

4.4.1 Sample morphology

LPE growth of LSO:Tb/A-LYSO:Ce and LSO:Tb/M-LYSO:Ce resulted in micro-structuration. Overviews of two such samples are presented in Figure 4.11. Here is a general homogeneity of the micro-structured growth revealed. For the LSO:Tb/M-LYSO:Ce sample (Figure 4.11b), some inhomogeneity is visible that will be discussed further below.

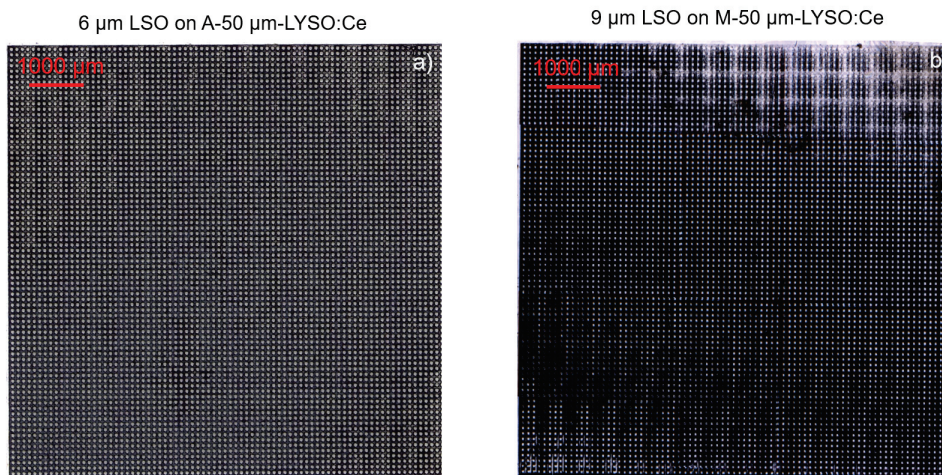


FIGURE 4.11: Overview of LSO:Tb grown on a) A-LYSO:Ce and b) M-LYSO:Ce. Micrographs are obtained with an optical microscope.

Studying the samples closer (Figure 4.12 and 4.13) reveals the morphology of the pillars was evolving differently for the two types of laser-treated substrates, especially with increasing thickness. This could be due to the difference in laser treatment (ablated or modified) or the crystallographic orientation of the surface. Since LYSO:Ce has a monoclinic structure, the difference in morphology can most likely be ascribed to the orientations that most likely favor different growth directions related to crystalline planes.

LSO:Tb/M-LYSO:Ce: The pillars grew towards a pyramidal shape and got more elongated in one direction as the thickness increased. For 10 µm LSO:Tb/M-LYSO:Ce-010, the initial square shape of the pillars was still maintained as seen in Figure 4.12a, but after another growth reaching 24 µm thickness, the pillars were going towards a

more pyramidal shape as seen in Figure 4.12b. Figure 4.12d-e shows 3D reconstructions of a $12\ \mu\text{m}$ LSO:Tb/M- $25\ \mu\text{m}$ -LYSO:Ce, revealing this pyramidal-like shape as well as some texture in the trench. Here a peculiar feature is also visible. Namely, a small valley at the top plateau. This was found for some of the samples, especially as they were grown thicker. The origin of this is unclear. It seems the pillars continued to evolve in this pyramidal shape with increasing thickness, and in some cases, the top would eventually be a point or a thin line, as in Figure 4.12c. The evolution of the pillar shape with thickness is comparable regardless of the trench width, and a thorough study of this is therefore not presented here. However, samples with larger trench widths generally appeared to have more growth in the trench, as seen in Figure 4.12f-h. This is ascribed to a more inefficient modification of the larger trench than the more narrow trenches and the increased probability of flux flowing well in the trench during growth. This would favor growth within the trench more than if the trench is narrow and the flux barely flows in the trench.

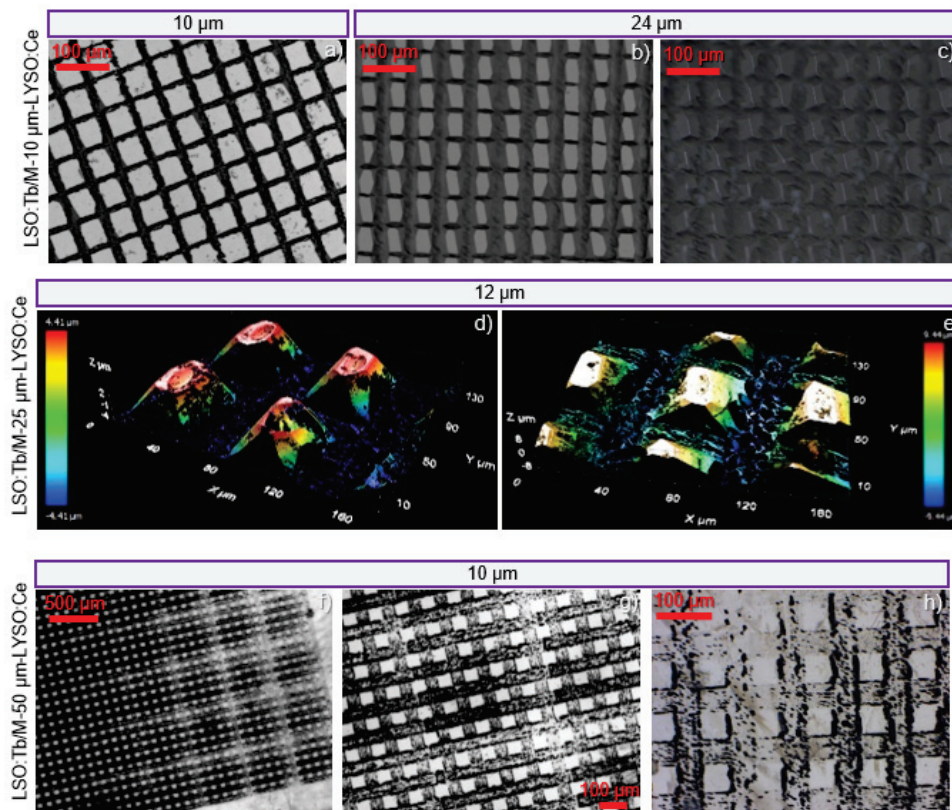


FIGURE 4.12: Micro-structured LSO:Tb grown on M-LYSO:Ce. a-c) and f-h) Micrographs from an optical microscope operated in reflection configuration. d-e) 3D reconstructions using a confocal microscope. The thickness of the samples is stated above each image, and other information is indicated on the left side of the row.

Since this is the first test, optimizing the laser processing can most likely overcome some of the above-mentioned issues. For example, by repeating the lines or making the line spacing smaller for the laser processing.

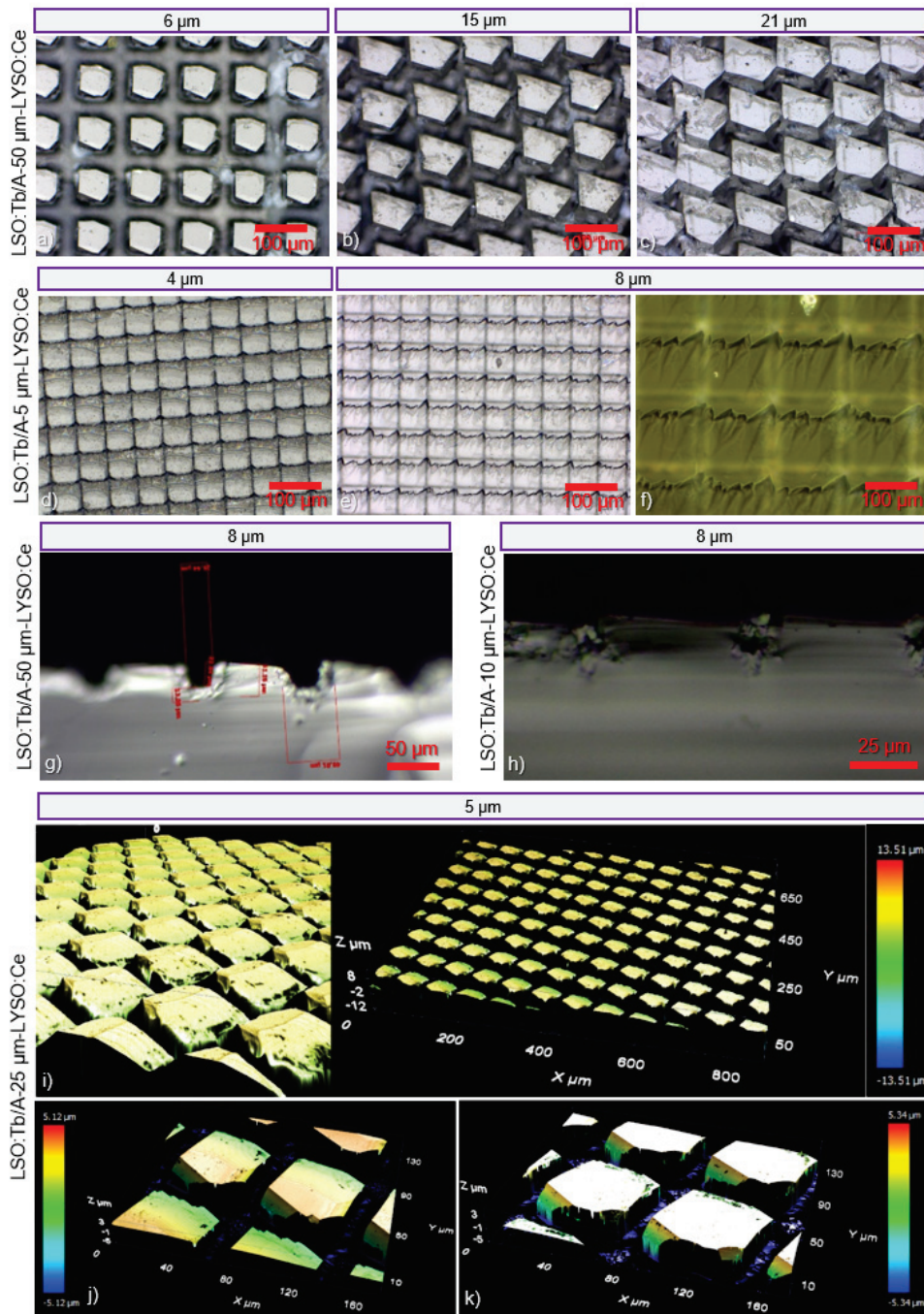


FIGURE 4.13: Micro-structured LSO:Tb/A-LYSO:Ce. a-h) Micrographs from an optical microscope, operated in reflection configuration for all except f), which is CDIC. i-k) 3D reconstructions using a confocal microscope. The thickness of the samples is stated above each image, and other information is indicated on the left side of the row.

LSO:Tb/A-LYSO:Ce: For these samples, the growth and morphology of the pillars depended on the trench size. The morphology of the pillars grown on larger trench size (25 and 50 μm) A-LYSO:Ce was going toward a trapezoidal-like shape as shown in Figure 4.13a-c. They also expanded laterally and therefore started to overlap as they

grew taller. For the pillars grown on smaller trench size (5 and 10 μm) A-LYSO:Ce, the overlap occurred when they were a few microns thin, as visible in Figure 4.13d-f. The lateral expansion was favored more in one direction, resulting in the pillars merging and overlapping in this direction. In Figure 4.13f, the position of the laser-ablated trench appears brighter, and from this, it is seen the border of the growth is shifted in comparison. There is not any separation between the pillars, and the growth seems to have been more like an overgrowth than pillar growth.

The cross-section of an 8 μm LSO:Tb/A-50 μm -LYSO:Ce is presented in Figure 4.13g. The ablated substrates already had a depth, meaning a height difference before growth. By studying the cross-section, it is visible that there was a rough textured layer growing in the trench, both at the bottom and up the sides of the pillar. This layer is evaluated at this micrograph as being around 13 μm thick, which is thicker than the estimated height from the weight gain (8 μm). The depth of pillar-top to trench-bottom has been measured to be around 23 μm , and therefore it seems this layer in the trench was growing as fast or faster than the layer on the pillars.

	Initial [μm]	Growth1 [μm]	Growth2 [μm]	Growth3 [μm]	After treatments [μm]
LSO:Tb/A-50 μm -LYSO:Ce	0 / 23	6 / 25	15 / 22	21 / 22	21 / 30
LSO:Tb/M-10 μm -LYSO:Ce	0 / 0	10 / 16	24 / 24	-	-

TABLE 4.3: Comparing the estimated *height* calculated from the weight gain after growth with the *depth* estimated with the microscope: height / depth.

The effective height difference has been investigated further for a LSO:Tb/A-50 μm -LYSO:Ce and LSO:Tb/M-10 μm -LYSO:Ce sample by evaluation with an optical microscope. The difference was estimated by observing the micro-structured sample from the top, first focusing on the pillar top and then on the bottom of the trench. This difference is estimated to be the depth. These observations are presented in Table 4.3 by comparing the height: estimated from the weight gain after a growth, with the depth: estimated using the focus of the microscope. The depth indicated here is the difference between the highest and the deepest point in focus of the pillar and the trench, respectively. For the LSO:Tb/A-50 μm -LYSO:Ce continued growth did not increase the depth. Whereas for LSO:Tb/M-10 μm -LYSO:Ce, it did increase. Considering that the ablation laser treatment is not altering the structure but merely removing material in the trenches, this must not be enough to hinder the growth there. It could maybe even give rise to faster growth due to its roughness. Based on these investigations, it has been concluded that the LPE growth on A-LYSO:Ce seems only to have reduced the aspect ratio of the pillars. The pillars did not grow faster than the material growing in the trench, where in some cases, it seems like the trench did grow faster, which is definitely not optimal for growing high aspect ratio micro-structured scintillators.

Etching

Since material was growing in the trenches of both types of laser-treated substrates, which is not favorable for this project, initial tests of removing it were performed. As indicated in Table 4.3 it was successful since the depth was enlarged.

It was found that a combination of heated nitric acid followed by hours in an ultrasonic bath was the most effective method. Diluted nitric acid also worked but took much longer time. First, the heated and stirred nitric acid would partly dissolve the trench material, which could then be removed by placing the sample with the micro-structure downward for hours in an ultrasonic bath. Overviews of a 21 μm LSO on A-50 μm -LYSO:Ce before and after the described treatment are presented in Figure 4.14a and b, respectively. The additional material deposited in the trench was removed, but the shape of the pillar was also modified. However, in this case, the pillar still had an enlarged height compared to the initial depth of the trench after ablation. Some residues of the material are visible in the lower right corner of Figure 4.14b. This could be removed by dipping it in the ultrasonic bath longer. A downside to this procedure is its harshness. The pillars inevitably suffered some damage, and it seems the growth on top of the pillars in some cases was partly removed as well during the treatments. A single test using hydrofluoric acid resulted in a significantly damaged pillar surface, and since it is a harsh treatment, this was not investigated further.

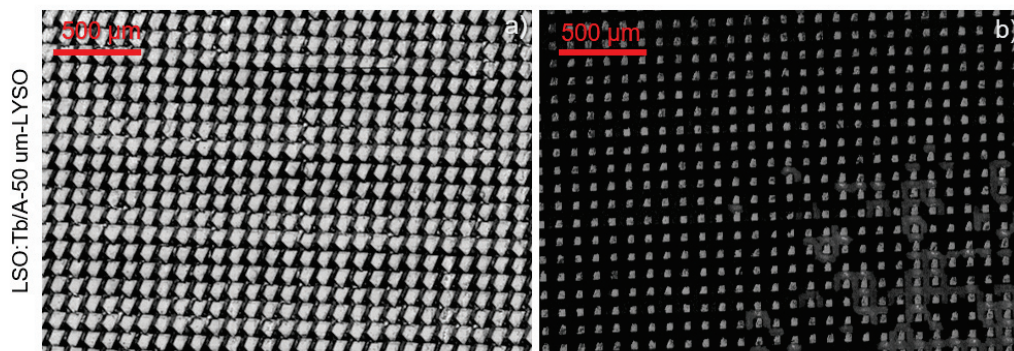


FIGURE 4.14: Before a) and after b) etching treatment of 21 μm LSO:Tb/A-50 μm -LYSO:Ce.

These tests were only performed on samples grown on A-LYSO:Ce, and further optimization is needed to avoid damaging the pillars. However, it is encouraging that this could be a valid procedure to optimize these types of samples.

4.4.2 Structural considerations

It has been shown in section 4.2.2 based on Raman and XRD measurements that the laser modification slightly altered the atomic structure of the substrates. In this section, the structure of the grown samples will be evaluated.

4.4.2.1 X-ray diffraction

XRD was performed to extract information on the long-range crystalline structure and especially to verify the pillars were growing in the same structure as the normal LPE-grown LSO:Tb films.

LSO:Tb/M-LYSO:Ce-010: In general, when performing 2θ - ω scans on the LSO:Tb/M-LYSO:Ce-010 samples, only diffraction peaks are present from the (0k0) planes. An example of this is presented in Figure 4.15a, where the sample is compared to a calculated reference with preferred orientation for (010), a M-LYSO:Ce-010 substrate, and a typical LSO:Tb/LYSO:Ce-010 sample. They all show matching with the calculated reference. This confirms LSO:Tb grows epitaxially from the M-LYSO:Ce-010 surface. From Figure 4.15b, it is seen the (020) peak position is the same for LSO:Tb grown on LYSO:Ce and M-LYSO:Ce, and therefore also the unit cell b-parameter is the same. This indicates that the normal and structured films grew similarly, with comparable terbium incorporation. However, the peaks corresponding to the structured film are slightly broader, indicating a distribution of the lattice b-parameter. Since the signal from the pillars and trenches cannot be distinguished, it cannot from this alone be concluded if it is from one or the other. The rocking curve (ω -scan) is also broader for the micro-structured part of the sample, as seen in Figure 4.15c. This suggests that there is strain present in the films, and the substrate and film are not perfectly parallel. Comparing the (020) peak arising from LSO:Tb and the M-LYSO:Ce-010 substrate, there is a difference in peak position, corresponding to a lattice mismatch of approximately -0.18%, meaning the micro-structured LSO:Tb lattice is larger than the lattice of LYSO:Ce. This is similar to the normal LSO:Tb/LYSO:Ce-010.

The lattice mismatch was first displayed in Section 1.3.3 calculated according to the a-parameter. For these samples, the lattice mismatch is calculated in relation to the b-parameter instead since it is related to the surface planes (0k0):

$$Mismatch = \frac{b_{film} - b_{sub}}{b_{sub}} \cdot 100\% \quad (4.1)$$

Since the substrate and film were growing in a monoclinic structure, the unit cell parameters are dissimilar, $a \neq b \neq c$ and $\alpha = \gamma = 90^\circ \neq \beta$. The lattice spacing, d, is therefore calculated for this type of lattice as follows:

$$\frac{1}{d_{hkl}^2} = \frac{h^2}{a^2 \cdot \sin^2\beta} + \frac{k^2}{b^2} + \frac{l^2}{c^2 \cdot \sin^2\beta} + \frac{2 \cdot h \cdot l \cdot \cos\beta}{a \cdot c \cdot \sin^2\beta} \quad (4.2)$$

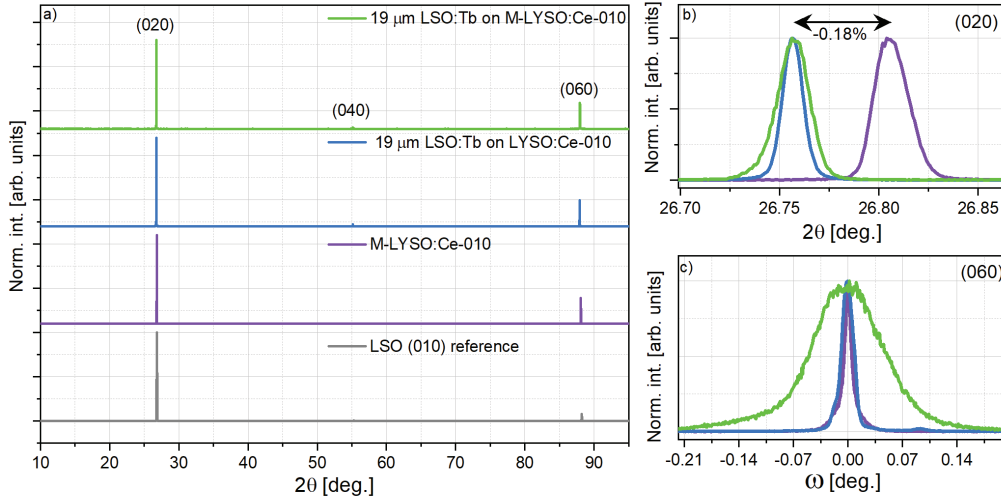


FIGURE 4.15: Results from XRD measurements on LYSO:Ce-010 samples. a) $2\theta - \omega$ specular scans on LSO:Tb/M-LYSO:Ce-010, LSO:Tb/LYSO:Ce-010, M-LYSO:Ce-010, and a calculated LSO reference with preferred orientation for (010). b) $2\theta - \omega$ scans around the (020) peak for the samples in a) except the calculated reference. c) ω scan (rocking curve) around (060) peaks. $\text{FWHM}(\text{LSO:Tb/M-LYSO:Ce})=0.09995^\circ$, $\text{FWHM}(\text{LSO:Tb/LYSO:Ce})=0.01803^\circ$ and $\text{FWHM}(\text{M-LYSO:Ce})=0.01418^\circ$. $\lambda = 1.5406 \text{ \AA}$ (Copper $K_{\alpha 1}$).

However, for the specular scans, only the out-of-plane component is considered, which are the (0k0) planes for these samples. This simplifies the relation above since $h=l=0$ and makes it possible to extract the b-parameter from these scans by combination with Bragg's law:

$$b = (k^2 \cdot d^2)^{1/2} = \left(k^2 \cdot \left(\frac{\lambda}{2 \cdot \sin\theta} \right)^2 \right)^{1/2} \quad (4.3)$$

b-parameters and the resulting lattice mismatch for a LSO:Tb/M-LYSO:Ce-010 and LSO:Tb/LYSO:Ce-010 are presented in Table 4.4. It is worth mentioning the b-parameters of the substrates were extracted from XRD measurements before growth since the layers are too thick to have a contribution from the substrate. The (060) peak position of LYSO:Ce and M-LYSO:Ce was found to be identical in section 4.2.2 and is therefore assumed here to have the same b-parameter.

	$b_{\text{LSO:Tb}}$	$b_{\text{LYSO:Ce}}$	Lattice mismatch
19 μm LSO:Tb/M-LYSO:Ce	6.658 Å	6.647 Å	0.18%
19 μm LSO:Tb/LYSO:Ce	6.658 Å	6.647 Å	0.18%

TABLE 4.4: Lattice b-parameter of a LSO:Tb/M-LYSO:Ce compared to a normal LSO:Tb/LYSO:Ce sample. The substrate b-parameter is extracted from XRD measurements before growth.

4.4.2.2 Raman spectroscopy

Excitation was performed individually on a pillar, trench, and non-patterned film (referred to as "film"), and their local structures can this way be compared. See the recorded spectra in Figure 4.16.

LSO:Tb/M-LYSO:Ce: The Raman spectra of the pillar and film have the same features indicating the local structures are very similar. The trench spectrum also has similar features, but several other peaks are present, some of which are indicated with arrows in Figure 4.16b. This is ascribed to the trench growing more randomly, meaning various orientations are present. This is visible in Figure 4.12, where the trench appears less ordered than the pillars. Since the structure is anisotropic, different Raman modes are active depending on the orientation. However, this structural disturbance is not observed in the XRD investigations. This indicates the long-range order is not disturbed or that the contribution from this is too small to detect with XRD and thereby hidden in the background of the diffractograms. The intensity of the peaks is relatively similar for the pillar and the trenches, but the intensity is lower for some of the Raman peaks for the trench, indicating slightly lower crystallinity. However, the intensity from the pillars is lower than that of the film, indicating that the reduced crystallinity observed with XRD cannot be exclusively ascribed to the contribution from the trench. It seems both the trench and pillars of the LSO:Tb/M-LYSO:Ce are lowered.

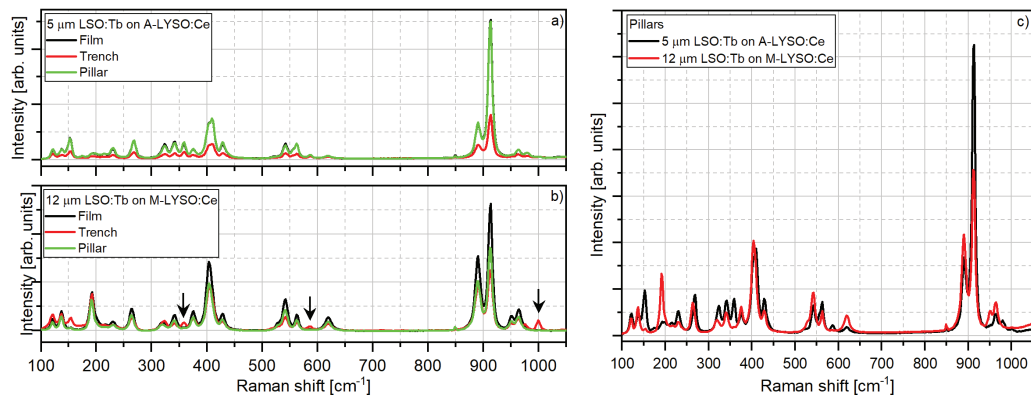


FIGURE 4.16: Raman spectra recorded after the excitation of a pillar, film, and trench. a) LSO:Tb/A-25 μm -LYSO:Ce, $\lambda_{exc} = 457$ nm. b) LSO:Tb/M-25 μm -LYSO:Ce, $\lambda_{exc} = 488$ nm. The arrows indicate additional peaks from the trench that are not present in the two other spectra. c) Comparing the pillar spectra of the two samples from a) and b).

LSO:Tb/A-LYSO:Ce: The Raman spectra of the pillar and film are so similar they are almost completely overlapping, which is why the curve for the film can be challenging to see in Figure 4.16a. All features are similar for the three spectra, indicating the local structures are almost identical. The trench spectrum has the same features as well, with no additional peaks present. Only its intensity is considerably lower, indicating a lower crystallinity.

Comparison: The two spectra from the pillars are compared in Figure 4.16c. They have all the same features but with variations in the intensities of the modes. This indicates some differences in the local environments of the two types of samples. This was expected since they have different orientations. Also, their thickness is dissimilar, and the contribution from the substrates can vary and give rise to these variations as well.

4.4.3 Luminescence

4.4.3.1 Photoluminescence

The photoluminescence spectra were also collected with a micro source, making it possible to excite individually pillar, trench, and film areas to record any variations.

LSO:Tb/A-LYSO:Ce: The spectra for LSO:Tb/M-LYSO:Ce are presented in Figure 4.17a and the spatial mapping of the intensity at 543 nm in Figure 4.17b. From these, the guiding of light appears different than for the LSO:Tb/M-LYSO:Ce. The intensity is highest at the sides of the pillars, and the middle of the trench gives the spectrum with the lowest intensity. The light seems to have been extracted more at the sides of the pillars. This is most likely due to the roughness of the trenches, which then enhance the light extraction.

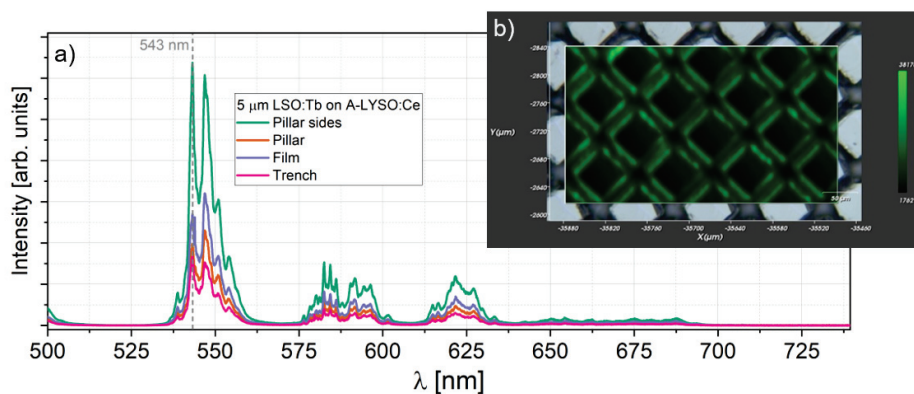


FIGURE 4.17: For a 5 μm LSO:Tb/A-LYSO:Ce sample, a) Photoluminescence spectra with individual excitation of pillar, trench, and film. b) Photoluminescence mapping, where the intensity for the emission peak at 543 nm is spatially plotted. For all spectra, $\lambda_{exc} = 488$ nm.

LSO:Tb/M-LYSO:Ce: For all three spectra (pillar, trench, and film), the features are similar, as seen in Figure 4.18a. This indicates that terbium is incorporated in all three. There are differences in the intensities between the three spectra, with the highest intensity being the pillar spectrum and the least being the trench spectrum. However, this can be provoked by the amount of terbium-activated volume being excited. For the trench, it could be less since its thickness is smaller than for the pillar. Whereas the same is valid for the film part. It can also simply be an effect of the structured nature of the pillars that enhance light extraction. Figure 4.18b-c displays

a spatial mapping of the intensity at 543 nm. It shows that the light generated within the pillars was guided through them and extracted. This supports the argument that the intensity is higher in the pillars due to enhanced light extraction. Since the b-parameter extracted from XRD is the same for a normal LSO:Tb film and the structured film, the terbium incorporated should be similar and, therefore, not affect the photoluminescence intensity.

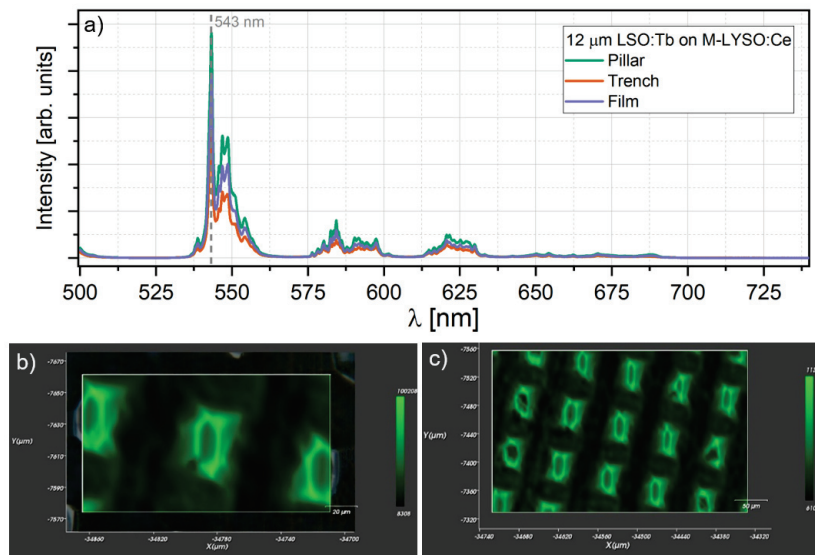


FIGURE 4.18: For a 12 μm LSO:Tb/M-25 μm -LYSO:Ce sample, a) Photoluminescence spectra recorded by excitation of pillar, trench, and film. b-c) Photoluminescence mapping, where the intensity for the emission peak at 543 nm is spatially revealed, using an $\times 50$ objective and $\times 20$ objective, respectively. For all spectra, $\lambda_{exc} = 488$ nm.

4.4.3.2 Radioluminescence

The radioluminescence was not collected using a micro-source as the excitation source. Instead, an area of approximately 2 mm \times 2 mm was excited with X-rays. It was made sure the excited parts were a micro-structured area. The spectra are presented for selected samples in Figure 4.19. Note the intensities of the spectra have been normalized. The LYSO:Ce substrate gives rise to a broad emission band centered at approximately 420 nm due to Ce^{3+} transitions. Due to the limited thickness of the films and the broad X-ray emission spectrum used, a part of the X-ray beam is absorbed within the LYSO:Ce substrate, giving rise to this emission. In Figure 4.19 on the left side is a micrograph of the cross-section of an 8 μm LSO:Tb/A-50 μm -LYSO:Ce sample that is excited with a UV lamp. Here, it is clear that the substrate emits blue light while the pillars emit green.

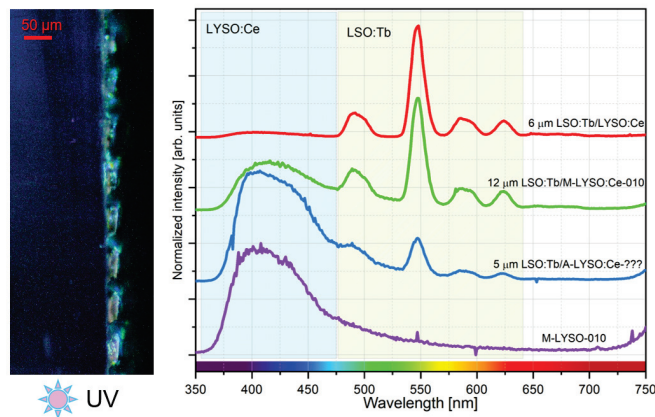


FIGURE 4.19: Radioluminescence spectra of relevant samples. The sample references are indicated above each curve. For all spectra, excitation was performed using a molybdenum X-ray tube. On the left is a micrograph of the cross-section of $8 \mu\text{m}$ LSO:Tb/A- $50 \mu\text{m}$ -LYSO:Ce excited by a UV lamp.

4.4.3.3 Comparison

Comparing the photoluminescence and radioluminescence spectra of $12 \mu\text{m}$ LSO:Tb/M-LYSO:Ce in Figure 4.20, similar features are observed. Consistently with Tb^{3+} emission the bands characteristic for the ${}^5\text{D}_4$ to ${}^7\text{F}_j$ ($j=6,5,4,3$) transitions are present as indicated in the figure.

It is worth mentioning that the emission from the LYSO:Ce substrate can be reduced by using an optical filter when performing imaging experiments. Choosing a fitting optical filter makes it possible to remove the part of the spectrum corresponding to the emission from the substrate. This is a viable option since the emission from the substrate and the film are not overlapping.

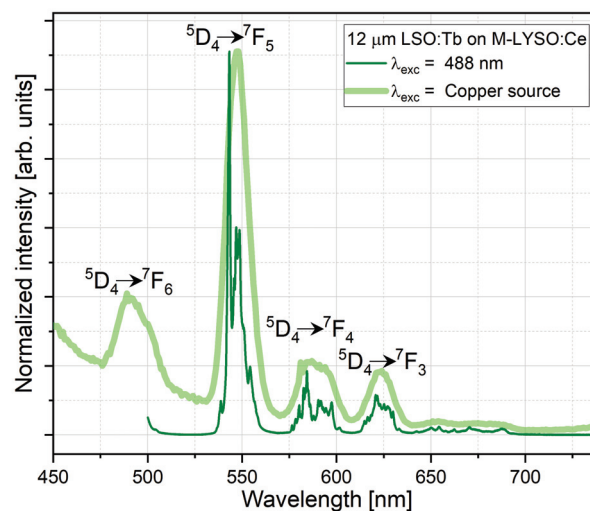


FIGURE 4.20: Comparison of the normalized radioluminescence and photoluminescence of a $12 \mu\text{m}$ LSO:Tb/M-LYSO:Ce. Excitation wavelengths are stated in the legend.

4.4.3.4 Color camera

As already discussed above, the LYSO:Ce substrates scintillate blue. This is seen in Figure 4.21 as well, where a color camera was used in reflection geometry. The thinnest samples visibly emit blue light, whereas the thickest seem only to emit green light. LSO:Tb with a thickness of approximately $24\ \mu\text{m}$ absorbs around 89% of the X-rays when using a copper source, whereas $5\ \mu\text{m}$ LSO:Tb will only absorb around 36% (calculated from NIST data [71]). The remaining X-rays will excite the substrate, enhancing the blue light emission. It is also visible that the area on the samples with structured growth emits more light, as well as the edges and scratches or similar features on the samples.

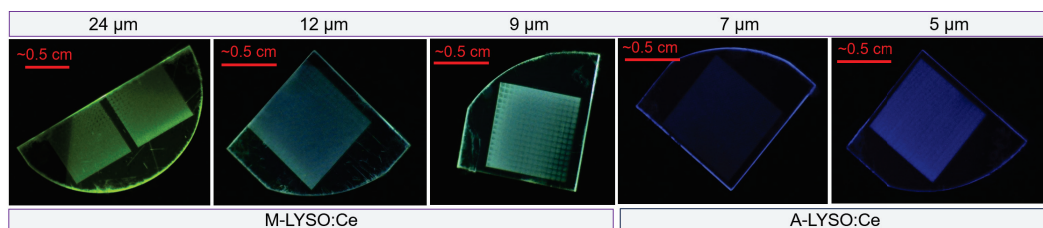


FIGURE 4.21: LSO:Tb/M-LYSO:Ce or A-LYSO:Ce excited by X-rays (copper source). The estimated thickness of the LSO:Tb is noted above each image, and the type of laser-treated LYSO:Ce under.

4.5 Micro-structured GGG:Eu

The purpose of this section is to present and discuss the findings for the GGG:Eu micro-structured samples. The structure of the chapter will be similar to the one on the microstructured LSO:Tb, including the morphology of the structuration, structural investigations, and finally, the luminescent properties.

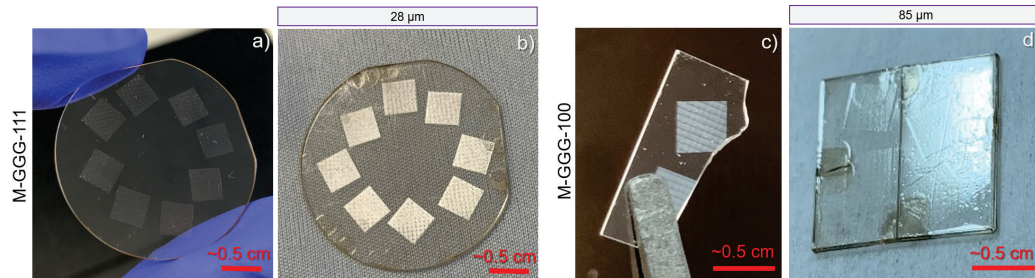


FIGURE 4.22: Pictures of M-GGG before and after growth, the estimated GGG:Eu thickness is indicated above each image. a-b) M-GGG-111. c-d) M-GGG-100.

The first successful attempts of micro-structured growth by LPE were performed on the laser-treated LYSO:Ce substrates. Based on the growth outcome of these, some parameters were changed for the GGG substrates. The GGG substrates were only laser treated with modification and not ablation since the aspect ratio of the pillars of LSO:Tb/M-LYSO:Ce was more promising than LSO:Tb/A-LYSO:Ce. The trench widths were fixed to $15\ \mu\text{m}$ for the GGG substrates since no significant differences were observed for the various trench widths of laser-treated LYSO:Ce. Instead, the grids have eight different orientations, meaning the grids are rotated relative to the surface, as seen in Figure 4.22. This is to study the pillar morphology when growing on grid orientation varied in relation to the atomic structure. Laser modifications have been performed on two different orientations of GGG, namely, (111) and (100).

4.5.1 Sample morphology

The LPE growth on M-GGG-111 and M-GGG-100 resulted in different morphologies in the laser-patterned areas. This was already revealed by visual inspection of the samples as displayed in Figure 4.24b and d. The GGG:Eu/M-GGG-111 is visibly structured, but for M-GGG-100 the light has to reflect on the surface before the structured part can be observed. From the optical microscope overviews of two samples in Figure 4.23, the grids appear brighter for M-GGG-100 than M-GGG-111, even though similar settings are used for the microscope for both samples. When studying the samples closer, it is found that the growth of GGG:Eu/M-GGG-111 resulted in a distinct micro-structure, but GGG:Eu/M-GGG-100 the trenches and features, in general, are not as well-defined as all the other micro-structured samples from this project. The structuration is not homogeneous, but this originates from the laser treatment from the tilt in the depth of the modification, as discussed in detail in

Section 4.2. These variations in the modified quality are carried on during the growth, proving how important the laser treatment step is for the final micro-structured quality.

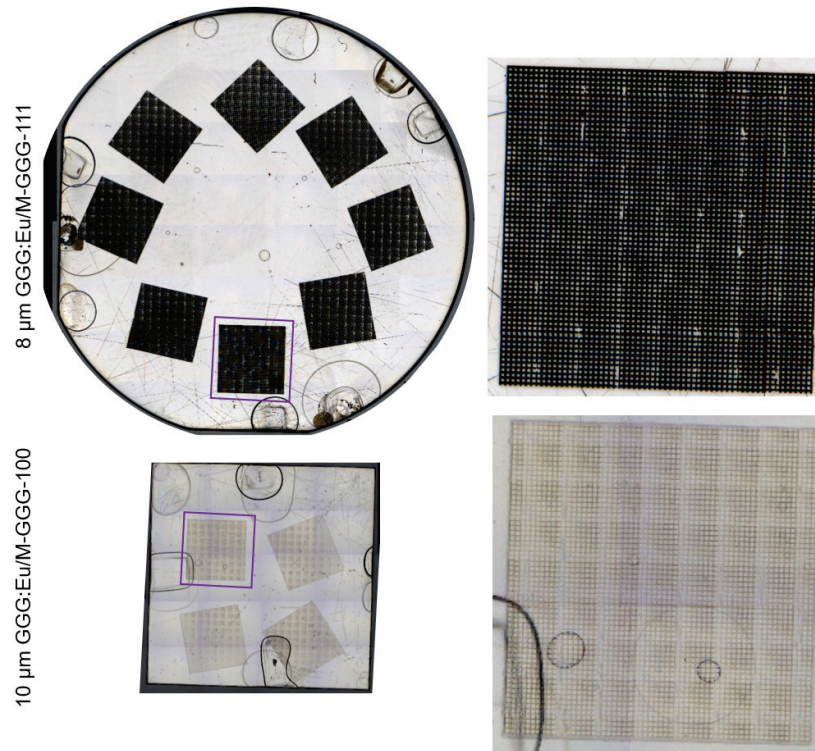


FIGURE 4.23: Overviews of GGG:Eu grown on M-GGG-111 and M-GGG-100 from microscope in reflection configuration. The marked grid indicates the enlarged grid on the right.

GGG:Eu/M-GGG-111: The pillar morphology evolved from square-shaped towards pyramidal with increasing thickness, as shown in Figure 4.24a-d. The surfaces of the pillars are very well defined, which is apparent in Figure 4.24e-g where the microscope was in CDIC configuration. However, there was also growth in the trenches, although at a slower rate than the pillars themselves. The base of the pillars expanded laterally and seemed to have merged into a network of paths. This is especially visible in Figure 4.24h-j, where 3D reconstructions of the micro-structure are presented. Further growth resulted in the pillars merging completely and making longer paths, as seen in Figure 4.24k-m. By comparing all eight grid orientations, the morphology and growth rate were comparable. The grid orientation is therefore concluded not to have affected the pillar morphology or the growth rate for GGG:Eu grown on M-GGG-100 and M-GGG-111.

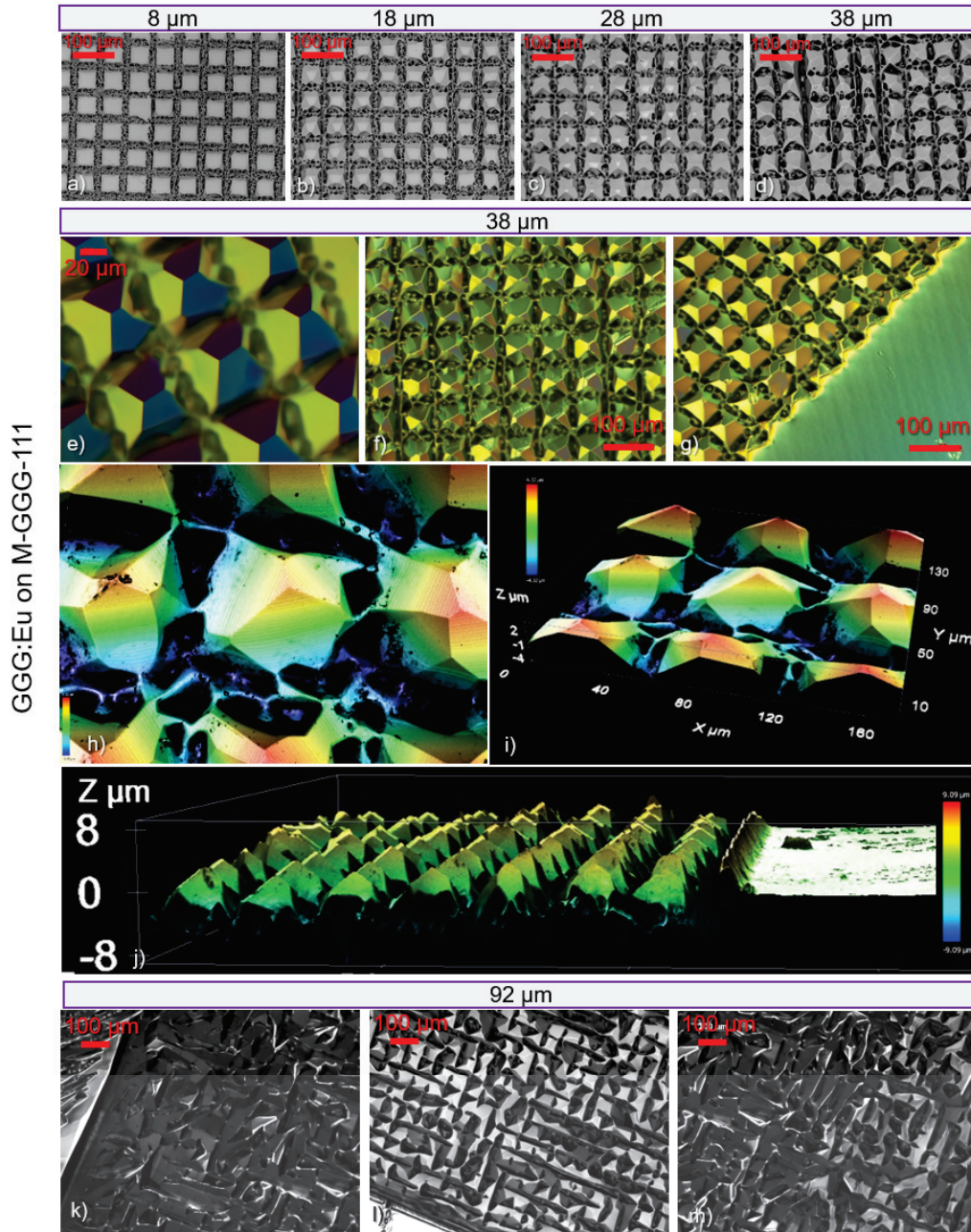


FIGURE 4.24: Microstructured GGG:Eu/M-GGG-111. a-d) Evolution of morphology. The microscope was operated in reflection configuration. e-g) The microscope was operated in CDIC configuration to enhance the features of the surface. h-j) 3D reconstructions created using a confocal microscope. k-m) Microscope in reflection configuration. The thickness is stated in the figure for each sample.

GGG:Eu/M-GGG-100: The layers were growing in a textured manner without any well-defined features. This is displayed in Figure 4.25. The squares and trenches are still visible under microscope observations, but the trenches get less visible as the thickness of the layer was increased. This results in a more pillow-like texture, as shown in Figure 4.25a-c. The morphology of the structuration was studied with the microscope in CDIC configuration since it was otherwise difficult to observe due to the soft features. This is demonstrated in Figure 4.25d-e, where micrographs obtained in reflection configuration of the microscope are displayed. The 3D reconstructions in Figure 4.25f-h also underline how smooth the structuration is compared to the other samples. Here it is visible that there is a height difference from the bottom of the trench to the top of the pillar. However, the difference is only around 0.5 to 1 μm . Using the optical microscope, it was not possible to identify the depth since it is so small, but also, there are no distinct features to focus on.

Comparison: *GGG:Eu/M-GGG-111* indeed succeeded the best for this project. The height, estimated by the gain in weight, compared to the depth, estimated using the optical microscope to find the difference in height from the top of a pillar to the bottom of the trench, is presented in Table 4.5. For *GGG:Eu/M-GGG-111*, the estimated depth increased with increased height. Material has been growing in the trenches, but more slowly than the pillars. For the *GGG:Eu/M-GGG-100*, the concept of pillars was lost from the beginning. If the orientation of the substrate causes this or that the laser treatment was not optimized for this orientation cannot be concluded from current observations. However, since the substrates behaved similarly to the laser treatment, it seems it could be an issue of preferred growth direction from this orientation and not the laser treatment itself.

	Growth1 [μm]	Growth2 [μm]	Growth3 [μm]	Growth4 [μm]	After treatments [μm]
M-GGG-111	9 / 6	18 / 11	38 / 15	92 / 35	
M-GGG-111	9 / 6	-	-	-	9 / 6
M-GGG-100	10 / 0	47 / 0	85 / 0		

TABLE 4.5: Comparing the estimated *height* calculated from the weight gain after growth with the *depth* estimated with the optical microscope: height / depth.

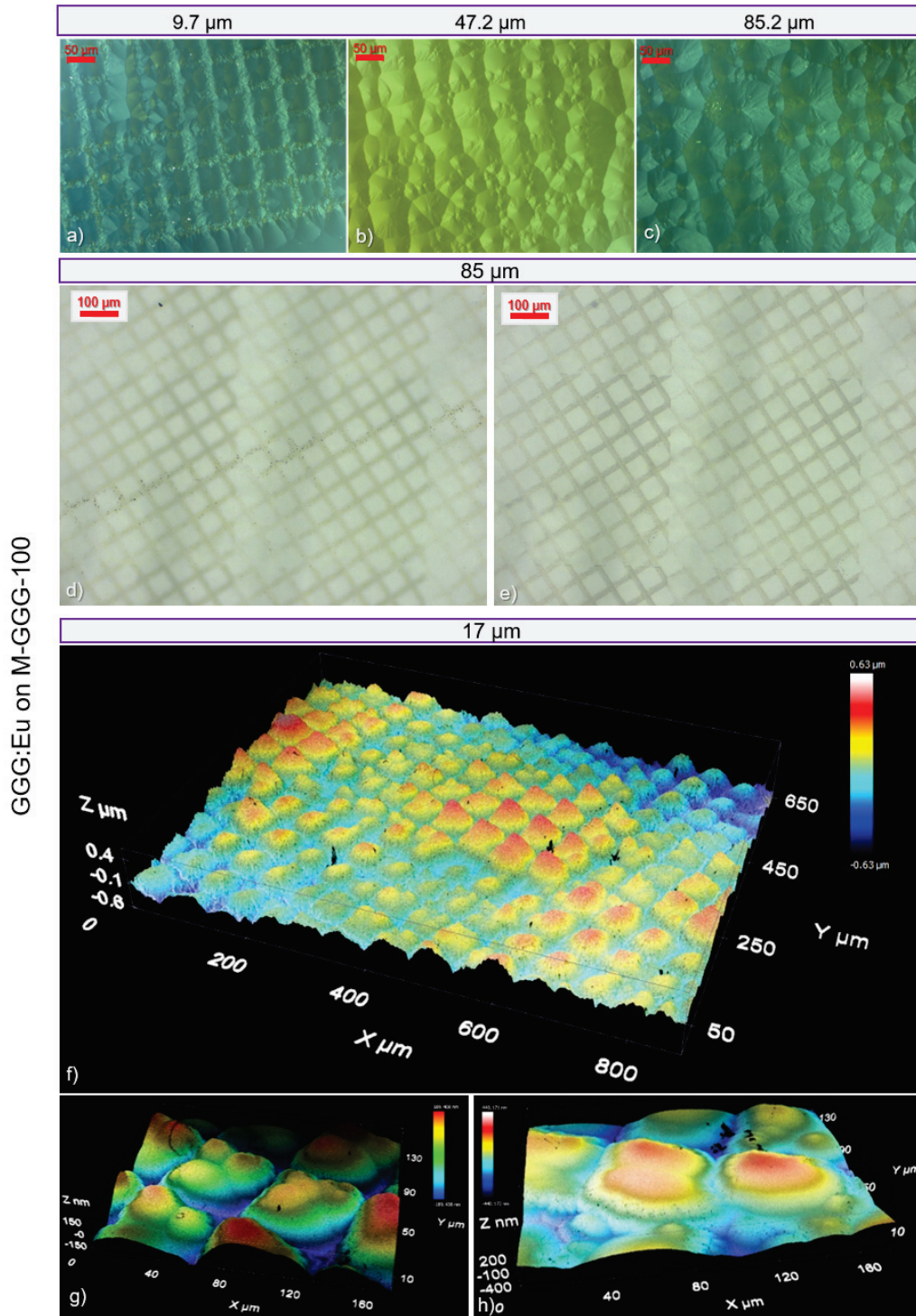


FIGURE 4.25: Microstructured GGG:Eu/M-GGG-100. a-c) Evolution of morphology with thickness. The microscope was operated in CDIC configuration to enhance the visibility of the soft structuration. d-e) Microscope operated in reflection configuration, focusing on the surface and into the volume, respectively. f-h) 3D reconstructions with a confocal microscope. The thickness is stated above the figure for each sample.

4.5.1.1 Etching

The etching procedure tested on the micro-structured GGG:Eu/M-GGG-111 samples is similar to that for the LSO:Tb/A-LYSO:Ce. Therefore, go to Section 4.4 for a detailed process description. It was found that using this etching treatment, material was removed from the trenches for GGG:Eu micro-structured samples. However, the pillars were damaged during the treatment and appeared more rough after. This is shown in Figure 4.26. Another issue is that for the tested sample, the depth was measured to be similar before and after the treatment (see Table 4.5). However, for this material, tests were performed only on one thin sample being 9 μm GGG:Eu/M-GGG-111. Perhaps the effect would be more apparent on thicker samples where more material can be removed, which also was observed for LSO:Tb/A-LYSO:Ce where the tests were performed on 21 μm LSO:Tb. More tests should be performed to make the treatment more gentle to the pillars while removing the material in the trenches.

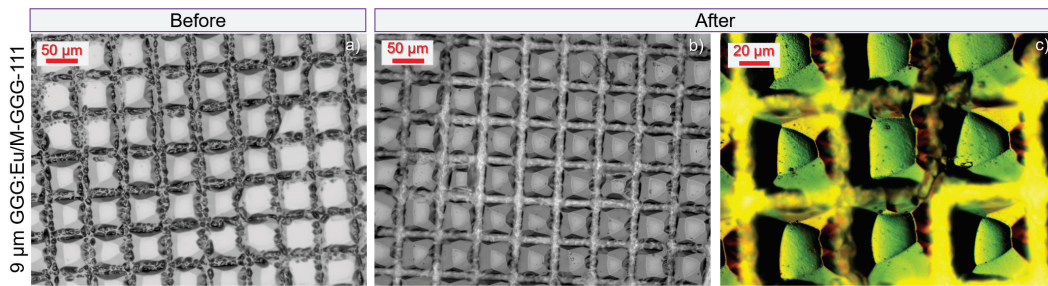


FIGURE 4.26: Before a) and after b) etching treatment of 9 μm GGG:Eu/M-GGG-111. The etching treatment is described in the text.

4.5.2 Structural considerations

4.5.2.1 X-ray diffraction

GGG:Eu/M-GGG-111: Performing specular scans on these samples displayed the expected diffraction peaks corresponding to diffraction on the planes (444) and (888). The diffractograms are displayed in Figure 4.27a compared to M-GGG-111 and a calculated reference of GGG-111 with preferred orientation. This confirms the structured GGG:Eu grew epitaxially on the M-GGG-111 surfaces since no other peaks are present. Studying the (888) peak of the 93 μm GGG:Eu/M-GGG-111 more closely in Figure 4.27b, a second peak is revealed at lower 2θ . This is similar to what was observed for the M-GGG substrates in Section 4.2.2 and is also visible for the M-GGG-111 in Figure 4.27b. For both the modified substrate and the microstructure, this secondary peak is well separated from the main peak but with lower intensity. For GGG:Eu/M-GGG-111, the two (888) diffraction peaks remain but shift to higher 2θ angles than the M-GGG-111. The ω scans (rocking curves) of these two peaks (in the figure denoted A and B) reveal the peak arising from the modification is much broader with an $\text{FWHM}(B)=0.03894^\circ$ compared to the main peak with $\text{FWHM}(A)=0.00943^\circ$.

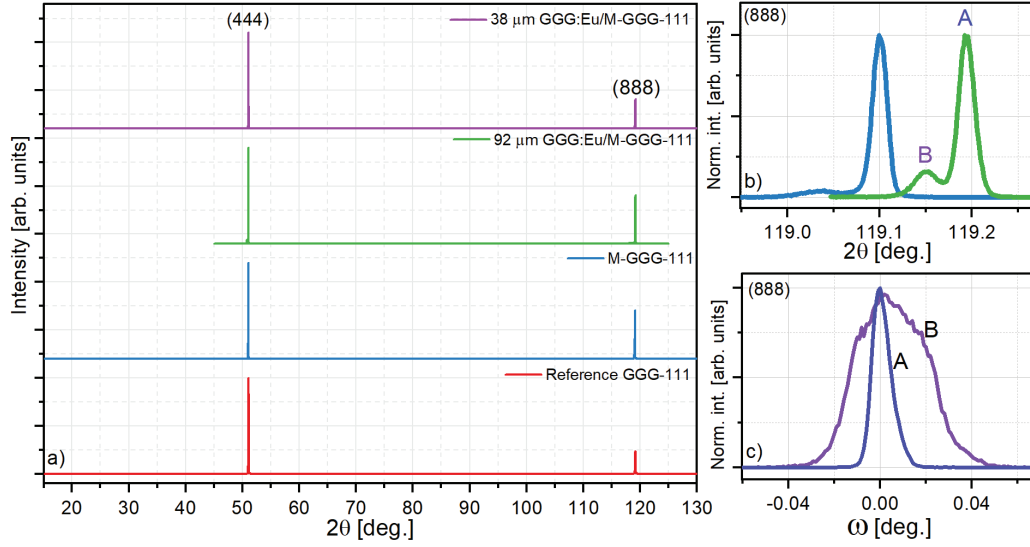


FIGURE 4.27: Results from XRD measurements on GGG-111 samples. a) $2\theta - \omega$ specular scans on GGG:Eu/M-GGG-111 sample, M-GGG-111 substrate, and a calculated reference with preferred orientation for (111). b) $2\theta - \omega$ scans only around the (888) peak(s) for GGG:Eu/M-GGG-111 sample and M-GGG-111 substrate. c) ω scan (rocking curve) around (888) peak in b) for peaks A and B of GGG:Eu/M-GGG-111, with the maximum centered at 0. $\text{FWHM}(A)=0.00943^\circ$ and $\text{FWHM}(B)=0.03894^\circ$. $\lambda = 1.5406 \text{ \AA}$ (Copper, $K\alpha_1$).

This indicates strain in the modified regions, most likely caused by the laser treatment, which is then carried on in the structured growth. From these measurements alone, it cannot be concluded if the modified peak is arising only due to contribution from the trench or if the pillars also suffer from increased strain.

GGG:Eu/M-GGG-100: The specular scans of GGG:Eu/M-GGG-100 also show the expected diffraction peaks corresponding to the (h00) planes. As seen in Figure 4.28a it is similar to the calculated reference with preferred orientation and the M-GGG-100 substrate. When investigating the peaks arising from M-GGG-100 more closely, the dual peaks at slightly lower angles for each main diffraction peak are also identified for this orientation. This is shown in Figure 4.28b. However, for the GGG:Eu/M-GGG-100, only one diffraction peak is present but with a rather large tail towards lower angles. When considering the ω scan of this sample, the peak has a shoulder and is probably corresponding to this secondary peak origin from the modification of the material (see Figure 4.28c).

	$a_{\text{GGG:Eu}}$	a_{GGG}	Lattice mismatch
2.5 μm GGG:Eu/GGG-111	12.373 \AA	12.382 \AA	-0.07%
38 μm GGG:Eu/M-GGG-111	12.375 \AA	12.381 \AA	-0.05%
85 μm GGG:Eu/M-GGG-100	12.378 \AA	12.382 \AA	-0.04%

TABLE 4.6: The lattice a-parameter on relevant samples and their substrates and the corresponding lattice mismatch. The a-parameters are extracted from $2\theta - \omega$ scans. The lattice parameters for the M-GGG substrates (a_{GGG}) are measured before growth.

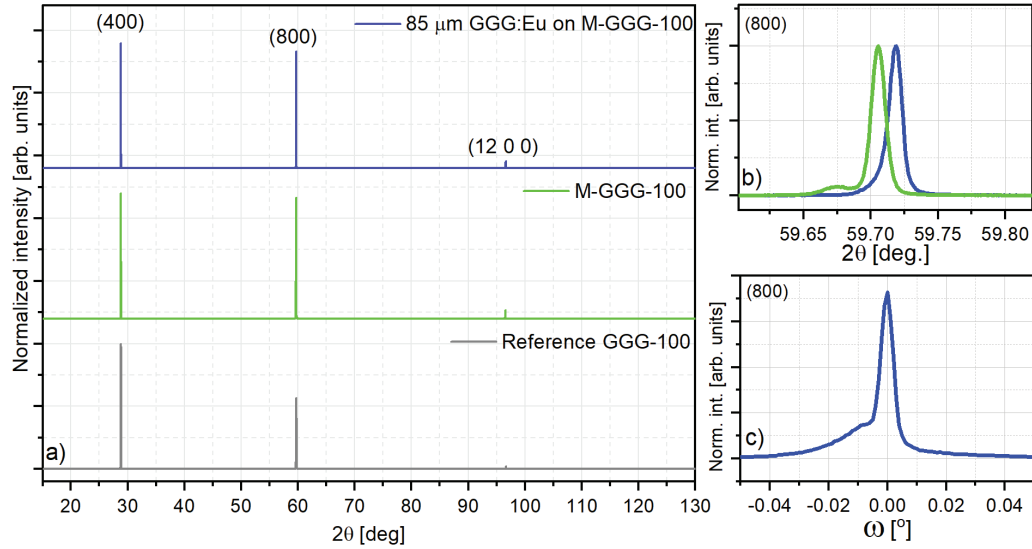


FIGURE 4.28: Results from XRD measurements on GGG-100 samples. a) $2\theta - \omega$ specular scans on GGG:Eu/M-GGG-100 sample, M-GGG-100, and a calculated reference with preferred orientation for (100), respectively. b) $2\theta - \omega$ scans only around the (800) peak for GGG:Eu/M-GGG-100 and M-GGG-100 substrate. c) ω scan (rocking curve) around (800) peak of GGG:Eu/M-GGG-100, with the maximum centered at 0. FWHM=0.0054°. $\lambda = 1.5406 \text{ \AA}$ (Copper, $K\alpha 1$).

The lattice parameter is extracted from the $2\theta - \omega$ scans using Equation 3.2 and is presented in Table 4.6 where the lattice mismatch calculated from Equation 4.1 is also compared. The lattice parameters are very similar for GGG:Eu/M-GGG-111 and GGG:Eu/M-GGG-100, and they are comparable to a normal LPE grown GGG:Eu/GGG-111 as well. The lattice mismatch is relatively low for all investigated samples, which is highly desirable. However, GGG:Eu has a shorter unit cell length than the GGG substrates. This indicates that doping with europium in the GGG lattice result in a contraction of the a-parameter. At first, this seems like an unusual result since europium substitutes with gadolinium in this structure, and its ionic radii are slightly larger, meaning the lattice should expand and not contract. See Table 4.7 for the relevant ionic radii. However, this is not unique for the micro-structured GGG:Eu samples. It is generally also observed for regular GGG:Eu/GGG grown by LPE. The explanation can be that the GGG substrates are grown at high temperatures with the Czochralski method. Growth at high temperatures typically induces more oxygen vacancies than LPE growth performed at lower temperatures. Oxygen vacancies in structures can, in some cases, lead to an expansion of the lattice, which is previously reported for GGG [141].

Element	Coordination number	Ionic radii
Gd ³⁺	8	1.053 Å
Eu ³⁺	8	1.066 Å

TABLE 4.7: Overview of the ionic radii relevant for GGG:Eu [82].

4.5.2.2 Raman spectroscopy

Pillar, trench, and film were individually excited, and the Raman spectrum was collected. The spectra for GGG:Eu/M-GGG-111 and GGG:Eu/M-GGG-100 are presented in Figure 4.29a and b, where the local structures are compared.

GGG:Eu/M-GGG-111: The same features are found for the spectra in Figure 4.29a. This indicates the pillars, trench, and film are growing iso-structurally and most likely with the same orientation, which XRD confirms for the long-range order. The intensity of the Raman peaks of the pillars is higher than the film, suggesting they have the highest crystallinity. The lowest intensity spectrum is from the trench. This agrees with the observations of reduced growth in the trenches. This combined suggests it must be less favorable for material to grow in the trench, which is desirable for this project.

GGG:Eu/M-GGG-100: All spectra have the same features as seen in Figure 4.29b. The pillars also have the highest intensity, and the trench and film have similar intensity. What was observed from the morphology of these samples is that the trench was growing, and pillow-like structuration was obtained instead of well-defined pillars. It was therefore expected the Raman spectra being similar for the pillar and trench.

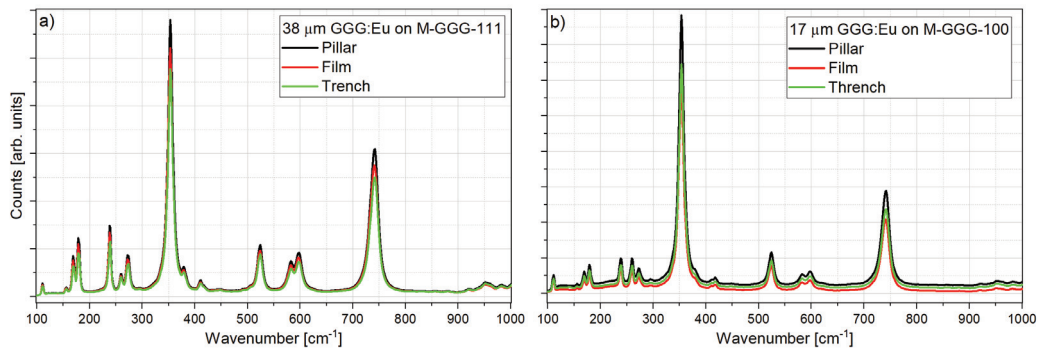


FIGURE 4.29: Micro-Raman scattering on samples with the excitation individually pillar, film, and trench. a) GGG:Eu/M-GGG-111, b) GGG:Eu/M-GGG-100. For all spectra, $\lambda_{exc} = 488$ nm.

Comparing Figure 4.29a and b, the two orientations of the samples have the same features but with variations in the intensities of the peaks.

4.5.3 Luminescence

4.5.3.1 Photoluminescence

The photoluminescence spectra were also collected by exciting with a micro source similar to Raman. The spectra features are all similar. This includes the spectra for pillar, trench, and film and comparing the two substrate orientations. This demonstrates that europium is incorporated in all.

GGG:Eu/M-GGG-111: The highest intensity for GGG:Eu/M-GGG-111 is from the pillar as seen in Figure 4.30b. The trench and film are of lower but similar intensity. There can be several reasons for this. One is the amount of europium incorporated not being the same, or the europium-activated volume being excited being effectively less for these.

GGG:Eu/M-GGG-100: For GGG:Eu/M-GGG-100, the spectra of the film is highest in intensity but similar to the pillar and trench (see Figure 4.30c). As discussed earlier, for these samples, the pillars are growing more like pillows (see, for example, Figure 4.25), and the difference between trench and pillar is small considering the morphology and is similar for the photoluminescent properties.

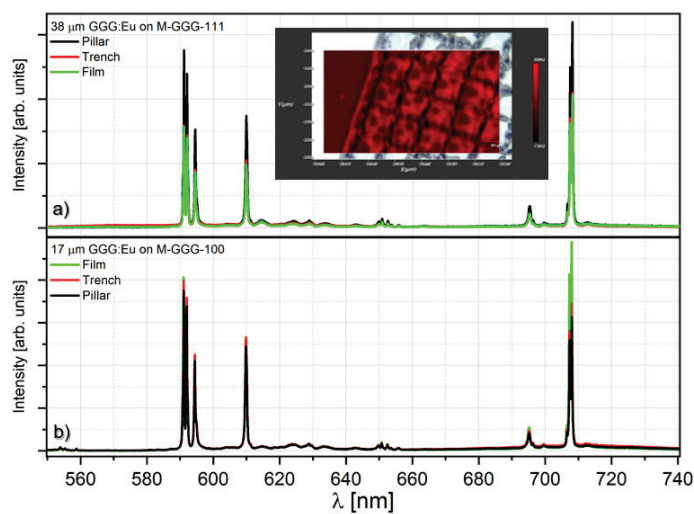


FIGURE 4.30: Photoluminescence investigations. Spectra recorded while excitation individually pillar, trench, and film a) GGG:Eu/M-GGG-111, with inset of spatial intensity mapping for 591 nm, and b) GGG:Eu/M-GGG-100. For all spectra, $\lambda_{exc} = 488$ nm.

4.5.3.2 Radioluminescence

Like described for the microstructured LSO:Tb, the X-ray excitation was performed on an area of approximately $2\text{ mm} \times 2\text{ mm}$, making sure to excite the micro-structured area mainly. Radioluminescence spectra are presented in Figure 4.31. It is important to note the intensities of the spectra have been normalized. Both orientations of the GGG substrates used for the laser treatment are slightly scintillating. This creates a background emission, which reduces the spatial resolution when used for high-resolution X-ray imaging experiments. However, optimizing the growth of these substrates can lead to emission-free substrates. The emission is not identical for the micro-structured samples on the two orientations. The GGG:Eu grown on M-GGG-100 have emission lines close to the UV due to the substrate emission, whereas this is not the case for GGG:Eu/M-GGG-111.

When a GGG:Eu/M-GGG-111 is excited with UV, the emission appears orange/red. This is shown in Figure 4.31 on the left. Here it is also seen that in addition to the edges of the scintillator, the micro-structured areas extract the light to a higher degree than the normal film areas.

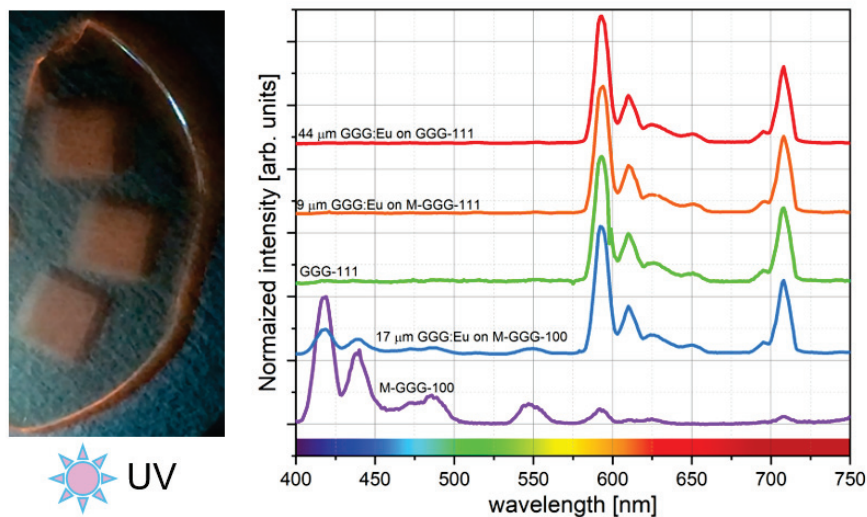


FIGURE 4.31: Normalized radioluminescence spectra of relevant samples and substrates. The sample references are indicated above each curve. For all spectra, excitation was performed using a molybdenum X-ray source. On the left is a photograph of $18\ \mu\text{m}$ GGG:Eu/M-GGG-111 excited by a UV lamp.

4.5.3.3 Comparison

Comparing photoluminescence and radioluminescence, the same features are found as presented in Figure 4.32. Under both UV and X-ray excitation, the micro-structured GGG:Eu samples show consistently with the Eu^{3+} emission the bands characteristic for the ${}^5\text{D}_0$ to ${}^7\text{F}_i$ ($i=0,1,2,3,4$) transitions, as marked in the figure.

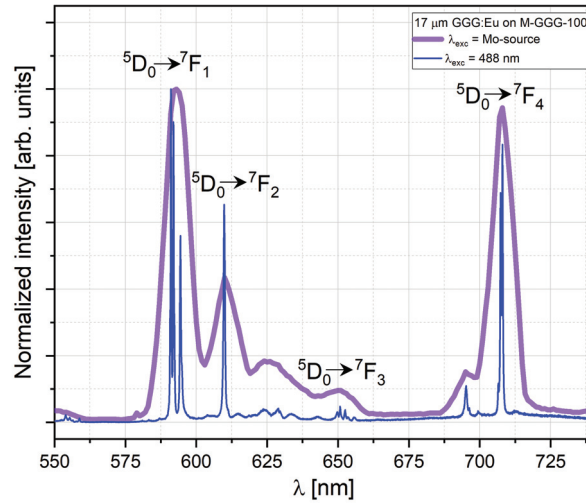


FIGURE 4.32: Comparison of the normalized radioluminescence and photoluminescence of $17 \mu\text{m}$ GGG:Eu/M-GGG-100.

4.6 Comparison and optimization

The results of the laser treatments and subsequent growth on the two types of materials have been presented and discussed separately. This section will then shortly compare and discuss the two micro-structured materials.

4.6.1 Results

4.6.1.1 Laser treatment and LPE growth

The crack formation was more severe for GGG than for LYSO:Ce. Of course, the laser treatment should be further optimized for each material, and maybe the parameters chosen and tested initially for LYSO:Ce was better guessed than for GGG. It can also be a possibility that LYSO:Ce is just more susceptible to this type of laser treatment.

The LPE growth itself for both materials and all orientations followed fairly the typical parameters and behavior as the growth of their normal films.

4.6.1.2 Morphology

The morphology of the micro-structured LSO:Tb and GGG:Eu is very different. This is expected since their structures are monoclinic and cubic, respectively, occupied by different elements. Therefore the favorable growth directions will not be the same. A comparison of the pillar morphologies is presented in Figure 4.33.

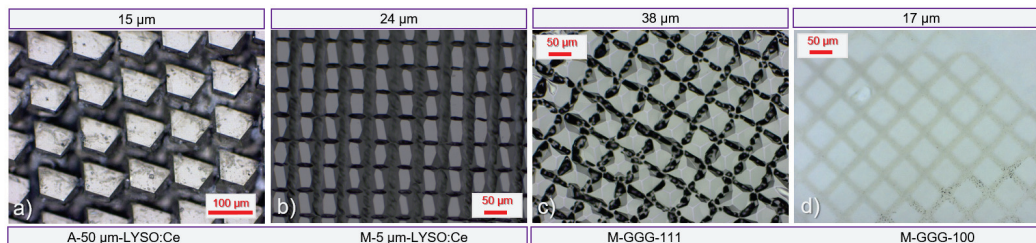


FIGURE 4.33: Comparing the morphology of the micro-structure with an optical microscope with the same magnification (x20) and operated in reflection configuration. a-b) LSO:Tb. c-d) GGG:Eu. The thickness and substrate are stated in the figures for each sample.

4.6.1.3 Structure

The laser treatment seems to have affected the materials differently. Considering the XRD measurements on M-GGG, the modification leads to an additional diffraction peak, the "modified" peak, where this is not observed for LYSO:Ce. However, considering the extracted FWHM from the ω scans, the microstructured LSO:Tb also has the highest FWHM, even higher than the FWHM extracted from the modified peak. A comparison of the extracted FWHM of selected samples is displayed in Table 4.8.

Both materials are growing epitaxially and similarly to the normal film. Even the investigations of the trenches show a very similar structure to the micro-structure

Sample	FWHM
19 μm LSO:Tb/LYSO:Ce-010	0.09995°
85 μm GGG:Eu/M-GGG-100	0.0054°
92 μm GGG:Eu/M-GGG-111 (A)	0.00943°
92 μm GGG:Eu/M-GGG-111 (B)	0.03894°

TABLE 4.8: Evaluation of the extracted FWHM of the ω -scans of relevant samples. A: normal peak, B: modified peak (see section 4.5.2 for further explanation).

and normal film parts. In general, the trenches seem to be less crystalline than the pillars, whereas the pillars seem to be highly crystalline.

4.6.1.4 Luminescence

An important observation and point of discussion are the enhanced light extraction in the pillars for LSO:Tb/M-LYSO:Ce and GGG:Eu/M-GGG-111. LSO:Tb/A-LYSO:Ce extracts the light in the trenches, presumably due to the roughness or texture of the trench, whereas the others seem to extract more light on parts of the pillars. This can be observed in Figure 4.34 from the photoluminescence mappings.

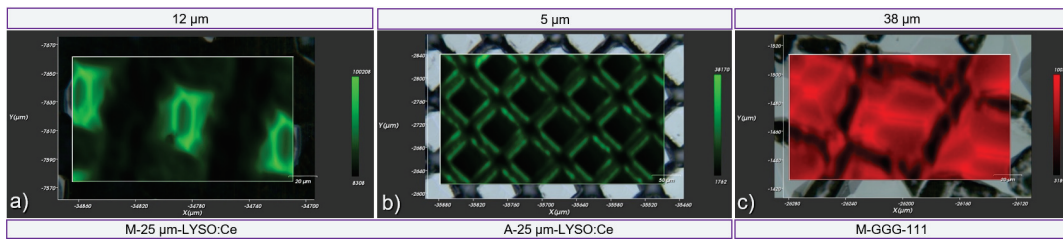


FIGURE 4.34: Spatial mapping of the photoluminescence intensity. a-b) LSO:Tb, intensity at 543 nm. c) GGG:Eu, intensity at 591 nm. The thickness and substrate are indicated in the figure for each sample. a) and b) have been included in figures in previous chapters.

4.6.2 Future perspectives

To our knowledge, there are no reports on using LPE growth to grow micro-structured samples like those presented in this chapter. There are examples of overgrowth methods where LPE is used in various ways, For example, by using gold seeds and subsequent LPE growth [142]. But what has been done in this project is truly unique. There are many challenges to be encountered and solved still, but this has been a successful proof of concept. Issues such as the low aspect ratio should be solved before the samples can be used for X-ray imaging. However, solving this would likely not be enough to proceed to the final application. This final section will discuss some possible optimization possibilities as well as further aspects that should be considered before the samples would be ready for application.

Improvement of laser treatment As mentioned and shown in the last sections, the laser treatment is imperfect. Optimization of the modification process and thereby

minimizing growth in the trenches could be obtained by decreasing the line spacing or doing repeated lines to ensure an entirely modified volume.

Perhaps a combination of ablation and modification could combine the best of the two approaches. From the results obtained from the two methods, growth in the trenches of the modified samples is less than for the ablated samples. However, having already a height difference before LPE growth could also be considered beneficial in terms of reducing the flow of the flux within the trenches and therefore having less growth triggered in the trenches in general. Therefore, having a depth of the trench before growth while making sure growth in the trenches are not very favorable could be a good combination. These are ideas and possibilities which are already under discussion with Fraunhofer ILT.

Polishing: After obtaining pillars of appropriate height, the substrate should be removed. Otherwise, the light is no longer contained in a well-defined space, and the spatial resolution will decrease. The substrate can be partly or entirely removed by polishing. Therefore, gluing the sample onto, for example, a glassy carbon substrate before the polishing is beneficial to support the microstructure and be able to remove the single crystalline substrate completely. This way, if there has been a bit of growth in the trenches, this can also be removed.

Dead space: In the ideal case for the final application, the trench size should not be 50 μm wide. There should preferably be no trench, or it should at least be as small as possible. Assuming the samples, after careful optimization, would have the light created and guided in the pillars perfectly. Then the final image created using this will have some dead space where this part is omitted from the image. When having a 15 μm trench and 50 μm \times 50 μm squares, the image will have approximately 40% dead space. Here it is assumed the pillars grow without any deviation from the square, meaning no lateral reduction or increase in the pillar dimensions while growing. Considering more ideal options, with the trench size reduced to the minimum, which is for this setup limited by the focal spot of the laser being around 2 μm , the dead space will be $\sim 8\%$, which is considerably better. Some calculations on this are shown in Table 4.9. Reducing the square size is not optimal for this approach since this increases the dead space. For the laser treatment, the microscope objective used for focusing the laser beam on the sample could be changed to create a smaller focal point, and a more narrow trench width could be obtained this way.

Square size [μm]	Trench size [μm]	Dead space [%]
50x50	15	~ 40
50x50	2	~ 8
25x25	2	~ 14
10x10	2	~ 31
5x5	2	~ 49

TABLE 4.9: Calculations of the dead space for various square and trench sizes without considering the shape of the pillar after growth.

Coatings: Ideally, the wall surfaces should be smooth, with low roughness. If the surface of the pillar walls is rough, the light will scatter and be extracted at the sides, similar to what was observed for the LSO:Tb/A-LYSO:Ce, where the light was not extracted mostly in the pillars but more in the trench that is rough. This will increase the risk of having significant cross-talk between the pillars and the trenches. The cross-talking could potentially be minimized by adding reflective coatings on the pillar walls to reflect the light more effectively inside the pillars.

Other treatments: Other treatments than laser patterning have been considered. Initial testing of depositing metals as a mask to avoid growth was briefly investigated in collaboration with Helia Photonics. A summary of the result is presented in Figure 4.35. First, photolithography was performed for patterning of the substrates and subsequent deposition of a metal, either hafnium or lead. Both these steps went well. The lift-off to remove the metals at the squares and leave the trenches covered by the metals is failing. Here most of the metal is removed. The results were similar for both GGG and LYSO:Ce substrates and both hafnium and lead metal deposition. Various lift-off procedures were tested, but the results were the same every time. An additional adhesion layer under the metal could increase the adhesion, but it is difficult to predict which would work, if any and was not explored further.

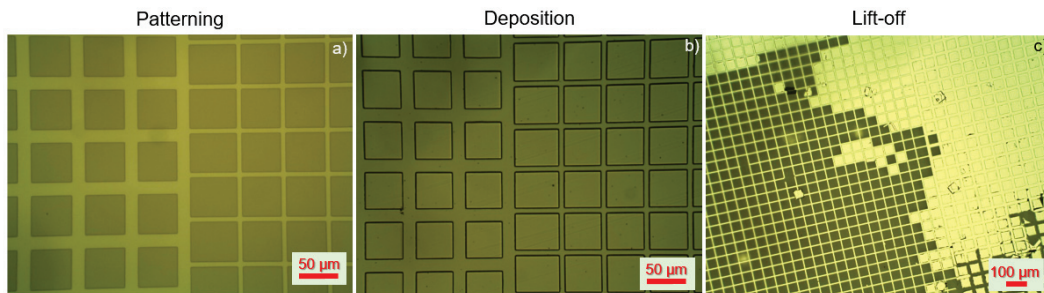


FIGURE 4.35: Treatment of GGG and LYSO substrates at Helia photonics. Patterning was performed by lithography, then metal deposition (hafnium and lead was tested), and finally, lift-off.

4.7 Conclusions

By performing laser patterning on single crystalline substrates and subsequently performing LPE growth, micro-structuration has successfully been obtained. This is, to the best of our knowledge, the first time this specific approach has been utilized. Laser patterning was performed on typical substrates used for LPE growth of state-of-the-art scintillators LSO:Tb and GGG:Eu: LYSO:Ce and GGG, respectively. For the LYSO:Ce substrates, two laser treatment procedures were used for the patterning, modification, and ablation. The trench width was varied, and it was concluded this did not have a significant effect on the growth. The structured growth from the modified substrates resulted in a higher aspect ratio of the pillars. Consequently, the GGG substrates were only laser modified while keeping the trench width at 15 μm . Instead, the laser-modified grids were patterned to have eight different orientations, and it was thereby found that the grid orientation relative to the orientation of the atomic structure, does not influence the growth morphology of the GGG:Eu micro-structure. Well-defined pillars were grown on GGG with crystallographic orientation (111), whereas for (100) the features were softer and without a well-defined trench. From XRD investigations, it was observed for all micro-structured samples, the atomic structure was the same as their non-structured counterparts, and that the unit cell lengths were comparable. With Raman spectroscopy, the pillar, trench, and normal film were also found to have similar local structures. Studying the photoluminescence, it was found the dopants were incorporated into pillar, trench, and film parts of all samples. Photoluminescence and radioluminescence have similar features that were ascribed to the characteristic transitions of the dopants. From all these results, it is concluded there is some growth in the trenches, and indeed optimization is required to reduce or avoid this to obtain the best possible micro-structure.

A proof of concept is thus demonstrated: by laser patterning single crystalline substrates and performing LPE growth, micro-structuration is achieved with atomic structure and luminescent properties similar to their normal thin film counterparts.

Bibliography

- [1] W. C. Röntgen. “On a new kind of rays”. In: *Science* 3.59 (1896), pp. 227–231.
- [2] S. Mobilio, F. Boscherini, and C. Meneghini. *Synchrotron Radiation*. Springer, 2016.
- [3] H. C. Pollock. “The discovery of synchrotron radiation”. In: *American Journal of Physics* 51.3 (1983), pp. 278–280.
- [4] S. Shin. “New era of synchrotron radiation: fourth-generation storage ring”. In: *AAPPS Bulletin* 31.1 (2021), pp. 1–16.
- [5] *Generation X-ray*. 2019. URL: <https://ebs.esrf.fr/2019/02/12/generation-x-ray/> (visited on 12/25/2022).
- [6] *ESRF history*. URL: <https://www.esrf.fr/home/about/History.html> (visited on 12/23/2022).
- [7] P. Raimondi. “ESRF-EBS: The extremely brilliant source project”. In: *Synchrotron Radiation News* 29.6 (2016), pp. 8–15.
- [8] P. F. Tavares et al. “Commissioning and first-year operational results of the MAX IV 3 GeV ring”. In: *Journal of synchrotron radiation* 25.5 (2018), pp. 1291–1316.
- [9] L. Liu, R. Neuenschwander, and A. Rodrigues. “Synchrotron radiation sources in Brazil”. In: *Philosophical Transactions of the Royal Society A* 377.2147 (2019), p. 20180235.
- [10] I. Agapov et al. “Status of the PETRA IV project”. In: *10th Int. Particle Accelerator Conf.(IPAC’19), Melbourne, Australia*. 2019.
- [11] B. Singh et al. “Lattice options for DIAMOND-II”. In: *Proc. IPAC 18* (2018), pp. 4050–4053.
- [12] J.-L. Revol et al. “ESRF-EBS: Implementation, performance and restart of user operation”. In: *Proceedings of IPAC’21* (2021).
- [13] G. Pacchioni. “An upgrade to a bright future”. In: *Nature Reviews Physics* 1.2 (2019), pp. 100–101.
- [14] *Beamline status*. 2022. URL: <https://www.esrf.fr/UsersAndScience/UserGuide/Applying/beamline-status> (visited on 01/20/2022).

- [15] F. Cianciosi et al. "BM18, the New ESRF-EBS Beamline for Hierarchical Phase-Contrast Tomography". In: *11th Mechanical Engineering Design of Synchrotron Radiation Equipment and Instrumentation (MEDSI'20), Chicago, IL, USA, 24-29 July 2021*. JACOW Publishing, Geneva, Switzerland. 2021, pp. 1–5.
- [16] D Chenevier and A Joly. "ESRF: inside the extremely brilliant source upgrade". In: *Synchrotron Radiation News* 31.1 (2018), pp. 32–35.
- [17] R Dimper et al. "ESRF Upgrade Programme Phase II (2015–2022), Technical Design Study, The Orange Book". In: *ESRF, ESRF* (2015).
- [18] P Fajardo et al. "Digital integration: a novel readout concept for XIDER, an X-ray detector for the next generation of synchrotron radiation sources". In: *Journal of Instrumentation* 15.01 (2020), p. C01040.
- [19] M Williams et al. "XIDER: First Prototypes and Results with the Digital Integration Readout Scheme". In: *2021 IEEE Nuclear Science Symposium and Medical Imaging Conference (NSS/MIC)*. IEEE. 2021, pp. 1–4.
- [20] M Collonge, P Fajardo, M Williams, et al. "Monte Carlo simulations for XIDer, a novel digital integration X-ray detector for the next generation of synchrotron radiation sources". In: *Journal of Instrumentation* 17.01 (2022), p. C01037.
- [21] D Magalhaes and P Fajardo. "Degradation of signal-to-noise ratio in counting detectors due to pile-up effects". In: *Journal of Instrumentation* 18.01 (2023), p. C01016.
- [22] K. Pauwels and P.-A. Douissard. "Indirect X-ray detectors with single-photon sensitivity". In: *Journal of Synchrotron Radiation* 29.6 (2022).
- [23] R. Ponsard. "High Throughput Low Latency Online Image Processing by GPU/FPGA Data Coprocessors using RDMA Techniques". PhD thesis. Université Grenoble Alpes [2020-....], 2020.
- [24] W. Mansour, P. Fajardo, N. Janvier, et al. "High performance RDMA-based DAQ platform over PCIe routable network". In: *Proc. ICALEPCS*. 2017, pp. 1131–1136.
- [25] K. E. Chapelle, V. Fernandez, and J. N. Choiniere. "Conserved in-ovo cranial ossification sequences of extant saurians allow estimation of embryonic dinosaur developmental stages". In: *Scientific reports* 10.1 (2020), pp. 1–10.
- [26] P. Cloetens et al. "Holotomography: Quantitative phase tomography with micrometer resolution using hard synchrotron radiation x-rays". In: *Applied physics letters* 75.19 (1999), pp. 2912–2914.
- [27] O. Lame et al. "In situ microtomography investigation of metal powder compacts during sintering". In: *Nuclear Instruments and Methods in Physics Research Section B: Beam Interactions with Materials and Atoms* 200 (2003), pp. 287–294.

- [28] W. Ludwig et al. "Three-dimensional grain mapping by x-ray diffraction contrast tomography and the use of Friedel pairs in diffraction data analysis". In: *Review of scientific instruments* 80.3 (2009), p. 033905.
- [29] W. Ludwig et al. "High-resolution three-dimensional mapping of individual grains in polycrystals by topotomography". In: *Journal of Applied Crystallography* 40.5 (2007), pp. 905–911.
- [30] B. I. Erkmén and J. H. Shapiro. "Ghost imaging: from quantum to classical to computational". In: *Advances in Optics and Photonics* 2.4 (2010), pp. 405–450.
- [31] D. Pelliccia et al. "Experimental x-ray ghost imaging". In: *Physical review letters* 117.11 (2016), p. 113902.
- [32] T. M. Buzug. "Computed tomography". In: *Springer handbook of medical technology*. Springer, 2011, pp. 311–342.
- [33] A. Mittone et al. "Multiscale pink-beam microCT imaging at the ESRF-ID17 biomedical beamline". In: *Journal of Synchrotron Radiation* 27.5 (2020).
- [34] Y. Chen et al. "In-situ Synchrotron imaging of keyhole mode multi-layer laser powder bed fusion additive manufacturing". In: *Applied Materials Today* 20 (2020), p. 100650.
- [35] H. Elleaume et al. "Instrumentation of the ESRF medical imaging facility". In: *Nuclear Instruments and Methods in Physics Research Section A: Accelerators, Spectrometers, Detectors and Associated Equipment* 428.2-3 (1999), pp. 513–527.
- [36] A. Mittone et al. "Characterization of a sCMOS-based high-resolution imaging system". In: *Journal of synchrotron radiation* 24.6 (2017), pp. 1226–1236.
- [37] W. R. Leo et al. *Techniques for Nuclear and Particle Physics Experiments: A How-To Approach*. Springer Science & Business Media, 1994.
- [38] S. Wilbur et al. "Flexible X-ray imaging detectors using scintillating fibers". In: *Journal of Instrumentation* 17.10 (2022), p. C10013.
- [39] M. Hamel. *Plastic Scintillators*. Springer, 2021.
- [40] T. J. Hajagos et al. "High-Z sensitized plastic scintillators: a review". In: *Advanced Materials* 30.27 (2018), p. 1706956.
- [41] J. Cao et al. "Synthesis and characterization of BaLuF₅:Tb³⁺ oxyfluoride glass ceramics as nanocomposite scintillator for X-ray imaging". In: *Ceramics International* 42.15 (2016), pp. 17834–17838.
- [42] J. Cao et al. "Enhanced emissions in self-crystallized oxyfluoride scintillating glass ceramics containing KTb₂F₇ nanocrystals". In: *Optical Materials Express* 6.7 (2016), pp. 2201–2206.
- [43] F. Tokanai et al. "Developments of optical imaging capillary plate gas detector". In: *Nuclear Instruments and Methods in Physics Research Section A: Accelerators, Spectrometers, Detectors and Associated Equipment* 567.1 (2006), pp. 376–380.

- [44] M. Chen et al. "Organic Semiconductor Single Crystals for X-ray Imaging". In: *Advanced Materials* 33.43 (2021), p. 2104749.
- [45] L.-J. Xu et al. "Highly efficient eco-friendly X-ray scintillators based on an organic manganese halide". In: *Nature communications* 11.1 (2020), pp. 1–7.
- [46] M. Nikl. "Scintillation detectors for x-rays". In: *Measurement Science and Technology* 17.4 (2006), R37.
- [47] G. F. Knoll. *Radiation detection and measurement*. John Wiley & Sons, 2010.
- [48] E.-J. Popovici et al. "Synthesis and characterisation of rare earth oxysulphide phosphors. I. Studies on the preparation of Gd₂O₂S:Tb phosphor by the flux method". In: *Optical materials* 27.3 (2004), pp. 559–565.
- [49] R. K. Swank. "Calculation of modulation transfer functions of x-ray fluorescent screens". In: *Applied optics* 12.8 (1973), pp. 1865–1870.
- [50] B. Grabmaier and W. Rossner. "New scintillators for X-ray computed tomography". In: *Nuclear tracks and radiation measurements* 21.1 (1993), pp. 43–45.
- [51] S. R. Miller et al. "Recent advances in columnar CsI(Tl) scintillator screens". In: *Penetrating Radiation Systems and Applications VII* 5923 (2005), pp. 99–108.
- [52] A. Sahlholm et al. "SELECTION OF DIMENSIONS AND GEOMETRY OF A STRUCTURED SCINTILLATOR FOR X-RAY IMAGING". In: ().
- [53] Z. Lin et al. "Structured Scintillators for Efficient Radiation Detection". In: *Advanced Science* 9.2 (2022), p. 2102439.
- [54] P. A. Douissard et al. "A versatile indirect detector design for hard X-ray microimaging". In: *Journal of Instrumentation* 7.09 (2012), P09016–P09016. ISSN: 1748-0221. DOI: [10.1088/1748-0221/7/09/P09016](https://doi.org/10.1088/1748-0221/7/09/P09016). URL: <https://iopscience.iop.org/article/10.1088/1748-0221/7/09/P09016>.
- [55] T. Martin and A. Koch. "Recent developments in X-ray imaging with micrometer spatial resolution". In: *Journal of Synchrotron Radiation* 13.2 (2006), pp. 180–194. ISSN: 0909-0495. DOI: [10.1107/S0909049506000550](https://doi.org/10.1107/S0909049506000550). URL: <http://scripts.iucr.org/cgi-bin/paper?S0909049506000550>.
- [56] A. Koch et al. "X-ray imaging with submicrometer resolution employing transparent luminescent screens". In: *JOSA A* 15.7 (1998), pp. 1940–1951.
- [57] J. Tous et al. "Single crystal scintillator plates used for light weight material X-ray radiography". In: *Journal of Physics: Conference Series*. Vol. 425. 19. IOP Publishing, 2013, p. 192017.
- [58] P. Capper and M. Mauk. *Liquid phase epitaxy of electronic, optical and optoelectronic materials*. John Wiley & Sons, 2007.
- [59] P. Capper, S. Irvine, and T. Joyce. "Epitaxial crystal growth: methods and materials". In: *Springer Handbook of Electronic and Photonic Materials*. Springer, 2017, pp. 309–319.

- [60] P. Capper and M. Mauk. *Liquid phase epitaxy of electronic, optical and optoelectronic materials*. John Wiley & Sons, 2007.
- [61] A Cecilia et al. "Investigation of the luminescence, crystallographic and spatial resolution properties of LSO:Tb scintillating layers used for X-ray imaging applications". In: *Radiation measurements* 62 (2014), pp. 28–34.
- [62] P.-A. Douissard et al. "A novel epitaxially grown LSO-based thin-film scintillator for micro-imaging using hard synchrotron radiation". In: *Journal of synchrotron radiation* 17.5 (2010), pp. 571–583.
- [63] T. Martin et al. "LSO-based single crystal film scintillator for synchrotron-based hard X-ray micro-imaging". In: *IEEE Transactions on Nuclear Science* 56.3 (2009), pp. 1412–1418.
- [64] P.-A. Douissard et al. "Epitaxial growth of LuAG:Ce and LuAG:Ce, Pr films and their scintillation properties". In: *IEEE Transactions on Nuclear Science* 63.3 (2016), pp. 1726–1732.
- [65] Y. Zorenko et al. "Scintillating screens based on the LPE grown $Tb_3Al_5O_{12}$:Ce single crystalline films". In: *Optical Materials* 65 (2017), pp. 73–81.
- [66] M. Abramowitz et al. "Basic principles of microscope objectives". In: *Biotechniques* 33.4 (2002), pp. 772–781.
- [67] E. Abbe. "XV.—The Relation of Aperture and Power in the Microscope (continued)". In: *Journal of the royal microscopical society* 3.6 (1883), pp. 790–812.
- [68] C. E. Shannon. "Communication in the presence of noise". In: *Proceedings of the IRE* 37.1 (1949), pp. 10–21.
- [69] H. Nyquist. "Certain topics in telegraph transmission theory". In: *Transactions of the American Institute of Electrical Engineers* 47.2 (1928), pp. 617–644.
- [70] F. Riva. "Development of new thin film scintillators for high-resolution X-ray imaging". PhD thesis. Université de Lyon, 2016.
- [71] M. Berger et al. *NIST Standard Reference Database 8 (XGAM)*. 2010. URL: <https://www.nist.gov/pml/xcom-photon-cross-sections-database> (visited on 05/14/2021).
- [72] M. Cotte et al. "Cultural and Natural Heritage at the ESRF: Looking Back and to the Future". In: *Synchrotron Radiation News* 32.6 (2019), pp. 34–40.
- [73] P. Tafforeau et al. "Applications of X-ray synchrotron microtomography for non-destructive 3D studies of paleontological specimens". In: *Applied Physics A* 83.2 (2006), pp. 195–202.
- [74] C. Walsh et al. "Imaging intact human organs with local resolution of cellular structures using hierarchical phase-contrast tomography". In: *Nature methods* (2021), pp. 1–10.
- [75] *The human organ atlas*. URL: <https://human-organ-atlas.esrf.eu/> (visited on 12/29/2022).

- [76] M. Stampanoni et al. "High resolution X-ray detector for synchrotron-based microtomography". In: *Nuclear Instruments and Methods in Physics Research Section A: Accelerators, Spectrometers, Detectors and Associated Equipment* 491.1-2 (2002), pp. 291–301.
- [77] C. Ponchut. "Characterization of X-ray area detectors for synchrotron beam-lines". In: *Journal of synchrotron radiation* 13.2 (2006), pp. 195–203.
- [78] G. D. Boreman. *Modulation transfer function in optical and electro-optical systems*. Vol. 4. SPIE press Bellingham, WA, 2001.
- [79] Y. M. Zhu et al. "Modulation transfer function evaluation of linear solid-state x-ray-sensitive detectors using edge techniques". In: *Applied optics* 34.22 (1995), pp. 4937–4943.
- [80] E. Samei, M. J. Flynn, and D. A. Reimann. "A method for measuring the presampled MTF of digital radiographic systems using an edge test device". In: *Medical physics* 25.1 (1998), pp. 102–113.
- [81] C. F. Klemenz Rivenbark. "Liquid-Phase Epitaxy of Advanced Materials". In: *Springer Handbook of Crystal Growth*. Ed. by G. Dhanaraj et al. Berlin, Heidelberg: Springer Berlin Heidelberg, 2010, pp. 1041–1068. ISBN: 978-3-540-74761-1. DOI: 10.1007/978-3-540-74761-1_31. URL: https://doi.org/10.1007/978-3-540-74761-1_31.
- [82] R. t. Shannon and C. Prewitt. "Revised values of effective ionic radii". In: *Acta Crystallographica Section B: Structural Crystallography and Crystal Chemistry* 26.7 (1970), pp. 1046–1048.
- [83] R. Geller and E. Bunting. "The system PbO-B₂O₃". In: *J. Res. Natl. Bur. Stand* 18 (1937), pp. 585–593.
- [84] L. Wollensen et al. "Scintillating Thin Film Design for Ultimate High Resolution X-ray Imaging". In: *Journal of Materials Chemistry C* (2022).
- [85] G. Shirane and S. Hoshino. "On the phase transition in lead titanate". In: *Journal of the Physical Society of Japan* 6.4 (1951), pp. 265–270.
- [86] D. H. Kang et al. "Characteristics of (Pb_{1-x}Sr_x)TiO₃ thin film prepared by a chemical solution processing". In: *Materials research bulletin* 36.1-2 (2001), pp. 265–276.
- [87] H.-Y. Chen et al. "Characteristics of (Pb,Sr)TiO₃ thin films with various Sr content". In: *Journal of crystal growth* 308.1 (2007), pp. 213–217.
- [88] X. Xing et al. "Solid solution Pb_{1-x}Sr_xTiO₃ and its thermal expansion". In: *Journal of alloys and compounds* 360.1-2 (2003), pp. 286–289.
- [89] A. Kholkin et al. "Piezoelectric properties of Ca-modified PbTiO₃ thin films". In: *Applied physics letters* 69.23 (1996), pp. 3602–3604.
- [90] S Yakovlev et al. "Structural and dielectric properties of Er substituted sol-gel fabricated PbTiO₃ thin films". In: *Applied Physics A* 82.4 (2006), pp. 727–731.

- [91] S Iakovlev, C.-H. Solterbeck, and M Es-Souni. "Structural and dielectric characterization of sol-gel fabricated PbTiO_3 thin films doped with lanthanide ions". In: *Journal of electroceramics* 10.2 (2003), pp. 103–110.
- [92] L. Wollensen et al. "Tunable crystalline structure and electrical properties in $(\text{Pb,Sr})\text{TiO}_3$ films grown by Liquid Phase Epitaxy". In: *CrystEngComm* (2023).
- [93] S. Agostinelli et al. "GEANT4—a simulation toolkit". In: *Nuclear instruments and methods in physics research section A: Accelerators, Spectrometers, Detectors and Associated Equipment* 506.3 (2003), pp. 250–303.
- [94] J. Apostolakis et al. *Geant4 low energy electromagnetic models for electrons and photons*. Tech. rep. 1999.
- [95] V. Ivanchenko et al. "Recent improvements in geant4 electromagnetic physics models and interfaces". In: *Progress in nuclear science and technology* 2 (2011), pp. 898–903.
- [96] M. Berger et al. *NIST Standard Reference Database 124 (estar)*. 2017. URL: <https://physics.nist.gov/PhysRefData/Star/Text/ESTAR-u.html> (visited on 10/13/2021).
- [97] H. Hopkins. "The frequency response of a defocused optical system". In: *Proceedings of the Royal Society of London. Series A. Mathematical and Physical Sciences* 231.1184 (1955), pp. 91–103.
- [98] A. Rack. "Hard X-ray Imaging at ESRF: Exploiting Contrast and Coherence with the New EBS Storage Ring". In: *Synchrotron Radiation News* 33.3 (2020), pp. 20–28. ISSN: 0894-0886. DOI: 10.1080/08940886.2020.1751519. URL: <https://www.tandfonline.com/doi/full/10.1080/08940886.2020.1751519>.
- [99] F Riva et al. "Single crystal lutetium oxide thin film scintillators for X-ray imaging". In: *Journal of Instrumentation* 11.10 (2016), p. C10010.
- [100] F Riva et al. "Epitaxial growth of gadolinium and lutetium-based aluminum perovskite thin films for X-ray micro-imaging applications". In: *CrystEngComm* 18.4 (2016), pp. 608–615.
- [101] C. Chantler et al. *X-ray Form Factor, Attenuation and Scattering Tables, NIST Standard Reference Database 66*. 2005. URL: <https://physics.nist.gov/PhysRefData/FFast/html/form.html> (visited on 10/13/2021).
- [102] E. A. Merritt. *X-ray Absorption Edges*. 2010. URL: http://skuld.bmsc.washington.edu/scatter/AS_periodic.html (visited on 12/20/2022).
- [103] E Ziegler et al. "The ESRF BM05 metrology beamline: Instrumentation and performance upgrade". In: *AIP Conference Proceedings*. Vol. 705. 1. American Institute of Physics. 2004, pp. 436–439.
- [104] F Riva et al. "Single crystal lutetium oxide thin film scintillators for X-ray imaging". In: *Journal of Instrumentation* 11.10 (2016), p. C10010.

- [105] S. Pathak et al. "Crystal structure of monoclinic hafnia (HfO_2) revisited with synchrotron X-ray, neutron diffraction and first-principles calculations". In: *Acta Crystallographica Section C: Structural Chemistry* 76.11 (2020), pp. 1034–1042.
- [106] T. Thoř et al. "Europium-doped Lu_2O_3 phosphors prepared by a sol-gel method". In: *IOP Conference Series: Materials Science and Engineering*. Vol. 465. 1. IOP Publishing, 2018, p. 012009.
- [107] D. Nakauchi et al. "Photoluminescence and scintillation properties of Ce-, Pr-, and Tb-doped $(\text{Gd,Lu})_2\text{Hf}_2\text{O}_7$ crystals". In: *Sens. Mater* 34 (2022), p. 611.
- [108] A. Cecilia et al. "LPE grown LSO:Tb scintillator films for high-resolution X-ray imaging applications at synchrotron light sources". In: *Nuclear instruments and methods in physics research section A: Accelerators, spectrometers, detectors and associated equipment* 648 (2011), S321–S323.
- [109] B. Johnson and J. L. Jones. "Structures, Phase Equilibria, and Properties of HfO_2 ". In: *Ferroelectricity in Doped Hafnium Oxide: Materials, Properties and Devices* (2019), pp. 25–45.
- [110] H. Fujimori et al. "Cubic–tetragonal phase change of yttria-doped hafnia solid solution: high-resolution X-ray diffraction and Raman scattering". In: *Chemical physics letters* 346.3-4 (2001), pp. 217–223.
- [111] J. A. Krogstad et al. "Effect of yttria content on the zirconia unit cell parameters". In: *Journal of the American Ceramic Society* 94.12 (2011), pp. 4548–4555.
- [112] B. Mandal et al. "Preparation, XRD and Raman spectroscopic studies on new compounds $\text{RE}_2\text{Hf}_2\text{O}_7$ (RE= Dy, Ho, Er, Tm, Lu, Y): Pyrochlores or defect-fluorite?" In: *Journal of Solid State Chemistry* 179.7 (2006), pp. 1990–1994.
- [113] A. Saiki et al. "STRUCTURAL CHANGE OF C-RARE EARTH SESQUIOXIDES Yb_2O_3 AND Er_2O_3 AS A FUNCTION OF TEMPERATURE." In: *Yogyo Kyokai Shi/Journal of the Ceramic Society of Japan* 93.10 (1985), pp. 649–654.
- [114] H. J. Levinstein et al. "Growth of high-quality garnet thin films from supercooled melts". In: *Applied Physics Letters* 19.11 (1971), pp. 486–488.
- [115] M. Subramanian, G. Aravamudan, and G. S. Rao. "Oxide pyrochlores—a review". In: *Progress in Solid State Chemistry* 15.2 (1983), pp. 55–143.
- [116] E. Aleshin and R. Roy. "Crystal chemistry of pyrochlore". In: *Journal of the American Ceramic Society* 45.1 (1962), pp. 18–25.
- [117] C. Stanek et al. "Predicted structure and stability of $\text{A}_4\text{B}_3\text{O}_{12}$ δ -phase compositions". In: *Physical Review B* 80.17 (2009), p. 174101.
- [118] N. Nadaud et al. "Structural studies of tin-doped indium oxide (ITO) and $\text{In}_4\text{Sn}_3\text{O}_{12}$ ". In: *Journal of Solid State Chemistry* 135.1 (1998), pp. 140–148.
- [119] L. Lopato et al. "Synthesis and Properties of the Compounds $\text{M}_4\text{Zr}_3\text{O}_{12}$ and $\text{M}_4\text{Hf}_3\text{O}_{12}$ (M: Rare Earth Element)." In: *ChemInform* 22.52 (1991), no–no.

- [120] K. J. Kim et al. "Growth of Lu_2O_3 and HfO_2 Based High Melting Temperature Single Crystals by Indirect Heating Method Using Arc Plasma". In: *Crystals* 10.7 (2020), p. 619.
- [121] A. Shlyakhtina et al. " δ -Phase to defect fluorite (order–disorder) transition in the $\text{R}_2\text{O}_3\text{–MO}_2$ (R= Sc, Tm, Lu; M= Zr, Hf) systems". In: *Materials Research Bulletin* 46.4 (2011), pp. 512–517.
- [122] M. Glerup, O. F. Nielsen, and F. W. Poulsen. "The structural transformation from the pyrochlore structure, $\text{A}_2\text{B}_2\text{O}_7$, to the fluorite structure, AO_2 , studied by Raman spectroscopy and defect chemistry modeling". In: *Journal of Solid State Chemistry* 160.1 (2001), pp. 25–32.
- [123] M. Borik et al. "The impact of structural changes in $\text{ZrO}_2\text{–Y}_2\text{O}_3$ solid solution crystals grown by directional crystallization of the melt on their transport characteristics". In: *Materials Letters* 205 (2017), pp. 186–189.
- [124] H. Fukushima et al. "Investigation of scintillation properties of Hf-based oxide materials". In: *Japanese Journal of Applied Physics* (2022).
- [125] C LeLuyer et al. "HfO₂: X (X= Eu³⁺, Ce³⁺, Y³⁺) sol gel powders for ultradense scintillating materials". In: *The Journal of Physical Chemistry A* 112.41 (2008), pp. 10152–10155.
- [126] E. V. Van Loef et al. "Recent advances in ceramic scintillators". In: *MRS Online Proceedings Library* 1038 (2007), pp. 1–8.
- [127] L. Havlak et al. "Preparation and luminescence of $\text{Lu}_4\text{Hf}_3\text{O}_{12}$ powder samples doped by trivalent Eu, Tb, Ce, Pr, Bi ions". In: *Optical Materials* 32.10 (2010), pp. 1372–1374.
- [128] D. Nakauchi et al. "Scintillation properties of $\text{RE}_2\text{Hf}_2\text{O}_7$ (RE= La, Gd, Lu) single crystals prepared by xenon arc floating zone furnace". In: *Japanese Journal of Applied Physics* 57.10 (2018), p. 100307.
- [129] D. Nakauchi, G. Okada, and T. Yanagida. "Scintillation, OSL and TSL properties of yttria stabilized zirconia crystal". In: *Journal of Luminescence* 172 (2016), pp. 61–64.
- [130] M. Akatsuka et al. "Scintillation Properties of Yttrium-stabilized Zirconia Crystals Synthesized by the Floating-zone Method". In: *Sensors and Materials* 31.4 (2019), pp. 1289–1295.
- [131] X. Wu et al. "Luminescence properties and energy transfer of $\text{Tm}^{3+}\text{–Eu}^{3+}$ double-doped LiLaSiO_4 phosphors". In: *Journal of Materials Science: Materials in Electronics* 32.13 (2021), pp. 17662–17673.
- [132] V. V. Osiko, M. A. Borik, and E. E. Lomonova. "Synthesis of refractory materials by skull melting technique". In: *Springer handbook of crystal growth* (2010), pp. 433–477.

- [133] W. Barthlott and C. Neinhuis. "Purity of the sacred lotus, or escape from contamination in biological surfaces". In: *Planta* 202.1 (1997), pp. 1–8.
- [134] C. Neinhuis and W Barthlott. "Characterization and distribution of water-repellent, self-cleaning plant surfaces". In: *Annals of botany* 79.6 (1997), pp. 667–677.
- [135] Y. T. Cheng et al. "Effects of micro-and nano-structures on the self-cleaning behaviour of lotus leaves". In: *Nanotechnology* 17.5 (2006), p. 1359.
- [136] M. Halbwax et al. "Micro and nano-structuration of silicon by femtosecond laser: Application to silicon photovoltaic cells fabrication". In: *Thin solid films* 516.20 (2008), pp. 6791–6795.
- [137] M. C. Tathavadekar et al. "Enhancing efficiency of perovskite solar cell via surface microstructuring: Superior grain growth and light harvesting effect". In: *Solar Energy* 112 (2015), pp. 12–19.
- [138] M. M. Hamada et al. "Radiation damage of CsI(Tl) scintillators: blocking of energy transfer process of V_k centers to Tl^+ activators". In: *Nuclear Instruments and Methods in Physics Research Section A: Accelerators, Spectrometers, Detectors and Associated Equipment* 486.1-2 (2002), pp. 330–335.
- [139] D. Sengupta et al. "Bright Lu_2O_3 : Eu thin-film scintillators for high-resolution radioluminescence microscopy". In: *Advanced healthcare materials* 4.14 (2015), pp. 2064–2070.
- [140] Q. Li et al. "Development of ZnO-based nanorod arrays as scintillator layer for ultrafast and high-spatial-resolution X-ray imaging system". In: *Optics Express* 26.24 (2018), pp. 31290–31298.
- [141] Z. T. Karipbayev et al. "Optical, Structural, and Mechanical Properties of $Gd_3Ga_5O_{12}$ Single Crystals Irradiated with $84Kr^+$ Ions". In: *physica status solidi (b)* 259.8 (2022), p. 2100415.
- [142] S. D. Golze et al. "Synergistic roles of vapor-and liquid-phase epitaxy in the seed-mediated synthesis of substrate-based noble metal nanostructures". In: *Nanoscale* 13.47 (2021), pp. 20225–20233.

Appendix A

**Published: Scintillating thin film
design for ultimate high resolution
X-ray imaging, 2022**



Cite this: DOI: 10.1039/d2tc01274j

Scintillating thin film design for ultimate high resolution X-ray imaging†

Laura Wollesen,^{ab} Federica Riva,^{ab} Paul-Antoine Douissard,^a Kristof Pauwels,^a Thiery Martin^a and Christophe Dujardin^{ab}*

Thin single crystalline film (SCF) scintillators are essential when performing high resolution X-ray imaging with micron to sub-micron resolution. Especially when high energy X-rays are required for the experiment, the absorption efficiency is reduced considerably due to the limited thickness of the SCF. The absorption efficiency can be maximized by tailoring the SCF to have a high density and effective Z number. However, the quest to find these optimized scintillators is both time consuming and expensive when performing material screening. By combining simulations performed using the Geant4 package with subsequent analytical calculations, we propose an efficient simulation tool. Geant4 simulations predict the spatial distribution of the deposited energy in the SCF and the analytical calculations mimic the blurring introduced by the microscope optics. Using our simulation method, we evaluated the performances of a selection of scintillating screens, extending from state-of-the-art to various potential scintillators for incoming X-rays with energies between 5 and 100 keV. To efficiently evaluate and compare the performance of (potential) scintillators for high resolution X-ray imaging experiments, we propose a figure of merit, which includes the modulation transfer function at 500 lp mm⁻¹ (corresponding to 1 μm features) and the energy deposited in the SCF. Our simulations also demonstrate the crucial role of the substrate for the spatial resolution performance of the device.

Received 29th March 2022,
Accepted 14th May 2022

DOI: 10.1039/d2tc01274j

rsc.li/materials-c

Introduction

X-ray imaging techniques applied at synchrotron sources are powerful tools to investigate 3D structures without using destructive analysis. Two-dimensional pixelized detectors are today preferred for imaging experiments,^{1,2} but also for many other X-ray applications like absorption³ and various scattering experiments.^{1,2,4} Current X-ray imaging techniques can be coupling optics with the detector resolve micrometer details even of dense and/or large specimens such as fossils.^{5,6} A spectacular example that displays the performance of such a technique was recently presented. Intact human organs, such as a covid infected lung, were successfully imaged using hierarchical phase contrast tomography.⁷ By first scanning the whole lung with low resolution and subsequently going to higher resolution for the interesting areas regional changes in the tissue architecture of the covid infected lung was identified. For this experiment, the smallest voxel size was 2 μm, which

was sufficient to resolve the desired features at X-ray energies up to 78 keV. High X-ray energies are indeed required in such experiments in order to penetrate large (or very dense) specimens and reduce the sample absorption, which is otherwise detrimental to the phase contrast. Many X-ray imaging experiments often require a detector system with spatial resolution down to micrometer or even sub-micrometer scale. In addition, it must be efficient over a wide range of X-ray energies and X-ray fluxes to be applicable for different types of samples demanding low to very high X-ray energies to fit the requirements in terms of X-ray penetration in the object. Detectors based on an indirect X-ray detection scheme are the only candidates potentially meeting these challenging criteria. They combine a converter screen, microscope optics and an imaging Charged Coupled Device (CCD) or Complementary metal-oxide-semiconductor (CMOS) camera.^{8,9} The converter screen is a scintillator, which absorbs X-ray photons and converts them into multiple optical photons, generally UV or visible. An optical image is thus formed, which is enlarged by the optics and finally projected through the lenses onto the camera. Scintillators can be produced from a variety of materials and technologies. Powders or ceramic phosphors, such as Gd₂O₂S:Tb¹⁰ (often referred to as GOS, Gadox or P43), are often the most economical solution. They can provide a large field of view but do not combine efficiency and spatial resolution because of

^a ESRF – The European Synchrotron, 71 avenue des Martyrs, 38000 Grenoble, France

^b Institut Lumière Matière, UMR5306 Université Lyon 1-CNRS, Université de Lyon, 69622 Villeurbanne cedex, France. E-mail: christophe.dujardin@univ-lyon1.fr

† Electronic supplementary information (ESI) available. See DOI: <https://doi.org/10.1039/d2tc01274j>



their diffusive aspect. Crystalline microcolumnar scintillators allow for a thick scintillator and thereby an increased absorption efficiency at high X-ray energies while maintaining a decent spatial resolution. Nevertheless, existing technologies, such as microcolumnar CsI:Tl¹¹ and microstructured CsI:Tl screens,¹² do not currently reach micrometer spatial resolution. In order to reach micrometer to sub-micrometer spatial resolution in X-ray imaging experiments, single crystalline film (SCF) scintillators are therefore required.^{8,9,13} This could either be scintillators grown by liquid phase epitaxy^{14–18} or polished wafers.¹⁹ In this case, it is crucial that the film thickness remains in the order of the depth of focus of the optics, otherwise the image will be partly out of focus reducing the resolution. However, reducing the film thickness decreases the X-ray absorption in the SCF considerably. The optimum SCF scintillator thickness is therefore a balance between the desired SCF X-ray absorption efficiency and spatial resolution both with respect to the applied X-ray beam energies. The absorption efficiency of scintillators is proportional to the density and effective atomic number of the material,⁹ which is why in high resolution X-ray imaging communities there is an ongoing quest for thin films fulfilling these criteria.

The European Synchrotron Radiation Facility (ESRF) recently upgraded its storage ring to become the first high energy 4th generation synchrotron source in operation, the Extremely Brilliant Source (ESRF-EBS).²⁰ This upgrade led to drastic improvements in both coherence and brilliance of the source. As a result, the synchrotron beamlines are able to run experiments at higher X-ray energies (e.g. up to 350 keV at the new BM18 EBSL3 beamline,²¹ ESRF) following the 10 to 100-fold gain in X-ray flux. In order to fully exploit the possibilities offered by this new generation of synchrotrons and reach the ultimate performance of the scintillators by combining optimized spatial resolution and stopping power, investigation of a new generation of SCF scintillators is now required. Unfortunately the variety of parameters to take into account, combined with varying experimental conditions at the beamlines render the material screening not efficient.

Because preparing real scintillating screens is time and money consuming, we propose in this contribution an efficient simulation tool, which combines the spatial distribution of the deposited energy in SCFs and the impact of the optical transfer for various numerical apertures of the optics. Experiments have been performed to validate our approach. As a result, we define a figure of merit evaluating (potential) scintillator screens and propose a selection of optimal SCFs for various X-ray energy configurations for high resolution X-ray imaging experiments at synchrotrons. We also identify the crucial role of choosing the X-ray energy in relation to the K-edge energies of elements comprised in the SCF as well as the substrate, which both have a huge impact on the final image resolution and the energy deposition. The simulation tool presented here is a very useful guide for material selection toward the preparation of scintillating SCFs showing ultimate performances in the field of high resolution X-ray imaging.

Simulation tool

The proposed simulation tool aims at evaluating the X-ray imaging performances of the SCFs focusing on their spatial

resolution limitations and X-ray stopping power. The former depends on the absorption processes in the screen combined with the light collection through the optics and the latter on the energy deposition that is driven by the composition and the geometry of the screen, *i.e.* the SCF film and the substrate. The light yield, as well as the matching of emission wavelength with the cameras spectral sensitivity do not impact the spatial resolution, but only the statistics that can be compensated by increasing the exposure time. In addition, the light yield of scintillators often highly depends on the synthesis method leading potentially to various types of defects, impurities. For the state-of-the-art SCF scintillators it can therefore vary from sample to sample which cannot be predicted. Because we are focusing our interest to the energy deposition impact on the spatial resolution, we have considered the same proportionality factor between the deposited energy and the number of emitted optical photons.

It is based on Geant4, a well-established Monte Carlo simulation package²² and subsequent analytical calculations. Geant4 is predicting the spatial distribution of deposited energy in the SCF, which is a result of the material interacting with the incoming monochromatic X-rays. This results in a mapping of the deposited energy that provides the ultimate scintillator response. Analytical calculations then compute the blurring by optical transport of the resulting image including diffraction of light and out-of-focus contributions. The resulting Line Spread Function (LSF) and Modulation Transfer Function (MTF) can then be extracted. We assume to be in a configuration where the camera itself does not influence the spatial resolution, which is the case when the effective pixel size and pitch are significantly smaller than the resolution limit. An overall scheme representing the applied principles is presented in Fig. 1 and each step will be evaluated in the following sections.

Since we are targeting high resolution imaging at synchrotron, the simulations are performed using monochromatic X-rays at various energies (5–100 keV). In the case of fast or

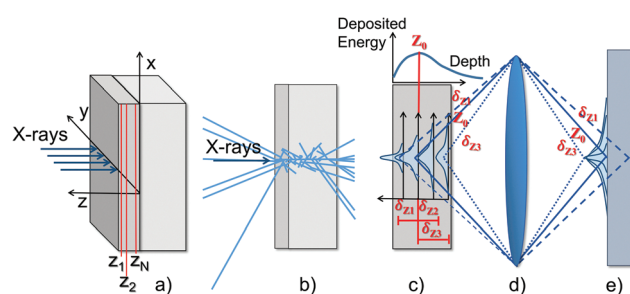


Fig. 1 Schematic presentations of: (a) Geometry and axis conversion applied in the simulation tool. (b) Geant 4, Monte Carlo simulation tracking the incident X-rays and the resulting secondary particles. The tracking reveal the spatial distribution of deposited energy in the SCF, which (we assume) correspond to the scintillator response. (c) Matrix describing the energy distribution for the depth of the scintillator. (d) Optics blurring estimated by taking the output from the simulation and use it as input for the analytical calculations. (e) Final response on the detector assumed as the sum of the response to every plane in the scintillator.



ultrafast imaging where the resolution can be compromised a pink beam (non-monochromatic X-ray beam) can be applied to obtain a higher X-ray flux.²³ However, this is out of scope for this study but could easily be implemented in the tool for a future new study.

Geant4 configuration

The SCF geometry is defined as a rectangular box of thickness t_s and a lateral length of 1.4 cm. For consistency, all simulations presented in this study were performed with $t_s = 5 \mu\text{m}$. The SCF is supported by a second $150 \mu\text{m}$ thick box representing the substrate corresponding to the currently applied substrates in high resolution X-ray imaging. The SCF has a surface normal to the incoming X-ray beam along the z -axis and when running the simulation a monochromatic one-dimensional X-ray beam distributed along the y -direction hits the SCF perpendicularly to its surface (see Fig. 1a).

For the energy deposition mapping, the size of the bins is defined as $0.1 \mu\text{m}$ in the x -direction and $0.2 \mu\text{m}$ in the z -direction. These bin sizes are a compromise between resolution and noise. In addition, since solid state aspects such as phonons and exciton migrations are not included in the Geant4 simulations a too small bin size could compromise the accuracy of the results. Due to the symmetry of the geometry no binning is set in the y -direction. The low energy Livermore Physics model^{24,25} was selected for the simulations. Every primary X-ray and generated secondary cascading particle are tracked individually (see Fig. 1b) with a production threshold for secondary particles at 250 eV. This threshold is not critical for our model since we are studying a diffraction-limited resolution, which is larger than the attenuation length of electrons at 250 eV.

The materials applied for the SCFs and substrates are defined by the density and the elemental stoichiometry. Depending on these two parameters the program estimates the probability of a particle traveling in the material to interact with a specific kind of atom and potentially deposit energy, while the concepts of crystals, namely the electronic band structure as well as phonons, are not included. For the state-of-the-art scintillators: GGG, LSO and LAG, the relevant λ_{emis} when they are doped with their usual dopants: GGG:Eu, LSO:Tb and LAG:Ce are applied. For the prospective scintillating SCFs, the λ_{emis} was chosen to be 615 nm. The emission from different dopants is rarely just one wavelength but for the sake of

simplicity of the optics calculations (described in next section) the commonly most intense or relevant emission wavelength for the specific dopant has been used. In the case of Europium the two main peaks are usually 595 and 710 nm but a wavelength of 615 nm was applied as a compromise. A list of all the materials and the information applied for the simulations and optics calculations (stoichiometry, density, λ_{emis} , refractive index) are summarized in Table 1.

The energy map provided by Geant4, is a two-dimensional matrix containing the spatial distribution of the energy deposited in the SCF. Every line corresponds to the LSF obtained at a different depth (z_i) in the SCF (Fig. 1c). The LSF and MTF as a function of the z -coordinate, the total LSF and MTF (without any consideration of the optical effects) can be deduced, as well as the energy deposited in the SCF as a function of depth ($E_{\text{dep}}(z_i)$).

Optics calculations

The modelling of the optical transport to the camera is based on the analytical model described by Hopkins,²⁶ which calculates the response of an aberration-free optical system. Taking into account the diffraction of light and the defect of focus (δz), the optical transfer function (OTF) of a defocused optical system is calculated as a convergent series of Bessel functions. The image from each plane is blurred by the optics as a function of the position of the plane along the thickness of the SCF (Fig. 1d). Assuming the system is focused at a certain position, z_0 (the focal plane), the planes within a thickness dz equal to the depth of field (DoF), around z_0 are projected as a focused image and thus only blurred by the diffraction of light. The planes outside dz are additionally blurred as a function of the distance from z_0 (denoted δz). The total MTF is then calculated as the average of every plane in the SCF, weighted by the deposited energy in the i^{th} slice (E_i^{dep}) while assuming the system is focused on the j^{th} bin in z :

$$\text{MTF}_{z_0=j}^{\text{tot}}(f) = \frac{\sum_{i=1}^N \text{MTF}_i^{\text{scint}}(f) \cdot \text{MTF}_i^{\text{opt}}(\delta z, f) \cdot E_i^{\text{dep}}}{\sum_{i=1}^N E_i^{\text{dep}}} \quad (1)$$

where N is the total number of bins along z , $\text{MTF}_i^{\text{scint}}(f)$ is here the MTF calculated from the energy deposited in the i^{th} slice obtained from the Geant4 simulations, $\text{MTF}_i^{\text{opt}}(f)$ is the modulus of the OTF and f is the spatial frequency in the object

Table 1 Materials and their short names, chemical formula, dopant and corresponding emission wavelengths, the density, refractive index and substrate applied in the Geant4 simulations. In reality the λ_{emis} is not a single line but composed of several lines or a broad band (indicated by *). Here is only the applied wavelength for the simulations indicated

Name	Short name	Chemical formula	Dopant	λ_{emis} [nm]	Density [g cm^{-3}]	n	Substrate
Gd–Al–Perovskite	GAP	GdAlO ₃	Eu	615	7.50	1.97	YAP
Lu–Oxide	Lu ₂ O ₃	Lu ₂ O ₃	Eu	615	9.50	1.935	Lu ₂ O ₃
Lu–Orthosilicate	LSO	Lu ₂ SiO ₅	Tb	550	7.40	1.82	YbSO
Lu–Al–Garnet	LAG	Lu ₃ Al ₅ O ₁₂	Ce	540*	6.73	1.84	YAG
Gd–Ga–Garnet	GGG	Gd ₃ Ga ₃ O ₁₂	Eu	615	7.10	1.97	GGG
Gd–Lu–Al–Perovskite	GdLuAP	Gd _{0.5} Lu _{0.5} AlO ₃	Eu	615	8.00	1.935	YAP
Pb–Titanate	PTO	PbTiO ₃	Eu	615	7.95	2.70	SrTiO ₃



plane. The position of z_0 was selected by calculating the maximum total MTF as a function of the focus position along z . This then provides the final estimate of the actual response, as seen by the imaging camera (Fig. 1e).

Results and discussion

Investigated materials

The materials under investigation in this study are the state-of-the-art SCF scintillators (formulas and applied parameters are given in Table 1): LSO:Tb on YbSO, GGG:Eu on GGG and freestanding LAG:Ce that are intensively applied on X-ray imaging beamlines.²⁷ LAG:Ce can also be grown by Liquid Phase Epitaxy (LPE) on YAG substrates¹⁷ and for the sake of comparing the different SCFs it is here simulated on a YAG substrate. Furthermore, the three more recently explored high density SCFs: Lu₂O₃:Eu on undoped Lu₂O₃,²⁸ GAP:Eu on undoped YAP²⁹ and PbTiO₃:Eu on undoped SrTiO₃ are included as prospective materials for ultimate high density SCFs.

Energy deposition

As discussed above, achieving ultimate spatial resolution ($\sim 1 \mu\text{m}$ or better) requires SCFs of thickness thinner than $10 \mu\text{m}$ rendering the X-ray absorption critical, especially when applying high energy X-rays. The X-ray absorption efficiency affects the Detective Quantum Efficiency (DQE) of the system and should therefore be considered when examining the overall performance of SCF potential scintillators.

In low dimensional systems, the effective energy deposition differs from the attenuated energy due to the escape of X-ray fluorescence and even hot electrons and Auger electrons in the particular case of nanoscintillators.^{30,31} The effective energy deposited in the investigated SCFs has been extracted from our simulations at X-ray energies from 15 to 100 keV (Fig. 2b). Its comparison to the attenuated energy in the freestanding SCFs using the photon cross section database from NIST³² (Fig. 2a) highlights notable differences at high energy, mainly at

energies higher than the K-edge, where the escape of secondary X-rays increases for both the film and substrate.

The attenuation as computed from the photon cross section provides a fair approximation of the effective deposited energy at X-ray energies below the K-edge energies of the high Z elements comprised in the SCF. When the X-ray energy exceeds these K-edge energies in the SCF, the modelling of X-ray fluorescence photons is thus needed to obtain an accurate estimate of the energy deposit. Secondary X-rays can indeed easily escape the thin SCF and do thereby not deposit their energy in the SCF. On the opposite, when the X-ray photons interact in the substrate, the secondary particles generated there can possibly reach the SCF and deposit energy, potentially far from the primary interaction.

Spatial resolution and contrast

The MTF describes the spatial response of a system by combining the concept of resolution and contrast. The spatial resolution of a system quantifies the smallest features that can be fully resolved. It generally corresponds to the spatial frequency for which the MTF equals $\sim 10\%$ taking into account the definition of the Rayleigh criteria for the diffraction limit. The contrast or modulation is defined as:³³

$$C(\nu) = \frac{I_{\max} - I_{\min}}{I_{\max} + I_{\min}} \quad (2)$$

for alternate black and white lines at a given frequency (ν). I_{\max} and I_{\min} are the corresponding maximum and minimum intensities (number of optical photons detected).

The MTF basically provides the transmission of contrast through the system at different spatial frequencies. The counterpart of the MTF, the LSF is helpful to further understand specific trends in the MTFs because it directly shows the spatial distribution of detected optical photons around the position of the primary interaction between the X-ray photon and the SCF. The energy of the incoming X-rays has a significant impact on the spatial distribution of deposited energy in the SCF and thereby the obtainable spatial resolution and contrast of the final image. Generally, when increasing the X-ray energy, the generated secondary particles deposit energy at an increasing distance from the initial point of interaction, resulting in a decreasing contrast. It is thus crucial to consider the major impacts on the contrast occurring when applying X-rays of energies close to the K-edge of the elements comprised in the SCF and substrate. In the next subsections we will then present and discuss quantitative improvement and degradation of the contrast for a selected set of relevant materials, restricting the description to the energy deposition effect.

Influence of X-ray fluorescence

We performed simulations of the standard SCF, namely LAG:Ce supported by YAG substrate to highlight the effects on the LSF and MTF when imaging is performed with X-ray energies below and above the K-edge of the heaviest element of the substrate (resp. the SCF), here Y at 17.04 keV (resp. Lu at 63.31 keV).

As shown in Fig. 3b, increasing the X-ray energy above the substrate K-edge of Y initiates a sharp decrease of $\sim 20\%$ in

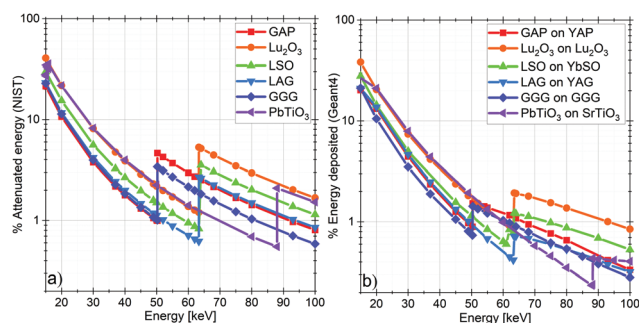


Fig. 2 (a) Percentage of the incident beam energy attenuated by various kinds of $5 \mu\text{m}$ thick SCFs, calculated using data from the NIST database.³² (b) Percentage of the incident beam energy deposited in various $5 \mu\text{m}$ SCFs supported by $150 \mu\text{m}$ substrates, calculated by tracking all the secondary X-rays and electrons using our application based on the Monte Carlo Geant4 toolkit.



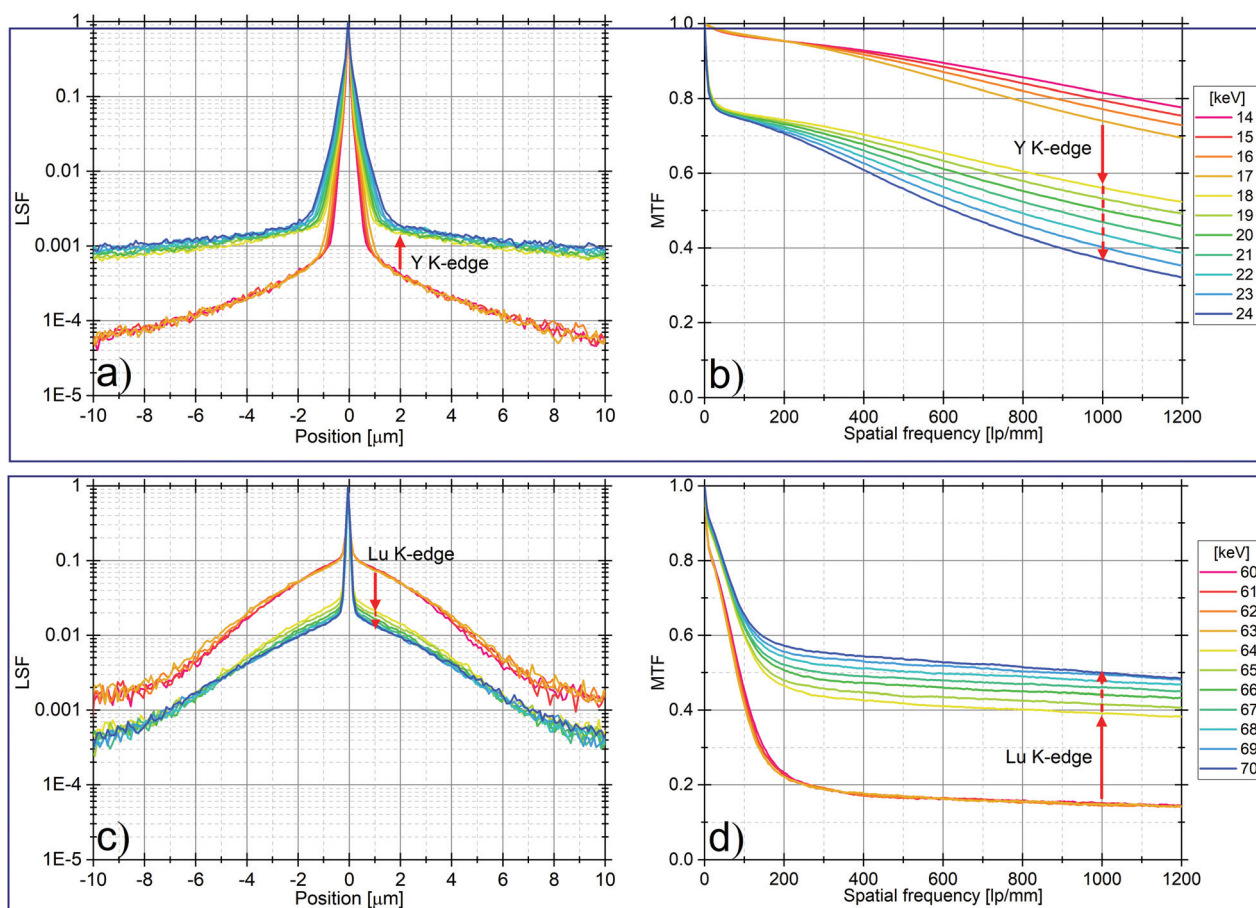


Fig. 3 Simulated LSFs (left) and MTFs (right) for a 5 μm LAG:Ce SCF supported by 150 μm YAG substrate. (a and b) X-ray energies from 14 to 24 keV. K-edge energy of Y is 17.04 keV. (c and d) X-ray energies from 60–70 keV. K-edge of Lu is 63.3 keV.

contrast. This drop in the MTF close to 0 lp mm^{-1} , corresponds to the increase of the tails in the LSF (Fig. 3a).

By isolating the contributions from the different particle types of the LSF, we note that a significant number of secondary X-rays deposit energy far from the initial interaction point when the incoming X-ray energy exceed the substrate K-edge. This is in agreement with fluorescent X-rays generated in the substrate and then interacting in the SCF. The isolated LSFs representing the contributions from the different particle types is presented in Fig. S1 (ESI[†]).

As shown in Fig. 3d, when exceeding the Lu K-edge energy there is a sudden increase in contrast of $\sim 25\%$ of the MTF. Further increase of the X-ray energy induces a continuous increase in contrast until it stabilizes around 70 keV with an additional gain of $\sim 10\%$. In the corresponding LSF (Fig. 3c) the effect is observed as a sudden decrease of the tails followed by a continuous decrease between 0.3 and 4 μm with increasing X-ray energy. The isolated LSFs for the contribution of different particles types are presented in Fig. S2 (ESI[†]). All types of generated electrons (primary and secondary photoelectrons and resulting electrons from electron–electron scattering) deposit more of their energy very close to the initial point of interaction when exceeding the SCF K-edge.

The sudden decrease of the tails is the result of the increased probability of the photoelectric effect when the incoming X-ray beam have energy above the SCF K-edge. This effect is especially present after normalization of the LSF, which is how to normally display it. The X-ray fluorescence mostly escapes from the SCF and do not contribute considerably to the image. Meanwhile, the photoelectrons have a sufficiently low energy resulting in short attenuation length, leading them to deposit energy very close to the initial point of interaction.

The continuous improvement is caused by photoelectrons created from primary X-ray interactions and subsequent electrons from electron–electron scattering events. We ascribe this effect to the increase of local energy deposition due to the increase of the X-ray beam energy. Indeed, the energy of the primary photoelectron will be ~ 0.7 to 6.7 keV (assuming they are created from 64–70 keV primary X-ray photons and the K-shell of Lu) the attenuation length will typically be shorter than 0.5 μm (CSDA, NIST³⁴), thereby containing the resulting energy deposit very close to the initial point of interaction.

Combined influence of SCF and substrate

We demonstrated above the opposite contribution of the SCF and the substrate on the MTF when the X-ray energy exceeds



the K-edge of their heaviest element. For some scintillators, the substrate and the host structure of the SCF can be of the same type, such as GGG:Eu supported by undoped GGG substrates. For this particular scintillating screen, we have simulated the LSF and MTF for X-ray energies around 48–58 keV (Gd K-edge at 50.24 keV). Fig. 4 shows that when exceeding the Gd K-edge it combines the two opposite effects, but acting at different frequencies, as observed in the previous section. There is the sharp decrease of the MTF at low frequencies below 150 lp mm^{-1} caused by the substrate fluorescence, while at higher frequencies the contrast is significantly increased owing to the photoelectrons created in the SCF. When further increasing the X-ray energy, the contrast above $\sim 200 \text{ lp mm}^{-1}$ is slowly increased due to the increased energy deposition close to the initial point of interaction until it stabilizes and starts to decrease again for higher energies.

When the X-ray energy exceeds the Gd K-edge energy two effects occur. First, the X-ray absorption cross section increases by about one order of magnitude, and second the probability of X-ray fluorescence also drastically increases. If absorption occurs in the substrate, part of the resulting X-ray fluorescence may be reabsorbed far from the primary interaction in the SCF, resulting in degradation of the low frequency contrast. When absorption occurs in the SCF, the dominant effect is the significant improvement of the absorption, generating photoelectrons interacting almost locally due to the small mean free path of such electrons, which corresponds to the ideal situation (high absorption and local energy deposition). Of course, X-ray fluorescence also occurs but its re-absorption will mainly occur out of the SCF. In this latter case, an improved contrast at high frequency is expected, and the degradation of the image is dominated by the optics. Further, the continuous improvement when the X-ray energy increases above the K-edge is caused by the increase of the local energy deposition.

Blurring by optics

The deposited energy is converted into optical photons in the SCF through the scintillation mechanism. Due to the thickness

of the SCF, the scintillation “image” is blurred while projected onto the camera by the microscope optics. Fig. 5 demonstrates the significant contribution of this blurring. At low energies especially, the optical blurring strongly degrades the exceptional spatial resolution that would be expected by only taking into account the energy deposit contribution. At high energies however, most of the MTF degradation is caused by the energy distribution in the SCF. Notice at 60 keV the MTF is better for GGG compared to LSO, especially without blurring, since we are above the Gd K-edge but still below the Lu K-edge. In the figure, a numerical aperture (NA) of 0.80 is chosen. For sake of completeness, the influence of the NA at various X-ray energies is presented in Fig. S3 (ESI†).

Figure of merit

It is not straightforward to evaluate the achievable performance of scintillating screens due to the overwhelming combination of factors which influence it. We thus propose a figure of merit (FoM) in order to estimate the best compromise between a sharp image and an efficient detector:

$$\text{FoM}(E) = \text{MTF}_{500 \text{ lp mm}^{-1}}^{\text{NA}=0.40}(E) \times E_{\text{dep}}(E) \quad (3)$$

This allows us to evaluate the materials as a function of X-ray energy, while simultaneously considering the spatial resolution, contrast (including blurring by optics) and absorption efficiency. The value of the MTF at 500 lp mm^{-1} is applied because it describes how well $1 \mu\text{m}$ sized features are resolved. The performance of the complete detector system will of course be best described by the Detective Quantum Efficiency (DQE).

The figure of merit for the evaluated SCFs are presented at energies from 5 to 100 keV in Fig. 6. We can see that below 50 keV and from 64 to 95 keV, Lu_2O_3 is material which performs the best, while between 50 keV and 64 keV GAP is superior. PbTiO_3 is similar to Lu_2O_3 between 20 and 50 keV and best above 95 keV.

The proposed figure of merit is the appropriate tool for investigating unexplored materials and find better alternatives to the state-of-the-art scintillators. It allows to perform a thorough screening of materials before attempting to produce them but is of course not able to predict if a material will be scintillating in practice. However, this figure of merit gives a

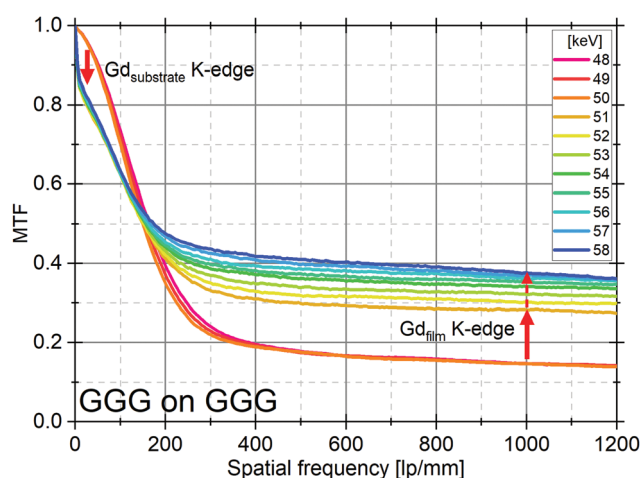


Fig. 4 Simulated MTFs for a $5 \mu\text{m}$ GGG:Eu SCF supported by $150 \mu\text{m}$ GGG substrate. X-ray energies from 48 to 58 keV. K-edge energy of Gd is 50.24 keV.

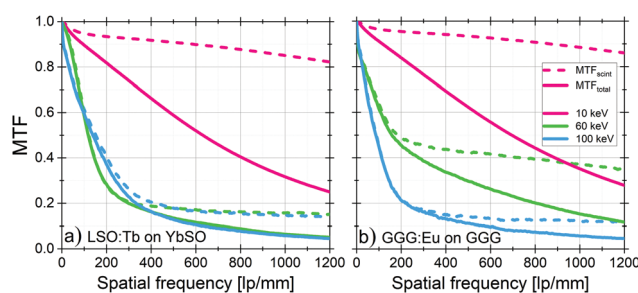


Fig. 5 MTF_{tot} (solid lines) and $\text{MTF}_{\text{scint}}$ (dashed lines) for $5 \mu\text{m}$ films supported by $150 \mu\text{m}$ substrates, evaluated for $\text{NA} = 0.80$ at different X-ray energies. The corresponding SCF, substrate and X-ray energies selected for the simulations are indicated in the figure.



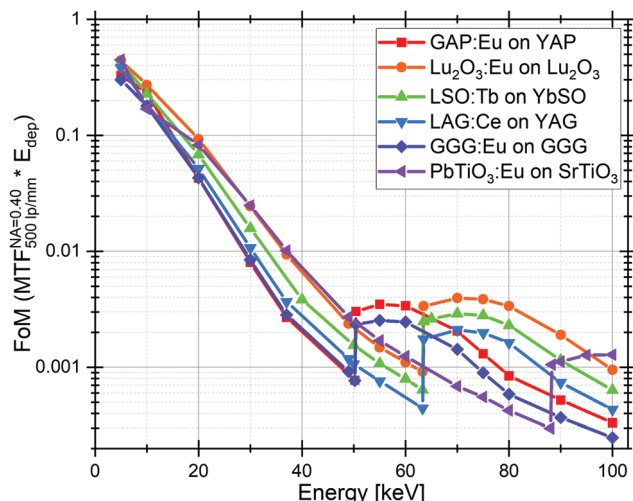


Fig. 6 The proposed figure of merit (FoM) calculated from the contrast in the MTF blurred by optics ($NA = 0.40$) at 500 lp mm^{-1} and the energy deposited in the SCF. Values are extracted from simulations at X-ray energies from 5–100 keV for $5 \mu\text{m}$ SCFs supported by $150 \mu\text{m}$ substrates.

limited vision of the potential scintillator performance especially because it only takes into account the MTF for a single spatial frequency (500 lp mm^{-1}). A more fulfilling figure of merit could be created by using an integration of the MTF over all spatial frequencies instead. For illustration, figure of merit are presented at 100 and 1000 lp mm^{-1} in Fig. S4 (ESI[†]).

Additionally, to truly examine and compare already existing scintillators one should consider other parameters like the light yield and adequate matching of the emission spectrum with the spectral sensitivity of the applied detector.

Experimental validation

In order to validate the proposed simulation method, MTF of several scintillating SCFs was evaluated experimentally with the slanted edge method.^{35,36} A $525 \mu\text{m}$ thick GaAs edge carefully cleaved and positioned 1–3 mm away from the scintillator was used to absorb part of the X-ray beam. Acquired edge images were corrected by flat-field and dark images and the edge spread function (ESF) was computed. Subsequently, the

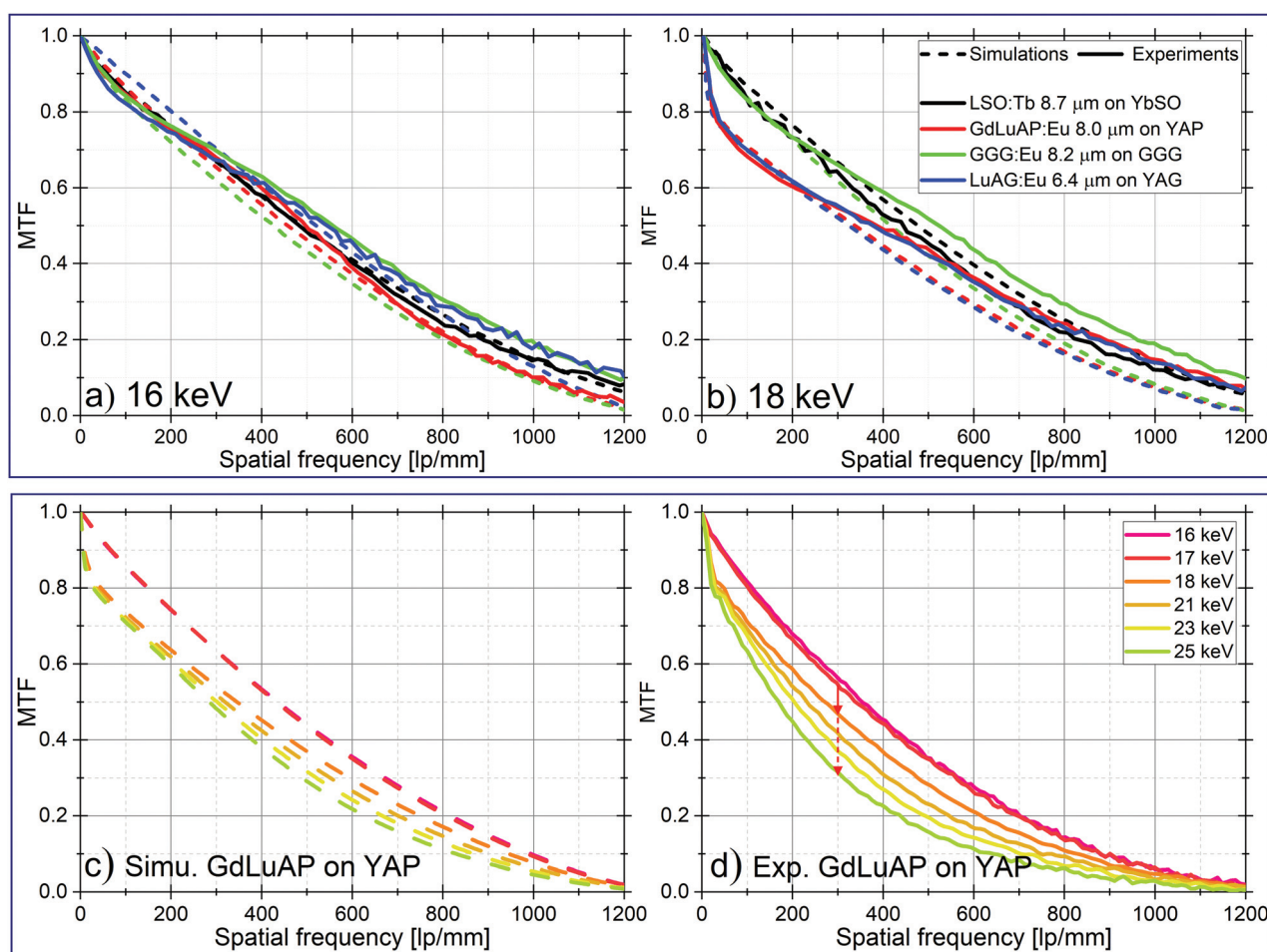


Fig. 7 Experimentally measured (continuous lines) and simulated (dashed lines) MTFs for various scintillating SCFs supported by substrates at (a) 16 keV and (b) 18 keV. MTFs obtained from simulations (c) and experiments (d) for an $\sim 11.5 \mu\text{m}$ GdLuAP:Eu scintillating SCF supported by $150 \mu\text{m}$ YAP, at X-ray energies from 16 to 25 keV. All experiments were performed with monochromatic X-ray beam at BM05, ESRF.



derivative gives the LSF and a Fast Fourier Transform provides the MTF.³³ Fig. S5 (ESI[†]) gives an illustration of the method.

The complete detector system comprises: the scintillator under investigation combined with microscope optics (numerical aperture (NA) of 0.4 and 10× magnification) followed by a 3.3× eyepiece magnification and either a PCO2000 camera (Fig. 7a and b) or PCO edge 4.2 (Fig. 7d) having respectively a pixel size of 7.4 μm and 6.5 μm. The measurements were performed using monochromatic synchrotron radiation at the beamline BM05 at the ESRF using a Si(111) crystal with energy resolution of $\Delta E/E \approx 10^{-4}$.³⁷

Fig. 7a and b show good agreement between simulations and experimental data. As predicted by the simulations, the MTFs of all the considered scintillators are similar at 16 keV (Fig. 7a) while at 18 keV (Fig. 7b) a sudden reduction of the contrast close to 0 lp mm⁻¹ is observed for scintillators with Y-based substrates (K-edge of Y is 17.04 keV). It is noteworthy that some of the experimentally obtained MTFs in Fig. 7 are out-competing the simulations. This can be attributed to the effect of phase contrast which artificially enhances the contrast and thereby the MTF.

In order to further validate the predicted behavior of the MTFs at energies around the substrate K-edge we have applied the slanted edge method on a ~11.5 μm GdLuAP:Eu SCF supported by 150 μm YAP substrate.²⁹ The experimental MTFs in Fig. 7b found for X-ray energies from 16–25 keV are again in good agreement with the simulations. The MTF undergoes a sharp decrease close to 0 lp mm⁻¹ when exceeding the substrate K-edge energy. When further increasing the X-ray energy, the contrast decreases also as expected. However, when carefully comparing the MTFs from simulations (Fig. 7c) with the experiments (Fig. 7d) a difference up to 15% in contrast is observed. Several reasons can explain this. GdLuAP SCFs are found to undergo birefringence, which degrade the MTF. By rotating the SCF perpendicular to the X-ray beam, the degree of birefringence varies and the optimum MTF affected the least by birefringence can thereby be found.²⁹ The MTFs in Fig. 7(d) is recorded at what we found to be the optimum rotation angle. Since the rotation is manually adjusted the truly optimum angle may not be used, which then results in a slight degradation of the MTF. Furthermore, the YAP substrate scintillates slightly and to filter out this emission a bandwidth filter (634 nm, FWHM: 70 nm) was inserted in the optical path. If part of this emission was not fully filtered out it could have partly degraded the MTF. Also, the observed deviation between simulations and experiments can simply be caused by a slight defect of focus in the optics. The experiment nevertheless confirm in a large extent the observed trends in the simulations.

Conclusion

We presented the principles of our simulation tool based on Geant4 and subsequent analytical calculations and applied it to investigate the behavior of the MTFs especially at X-ray energies

close to the K-edges of elements in the SCF and substrate. Exceeding the K-edge energy of an element in the SCF gives rise to an increase in the MTF above ~200 lp mm⁻¹ whereas for a substrate element the MTF is reduced close to 0 lp mm⁻¹. These trends are assigned to the increased probability of the photoelectric effect combined with short attenuation length of the created photoelectrons and substrate fluorescence, respectively. The latter trend was confirmed by experimental data collected using monochromatic synchrotron radiation and we plan to measure and validate the effect around the K-edge energy of high Z elements comprised in the SCF in future work. Simulations including blurring introduced by microscope optics was presented and shortly discussed. It is clear that especially at low energy the optics strongly reduce the MTF, where at higher energies most of the degradation is caused by the energy distribution in the SCF. We also proposed a figure of merit to evaluate potential scintillators in terms of spatial resolution and contrast but also absorption efficiency. Of the investigated SCFs, Lu₂O₃ and PbTiO₃ may outperform the other investigated SCFs below 50 keV and above 64 keV while between 50 and 64 keV GAP is the best compromise. At 100 keV and above PbTiO₃ is the better choice. We believe that such an approach is a great support for the scintillating screen development aiming to reach ultimate performances.

Author contributions

L. W. and F. R. designed and conducted the modeling of the imaging response of the thin scintillating films. F. R., and P.-A. D. fabricated the films for experimental validation. L. W., P.-A. D. and K. P. performed the X-ray imaging validation experiments and data analysis. T. M. and C. D. conceived and designed the project.

Conflicts of interest

There are no conflicts to declare.

Acknowledgements

Part of this work was performed in the frame of the ESRF-EBS Detector Development Plan (DDP), T1C: High resolution scintillators for imaging detectors. The authors thank the beamline staff at BM05, ESRF.

Notes and references

- M. Kutsal, P. Bernard, G. Berruyer, P. Cook, R. Hino, A. Jakobsen, W. Ludwig, J. Ormstrup, T. Roth and H. Simons, *et al.*, *IOP Conf. Ser.: Mater. Sci. Eng.*, 2019, p. 012007.
- J. Wright, C. Giacobbe and M. Majkut, *Curr. Opin. Solid State Mater. Sci.*, 2020, **24**, 100818.



- 3 I. Kantor, J.-C. Labiche, E. Collet, L. Siron, J.-J. Thevenin, C. Ponchut, J. Borrel, T. Mairs, C. Marini and C. Strohm, *et al.*, *J. Synchrotron Radiat.*, 2014, **21**, 1240–1246.
- 4 T. Narayanan, M. Sztucki, T. Zinn, J. Kieffer, A. Homs-Puron, J. Gorini, P. Van Vaerenbergh and P. Boesecke, *J. Appl. Crystallogr.*, 2022, **55**, 98–111.
- 5 M. Cotte, P.-O. Autran, C. Berruyer, C. Dejoie, J. Susini and P. Tafforeau, *Synchrotron Radiat. News*, 2019, **32**, 34–40.
- 6 P. Tafforeau, R. Boistel, E. Boller, A. Bravin, M. Brunet, Y. Chaimanee, P. Cloetens, M. Feist, J. Hoszowska and J.-J. Jaeger, *et al.*, *Appl. Phys. A*, 2006, **83**, 195–202.
- 7 C. Walsh, P. Tafforeau, W. Wagner, D. Jafree, A. Bellier, C. Werlein, M. Kühnel, E. Boller, S. Walker-Samuel and J. Robertus, *et al.*, *Nat. Methods*, 2021, 1–10.
- 8 P. A. Douissard, A. Cecilia, X. Rochet, X. Chapel, T. Martin, T. van de Kamp, L. Helfen, T. Baumbach, L. Luquot, X. Xiao, J. Meinhardt and A. Rack, *J. Instrum.*, 2012, **7**, P09016–P09016.
- 9 A. Koch, C. Raven, P. Spanne and A. Snigirev, *JOSA A*, 1998, **15**, 1940–1951.
- 10 E.-J. Popovici, L. Muresan, A. Hristea-Simoc, E. Indrea, M. Vasilescu, M. Nazarov and D. Y. Jeon, *Opt. Mater.*, 2004, **27**, 559–565.
- 11 S. R. Miller, V. Gaysinskiy, I. Shestakova and V. V. Nagarkar, *Penetrating Radiation Systems and Applications VII*, 2005, p. 59230F.
- 12 A. Sahlholm, O. Svenonius, P. Wiklund and J. Linnros, *Selection of Dimensions and Geometry of a Structured Scintillator for X-ray Imaging*, 2009.
- 13 T. Martin and A. Koch, *J. Synchrotron Radiat.*, 2006, **13**, 180–194.
- 14 A. Cecilia, V. Jary, M. Nikl, E. Mihokova, D. Hänschke, E. Hamann, P.-A. Douissard, A. Rack, T. Martin and B. Krause, *et al.*, *Radiat. Meas.*, 2014, **62**, 28–34.
- 15 P.-A. Douissard, A. Cecilia, T. Martin, V. Chevalier, M. Couchaud, T. Baumbach, K. Dupré, M. Kühbacher and A. Rack, *J. Synchrotron Radiat.*, 2010, **17**, 571–583.
- 16 T. Martin, P.-A. Douissard, M. Couchaud, A. Cecilia, T. Baumbach, K. Dupre and A. Rack, *IEEE Trans. Nucl. Sci.*, 2009, **56**, 1412–1418.
- 17 P.-A. Douissard, T. Martin, F. Riva, Y. Zorenko, T. Zorenko, K. Paprocki, A. Fedorov, P. Bilski and A. Twardak, *IEEE Trans. Nucl. Sci.*, 2016, **63**, 1726–1732.
- 18 Y. Zorenko, P.-A. Douissard, T. Martin, F. Riva, V. Gorbenko, T. Zorenko, K. Paprocki, A. Iskalieva, S. Witkiewicz and A. Fedorov, *et al.*, *Opt. Mater.*, 2017, **65**, 73–81.
- 19 J. Tous, K. Blazek, M. Nikl and J. Mares, *J. Phys.: Conf. Ser.*, 2013, 192017.
- 20 P. Raimondi, *Synchrotron Radiat. News*, 2016, **29**, 8–15.
- 21 D. Chenevier and A. Joly, *Synchrotron Radiat. News*, 2018, **31**, 32–35.
- 22 S. Agostinelli, J. Allison, K. A. Amako, J. Apostolakis, H. Araujo, P. Arce, M. Asai, D. Axen, S. Banerjee and G. Barrand, *et al.*, *Nucl. Instrum. Methods Phys. Res., Sect. A*, 2003, **506**, 250–303.
- 23 A. Mittone, L. Fardin, F. Di Lillo, M. Fratini, H. Requardt, A. Mauro, R. A. Homs-Regojo, P.-A. Douissard, G. E. Barbone and J. Stroebel, *et al.*, *J. Synchrotron Radiat.*, 2020, **27**, 1347–1357.
- 24 J. Apostolakis, M. Pia, S. Giani, P. Nieminen, M. Maire and L. Urban, *Geant4 low energy electromagnetic models for electrons and photons*, 1999.
- 25 V. Ivanchenko, J. Apostolakis, A. Bagulya, H. B. Abdelouahed, R. Black, A. Bogdanov, H. Burkhard, S. Chauvie, G. A.-P. Cirrone and G. Cuttone, *et al.*, *Prog. Nuclear Sci. Technol.*, 2011, **2**, 898–903.
- 26 H. Hopkins, *Proc. R. Soc. London, Ser. A*, 1955, **231**, 91–103.
- 27 A. Rack, *Synchrotron Radiat. News*, 2020, **33**, 20–28.
- 28 F. Riva, T. Martin, P. Douissard and C. Dujardin, *J. Instrum.*, 2016, **11**, C10010.
- 29 F. Riva, P.-A. Douissard, T. Martin, F. Carlá, Y. Zorenko and C. Dujardin, *CrystEngComm*, 2016, **18**, 608–615.
- 30 A.-L. Bulin, A. Vasil'ev, A. Belsky, D. Amans, G. Ledoux and C. Dujardin, *Nanoscale*, 2015, **7**, 5744–5751.
- 31 A.-l. Bulin, M. Broekgaarden, F. Chaput, V. Baisamy, J. Garrevoet, B. Busser, D. Brueckner, A. Youssef, J.-l. Ravanat, C. Dujardin, V. Mottoâ-Ros, F. Lerouge, S. Bohic, L. Sancey and H. Elleaume, *Adv. Sci.*, 2020, **2001675**, 2001675.
- 32 M. Berger, J. Hubbell, S. Seltzer, J. Chang, R. Coursey, J. S. Sukumar, D. Zucker and K. Olsen, NIST Standard Reference Database 8 (XGAM), 2010, <https://www.nist.gov/pml/xcom-photon-cross-sections-database>.
- 33 G. D. Boreman, *Modulation transfer function in optical and electro-optical systems*, SPIE Press, Bellingham, WA, 2001, vol. 4.
- 34 M. Berger, J. Coursey, M. Zucker and J. Chang, NIST Standard Reference Database 124 (estar), 2017, <https://physics.nist.gov/PhysRefData/Star/Text/ESTAR-u.html>.
- 35 Y. M. Zhu, V. Kaftandjian, G. Peix and D. Babot, *Appl. Opt.*, 1995, **34**, 4937–4943.
- 36 E. Samei, M. J. Flynn and D. A. Reimann, *Med. Phys.*, 1998, **25**, 102–113.
- 37 E. Ziegler, J. Hoszowska, T. Bigault, L. Peverini, J. Massonnat and R. Hustache, *AIP Conf. Proc.*, 2004, 436–439.








Appendix B

Published: Tunable crystalline structure and electrical properties in (Pb,Sr)TiO₃ films grown by Liquid Phase Epitaxy, 2023



Cite this: DOI: 10.1039/d3ce00020f

Tunable crystalline structure and electrical properties of (Pb,Sr)TiO₃ films grown by liquid phase epitaxy†

 Laura Wollesen, *^{ab} Paul-Antoine Douissard,^a Ingrid C. Infante, ^c
 Jeremie Margueritat, ^b Brice Gautier, ^c
 Thierry Martin^a and Christophe Dujardin *^b

Ferroelectric epitaxial films of Pb_{1-x}Sr_x TiO₃ (PST) with nominal compositions of $x = 0, 0.33, 0.39,$ and $0.43,$ supported by (100) SrTiO₃ (STO) substrates, have been successfully grown by liquid phase epitaxy (LPE). Energy dispersive X-ray measurements performed on selected films reveal an increase in the Sr-content for each nominal increase in the growth solution. Structural and spectroscopic investigations, from X-ray diffraction and Raman spectroscopy, unveil that all of the PST films possess a tetragonal structure at room temperature, and with increasing Sr-content, the tetragonality and Curie temperature decrease accordingly with values approaching those of reference bulk compound materials. These results confirm we achieved full control of the composition, structure, and transition temperature of the ferroelectric films, by adapting the nominal composition of the LPE growth solution, performing epitaxial growth while maintaining the bulk-like properties. Finally, using piezoresponse force microscopy, various nanoscale polar domain configurations for the PST epitaxial films were disclosed. This indicates that films having a higher Sr content can have polar domain configurations compatible with different a/c and c nanodomains. This work underlines the usefulness of the LPE method for controlling tetragonal ferroelectric PST film growth, in order to tune the nanoscale polarisation landscape in films having bulk-like structures and ferroelectric transition temperatures. This opens a path to new investigations fully exploiting the combined advantages of multiple nanoscale electrical boundary configurations within bulk-like ferroelectric films.

 Received 6th January 2023,
Accepted 17th February 2023

DOI: 10.1039/d3ce00020f

rsc.li/crystengcomm

Introduction

The perovskite structure is adopted by numerous elements and therefore exhibits a wide range of various properties including ferroelectricity,¹ superconductivity,² and magnetism.³ The perovskite PbTiO₃ (PTO) is a promising and well-studied multiferroic material. At room temperature, it is ferroelectric and ferroelastic with a tetragonal structure (space group: $P4mm$), and above the Curie temperature (T_{Curie}) that is around 490 °C,⁴ it becomes paraelectric with a cubic structure (space group: $Pm3m$). It has been extensively studied with various elemental substitutions to obtain different polar phases and tunable piezoelectric and ferroelectric

properties.⁵⁻⁷ When substituting Sr onto the Pb-site, Pb_{1-x}Sr_x-TiO₃ (PST), the tetragonality of the structure is reduced and the cubic structure is reached at room temperature for $x = 0.5$.⁸⁻¹⁰ Controlling the Sr-content and thereby the structure allows the electrical properties to be tuned.^{9,11} This includes reducing the T_{Curie} but also stabilizing a -domains having interesting nanoscale switching phenomena when grown as thin films.¹²

It is possible to grow ferroelectric (thin) films using various techniques that have their own strengths and weaknesses^{13,14} depending on the requirements of the final application. The technique for growing samples should therefore be chosen depending on the desired properties while including considerations such as homogeneous doping and impurity incorporation. Here, a relatively unexplored technique for the growth of ferroelectric films, namely liquid phase epitaxy (LPE), has been applied. LPE is a unique and powerful technique that is normally applied for growing complex oxides supported by single crystalline substrates. It is especially relevant for the growth of single crystalline films for high spatial resolution X-ray imaging at synchrotron sources.¹⁵⁻¹⁷ The growth is initiated from a supersaturated

^a ESRF - The European Synchrotron, 71 avenue des Martyrs, 38000, Grenoble, France

^b Institut Lumière Matière, UMR5306 Université Lyon 1-CNRS, Université de Lyon, 69622 Villeurbanne Cedex, France. E-mail: christophe.dujardin@univ-lyon1.fr

^c Univ Lyon, INSA Lyon, CNRS, Ecole Centrale de Lyon, Université Claude Bernard Lyon 1, CPE Lyon, INL, UMR5270, 69622 Villeurbanne, France

 † Electronic supplementary information (ESI) available. See DOI: <https://doi.org/10.1039/d3ce00020f>

solution composed of the desired film oxide components and an appropriate solvent. The growth rate is high compared to those of other (thin) film deposition techniques, in the range of $0.1\text{--}1\text{ m min}^{-1}$, which is 10 to 100 times faster than molecular beam epitaxy (MBE) or metalorganic vapor-phase epitaxy (MOVPE).¹⁸ Since LPE is a near thermodynamic equilibrium technique and the growth temperature is considerably lower than that for bulk crystal growth, the defect concentration is often low.^{18,19}

In this contribution, the results from the LPE growth of PST films with a nominal $x = 0, 0.33, 0.39,$ and 0.43 on STO substrates with the crystallographic orientation (100) are presented. We demonstrate through thorough characterization of selected samples that it is possible to control the elemental composition, crystalline structure, and T_{Curie} of the films by adapting the nominal composition of the LPE melt.

Experimental section

Growth

The films were grown from two different LPE melts. One targeting films of PTO (melt 1) and the other PST with $x = 0.33, 0.39,$ and 0.43 (melt 2). All films were supported by single crystalline STO substrates with the crystallographic orientation (100). Both surfaces of the substrates are of an epi-ready quality, which is necessary for the growth of high-quality epitaxial films. The substrates are $500\text{ }\mu\text{m}$ thick and 1 inch in diameter with two truncations. However, before growth, they would be cleaved into smaller pieces. The substrates are purchased from Crystal GmbH (grown using the Verneuil method).²⁰ They report the orientation accuracy (miscut) of the substrates as $\pm 0.5\text{ }^\circ\text{C}$ but it is typically $< 0.3\text{ }^\circ\text{C}$.²¹ $\text{PbO-B}_2\text{O}_3$ was applied as the solvent and the starting powders were PbO (4 N), B_2O_3 (4 N), and TiO_2 (4 N) for melt 1 and for melt 2, SrO (3 N) powder was added increasingly between growths. Since Pb was part of both solvent (flux) and solute (film components) for these melts, meaning it is a self-flux, the Sr-content was calculated from the Ti-content even though it is expected to occupy only the Pb-site in the structure.

For LPE growth at the European Synchrotron Radiation Facility (ESRF), the melt is contained in a platinum crucible positioned in the lower part of a specially designed vertical furnace for LPE (see the schematic drawing in Fig. 1a). The furnace consists of two resistive heating zones to control the heat gradient at the furnace opening. This is important because a too steep heat gradient can cause the sample to break when entering or exiting the furnace. Three thermocouples are used to monitor the temperature: one directly on the crucible, and on the lower and upper parts of the tube. With this LPE furnace, there are normally temperature fluctuations of only approximately $0.1\text{ }^\circ\text{C}$. However, during the experiments of this study, the temperature fluctuations are estimated to be around $\pm 2\text{ }^\circ\text{C}$. The substrate is attached to a special customized platinum sample holder and growth is induced by the vertical dipping

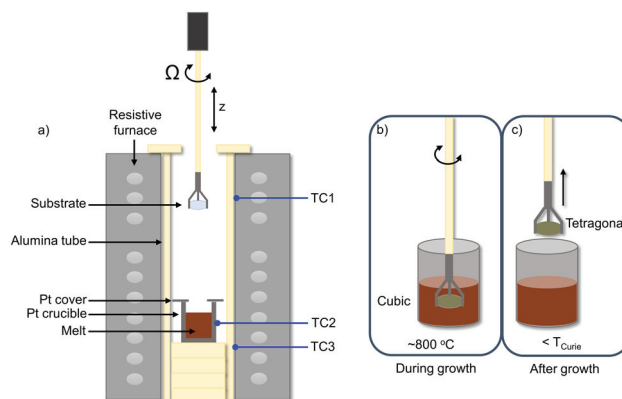


Fig. 1 a) Schematic depicting a cross-section of the applied vertical dipping method LPE furnace, where the yellow color indicates ceramic parts and TC represents thermocouples. The sample rotation (Ω) and vertical translation (z) can be controlled as well as the temperature of the two resistive heating zones. b) During film growth, the temperature of the melt was around $800\text{ }^\circ\text{C}$, meaning the film grows in the paraelectric cubic perovskite structure. c) When the sample is transferred out of the furnace, the temperature will decrease and reach below the Curie temperature (T_{Curie}). Here, the sample transforms to be ferroelectric with the tetragonal perovskite structure.

method.²² The sample rotates during the growth process with alternating directions to ensure homogeneity. After growth, the sample is positioned just above the melt, while still in the crucible, and an ejection procedure with an accelerated rotation speed is performed. This is done to remove as much of the flux still present on the sample surface as possible. The thickness of the films is estimated from their density and weight gain after growth.

Characterization

The grown films were studied using a Zeiss microscope with various objectives and geometries (reflection, transmission). For elemental analysis, a SEM-EDX instrument was used. It has an LEO 1530 scanning electron microscope equipped with an Oxford X-Max spectrometer and before elemental analysis, the instrument was calibrated with a Co sample. X-ray diffraction (XRD) and reciprocal space mapping (RSM) were performed on a Rigaku Smartlab diffractometer equipped with a Cu anode, operated at 45 kV and 200 mA . Due to the large thicknesses of the studied films ($10\text{--}17\text{ }\mu\text{m}$), there is no contribution from the substrate, and the alignment was performed in relation to the sample surface. For Raman spectroscopy, the samples were excited with a 532 nm laser operated at a power of 20 mW using a microscope Nikon $\times 20$ long working distance objective with a numerical aperture of 0.35 and a DILOR XY 500 spectrometer. A LINKAM stage was used for sample temperature control from 18 to $600\text{ }^\circ\text{C}$. Temperature-resolved spectra were collected, both with polarized (VV) and cross-polarized (HV) configurations. Piezoresponse force microscopy (PFM) was performed using an NT-MDT NTGRA microscope completed with a Zurich Instruments HF2LI system working in dual

Table 1 Atomic ratios (R) applied in the two melts: Pb/B (R1), Pb/Ti (R2), and Sr/(Sr + Ti) (R3). For the four samples focused upon in this study, the following values are given: Sample references, film thicknesses (t), applied growth temperatures (T_g), growth rate (GR), nominal content in the melt, and the estimated content in the specific films by SEM-EDX

	R1	R2	R3	Sample reference	t [μm]	T_g [°C]	GR [m s ⁻¹]	Nominal content	SEM-EDX
Melt 1	2.1	24	0	M1-17 μm	17	800 2	1.65	—	PbTiO ₃
Melt 2	2.0	32	0.33	M2-Sr0.22-10 μm	10	800 2	1.00	Pb _{0.67} Sr _{0.33} TiO ₃	Pb _{0.78} Sr _{0.22} TiO ₃
	2.0	32	0.39	M2-Sr0.25-13 μm	13	805 2	1.34	Pb _{0.61} Sr _{0.39} TiO ₃	Pb _{0.75} Sr _{0.25} TiO ₃
	2.0	32	0.43	M2-Sr0.31-12 μm	12	815 2	1.23	Pb _{0.57} Sr _{0.43} TiO ₃	Pb _{0.69} Sr _{0.31} TiO ₃

frequency resonance tracking (DFRT) mode. PtIr coated tips were used with a stiffness between 2 and 10 N m⁻¹. Both the vertical and lateral deflections were recorded to detect the component of the polarisation perpendicular to the surface (vertical) and in the plane of the surface (lateral). These are referred to as VPFM and LPFM, respectively.

Results and discussion

LPE growth

Each specific melt composition is given a reference name and for simplicity, only the samples under investigation in this paper are presented with the film thickness, growth temperature, and growth rate in Table 1. For LPE melt 2, the atomic ratios were adjusted during the experiment to investigate the influence of Sr-content, as indicated in the table. When discussing the specific samples, the reference name indicated for the specific melt composition and the estimated film thickness will be noted. An example could be M2-Sr0.31-12 μm, where M2 refers to the film grown in melt 2, Sr0.31 indicates that the film is estimated by SEM-EDX to

contain Sr/(Sr + Ti) = 0.31, and the film thickness is estimated to 12 μm. When making a general statement about the samples, the thickness is then omitted.

Melt 1. According to the description of LPE growth of PTO films by Morikoshi *et al.*,²³ a Pb/B ratio of 2.1 was used. However, the high B₂O₃ content resulted in a viscous melt. The films are transparent but have a faint brown/yellow color and have a structured appearance of lines even by visual inspection. The films would often partially separate from the substrates, see Fig. 2a, and in some cases, the samples would even break when handled after growth. This is ascribed to the large structural deformation happening in the cubic to tetragonal phase transition at 490 °C (ref. 4) and the consequent formation of polar/structural domains when cooling the sample, or in other words transferring it out of the furnace, see Fig. 1b and c. Attempts to reduce this effect have been tested for example by slowing down the cooling by transferring the sample slowly out of the furnace and applying a more gentle cleaning method of samples after growth. However, these attempts did not cause any substantial improvement.

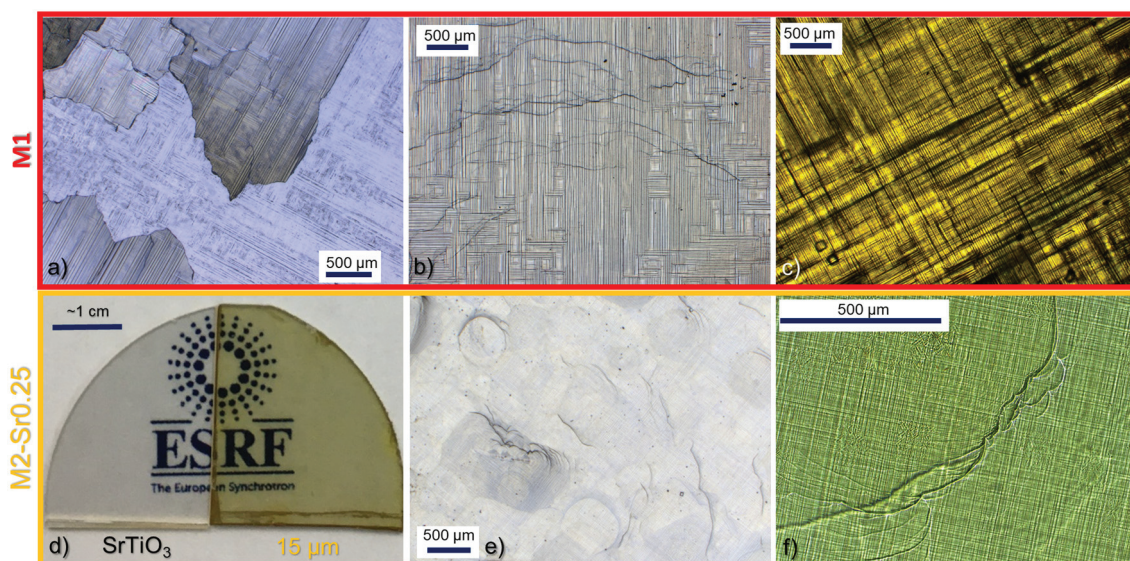


Fig. 2 Surface morphology of samples from M1 investigated with an optical microscope: a) M1-46 μm, partially detaching from the substrate, microscope in reflection geometry. b) M1-17 μm, microscope in reflection geometry. c) M1-17 μm, microscope in transmission geometry. Samples from M2: d) photograph of M2-Sr0.25-15 μm compared to an STO (100) substrate. Surface morphology of samples from M2 investigated with an optical microscope: e) M2-Sr0.25-15 μm, microscope in reflection geometry. f) M2-Sr0.31-12 μm, microscope in transmission geometry.

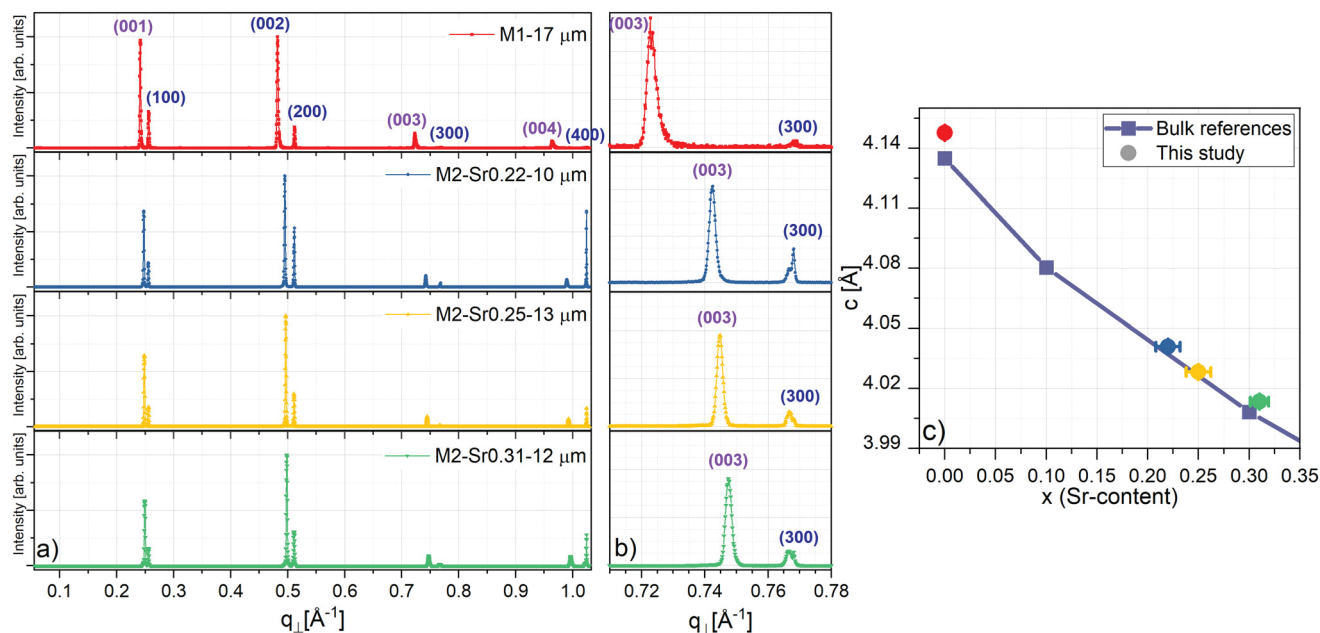


Fig. 3 X-ray diffraction 2θ - ω specular scans with indications of ($H00$) and ($00L$) peaks for the different films, with $q_{\perp} = 2/\lambda \sin(\theta)$ and $\lambda = 1.54056 \text{ \AA}$. a) Full scans. b) Zoomed-in scans of the (003) and (300) peaks for each investigated sample. c) The c -parameter calculated from the (003) and (004) 2θ values as a function of the SEM-EDX estimated Sr-content. The error bars on the c -parameter are smaller than the symbols and are calculated as the difference between the c -parameters found from the (004) and (003) peaks. The error bars on the Sr-content are calculated from the data from the SEM-EDX measurements. The results are compared to crystalline bulk references here included in symbols connected by lines corresponding to c -parameters from $\text{Pb}_{0.7}\text{Sr}_{0.3}\text{TiO}_3$ (00-057-0222), $\text{Pb}_{0.9}\text{Sr}_{0.1}\text{TiO}_3$ (00-057-0221) and PbTiO_3 (01-070-4258). See ESI† Fig. S3 for the complete series of crystalline bulk references.

Melt 2. The next attempt to avoid the film separation from the substrates was to increasingly add SrO to the melt to substitute Sr onto the Pb-site, $(\text{Pb,Sr})\text{TiO}_3$, and thereby reduce the otherwise high tetragonality of the structure. The obtained films were also a faint brown/yellow color but did not separate from the substrates, see Fig. 2d. The samples still have a structured appearance as well as a bumpy surface for all Sr-contents, see Fig. 2e and f. This can be explained by the residual flux not being easily removed after growth due to the high melt viscosity, which can result in uncontrolled growth when transferring the samples out of the furnace and thereby a bumpy surface.

Film composition

The elemental analysis by SEM-EDX validated that by adding SrO to melt 2, there was increased Sr incorporation in the films, see Table 1. The segregation coefficient²² from these results suggests that the corresponding values should be lower than 1 for the Sr incorporation. This is usual for LPE growth when adding elements as dopants or substitutions.^{24,25} Considering the ionic radii and coordination numbers of Pb^{2+} (coordination number: 12) = 1.49 Å and Ti^{4+} (coordination number: 6) = 0.61 Å in the PbTiO_3 structure, it is most favorable for Sr^{2+} to substitute into the Pb-site since its ionic radius (coordination number: 12) = 1.44 Å.

From specular 2θ - ω spectral scans, both ($00L$) and ($H00$) peaks are identified, see Fig. 3a. From this and the XRD-RSM

patterns presented in Fig. 4 (discussed in the next section), it is confirmed that all films have tetragonal symmetry and that c - and a -oriented domains are both present. In addition, there are no detectable secondary phases present, see the ESI† for Fig. 3a in log-scale (Fig. S2).

The unit cell c -parameter for each film is calculated from the peak positions of (003) and (004). Since the ionic radius²⁶ of Pb^{2+} (coordination number: 12) = 1.49 Å and Sr (coordination number: 12) = 1.44 Å, it is expected that the unit cell parameter decreases with increasing Sr while keeping the same space group. When considering the c -parameter behavior as a function of the SEM-EDX estimated Sr-content, it clearly follows this trend: increasing Sr-content results in decreasing c -parameter and thereby a decreased tetragonality, see Fig. 3c. This also supports the film composition obtained from SEM-EDX being an accurate estimation. However, when comparing M1-17 μm to the reference curve, there is a small offset (0.013 Å), which is postulated to be due to some remaining strain in the film.

Domain structure

During the phase transition from the paraelectric cubic structure to the ferroelectric tetragonal structure, various domain configurations form depending on the relative orientation of the long axis (c -axis) and short axis (a -axis) of the tetragonal lattice against the surface and other neighboring domains. Already by visual inspection, the films

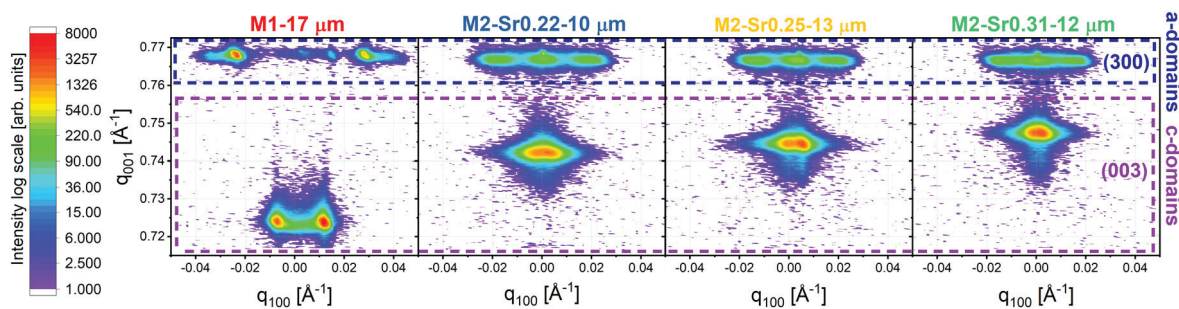


Fig. 4 XRD-RSM patterns around the (003) and (300) peaks with the sample references indicated above each figure. The types of domains and peaks are indicated on the right side of the figure.

are observed to have a microscopic domain structure as verified using an optical microscope, see Fig. 2.

By applying XRD-RSM, details are revealed about the domain structure. Due to the large thicknesses of the investigated films (10–17 μm) there are no contributions from the substrate. To have well-separated peaks, and thereby better be able to study the domain structure, RSM was performed around the (300) and (003) diffraction peaks, see Fig. 4. A tetragonal component is revealed for all the samples including a decreasing c -parameter ($q \propto d^{-1}$) with increasing Sr-content. Indeed, domains of both a -type (in-plane) and c -type (out-of-plane) are present for all the samples and the domain structure evolves with increasing Sr-content; namely, the relative domain tilts are decreasing. The tilt angle between the a - and c -domains, $\Delta\omega' = 2 \times \arctan(c/a) - \pi/2$ as defined in ref. 27, of M1–17 μm is calculated to be 3.47°. For the investigated M2 samples, it spans from 1.96 to 1.56° with

increasing Sr-content. This is consistent with the decreasing c -parameter as well as the change in surface morphology from M1 to M2 samples, for example by comparing Fig. 2b and e.

To further investigate the domain structure, PFM was applied on the investigated samples, see Fig. 5. The results from M2–Sr0.22–10 μm are not included here due to its low signal. The PFM analysis reveals for all investigated samples the existence of polar a - and c -domains consistent with the XRD-RSM measurements. The domain structure for all studied samples consists of domains with a polarisation both in and out-of-plane. There are large (several microns) superdomains inside, in which a combination of relative orientations can be found. The introduction of Sr seems to lead to a more complex domain scenery, with more and smaller different superdomains and different configurations of orientations. In particular, M2–Sr0.31–12 μm exhibits a

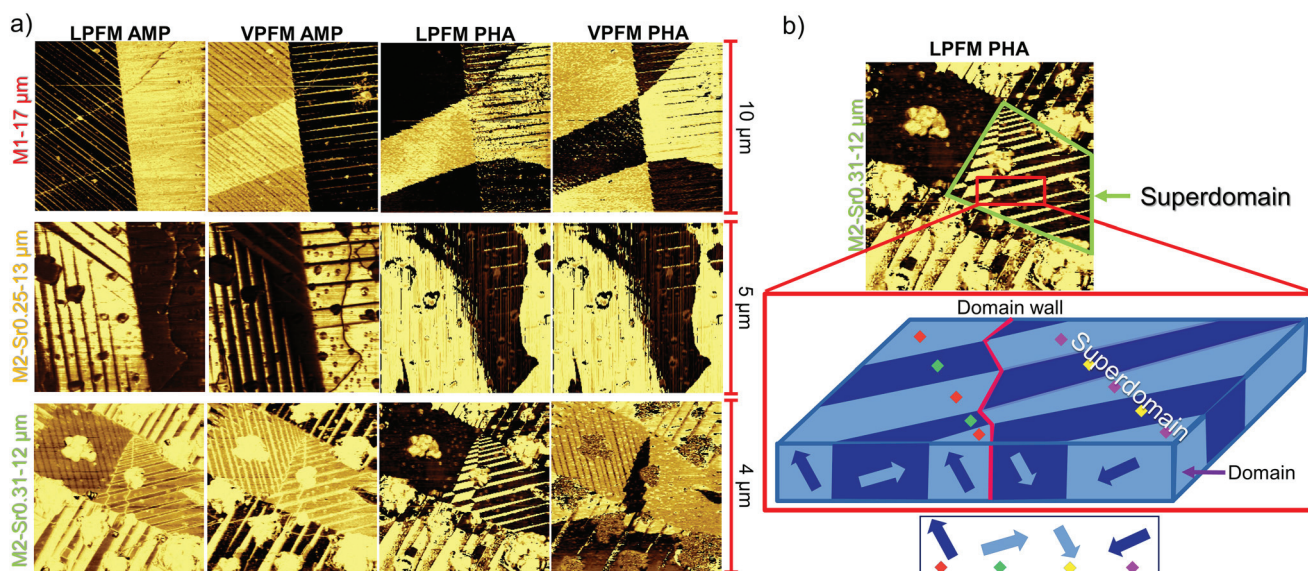


Fig. 5 a) PFM applied on three of the investigated samples. Each row corresponds to a different sample with the sample reference stated on the left. Each column corresponds to a different signal with the type stated at the top where LPFM: longitudinal PFM (in-plane contribution) and VPFM: vertical PFM (out-of-plane contribution). For the amplitude images (AMP): bright indicates low amplitude and dark high amplitude. For the phase images (PHA), there is 180° from dark to bright. Notice the difference in the size of the investigated area indicated at the right. b) LPFM of M2–Sr0.31–12 μm , the same as in a), including a schematic drawing of a possible (qualitative) configuration of domains, where the red lines indicate a domain wall.

very complex domain structure where various domain structures can be found in a small area of the sample. The same kind of configuration is also visible on the M2-Sr0.25-13 μm surface. The domain landscape becomes more complicated, with different shapes, angles, relative extensions, and locations of the different domains when the Sr-content is increased.

An example of a qualitative polarisation mapping is shown in Fig. 5b, where the relative orientation of the polarisation in a small region of the M2-Sr0.31-12 μm sample was derived by considering both VPFM and LPFM images. This detailed analysis of the polar domain configuration reveals the coexistence of a/c to c domains.

Fig. 2d and f demonstrate that the domain structure influences the optical transmittance. Detailed transmission spectra are presented in Fig. S7.†

Curie temperature

The development of the phase transition temperature and thereby the T_{curie} were investigated by temperature-resolved Raman spectroscopy, see Fig. 6a. According to the selection rules, there are several Raman modes active for the tetragonal perovskite structure that are not active for the cubic structure,²⁸ theoretically making it easier to recognize this phase transition.

The in-depth focus of the applied optics for the Raman scattering is estimated to be larger than the film thicknesses, meaning any potential substrate contribution cannot be ignored. Since STO is cubic in the applied temperature range, there should not be any contribution from active Raman

modes originating from it. However, there are indeed second-order bands arising from two phonon scattering.²⁸⁻³⁰ Spectra were recorded both in HV and VV configurations. As it appears, the second-order bands are partially suppressed when working in HV, in accordance with the result in ref. 29. Therefore, only spectra in HV are presented for the relevant temperatures. All other scans are shown in the ESI† for completeness, see Fig. S5 and S6, respectively.

For M1-17 μm at room temperature, all the observed Raman peaks can be assigned to the modes for tetragonal PTO.^{28,31} See the assignment in Fig. S4 in the ESI.† The Raman spectra of the M2 samples are dominated by broad bands in the frequency ranges of ~ 200 -550 and ~ 550 -800 cm^{-1} , which persist also during heating. These broad bands are similar to the second-order bands for STO and are reported for (Pb,Sr)TiO₃ ceramics^{28,32} as well as BaTiO₃ ceramics and single crystals.³³

To follow the phase transition, the E(TO1) mode, marked by * in Fig. 6a, was integrated as a function of temperature for all investigated samples. The T_{curie} is here assumed to be attained when the integrated intensity for E(TO1) reaches zero. The result of this is presented in Fig. 6b with the integrated intensity normalized to the maximal value. The estimated T_{curie} is presented as a function of the SEM-EDX estimated Sr-content in Fig. 6c together with the two references noted as [Xing]¹⁰ and [Nomura].³⁴ The samples follow the general trend of a decreasing T_{curie} with increasing Sr-content. However, the T_{curie} values are higher than the reference ones for a Sr-content below $x = 0.25$. This has been reported previously where the heightened phase transition temperature (up to 80 °C) was attributed to the formation of

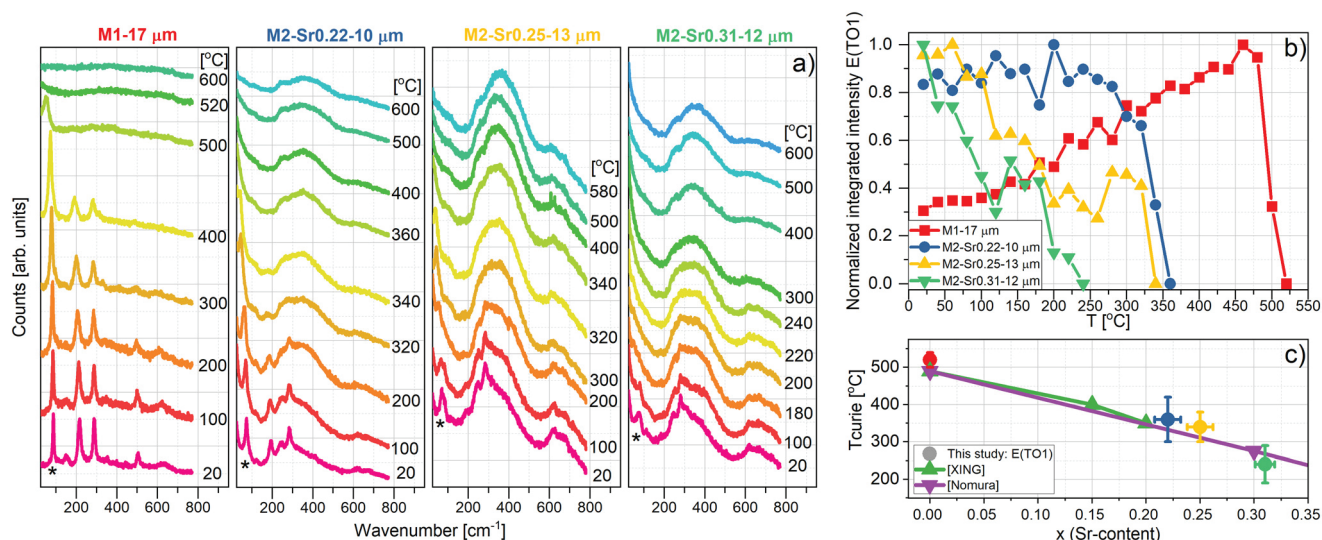


Fig. 6 a) Selected HV Raman spectra, with the sample reference stated above each figure, at selected temperatures from 20 to 600 °C. The stars (*) indicate the position of the E(TO1) mode, in which the disappearance temperature is estimated to be the T_{curie} in our study. b) Temperature dependence of the normalized integrated intensity of the E(TO1) soft mode collected in HV configuration. c) The estimated T_{curie} from a) as a function of the SEM-EDX estimated Sr-content. The error bar for T_{curie} is calculated as the difference between the HV and VV T_{curie} values. However, it is most probably overestimated both because in VV, the modes are harder to identify due to the overlapping secondary bands and for most series of spectra, the temperature step size is 20 °C. The error bars on the Sr-content are calculated from the data from the SEM-EDX measurements. The experimental data are compared with earlier reported results from the literature: [XING]¹⁰ and [Nomura].³⁴

microscale polar regions and related local symmetry breaking.²⁸ This was postulated since it was only observed when studying the short-range order probed by Raman scattering, whereas the long-range order, probed by temperature-resolved XRD, was showing the expected phase transition temperatures.

The error bar on the T_{curie} values for the samples of this study is calculated as the difference between the results of HV and VV. It is most likely overestimated since in VV, the overlapping second-order bands are more intense and therefore it makes the integration of the modes more difficult. In addition, the temperature step size is 20 °C for each spectrum, introducing further uncertainty on the estimation of the T_{curie} . However, within all these considerations, the results and trend of the T_{curie} values for all explored compositions agree with the corresponding bulk data.

Conclusion

Films of PTO and PST on STO (100) substrates have successfully been grown with the LPE crystal growth technique. By increasingly adding SrO to the LPE growth melt, the Sr-content in the films increases with the tetragonality and T_{curie} decreasing. The values approach those of bulk references, showing that the investigated PSTs maintain bulk-like properties while being grown epitaxially by LPE. The investigated samples were found by XRD-RSM and PFM to have both *a*- and *c*-oriented domains. In addition, PFM investigations revealed that the domain structures are indeed polar and the complexity of domain configuration increases for the Sr-containing samples. This study shows that LPE is a promising method for growing PST as films while preserving the bulk properties. It is the authors' hope that these encouraging results inspire others to explore LPE as a synthesis route for ferroelectric materials.

Author contributions

L. W. and P.-A. D. fabricated the films investigated in this study. I. C. I. performed XRD and XRD-RSM. J. M. performed Raman spectroscopy. B. G. performed the PFM study. L. W., T. M. and C. D. managed the project. L. W. and C. D. wrote the majority of this paper. All the authors contributed to the analysis and discussion of the results as well as proofreading the manuscript.

Conflicts of interest

There are no conflicts to declare.

Acknowledgements

Part of this work was performed within the framework of the ESRF-EBS Detector Development Plan (DDP), T1C: high-resolution scintillators for imaging detectors. The authors

thank Irina Sniguirev (ESRF, Grenoble) for performing SEM-EDX on selected samples.

Notes and references

- 1 J. Scott, *Science*, 2007, **315**, 954–959.
- 2 F. S. Galasso, *Perovskites and high-Tc superconductors*, Gordon and Breach Science Publishers Inc., 1990.
- 3 A. K. Kundu, *Magnetic perovskites*, Springer, 2016.
- 4 G. Shirane and S. Hoshino, *J. Phys. Soc. Jpn.*, 1951, **6**, 265–270.
- 5 A. Kholkin, M. Calzada, P. Ramos, J. Mendiola and N. Setter, *Appl. Phys. Lett.*, 1996, **69**, 3602–3604.
- 6 S. Yakovlev, C.-H. Solterbeck, E. Skou and M. Es-Souni, *Appl. Phys. A: Mater. Sci. Process.*, 2006, **82**, 727–731.
- 7 S. Iakovlev, C.-H. Solterbeck and M. Es-Souni, *J. Electroceram.*, 2003, **10**, 103–110.
- 8 D. H. Kang, J. H. Kim, J. H. Park and K. H. Yoon, *Mater. Res. Bull.*, 2001, **36**, 265–276.
- 9 H.-Y. Chen, J.-M. Wu, H.-E. Huang and H.-Y. Bor, *J. Cryst. Growth*, 2007, **308**, 213–217.
- 10 X. Xing, J. Chen, J. Deng and G. Liu, *J. Alloys Compd.*, 2003, **360**, 286–289.
- 11 S. Liu, Y. Lin, J. Weaver, W. Donner, X. Chen, C. Chen, J. Jiang, E. Meletis and A. Bhalla, *Appl. Phys. Lett.*, 2004, **85**, 3202–3204.
- 12 S. Matzen, O. Nesterov, G. Rispens, J. Heuver, M. Biegalski, H. Christen and B. Noheda, *Nat. Commun.*, 2014, **5**, 1–8.
- 13 Y. Wang, W. Chen, B. Wang and Y. Zheng, *Materials*, 2014, **7**, 6377–6485.
- 14 E. Sun and W. Cao, *Prog. Mater. Sci.*, 2014, **65**, 124–210.
- 15 P.-A. Douissard, A. Cecilia, T. Martin, V. Chevalier, M. Couchaud, T. Baumbach, K. Dupré, M. Kühbacher and A. Rack, *J. Synchrotron Radiat.*, 2010, **17**, 571–583.
- 16 F. Riva, T. Martin, P. Douissard and C. Dujardin, *J. Instrum.*, 2016, **11**, C10010.
- 17 T. Martin and A. Koch, *J. Synchrotron Radiat.*, 2006, **13**, 180–194.
- 18 P. Capper and M. Mauk, *Liquid phase epitaxy of electronic, optical and optoelectronic materials*, John Wiley & Sons, 2007.
- 19 P. Capper, S. Irvine and T. Joyce, in *Springer Handbook of Electronic and Photonic Materials*, Springer, 2017, pp. 309–319.
- 20 https://www.crystal-gmbh.com/en/products/substrates.php?gelid=CjwKCAjwj42UBhAAEiwACIhADQbaz1tuMYoMlwNN_wxutvJEgipu7kxs2yEPPXfgxw6hvlm5Qzg7LxoC1FoQAvD_BwE.
- 21 <https://crystal-gmbh.com/en/products/substrates.php>.
- 22 C. F. K. Rivenbark, in *Liquid-Phase Epitaxy of Advanced Materials*, ed. G. Dhanaraj, K. Byrappa, V. Prasad and M. Dudley, Springer Berlin Heidelberg, Berlin, Heidelberg, 2010, pp. 1041–1068.
- 23 H. Morikoshi, N. Uchida, A. Nakata, K. Yamasawa and Y. Narumiya, *Jpn. J. Appl. Phys.*, 1996, **35**, 4991.
- 24 C.-P. Klages and W. Tolksdorf, *J. Cryst. Growth*, 1986, **79**, 110–115.
- 25 J. Vilms and J. Garrett, *Solid-State Electron.*, 1972, **15**, 443–455.

- 26 R. T. Shannon and C. Prewitt, *Acta Crystallogr., Sect. B: Struct. Crystallogr. Cryst. Chem.*, 1970, **26**, 1046–1048.
- 27 S. Venkatesan, B. Kooi, J. De Hosson, A. Vlooswijk and B. Noheda, *J. Appl. Phys.*, 2007, **102**, 104105.
- 28 Y. I. Yuzyuk, *Phys. Solid State*, 2012, **54**, 1026–1059.
- 29 N. V. Krainyukova, V. Hamalii, A. Peschanskii, A. Popov and E. A. Kotomin, *Low Temp. Phys.*, 2020, **46**, 740–750.
- 30 W. Nilsen and J. Skinner, *J. Chem. Phys.*, 1968, **48**, 2240–2248.
- 31 C. Foster, Z. Li, M. Grimsditch, S.-K. Chan and D. Lam, *Phys. Rev. B: Condens. Matter Mater. Phys.*, 1993, **48**, 10160.
- 32 M. Jain, Y. I. Yuzyuk, R. Katiyar, Y. Somiya and A. Bhalla, *J. Appl. Phys.*, 2005, **98**, 024116.
- 33 J. Petzelt, S. Kamba and J. Hlinka, in *Ferroelectric soft modes in ceramics and films*, ed. L. Mitoseriu, Transworld Research Network, 2007, pp. 387–421.
- 34 S. Nomura and S. Sawada, *J. Phys. Soc. Jpn.*, 1955, **10**, 108–111.

Journal Name

ARTICLE TYPE

Cite this: DOI: 00.0000/xxxxxxxxxx

Supplementary information: Tunable crystalline structure and electrical properties in (Pb,Sr)TiO₃ films grown by Liquid Phase Epitaxy[†]

Laura Wollesen,^{*ab} Paul-Antoine Douissard,^a Ingrid C. Infante^c, Jeremie Margueritat^b, Brice Gautier^c, Thierry Martin^a and Christophe Dujardin^{*b}

Received Date

Accepted Date

DOI: 00.0000/xxxxxxxxxx

SEM-EDX

Table 1 gives an overview of the results from the SEM-EDX measurements performed on the studied samples and the subsequent calculations made to obtain the chemical formulas. When calculating the chemical formula of the perovskite structure (ABO₃), Ti is assumed to only occupy the B-site, Pb and Sr are assumed to occupy only A-site. For the nominal values in the LPE growth melt we refer to the main article. In Figure 1 the three spectra from the SEM-EDX measurement are presented for the three Sr-containing samples.

X-ray diffraction

In Figure 2 is the $2\theta - \omega$ specular scans from the main article presented, but here with a logarithmic Y-scale. Besides the (H00) and (00L) peaks some low intensity satellite peaks, indicated with *, for samples M2-Sr0.22-10 μm and M2-Sr0.25-12 μm are here revealed. These low intensity peaks fits with diffraction on (H0L) planes but correspond to a negligible part of the sample.

Raman spectroscopy

For M1-17 μm at room temperature all the observed Raman peaks can be assigned to the modes for tetragonal PTO^{1,2}, see Figure 4 for both HV and VV configuration.

In figure 6 and Figure 5 is all recorded Raman spectra in HV

^a ESRF - The European Synchrotron, 71 avenue des Martyrs 38000 Grenoble, France.

^b Institut Lumière Matière, UMR5306 Université Lyon 1-CNRS, Université de Lyon, 69622 Villeurbanne cedex, France.

^c Institut des Nanotechnologies de Lyon, UMR5270 Université Lyon 1-CNRS, Université de Lyon, 69621 Villeurbanne cedex, France.

[†] Electronic Supplementary Information (ESI) available: [details of any supplementary information available should be included here]. See DOI: 00.0000/00000000.

‡ Additional footnotes to the title and authors can be included e.g. 'Present address:' or 'These authors contributed equally to this work' as above using the symbols: ‡, §, and ¶. Please place the appropriate symbol next to the author's name and include a `\footnotetext` entry in the the correct place in the list.

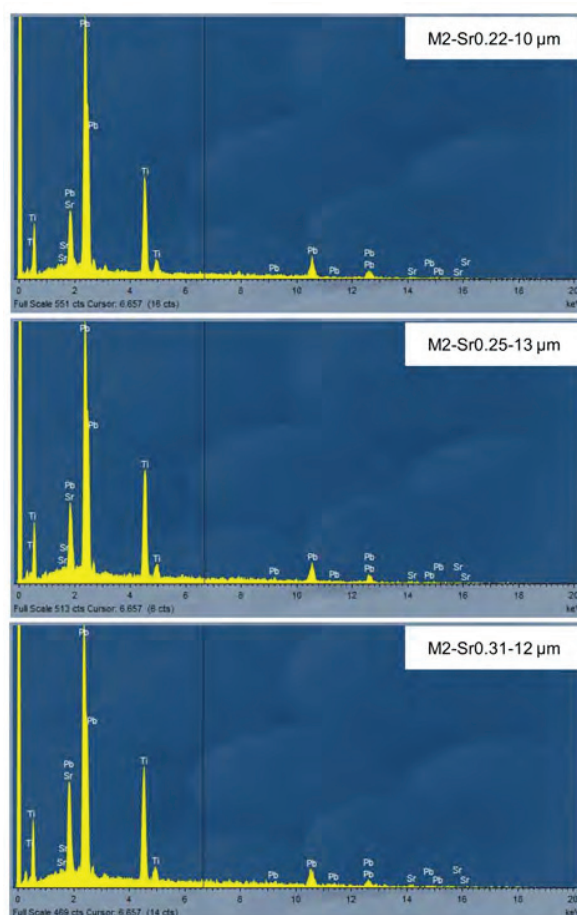


Figure S 1 SEM-EDX spectra on the Sr-containing samples. Sample references are indicated on each spectrum.

Table 1 SEM-EDX. Line: Characteristic X-ray lines, wt%: weight percent, at%: atomic weight percent, Formula: chemical formula. σ : error at first sigma level.

Sample reference	Element	Line	wt%	σ (wt%)	at%	σ (at%)	Formula	σ (Formula)
M1-17 μm	Ti	K-series	20.32	0.80	52.45	0.73		
	Pb	M-series	79.68	0.80	47.55	0.73		
M2-Sr0.22-10 μm	Ti	K-series	22.52	0.82	52.35	0.60	1	
	Sr	L-series	8.22	0.86	10.44	0.83	0.22	0.012
	Pb	M-series	69.26	1.09	37.21	0.35	0.78	0.0120
M2-Sr0.25-13 μm	Ti	K-series	23.47	0.84	53.13	0.59	1	
	Sr	L-series	9.57	0.90	11.84	0.82	0.25	0.012
	Pb	M-series	66.96	1.12	35.03	0.28	0.75	0.012
M2-Sr0.31-12 μm	Ti	K-series	22.27	0.83	50.42	0.63	1	
	Sr	L-series	12.44	0.94	15.4	0.78	0.31	0.009
	Pb	M-series	65.3	1.15	34.18	0.24	0.69	0.009

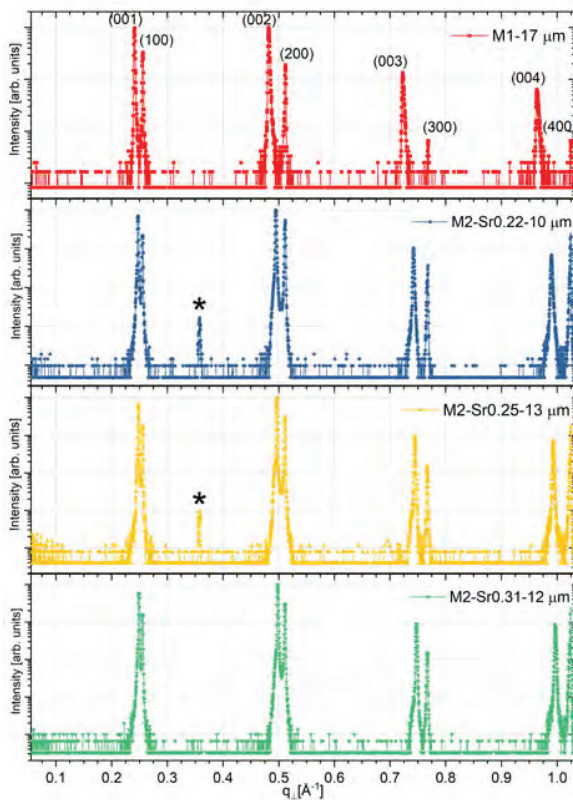


Figure S 2 X-ray diffraction $2\theta - \omega$ specular scans with indications of (H00) and (00L) peaks for the studied samples, with $q_{\perp} = 2/\lambda \cdot \sin(\theta)$ and $\lambda = 1.54056 \text{ \AA}$ and Y-axis in logarithmic scale.

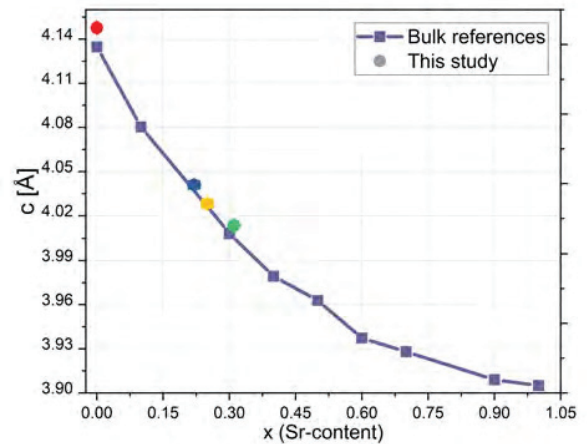


Figure S 3 The c-parameter of the investigated samples calculated from the (003) and (004) 2θ values as a function of the SEM-EDX estimated Sr-content. The error bar on the c-parameter is smaller than the symbol (difference between c parameter found by the (004) and the (003) peaks). Results compared to crystalline bulk references here included in symbols corresponding to c-parameters from SrTiO_3 (00-035-0734), $\text{Pb}_{0.1}\text{Sr}_{0.9}\text{TiO}_3$ (000570220), $\text{Pb}_{0.3}\text{Sr}_{0.7}\text{TiO}_3$ (00-062-0320), $\text{Pb}_{0.4}\text{Sr}_{0.6}\text{TiO}_3$ (00-062-0321), $\text{Pb}_{0.5}\text{Sr}_{0.5}\text{TiO}_3$ (00-052-1119), $\text{Pb}_{0.6}\text{Sr}_{0.4}\text{TiO}_3$ (00-057-0223), $\text{Pb}_{0.7}\text{Sr}_{0.3}\text{TiO}_3$ (00-057-0222), $\text{Pb}_{0.9}\text{Sr}_{0.1}\text{TiO}_3$ (00-057-0221) and PbTiO_3 (01-070-4258)

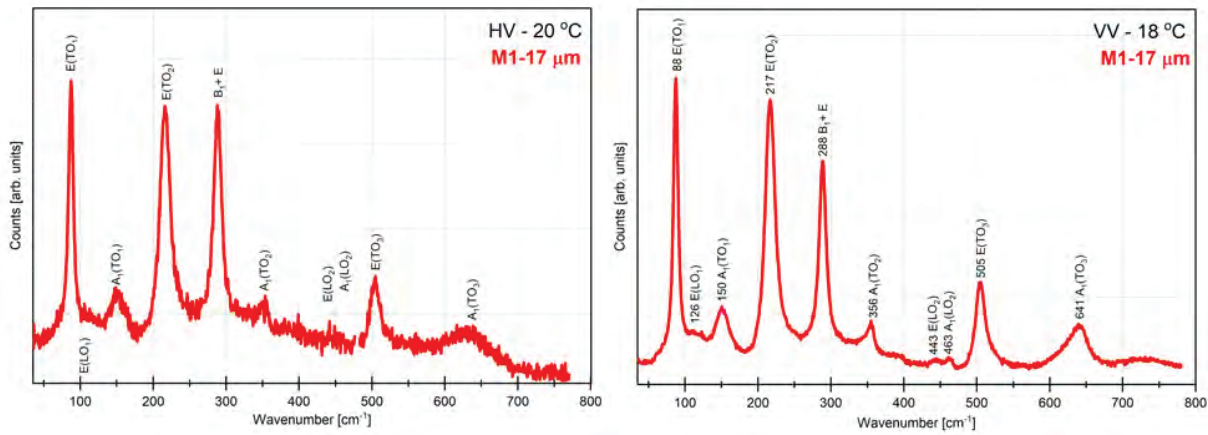


Figure S 4 Raman spectra at room temperature for M1-17 μm in VV and HV configuration with assignment of the modes according to ^{1,2}.

and VV configuration, respectively presented as a function of temperature for the four investigated samples.

Transmission spectra

The transmission spectra were collected using a Xenon lamp placed in an APEX illuminator (Newport). The lamp was coupled to a Cornerstone C260 monochromator with a 1200 lines/mm grating blazed at 350 nm. The transmitted beam reaches the sample with a spot size of $\sim 3 \times 3$ mm. The transmitted intensity was measured with a 918D-UV detector (Newport) and the sample-to-detector distance is ~ 8 mm. The substrates both used for growth and for reference here, SrTiO_3 , is 500 μm thick. The samples consist of a substrate with film on both sides, which is a consequence of growth by LPE.

The recorded transmission spectra are shown in Figure 7. The transmission for all the studied samples is lower than what is reported for thin films of similar compositions³⁻⁵. However, these thin films have a thickness in the range of 280-620 nm whereas the samples grown for this study are several micrometers thick. Indeed M1-13 m (PbTiO_3) has a reduced transmission compared

to the Sr-containing samples, which are more comparable to the substrate. The different types of domains will have various transmittance and possibly scatter/deflect the light in different ways. Since the spot size of the incoming light is considerably larger than a single domain, a mix of contributions from the different types of domains in the film on both sides and the substrate contribute to the transmission spectra. Single domain transmission spectra will be the subject of a future analysis.

Notes and references

- 1 Y. I. Yuzyuk, *Physics of the Solid State*, 2012, **54**, 1026–1059.
- 2 C. Foster, Z. Li, M. Grimsditch, S.-K. Chan and D. Lam, *Physical Review B*, 1993, **48**, 10160.
- 3 D. Ambika, V. Kumar, C. Suchand Sandeep and R. Philip, *Applied Physics B*, 2009, **97**, 661–664.
- 4 J. Yang, Y. Gao, Z. Huang, X. Meng, M. Shen, H. Yin, J. Sun and J. Chu, *Journal of Physics D: Applied Physics*, 2009, **42**, 215403.
- 5 E. Dogheche, B. Jaber and D. Rémiens, *Applied optics*, 1998, **37**, 4245–4248.

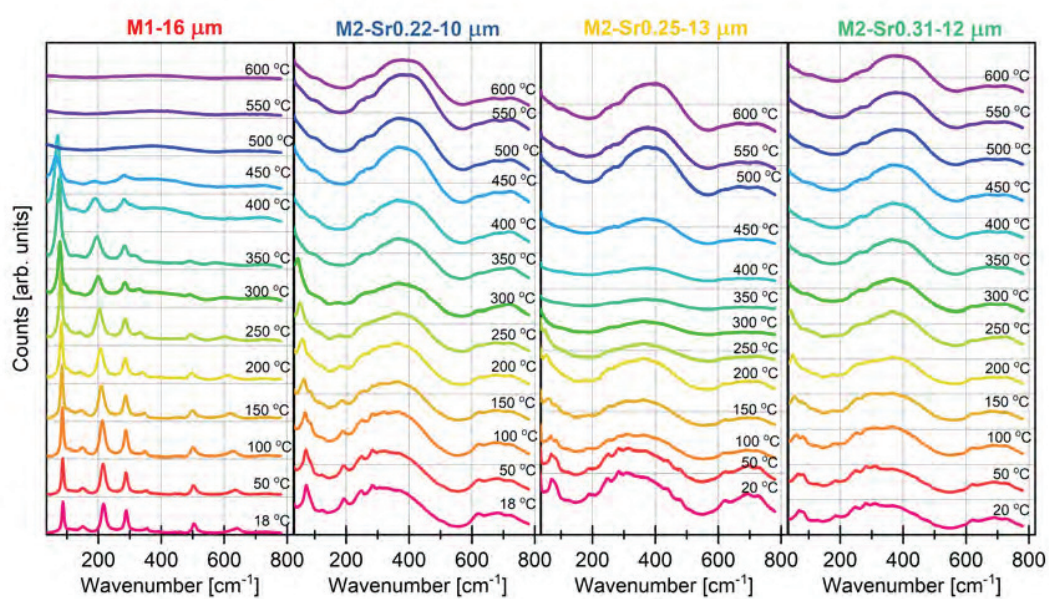


Figure S 5 All collected Raman spectra obtained in VV configuration, with the sample reference stated above each figure, at temperatures from 20 to 600 $^{\circ}\text{C}$.

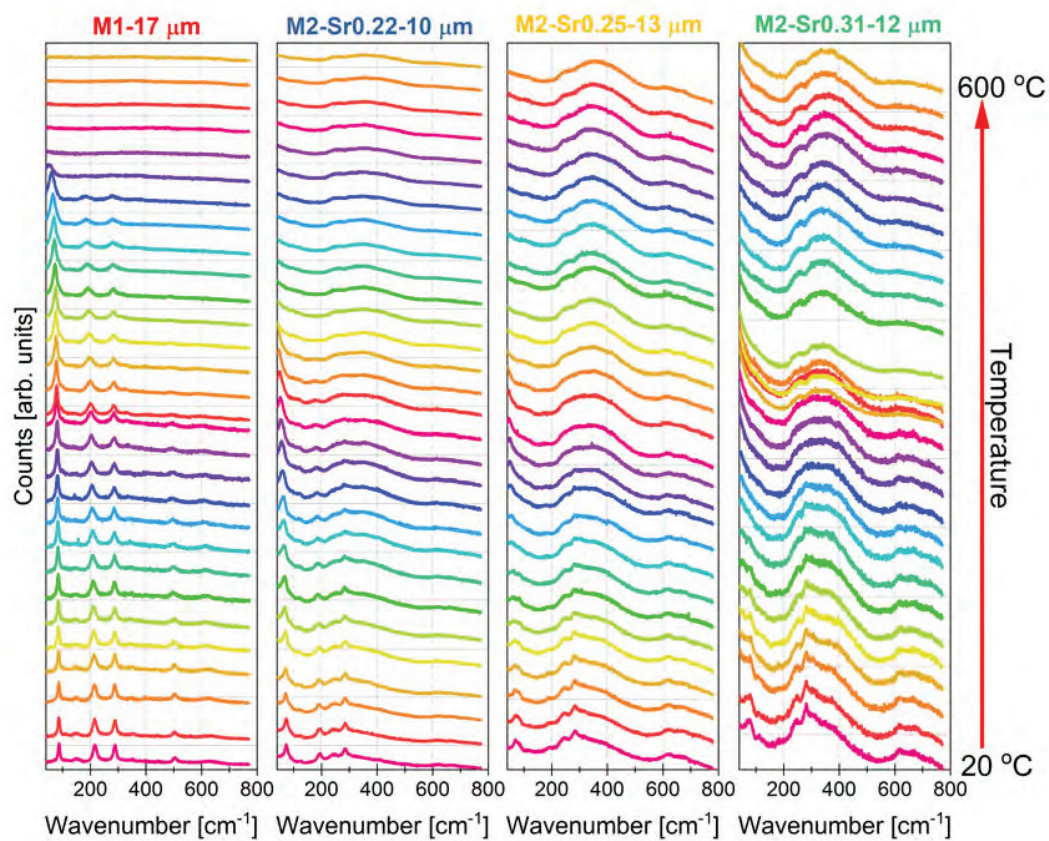


Figure S 6 All collected Raman spectra were obtained in HV configuration, with the sample reference stated above each figure, at temperatures from 20 to 600 $^{\circ}\text{C}$.

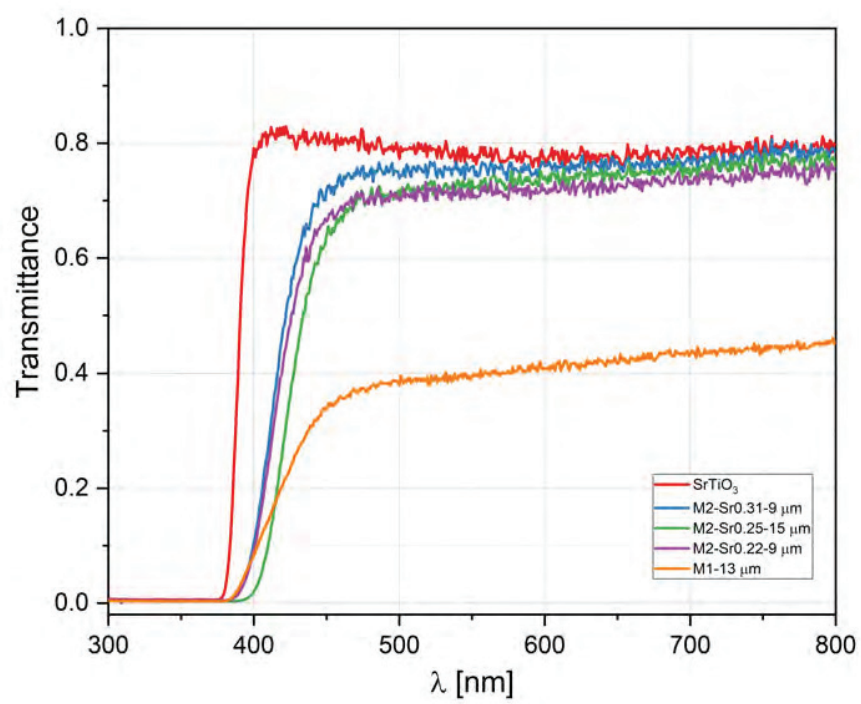


Figure S 7 Transmittance of selected samples, including a substrate. See the explanation for the sample notation in the main article.

Appendix C

Experimental technical details

C.1 Microscopes

C.1.1 Optical

To investigate the quality of the as-grown epitaxial films and micro-structures, a Zeiss Axio Imager optical microscope was used with various objectives (x2.5, x10, x20, and x50) and imaging configurations such as bright field and dark field in both transmission and reflection configuration as well as Circular polarized light - Differential Interference Contrast (CDIC).

C.1.2 Confocal

Confocal microscopy was performed at CIMAP with the help of Gurvan Brasse. To produce the 3D reconstructed surfaces, a Sensofar S neox microscope was applied using its confocal configuration. By performing micrographs during a z-scan, the software reconstructs the surface topology.

C.2 Raman spectroscopy and photoluminescence

The Raman spectroscopy and photoluminescence included in this thesis were performed at CIMAP with the help of Pavel Loiko. For both the Raman and photoluminescence, the excitation source was a pulsed laser that was micro-focused to around $2\ \mu\text{m}$. The instrument for the measurements is a Renishaw inVia Raman microscope and was handled in a back-scattered configuration. The excitation wavelength could be chosen to be either 488 nm, 457 nm or 514 nm. Various microscope objectives can be applied using this instrument. In this thesis, a x20 (NA: 0.4) or a x50 (NA: 0.3) was applied.

C.3 Radioluminescence and light output

The X-ray excitation source for both radioluminescence and light output measurements was a laboratory Phillips X-ray generator with interchangeable X-ray tubes.

For the radioluminescence spectra, the generator was equipped with a molybdenum anode X-ray tube and operated at 40 kV and 40 mA without any additional filtration. The spectra were registered with an R3896 photomultiplier tube fitted at the output of an Oriel 77200 monochromator using a 1200 lines/mm grating with 500 nm blaze wavelength.

For the light output measurements, the generator was equipped with a copper anode X-ray tube and operated at 20 kV and 40 mA. A copper filter was used to maximize the copper K-alpha contribution. The sample (scintillator) is inserted in a high-resolution setup consisting of the scintillator followed by microscope optics, a mirror reflecting the scintillating light towards the CCD Sensicam. A binning of 4x4 was applied and an exposure time of 60 s. The samples are compared to a 500 μm thick YAG:Ce and are therefore expressed as a percentage of this. The light output is corrected accordingly to the expected absorption taking into account the thickness as well as the spectral matching with the CCD sensor.

C.4 Diffractometer

XRD was performed at room temperature with a multi-purpose Panalytical Empyrean diffractometer equipped with a Ge (220) monochromator generating monochromatic copper $K_{\alpha 1}$ radiation. Measurements were performed with diffracted-beam anti-scatter slits of 7.5 mm, diffracted-beam soller slits of 0.04 Rad, and data were acquired with a 2D Hybrid photon counting Pixel detector.